

# One-Quadrupole-Phonon States of Heavy Vibrational Nuclei Studied in Coulomb Excitation

**Einquadrupolphononenzustände schwerer vibrationeller Atomkerne, untersucht mittels Coulomb-Anregung**

Zur Erlangung des Grades eines Doktors der Naturwissenschaften (Dr. rer. nat.) genehmigte Dissertation von Robert Stegmann, M.Sc. aus Offenbach am Main  
Tag der Einreichung: 13. Juni 2017, Tag der Prüfung: 17. Juli 2017  
2017 — Darmstadt — D 17

1. Gutachten: Prof. Dr. Dr. h.c. Norbert Pietralla
2. Gutachten: Prof. Dr. Thomas Aumann



TECHNISCHE  
UNIVERSITÄT  
DARMSTADT

Fachbereich Physik  
Institut für Kernphysik  
AG Pietralla



# One-Quadrupole-Phonon States of Heavy Vibrational Nuclei Studied in Coulomb Excitation

Einquadrupolphononenzustände schwerer vibrationeller Atomkerne, untersucht mittels Coulomb-Anregung

Genehmigte Dissertation von Robert Stegmann, M.Sc. aus Offenbach am Main

1. Gutachten: Prof. Dr. Dr. h.c. Norbert Pietralla
2. Gutachten: Prof. Dr. Thomas Aumann

Tag der Einreichung: 13. Juni 2017

Tag der Prüfung: 17. Juli 2017

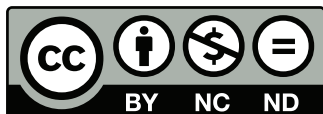
Darmstadt — D 17

Bitte zitieren Sie dieses Dokument als:

URN: [urn:nbn:de:tuda-tuprints-69399](http://nbn:de:tuda-tuprints-69399)

URL: <http://tuprints.ulb.tu-darmstadt.de/6939>

Dieses Dokument wird bereitgestellt von tuprints,  
E-Publishing-Service der TU Darmstadt  
<http://tuprints.ulb.tu-darmstadt.de>  
[tuprints@ulb.tu-darmstadt.de](mailto:tuprints@ulb.tu-darmstadt.de)



Die Veröffentlichung steht unter folgender Creative Commons Lizenz:  
Namensnennung – Keine kommerzielle Nutzung – Keine Bearbeitung 4.0 International

<http://creativecommons.org/licenses/by-nc-nd/4.0/>

---

# Abstract

One-quadrupole-phonon states of vibrational nuclei have been observed throughout the nuclear chart. Collective quadrupole excitations of symmetric and mixed-symmetric character allow for investigating the underlying microscopic nuclear structure as well as the effective proton-neutron interaction. Isovector valence-shell excitations are distinct especially near shell closures.

The  $N = 80$  isotones around the doubly-magic nucleus  $^{132}\text{Sn}$  and the region around the doubly-magic nucleus  $^{208}\text{Pb}$  are of particular interest. Projectile Coulomb-excitation experiments on the radioactive nucleus  $^{142}\text{Sm}$  and the stable nuclei  $^{202,204}\text{Hg}$  were performed in order to further our understanding of nuclear structure in these regions.

The decay strength of the first excited state of  $^{142}\text{Sm}$  is determined to  $B(E2; 2_1^+ \rightarrow 0_{1,\text{gs}}^+) = 32(4) \text{ W.u.}$  It is a foundation for the investigation of a possible *restoration of shell stabilization* in  $N = 80$  isotones above the  $Z = 58$  subshell closure.

The  $2_{1,\text{ms}}^+$  state of  $^{212}\text{Po}$  has recently been identified. The nucleus  $^{204}\text{Hg}$  is the particle-hole conjugate to  $^{212}\text{Po}$  with respect to the doubly-magic nucleus  $^{208}\text{Pb}$ .  $^{204}\text{Hg}$  was investigated together with its neighboring even-even isotope  $^{202}\text{Hg}$  for comparison to the situation in  $^{212}\text{Po}$ . One quadrupole-phonon mixed-symmetry states are identified in both nuclei, with transition strengths of  $B(M1; 2_7^+ \rightarrow 2_1^+) = 0.16(7) \mu_N^2$  in  $^{202}\text{Hg}$  and  $B(M1; 2_2^+ \rightarrow 2_1^+) = 0.20(2) \mu_N^2$  in  $^{204}\text{Hg}$ . This is the first time, that isovector valence-shell excitations have been identified in this mass region, using complete sets of decay strengths.





---

# Zusammenfassung

Einquadrupolphononen-Zustände vibrationeller Kerne konnten über die gesamte Nuklidkarte verteilt beobachtet werden. Kollektive Quadrupolanregungen symmetrischen und gemischt symmetrischen Charakters erlauben die Untersuchung der zugrundeliegenden mikroskopischen Struktur, wie auch der effektiven Proton-Neutron-Wechselwirkung. Isovektorielle Valenzraumanregungen sind nahe abgeschlossener Schalen besonders ausgeprägt.

Aus diesem Grund sind die  $N = 80$ -Isotone um das doppeltmagische  $^{132}\text{Sn}$  und die Region um das doppeltmagische  $^{208}\text{Pb}$  von Bedeutung. Um das Verständnis der Kernstruktur in diesen Regionen weiterzuentwickeln, wurden Projektil-Coulombanregungsexperimente an dem radioaktiven Kern  $^{142}\text{Sm}$  und den stabilen Kernen  $^{202,204}\text{Hg}$  durchgeführt.

Als Grundlage der Untersuchung einer möglichen *Wiederherstellung der Schalenstabilisation* in den  $N = 80$ -Isotonen oberhalb des  $Z = 58$ -Unterschalen- abschlusses, wurde die Zerfallsstärke des ersten angeregten Zustands von  $^{142}\text{Sm}$  zu  $B(E2; 2_1^+ \rightarrow 0_{1,gs}^+) = 32(4) \text{ W.u.}$  bestimmt.

Nach der kürzlichen Identifikation des  $2_{1,ms}^+$ -Zustands von  $^{212}\text{Po}$ , wird der Teilchen-Loch-Spiegelkern, bezogen auf  $^{208}\text{Pb}$ ,  $^{204}\text{Hg}$ , neben  $^{202}\text{Hg}$ , untersucht. Einquadrupolphononen gemischt-symmetrische Zustände konnten in beiden Kernen identifiziert werden, mit Übergangsstärken von  $B(M1; 2_7^+ \rightarrow 2_1^+) = 0.16(7) \mu_N^2$  in  $^{202}\text{Hg}$  und  $B(M1; 2_2^+ \rightarrow 2_1^+) = 0.20(2) \mu_N^2$  in  $^{204}\text{Hg}$ . Damit gelingt es zum ersten Mal isovektorielle Valenzraumanregungen mittels kompletten Sätzen von Übergangsstärken zu identifizieren.



---

# Contents

<b>Abstract / Zusammenfassung</b>	<b>1</b>
<b>Contents</b>	<b>5</b>
<b>1. Introduction</b>	<b>9</b>
<b>2. Experimental Techniques</b>	<b>13</b>
2.1. Coulomb Excitation . . . . .	13
2.1.1. Semi-Classical Description . . . . .	13
2.1.2. Connection to Nuclear Structure Observables . . . . .	25
2.2. Angular Distributions . . . . .	28
2.2.1. Nuclear Orientation in the Case of Axial Symmetry . . . . .	28
2.2.2. Particle- $\gamma$ Angular Correlation . . . . .	33
2.3. Recoil in Vacuum . . . . .	34
2.4. Inverse Kinematics . . . . .	37
<b>3. Nuclear Structure Theory</b>	<b>41</b>
3.1. Surface Excitations . . . . .	41
3.2. Shell Model . . . . .	46
3.3. Interacting Boson Model . . . . .	50
3.4. Quasi-Particle Phonon Model . . . . .	54
<b>4. Experimental Setup</b>	<b>57</b>
4.1. REX-ISOLDE & Miniball . . . . .	57
4.1.1. Isotope Production . . . . .	57
4.1.2. Purification . . . . .	60
4.1.3. Post Acceleration . . . . .	60
4.1.4. Gamma Spectroscopy . . . . .	63
4.2. ATLAS & Gammasphere . . . . .	67
4.2.1. Beam Production . . . . .	67
4.2.2. Acceleration . . . . .	68
4.2.3. Target Chamber & Detectors . . . . .	69

<b>5. Data Analysis and Results</b>	<b>73</b>
5.1. Data Preparation	73
5.1.1. Sorting Gammasphere Data	74
5.1.2. Kinematics and Doppler Correction	76
5.1.3. Background Subtraction	79
5.1.4. Efficiency Calibration	82
5.1.5. Coincidences	86
5.2. Angular Distribution Analysis	90
5.3. Coulomb-Excitation Calculations	91
5.4. Radioactive $^{142}\text{Sm}$	97
5.5. Stable $^{202,204}\text{Hg}$	109
5.5.1. $^{202}\text{Hg}$ Analysis	109
5.5.2. $^{204}\text{Hg}$ Analysis	118
<b>6. Discussion</b>	<b>125</b>
6.1. Shell Stabilization in the $N = 80$ Isotones	125
6.2. Mixed-Symmetry States of $^{202,204}\text{Hg}$	131
6.2.1. $^{204}\text{Hg}$	133
6.2.2. $^{202}\text{Hg}$	137
6.2.3. Mixed-Symmetry States in the Proximity of $^{208}\text{Pb}$	141
<b>7. Summary and Outlook</b>	<b>143</b>
<b>A. CLX Input</b>	<b>145</b>
<b>B. GOSIA Input</b>	<b>147</b>
<b>C. GOSIA2 Input</b>	<b>151</b>
<b>D. Relativistic Transformations</b>	<b>161</b>
<b>E. Spectra</b>	<b>167</b>
E.1. $^{142}\text{Sm}$	167
E.2. $^{202}\text{Hg}$	170
E.3. $^{204}\text{Hg}$	176
<b>Bibliography</b>	<b>183</b>
<b>List of Publications</b>	<b>199</b>



<b>List of Figures</b>	<b>203</b>
<b>List of Tables</b>	<b>205</b>
<b>Acknowledgments</b>	<b>207</b>
<b>Lebenslauf</b>	<b>209</b>



---

# 1 Introduction

The contemporary understanding of the nucleus being composed of one to about 300 nucleons was already formed in the early 1900's. Although over a century has passed since, the interactions of protons and neutrons are still subject to investigations. Various observables have been investigated, *i.e.*, energies and transition strengths of excited nuclear states. Several structures are found repeatedly among different regions of the nuclear chart. An example are the excitation energies of the  $2_1^+$  and  $4_1^+$  states of nuclei with even numbers of protons and neutrons as well as the ratio of these energies: The ratio is an indication for the deformation of a nucleus. A ratio near 2 indicates a near-spherical shape, whilst a ratio of 3.33 represents a rotating, deformed rigid body. The ratio is shown among the nuclear chart in Figure 1.1. The color code measures the degree of deformation, indicating spherical shapes near shell closures and deformed shapes in midshell regions. This led to the development of theoretical models describing the atomic nucleus under the assumption of different nature. The *Liquid-Drop model*, in the version of Bohr and Mottelson [1] describes the nucleus in a macroscopic picture as consisting of a nucleon liquid, being able to perform vibrations and rotations, while also changing its overall shape. Other approaches, like the *Shell Model* [2] are based on a microscopic approach considering individual constituent nucleons. A third class of approaches focuses on the symmetries of the nuclear quantum object, and can even be algebraic, *e.g.*, is the behavior of the nucleons in the *Interacting Boson Model* [3, 4] described by phonon bosons in second quantization [5, 6].

The degree of deformation is one particular measure for the collectivity of a nucleus, *i.e.*, the number of nucleons involved in transitions. However, the collectivity is particularly sensitive to the total number of nucleons taking part in the excitation. This is, the excitation of protons and neutrons to their respective higher-lying orbitals and the interaction between like nucleons, leading, *e.g.*, to the formation of *seniority* states. Up to this point it might seem, that the interaction of like nucleons is of uttermost importance, but the interaction of protons and neutrons is at least just as important. This is already obvious in the simplest many-body nucleon system, the Deuteron: While systems consisting of two protons or two neutrons are unbound, is a system consisting of one proton and one neutron bound. Further evidence is provided by inspection of the nuclear chart: The repulsion of protons is compensated by increased neutron numbers, which separate the protons. However, if this was the only restriction, atomic nuclei exhibiting neutron excesses would be

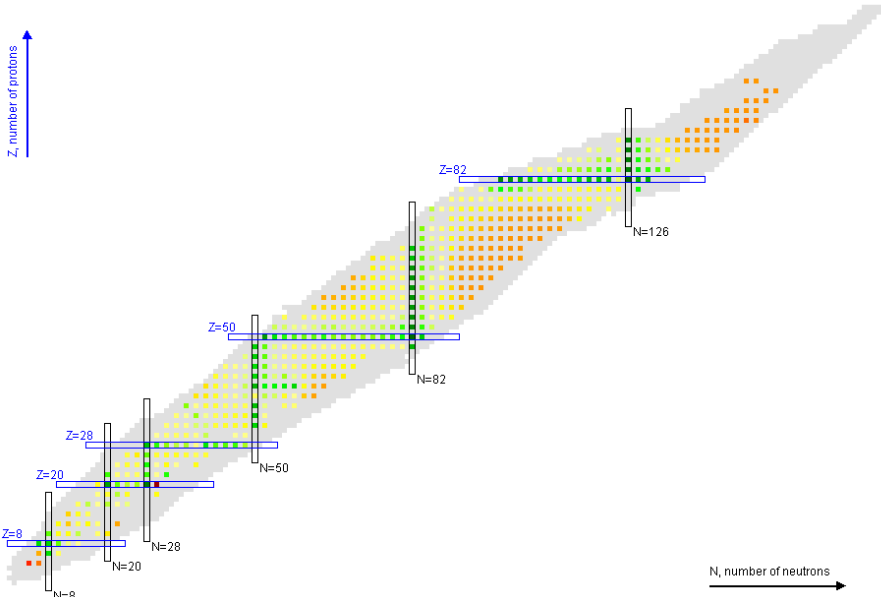


**Figure 1.1.:** Overview of the chart of nuclei. The colors code the  $R_{4/2}$  ratios of even-even nuclei, indicating shape and behavior, for values from  $< 2$  (green, spherical shape) to 3.33 (red, well deformed). The onset of deformation when moving from closed shells to midshell regions is apparent.

as stable as those with few (but not too few) neutrons. In contrast to that, real nuclei featuring an excessive number of neutrons are as unstable as those featuring an excessive number of protons, *i.e.*, possessing too few neutrons.

The formation of collectivity is still one of the fundamental issues in modern nuclear structure physics [7]. The proton-neutron interaction plays a crucial role in this process [8]. The properties of collective states in which valence protons and neutrons move out of phase contain sensitive information about the isovector part of the proton-neutron interaction, while those where they move in phase contain information about the isoscalar part of the interaction. These isovector valence-shell excitations are dubbed mixed-symmetry states (MSSs). They appear naturally in the framework of the Interacting Boson Model-2 (IBM-2) [3, 4] which distinguishes between proton and neutron bosons, alongside so-called fully-symmetric states (FSSs), where protons and neutrons are formally interchangeable.

In weakly-collective, vibrational nuclei distinct examples of one-phonon MSSs have



---

been found in stable nuclei of the mass  $A \approx 90$  region [9–11]. Several examples of MSSs have been identified in the mass  $A \approx 130$  region [12–17], as well. In the vicinity of the doubly-magic  $^{208}\text{Pb}$ , so far only a single low-lying isovector state has been identified in  $^{212}_{84}\text{Po}$  [18] recently.

The information given above is the basis of this work. An issue arose when further investigating the  $N = 80$  isotonic chain: For  $50 < Z < 58$  well-developed, single isolated MSS have been identified. In  $^{138}_{58}\text{Ce}$ , on the contrary, the MSS mixed more strongly with other states, distributing the transition strength among several levels, which is a characteristic of the so-called *lack of shell stabilization* [12]. The subshell closure takes already effect in the isoscalar quadrupole collective excitation forming the  $2_1^+$  states: A jump of the  $B(E2; 2_1^+ \rightarrow 0_{1,\text{gs}}^+)$  value is found, when passing over the subshell closure towards  $^{140}_{60}\text{Nd}$ . It shall be investigated how this evolution continues while further filling the proton  $d_{5/2}$  subshell, for which reason  $^{142}_{62}\text{Sm}$  is investigated within this work. From an experimental point of view, knowledge of the  $B(E2; 2_1^+ \rightarrow 0_{1,\text{gs}}^+)$  value is a prerequisite for the identification of the MSSs, and the investigation whether the *shell stabilization* is restored.

The method of choice for the investigation of the  $N = 80$  isotonic chain is, due to their radioactive nature and the existence of a high-lying long-lived isomeric state, projectile Coulomb excitation.

The search for MSSs, using projectile Coulomb excitation, was extended towards doubly-magic  $^{208}_{82}\text{Pb}$  in order to test the experimental method with regard to the investigation of MSSs, but also to check the applicability for heavy ions,

The investigation of  $^{202,204}\text{Hg}$ , with regard to the identification of MSSs, shall shed light on the applicability of the concepts of the IBM-2 for heavy nuclei, and provides additional benchmark points for state-of-the-art nuclear models.



---

## 2 Experimental Techniques

---

### 2.1 Coulomb Excitation

---

When investigating nuclear structure, the choice of the experimental technique is crucial. Multiple techniques are available and many of them may be applicable to a wide range of nuclei. But restrictions exist in terms of the extraction of absolute transition strength. Especially the investigation of unstable nuclei excludes different experimental techniques, *e.g.*, nuclear resonance fluorescence. For radioactive nuclei near stability fusion-evaporation reactions are generally a well-understood and widely used method for production of nuclei and simultaneous population of nuclear levels. Although this method is well-suited for a broad range of particle accelerator systems, it is restricted by the existence of long-lived isomeric nuclear states, caused by the loss of temporal correlations in typical  $\gamma$ -ray spectroscopy setups. In such cases, projectile Coulomb excitation is an appropriate choice for the population of nuclear levels. An additional advantage of this technique is its sole dependence on nuclear level energies and nuclear matrix elements as vital information for describing the complete scattering and excitation process. The mathematical description of Coulomb excitation was developed by Alder and Winther [19–21].

---

#### 2.1.1 Semi-Classical Description

---

In general, measurements in physics are performed within the frame of reference of the laboratory, while often the reaction process can be described in the center-of-mass frame of reference. The transformation between the two systems can be done by decoupling the motion of the center-of-mass from the complete kinematics, leaving the relative motion of the two nuclei in the center-of-mass system. From a kinematics point of view, the Coulomb-excitation experiment may be divided into three subsequent parts: First, the transformation of the kinetic energy of the accelerated projectile from the laboratory to the center-of-mass system, second the scattering process, and third the transformation of kinetic energies and angles of nuclei and radiation stemming from de-excitation back to the laboratory system. The first step is the transformation of the kinetic energy of the projectile from the

laboratory system to the center-of-mass system. This information is not only vital for the whole reaction process, but also essential for the preparation of a Coulomb-excitation experiment.

The transformation of the kinetic energy  $E_p$  of the projectile to the energy of the relative motion in the center-of-mass system  $E$  is, from a formal point of view, straight forward [21]:

$$E = E_p \cdot \left(1 + \frac{m_p}{m_T}\right)^{-1}, \quad (2.1)$$

with the projectile mass  $m_p$  and the target mass  $m_T$ . The ratio  $\frac{m_p}{m_T}$  can be approximated by the ratio  $\frac{A_p}{A_T}$  of the mass numbers  $A_p$  and  $A_T$  of projectile and target, respectively, at least to a precision sufficient for the kind of experiments presented within this work.

Using this transformation, the maximum beam energy for this type of measurement can be estimated. For the semi-classical description of Coulomb excitation pure electromagnetic interaction has to be guaranteed. This can be achieved by assuring to have energies below the Coulomb barrier, before nuclear forces are starting to appear. The height of the Coulomb barrier can be approximated via

$$V_C = \frac{1}{4\pi\epsilon_0} \frac{Z_p Z_T e^2}{d}, \quad (2.2)$$

where  $d$  is the distance between the centers of both nuclei,  $Z_p$  and  $Z_T$  denote the nuclear charge of projectile and target, respectively. For a spherical nucleus the radius can be calculated via  $r \approx 1.2 \text{ fm} \times A^{1/3}$ . The height of the Coulomb barrier can be derived by inserting  $d = 1.2 \text{ fm} \times (A_p^{1/3} + A_T^{1/3})$ . It is convenient in nuclear physics to give energies in terms of eV, thus the height of the Coulomb barrier is

$$V_C[\text{MeV}] = 1.2 \frac{Z_p Z_T}{A_p^{1/3} + A_T^{1/3}}. \quad (2.3)$$

A better condition is the requirement for the kinetic energy of the projectile in the laboratory system [22]

$$E_p[\text{MeV}] \lesssim 1.44 \left(1 + \frac{A_p}{A_T}\right) \frac{Z_p Z_T}{1.2 \cdot (A_p^{1/3} + A_T^{1/3}) + 5}. \quad (2.4)$$

The “+5” in the denominator indicates a safety distance of 5 fm between the surfaces of projectile and target nuclei. This might not be sufficient for collisions of light ions, but it is a valid estimate for reactions involving heavy ions.

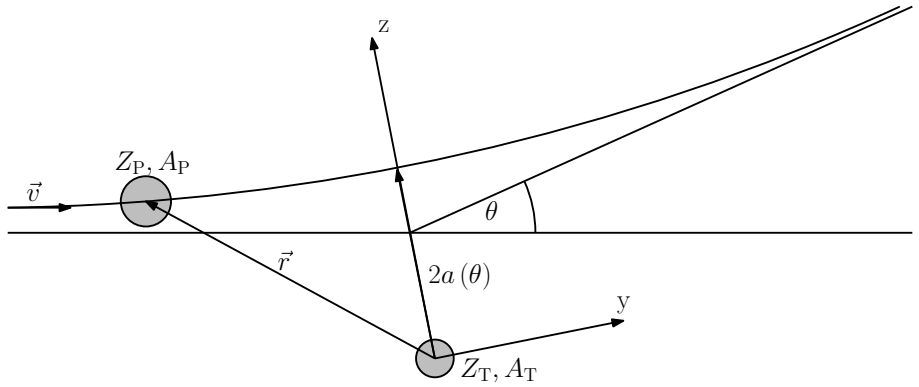


**Figure 2.1.:** Classical picture of the Coulomb-excitation scattering process, shown in the rest frame of reference of the target nucleus. Projectile and target nuclei are denoted by "P" and "T", respectively. The distance of closest approach is given by  $2a$ , which depends on the scattering angle  $\theta$  and the velocity  $\vec{v}$  of the incoming projectile ion.

The following short description of the Coulomb-excitation process can be found in great detail in [19, 21].

The scattering process in the collision of two nuclei, depicted in Figure 2.1, is – at least partly – determined by the interaction of the electromagnetic forces of both nuclei. The great simplification in sub-barrier Coulomb excitation is, besides the lack of an influence of nuclear forces, the almost complete determination of the scattering process by the electromagnetic monopole-monopole interaction of the nuclei. This interaction also ensures that the projectile nucleus does not penetrate the target nucleus. The condition

$$\eta = \frac{Z_P Z_T e^2}{\hbar v} \gg 1 \quad (2.5)$$

is a requirement for the validity of this assumption.  $v$  represents their relative velocity at large distances. In this situation the scattering itself depends only on the charges and the kinetic energy and the scattering cross section is given by the Rutherford cross section

$$\left( \frac{\partial \sigma}{\partial \Omega} \right)_R = \frac{1}{4} a^2 \frac{1}{\sin^2 \left( \frac{\theta}{2} \right)}, \quad (2.6)$$

where  $a = Z_P Z_T e^2 / m_0 v^2$ , with the reduced mass  $m_0$ , is half the distance of closest approach in a head-on collision. The condition is fulfilled in the case of  $\eta = a/\lambda \gg 1$ ,

where the wavelength  $\lambda$  of the projectile is small compared to  $a$ , implying movement of the wave packet according to the classical laws of motion. For the case of Coulomb excitation, vital information after the scattering process is not only the scattering angle, but also the state  $|n\rangle$  the nucleus is excited to. Thus the Rutherford scattering cross section is modified by the probability  $P_n$  of finding the nucleus in the state  $|n\rangle$  after the scattering process. The cross-section is then given by

$$\left(\frac{d\sigma}{d\Omega}\right)_n = \left(\frac{d\sigma}{d\Omega}\right)_R P_n. \quad (2.7)$$

Additionally, the energy transfer  $\Delta E$  from the motion of the projectile to intrinsic degrees of freedom has to be small compared to the total kinetic energy  $E$ . Otherwise the semi-classical treatment is not applicable anymore and a complete quantum-mechanical description has to be applied. Weak, inelastic processes are in general limited to the excitation of degrees of freedom if the corresponding frequency is smaller than or equal to  $1/\tau$ , where  $\tau$  is the collision time which may be approximated by  $a/v$  in the case of Coulomb excitation. Non-vanishing excitation probabilities are thus limited to states for which in first order

$$\xi_{0 \rightarrow n} = \frac{\Delta E_n}{\tau \hbar} = \frac{\Delta E_n}{\hbar} \frac{a}{v} \lesssim 1 \quad (2.8)$$

holds true for the transition from the ground state  $|0\rangle$  to the excited state  $|n\rangle$ . For excitations which cannot be considered weak, the relation is altered to  $\xi_{0 \rightarrow n} \lesssim \chi$ , where  $\chi = \sum_{\lambda} \chi^{(\lambda)}$ .  $\chi^{(\lambda)}$  is a measure for the number of exchanged gamma quanta of polarity  $\lambda$ . For weak excitations, this is naturally fulfilled but in the case of strong excitation ( $\chi > 1$ ), the condition is only fulfilled if  $\eta \gg \chi$ .

Additionally, the angular momentum transfer from the orbital motion towards intrinsic degrees of freedom  $\Delta l$  must be negligible compared to the total angular momentum  $l \approx m_0 v a = \hbar \eta$  for the classical hyperbola still being a valid assumption for the trajectory. For weak transitions,  $\Delta l$  can be estimated by  $\Delta l \leq \lambda \hbar$ , however, for strong transitions,  $\Delta l \sim \lambda \chi^{(\lambda)} \hbar$  is more realistic. In this case,  $\Delta l / l \ll 1$  is only fulfilled automatically if  $\eta \gg \chi^{(\lambda)} \lambda$ . This expresses that the multipole field has to be small, compared to the monopole field, for the theory to be applicable since  $\eta = Z_p Z_T e^2 / \hbar v = \chi^{(0)}$ .

If energy and momentum transfers are small, the center-of-mass motion of both nuclei can be completely separated from any occurring intrinsic motion. This is governed by the intrinsic wavefunction  $|\Psi_{\text{int}}\rangle$ , which is described by

$$i\hbar \frac{\partial}{\partial t} |\psi_{\text{int}}(t)\rangle = \left( H_0(P) + H_0(T) + W(P, T, \vec{r}(t)) - \frac{Z_p Z_T e^2}{|\vec{r}(t)|} \right) |\psi_{\text{int}}(t)\rangle. \quad (2.9)$$

$H_0(P)$  and  $H_0(T)$  denote the intrinsic free Hamiltonian of the projectile and target nuclei, respectively.  $\vec{r}(t)$  is the relative position of the projectile w.r.t. the target, and vice versa, and  $W(P, T, \vec{r}(t))$  is the electromagnetic interaction. The main interaction between the nuclei for the excitation of intrinsic degrees of freedom is the interaction of the monopole field of one nucleus with the multipole moments of the other one. Neglecting weaker interaction terms allows for the separation of the Schrödinger equation (2.9). This results in two equations, each depending on the intrinsic degrees of freedom of one nucleus, only:

$$i\hbar \frac{\partial}{\partial t} |\psi(t)\rangle = (H_0 + V(t)) |\psi(t)\rangle. \quad (2.10)$$

$H_0$  denotes the Hamiltonian of the free nucleus with eigenstates  $|n\rangle$ , defined via  $H_0 |n\rangle = E_n |n\rangle$ , and  $V(t)$  is the time-dependent external field at the location of the nucleus. From this, one may introduce time-dependent excitation amplitudes

$$a_n(t) = \langle n | \psi \rangle e^{iE_n t/\hbar}. \quad (2.11)$$

Under the condition that the nucleus is in its ground state at  $t \rightarrow -\infty$ , *i.e.*,  $a(-\infty) = \delta_{0n}$ , the excitation amplitudes for  $t \rightarrow +\infty$  are the square roots of the excitation probabilities, *i.e.*,

$$P_n = |a_n|^2. \quad (2.12)$$

$a_n$  denotes a state of the nucleus under investigation with spin  $J$  and magnetic quantum number  $M$ . The excitation amplitude may thus also be written as  $a_{J_f M_f, J_0 M_0}$  for an excitation from a state  $|J_0 M_0\rangle$  to a state  $|J_f M_f\rangle$ . In order to evaluate the excitation probability  $P_f$  of a certain state  $J_f$  for an ion prepared in an unpolarized ground state of spin  $J_0$ , an average over magnetic substates is taken:

$$P_f = \frac{1}{2J_0 + 1} \sum_{M_0 M_f} |a_{J_f M_f, J_0 M_0}|^2. \quad (2.13)$$

Using the amplitudes (2.12), Equation (2.10) can be transformed to a set of coupled differential equations

$$i\hbar \dot{a}_n = \sum_m \langle n | V(t) | m \rangle e^{i(E_n - E_m)t/\hbar} a_m(t). \quad (2.14)$$

It is important to outline, that this set of coupled differential equations includes the whole Coulomb excitation process, and solving this set of equations will yield all

excitation probabilities for a given nucleus. So the complete Coulomb excitation process is defined via this set of equations. The electromagnetic interaction  $V(t)$  may be expressed in a multipole expansion representation via [21, 23]

$$V(t) = \sum_{\lambda=1, \mu}^{\infty} \frac{4\pi Z_p e}{(2\lambda+1)} (-1)^\mu \bar{S}_{\lambda\mu} \mathfrak{M}(\lambda, -\mu), \quad (2.15)$$

where  $l$  denotes the multipolarity,  $\mu$  denotes the projection of the multipolarity on the symmetry axis and  $\mathfrak{M}(\lambda, -\mu)$  denotes the respective multipole operators, given by

$$\begin{aligned} \mathfrak{M}(E\lambda, \mu) &= \int \rho(\vec{r}) r^\lambda Y_{\lambda\mu}\left(\frac{\vec{r}}{r}\right) d\vec{r}, \\ \mathfrak{M}(M\lambda, \mu) &= \frac{-i}{c(\lambda+1)} \int \vec{j}(\vec{r}) r^\lambda \hat{L} Y_{\lambda\mu}\left(\frac{\vec{r}}{r}\right) d\vec{r}, \end{aligned} \quad (2.16)$$

where  $\hat{L} = -i\vec{r} \times \nabla$  is the angular momentum operator, and the point of origin coincides with the center-of-mass of the respective nucleus.  $Y_{\lambda\mu}$  denotes spherical harmonics. The orbital integrals are defined by

$$\bar{S}_{E\lambda\mu} = [r(t)]^{-\lambda-1} Y_{\lambda\mu}(\theta(t), \phi(t)) \quad (2.17)$$

for electric excitations, while for magnetic excitations they are given via

$$\bar{S}_{M\lambda\mu} = \frac{i}{\lambda} \frac{1}{r^{\lambda+1}(t)} \frac{\dot{\vec{r}}(t) \hat{L}}{c} Y_{\lambda\mu}(\theta(t), \phi(t)). \quad (2.18)$$

---

## First-Order Perturbation Theory

---

In the preceding section the issue of the evaluation of excitation probabilities and cross sections from the excitation amplitudes was broached. This shifts the problem of obtaining the cross sections towards the evaluation of the excitation amplitudes. These may be calculated via solving the coupled differential Equation (2.10), but approximately similar and more comprehensible results can be obtained by treating this issue using perturbation theory. A first step of the application of first-order perturbation theory will be outlined within this section.

The first-order perturbation treatment is limited to cases of weak interaction between the projectile and the target nuclei. This is equivalent to the condition that



the ground state and the final state are not strongly coupled to other states and imposes the practical restriction to projectiles of low charge for the validity of this approximation. The excitation amplitude for the excitation of a state  $|J_f M_f\rangle$  from the ground state  $|J_0 M_0\rangle$  is in first-order perturbation theory given by

$$a_{J_f M_f, J_0 M_0} = \frac{1}{i\hbar} \int_{-\infty}^{\infty} \langle J_f M_f | V(t) | J_0 M_0 \rangle e^{i(E_f - E_0)t/\hbar} dt, \quad (2.19)$$

where  $E_f$  and  $E_0$  are the energies of the excited state and the ground state, respectively. The amplitude may be rewritten to

$$a_{J_f M_f, J_0 M_0} = \frac{4\pi Z e}{i\hbar} \sum_{\lambda\mu} \frac{(-1)^\mu}{2\lambda + 1} \langle J_f M_f | \mathfrak{M}(\sigma\lambda, -\mu) | J_0 M_0 \rangle S_{\sigma\lambda\mu}, \quad (2.20)$$

where  $\sigma \in \{E, M\}$ ,  $Z$  is the nuclear charge of the nucleus providing the external field and  $S_{\sigma\lambda\mu} = \int_{-\infty}^{+\infty} \tilde{S}_{\sigma\lambda\mu} e^{i(E_f - E_0)t/\hbar} dt$ . It is obvious that nuclear structure properties enter only through the multipole matrix elements connecting the initial and final states. The properties of the collision solely influence the orbital integrals  $S_{\sigma\lambda\mu}$ . From the definition of the multipole operators follows the relation  $(-1)^\mu \mathfrak{M}(\sigma\lambda, -\mu) = \mathfrak{M}(\sigma\lambda, \mu)^\dagger$ . The matrix elements themselves can be expressed as products of 3j symbols and reduced matrix elements according to the definition

$$\langle J_0 M_0 | \mathfrak{M}(\sigma\lambda, \mu) | J_f M_f \rangle = (-1)^{J_0 - M_0} \begin{pmatrix} J_0 & \lambda & J_f \\ -M_0 & \mu & M_f \end{pmatrix} \langle J_0 || \mathfrak{M}(\sigma\lambda) || J_f \rangle. \quad (2.21)$$

Using the above mentioned relations, Equation (2.20) may be rewritten into the form

$$a_{J_f M_f, J_0 M_0} = \frac{4\pi Z e}{i\hbar} \sum_{\lambda\mu} \frac{1}{2\lambda + 1} (-1)^{J_0 - M_0} \begin{pmatrix} J_0 & \lambda & J_f \\ -M_0 & \mu & M_f \end{pmatrix} \langle J_0 || \mathfrak{M}(\sigma\lambda) || J_f \rangle S_{\sigma\lambda\mu}, \quad (2.22)$$

where the nuclear properties are completely enclosed within the reduced matrix elements, and separated from the properties of the scattering process. The orbital integral  $S_{\sigma\lambda\mu}$  covers the whole relative orbital motion of projectile and target nuclei and can be expressed by the dimensionless integral  $R_\lambda$  depending only on the scattering angle  $\theta$  and the parameter  $\xi$ . The excitation probabilities may then be written as

$$P_f = \sum_{\lambda} \left| \chi_{0 \rightarrow f}^{(\sigma\lambda)} \right|^2 R_{\sigma\lambda}^2(\theta, \xi), \quad (2.23)$$

where  $\chi_{0 \rightarrow f}^{(\sigma\lambda)}$  denotes the strength parameter, which square measures the excitation probability of a state  $|f\rangle$  from electromagnetic radiation of multipolarity  $\lambda$ . Its definition is

$$\chi_{0 \rightarrow f}^{(E\lambda)} = \frac{\sqrt{16\pi}Ze}{\hbar v} \frac{(\lambda-1)!}{(2\lambda+1)!!} \frac{\langle J_0 \| \mathfrak{M}(E\lambda) \| J_f \rangle}{a^\lambda \sqrt{2J_0+1}}, \text{ and} \quad (2.24)$$

$$\chi_{0 \rightarrow f}^{(M\lambda)} = \frac{\sqrt{16\pi}Ze}{\hbar c} \frac{(\lambda-1)!}{(2\lambda+1)!!} \frac{\langle J_0 \| \mathfrak{M}(M\lambda) \| J_f \rangle}{a^\lambda \sqrt{2J_0+1}}. \quad (2.25)$$

This parameter covers the whole nuclear structure of the nucleus under investigation and only depends on the multipolarity of the radiation and the matrix element connecting the initial and final states.

The integral  $R_\lambda^2$  covering the kinematics of the reaction may be expressed in terms of spherical harmonics and Coulomb excitation functions

$$I_{\lambda\mu} = \int_{-\infty}^{+\infty} \frac{[\epsilon + \cosh(w) + i\sqrt{\epsilon^2-1} \sinh(w)]^\mu}{[1 + \epsilon \cosh(w)]^{\lambda+\mu}} \exp[i\xi(\epsilon \sinh(w) + w)] dw, \quad (2.26)$$

where  $\epsilon = [\sin(\theta/2)]^{-1}$  for  $0 \leq \theta \leq 180^\circ$ , via

$$R_{E\lambda}^2(\theta, \xi) = \left| \frac{(2\lambda-1)!!}{(\lambda-1)!} \right|^2 \frac{\pi}{2\lambda+1} \sum_{\mu} |Y_{\lambda\mu}(\pi/2, 0) I_{\lambda\mu}(\theta, \xi)|^2, \text{ and} \quad (2.27)$$

$$R_{M\lambda}^2(\theta, \xi) = \frac{\pi}{2\lambda+3} \left( \frac{(2\lambda-1)!!}{(\lambda-1)!} \right)^2 \sum_{\mu} [(\lambda+1)^2 - \mu^2] \\ \times |Y_{\lambda+1,\mu}(\pi/2, 0)|^2 |I_{\lambda+1,\mu}(\theta, \xi)|^2 \cot^2(\theta/2). \quad (2.28)$$

This allows the computation of the first-order Coulomb excitation cross sections for electric and magnetic excitations. For the first-order perturbation theory, effects of multipole-multipole interactions are of the order  $1/\eta^2$ . However, for the first-order  $\eta \gg 1$  must be required, thus, multipole-multipole interactions can be neglected. But energy loss during the collision can be relevant, if  $\eta$  is in the order of 1-10, which leads to the natural occurrence of so-called symmetrized parameters  $a$  and  $\xi$ . They are defined as follows:

$$a_{if} = \frac{Z_p Z_T e^2}{m_0 v_i v_f} \quad (2.29)$$

$$\xi = \frac{\Delta E}{\hbar} \frac{a_{if}}{v_i + v_f/2} = \eta_f - \eta_i, \quad (2.30)$$

where  $i$  and  $f$  denote quantities before ( $t \rightarrow -\infty$ ) and after ( $t \rightarrow +\infty$ ) the collision takes place, respectively. This results in a slight modification of the Coulomb-excitation cross section of a state  $|f\rangle$  from the ground state  $|0\rangle$  towards

$$\frac{d\sigma}{d\Omega} = \frac{v_f}{v_i} P_f \frac{1}{4} a_{if}^2 \frac{1}{\sin^4(\theta/2)}. \quad (2.31)$$

From this it is clearly visible, that the first-order excitation cross-section only depends, in terms of nuclear properties, on the matrix element connecting the ground and the final state and represents thus the one-step excitation-process. But the assumption, that this renders the complete Coulomb excitation process is only approximately valid in the case of  $\chi_{0 \rightarrow f}^{(\sigma\lambda)} \ll 1$ .

---

## Second- / Higher-Order Perturbation Theory

---

A complete quantum mechanical solution approach has to be used, for cases where  $\chi \gtrsim 1$ . However, in some situations considering higher order corrections to first order perturbation theory can be sufficient to describe the excitation process quite well. In most cases including second order terms already covers most excitations occurring during the scattering process.

Advancing from first to second order terms modifies the excitation amplitude of a state  $|f\rangle$  such that it is the sum of the excitation amplitudes  $a_n = a_n^{(1)} + a_n^{(2)}$ , where  $a_n^{(x)}$ ,  $x \in \{1, 2\}$  denote the excitation amplitudes of first and second order, respectively. While the first order amplitude was given as sum over the magnetic quantum numbers over Equation (2.22), the second order amplitude in the case of electric excitation is given by

$$\begin{aligned} a_{J_f M_f, J_0 M_0}^{(2)} = & -\frac{16\pi^2 Z^2 e^2}{\hbar^2} \sum_{\substack{\lambda\lambda' \\ \mu\mu' z}} \frac{1}{(2\lambda+1)(2\lambda'+1)} \\ & \times \langle J_0 M_0 | \mathfrak{M}(E\lambda, \mu) | J_z M_z \rangle^* \langle J_z M_z | \mathfrak{M}(E\lambda', \mu') | J_f M_f \rangle^* \\ & \times \int_{-\infty}^{+\infty} dt \bar{S}_{E\lambda'\mu'}(t) e^{i\omega_{fz}t} \int_{-\infty}^t dt' \bar{S}_{E\lambda\mu}(t') e^{i\omega_{z0}t'}. \end{aligned} \quad (2.32)$$

This closely resembles the structure of a product of two first order amplitudes, but the equation is not just the excitation and deexcitation of a state, but covers all two-step excitation paths of a state with intermediate states  $|z\rangle$ . The evaluation

of this amplitude requires not only consideration of intermediate states  $|z\rangle$  with lower energy than the final state  $|f\rangle$ , but all possible states and resonances which may be reached via Coulomb excitation, in general. Although only states fulfilling  $\xi_{0 \rightarrow n} \lesssim \chi$  have a non-vanishing excitation amplitude, non-excited intermediate states can still influence the excitation amplitudes of lower lying final states (so-called *polarization effects*).

The evaluation of the second order excitation probability of a state  $|f\rangle$  yields

$$P_f = P_f^{(1)} + P_f^{(1,2)} + P_f^{(2)}, \quad (2.33)$$

where  $P_f^{(1)}$  denotes the first order excitation probability given in Equation (2.23) as  $P_f$ . The different terms are visualized in Figure 2.2. It should be emphasized that this probability scales with the sum of the absolute squares of the  $\chi$  parameters, ensuring they are positive real numbers.

The third term  $P_f^{(2)}$  is the square of the second order excitation amplitude, covering pure two-step excitations over the complete set of intermediate states. Using 6-j symbols, it is defined as

$$\begin{aligned} P_f^{(2)} = & \frac{1}{4} \sum_{\substack{\lambda_1 \lambda'_1 \lambda_2 \lambda'_2 \\ J_z J_{z'} k}} \sqrt{(2J_z + 1)(2J_{z'} + 1)(2\lambda_1 + 1)(2\lambda'_1 + 1)(2\lambda_2 + 1)(2\lambda'_2 + 1)} \\ & \times (2k + 1) \begin{Bmatrix} \lambda_1 & \lambda_2 & k \\ J_f & J_0 & J_z \end{Bmatrix} \begin{Bmatrix} \lambda'_1 & \lambda'_2 & k \\ J_f & J_0 & J_{z'} \end{Bmatrix} \chi_{0 \rightarrow z}^{(\lambda_1)} \chi_{z \rightarrow f}^{(\lambda_2)} \chi_{0 \rightarrow z'}^{(\lambda'_1)} \chi_{z' \rightarrow f}^{(\lambda'_2)} \\ & \times \sum_{\kappa} \left[ R_{(\lambda_1 \lambda_2)k\kappa}^* R_{(\lambda'_1 \lambda'_2)k\kappa}^* + G_{(\lambda_1 \lambda_2)k\kappa}^* G_{(\lambda'_1 \lambda'_2)k\kappa}^* \right], \end{aligned} \quad (2.34)$$

where  $R_{(\lambda_1 \lambda_2)k\kappa}$  and  $G_{(\lambda_1 \lambda_2)k\kappa}$  denote complex double integrals defined in [21].

The second term  $P_f^{(1,2)}$  is the interference between first and second order amplitudes. This term couples the processes of one- and two-step excitation

$$\begin{aligned} P_f^{(1,2)} = & \sum_{\lambda \lambda' \lambda'' J_z} \sqrt{(2J_z + 1)(2\lambda + 1)(2\lambda' + 1)(2\lambda'' + 1)} (-1)^{J_0 + J_f} \begin{Bmatrix} \lambda & \lambda' & \lambda'' \\ J_z & J_f & J_0 \end{Bmatrix} \\ & \times \chi_{0 \rightarrow f}^{(\lambda)} \chi_{0 \rightarrow z}^{(\lambda')} \chi_{z \rightarrow f}^{(\lambda'')} \sum_{\mu} R_{\lambda\mu}^*(\theta, \xi_{0 \rightarrow f}) G_{(\lambda' \lambda'')\lambda\mu}(\theta, \xi_{0 \rightarrow z}, \xi_{z \rightarrow f}). \end{aligned} \quad (2.35)$$

The terms appearing in the second order approach give rise to a number of interesting effects, allowing for a more detailed investigation of nuclear structure.

Consider following situation: A  $2^+$  state is excited either directly from the ground

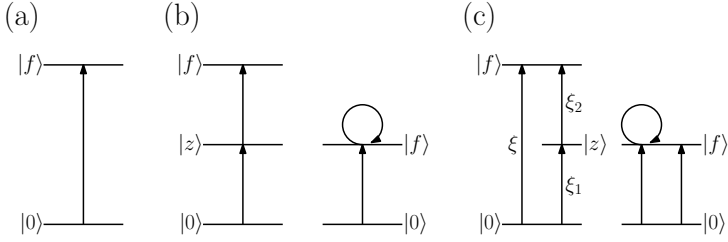


**Figure 2.2.:** Schematic view of the first and second order perturbation theory contributions to Coulomb excitation.  $|0\rangle$  indicates the ground state of the nucleus under investigation,  $|f\rangle$  indicates the final state to populate and  $|z\rangle$  indicates intermediate states. (a) depicts the first order term, where the final state is populated directly from the ground state. (b) shows the second order term, with two-step excitation on the left and the reorientation effect on the right. (c) shows the interference of first and second order terms. The excitation probabilities of the states depend on  $\xi = a \Delta E / \hbar v$ .

state via an E2 transition or by double excitation via another  $2^+$  state. This is visualized on the left side of Figure 2.2(c). The excitation probability may be written in compact form

$$P_{2'} = |\chi_{0 \rightarrow 2'}|^2 R_2^2(\theta, \xi_{0 \rightarrow 2'}) [1 + y c(\theta, s, \xi_{0 \rightarrow 2'})], \quad (2.36)$$

where  $s = \frac{\xi_{0 \rightarrow 2}}{\xi_{0 \rightarrow 2'}} = \frac{\xi_{0 \rightarrow 2}}{\xi_{0 \rightarrow 2} + \xi_{2 \rightarrow 2'}}$  measures the excitation energy of the first  $2^+$  state relative to the one of the second  $2^+$  state, while

$$y = \frac{\chi_{0 \rightarrow 2} \chi_{2 \rightarrow 2'}}{\chi_{0 \rightarrow 2'}} = \chi_{0 \rightarrow 2} \frac{1}{\sqrt{5}} \frac{\langle 2 || \mathfrak{M}(E2) || 2' \rangle}{\langle 0 || \mathfrak{M}(E2) || 2' \rangle} \quad (2.37)$$

measures the relative transition strengths. In this case of assumed pure electric transitions  $R_2^2(\theta, \xi_{0 \rightarrow 2'})$  is given by Equation (2.27).

$$c(\theta, s, \xi_{0 \rightarrow 2'}) = 5 \sum_{\mu} \frac{R_{2\mu}(\theta, \xi_{0 \rightarrow 2'})}{R_2^2(\theta, \xi_{0 \rightarrow 2'})} G_{(22)2\mu}(\theta, \xi_{0 \rightarrow 2}, \xi_{2 \rightarrow 2'}) \quad (2.38)$$

is a measure for the deviation of the angular dependence of the second order excitation relative to the angular dependence of the first order approximation. The sole

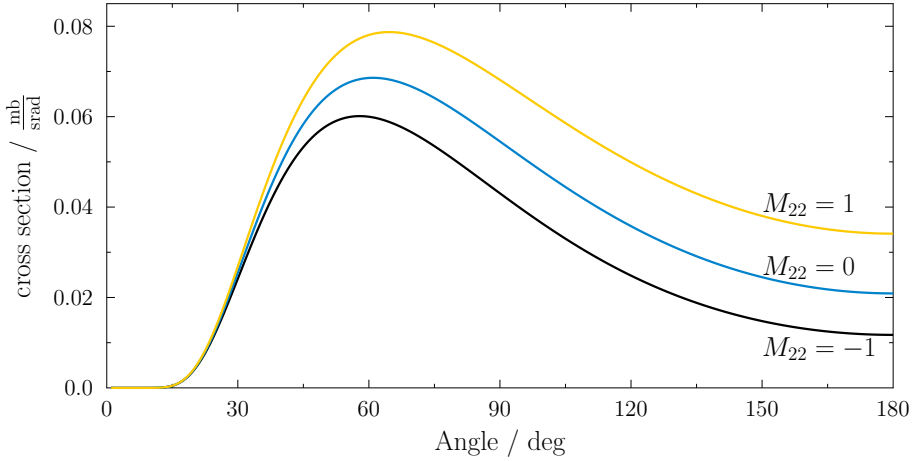


**Figure 2.3.:** Evolution of the Coulomb excitation cross section for the reaction  $^{94}_{42}\text{Mo}_{52}(^{142}_{62}\text{Sm}_{80}, ^{142}_{62}\text{Sm}^*_{80})^{94}_{42}\text{Mo}^*_{52}$  in the center-of-mass system in order to evaluate the quadrupole moment of the  $2^+_1$  state of  $^{142}\text{Sm}$ . This highlights the importance of measuring the angles of the scattered particles. In particular the shift of the maximum of the curve allows for distinction of the effect of a non-vanishing quadrupole moment or an increased decay matrix element.

existence and necessity of the function  $c(\theta, s, \xi)$  emphasizes the supplementary information which can be gained by measuring the angle of the scattered projectile and target nuclei.

While this might not be necessary for the investigation of transitions between excited nuclear states, this information is vital for the measurement of static moments of excited states. The differing angular dependence only allows for the measurement of static moments of excited states. A non-vanishing static moment will change the slope of the cross section with respect to the scattering angle. In particular, the maximum of the cross section will be shifted towards larger angles for positive static moments or to smaller angles for negative moments (cf. Figure 2.3). This shift also allows for the measurement of the sign of static moments. The excitation probability for the case of a static quadrupole moment of an excited  $2^+$  state can be retrieved from Equation (2.36) for  $2' = 2$ , resulting in

$$P_2 = \left| \chi_{0 \rightarrow 2}^{(2)} \right|^2 R_2^2(\theta, \xi_{0 \rightarrow 2}) \left[ 1 + \chi_{2 \rightarrow 2}^{(2)} c(\theta, s = 1, \xi_{0 \rightarrow 2}) \right]. \quad (2.39)$$

The parameter  $\chi_{2 \rightarrow 2}^{(2)}$  is proportional to the matrix element connecting the magnetic substates of the excited  $2^+$  states. This implies a proportionality to the spectroscopic quadrupole moment of the state:

$$\chi_{2 \rightarrow 2}^{(2)} = \frac{4}{15} \sqrt{\frac{\pi}{5}} \frac{Ze}{\hbar v} \frac{1}{a^2} \langle 2 \| \mathfrak{M}(E2) \| 2 \rangle = \sqrt{\frac{7}{90}} \frac{Ze}{\hbar v} Q_2, \quad (2.40)$$

with  $\langle 2 \| \mathfrak{M}(E2) \| 2 \rangle = \sqrt{7/2\pi}^{5/4} Q_2 = 1.319 Q_2$ . This allows determination of static moments of excited states by measuring relative cross sections under various scattering angles of the nucleus under investigation. The influence of such a static moment manifests in transitions between the different m-substates of an excited state, causing the change in the slope of the cross section, and is called the “reorientation effect” [21].

---

## 2.1.2 Connection to Nuclear Structure Observables

---

The structure of a nucleus is given by the wave functions of its states. These wave functions are not directly accessible experimentally. However, the overlap of the wave functions of two nuclear states is described by the matrix elements connecting these states. It can be seen from section 2.1.1 that these matrix elements influence the excitation cross-sections. Ratios of matrix elements are related, amongst others via the corresponding transition energies, to ratios of measured  $\gamma$  ray intensities.

Typical experimental setups comprise HPGe<sup>1</sup> detectors, suitable for measuring  $\gamma$  rays, and, in part, highly segmented DSSSDs<sup>2</sup> for the measurement of particle scattering angles and energies. The prime information obtained from the experiment is limited to  $\gamma$ -ray energies and intensities as well as scattering angles of projectile and recoiling target-like nuclei. However, the interesting information about the nuclear structure is contained in the transition matrix elements, requiring a connection of the prime experimental information to the nuclear structure.

$\gamma$  radiation is produced in the decay of excited nuclear states. Analogous to connecting (excited) nuclear states in the Coulomb-excitation process, the electromagnetic interaction operator is also able to connect states for the purpose of decay. Although the multipole decomposition leads in general to an infinite sum of terms

---

<sup>1</sup> High Purity Germanium

<sup>2</sup> Double-Sided Silicon-Strip Detector

over all multipolarities, angular momentum coupling and the parities of the initial and final states restrict the possible transition characters:

$$|J_i - J_f| \leq \lambda \leq J_i + J_f \quad (2.41)$$

$$\pi_\gamma = \pi_i \cdot \pi_f = \begin{cases} (-1)^\lambda & \text{for electric character,} \\ (-1)^{\lambda+1} & \text{for magnetic character.} \end{cases} \quad (2.42)$$

It is seen from these equations that transitions between two states are not restricted to one multipolarity, but can decay, in general, through several of them. Special cases are transitions connected to  $0^+$  states, which exhibit pure multipolarities. Commonly, decays of lower multipolarities dominate over such with higher ones, whereas electric transitions dominate over magnetic ones. From these information, the domination of the two decays of lowest multipolarity can be deduced.  $\pi\lambda$  is in fact an observable as the decay radiation of an aligned nucleus exhibits a clear angular distribution, which only depends on the multipolarity and the transition character. In the non-pure case the problem arises, that the measured angular distribution is a superposition of the angular distributions of all the possible transitions. Combining these findings allows to define a ratio of the most intense transitions:

$$\delta^2 = \frac{\Gamma_i(\sigma'\lambda')}{\Gamma_i(\sigma\lambda)}, \quad (2.43)$$

where  $\sigma' \neq \sigma$  and  $\delta$  is the so-called multipole-mixing ratio. It is defined as the ratio of the partial width  $\Gamma_i$  of transition  $i$ . It is connected to the natural width of a state by the sum over all depopulating transitions

$$\Gamma = \sum_i \Gamma_i. \quad (2.44)$$

The widths, partial and natural, are directly connected to the lifetime of a state

$$\Gamma = \frac{\hbar}{\tau}. \quad (2.45)$$

From equations (2.44) and (2.45) it is obvious that the lifetime of a state is given by the inverse sum of the partial lifetimes

$$\frac{1}{\tau} = \sum_i \frac{1}{\tau_i}. \quad (2.46)$$

This emphasizes the domination of the overall lifetime of a state by short partial lifetimes. This relation hints information when doing lifetime measurements where



a short overall lifetime indicates a dominating depopulating transition.

The intensities  $I_i$  observed in  $\gamma$ -ray spectroscopy are proportional to the partial width  $I_i \propto \Gamma_i$ . The partial width itself is determined by nuclear structure properties only:

$$\Gamma(\sigma\lambda) = 8\pi \frac{\lambda + 1}{\lambda [(2\lambda + 1)!!]^2} \cdot \left( \frac{E_\gamma}{\hbar c} \right)^{2\lambda+1} \cdot B(\sigma\lambda; J_i \rightarrow J_f)_\downarrow. \quad (2.47)$$

Here  $E_\gamma$  denotes the energy of the  $\gamma$  ray, i.e., the energy difference of the initial level  $J_i$  and the final level  $J_f$ , and  $B(\sigma\lambda)$  denotes the reduced transition strength, which is given as an average of the matrix elements over the magnetic substates of the decaying state

$$\begin{aligned} B(\sigma\lambda; J_i \rightarrow J_f)_\downarrow &= \sum_{\mu, m_i, m_f} |\langle J_i m_i | \mathfrak{M}(\sigma\lambda, \mu) | J_f m_f \rangle|^2 \\ &\stackrel{(2.21)}{=} \frac{1}{2J_i + 1} |\langle J_i || \mathfrak{M}(\sigma\lambda) || J_f \rangle|^2. \end{aligned} \quad (2.48)$$

For practical purposes often a shortened form of Equation (2.47) is used

$$\Gamma(\sigma\lambda) = c_{\sigma\lambda} \cdot \left( \frac{E_\gamma}{\text{MeV}} \right)^{2\lambda+1} \cdot B(\sigma\lambda; J_i \rightarrow J_f)_\downarrow. \quad (2.49)$$

$c_{\sigma\lambda}$  are constants which are unique for each transition character and multipolarity, but are common for all transitions of the same kind. The constants for transitions investigated within this work are:

$$\begin{aligned} c_{E1} &= 1.0466609 \cdot 10^5 \text{ meV/e}^2\text{b} & c_{M1} &= 11.574 \text{ meV}/\mu_N^2 \\ c_{E2} &= 8.0638146 \text{ meV/e}^2\text{b}^2 \\ c_{E3} &= 3.7566888 \cdot 10^{-4} \text{ meV/e}^2\text{b}^3 \\ c_{E4} &= 1.1166183 \cdot 10^{-8} \text{ meV/e}^2\text{b}^4 \end{aligned}$$

While the absolute values of the reduced transitions strengths given in  $\text{e}^2\text{b}^\lambda$  and  $\mu_N^2$  probes the absolute overlap of the wave functions, it is often more convenient to give reduced transitions strength in single-particle units or *Weisskopf units* (W.u.). They give the strength for the case that only a single-particle is excited via a specific transition character. One *Weisskopf unit* is defined as the transition of a single

proton from  $j = 1/2$  to  $j = \lambda + 1/2$ , resulting in an approximate transition strength of [24]

$$B_W(E\lambda) = \frac{1.2^{2\lambda}}{4\pi} \left( \frac{3}{\lambda+3} \right)^2 A^{2\lambda/3} e^2 \text{fm}^{2\lambda}, \quad (2.50)$$

$$B_W(M\lambda) = \frac{10}{\pi} 1.2^{2\lambda-2} \left( \frac{3}{\lambda+3} \right)^2 A^{(2\lambda-2)/3} (\mu_N/c)^2 \text{fm}^{2\lambda}. \quad (2.51)$$

These equations yet only depend on the mass and the multipolarity of the transition, thus it is convenient to give the transition strengths for the various multipolarities:

$$\begin{aligned} B_W(E1) &= 6.446 \cdot 10^{-4} A^{2/3} e^2 \text{b} & B_W(M1) &= 1.790 \mu_N^2 \\ B_W(E2) &= 5.940 \cdot 10^{-6} A^{4/3} e^2 \text{b}^2 \\ B_W(E3) &= 5.940 \cdot 10^{-8} A^2 e^2 \text{b}^3 \\ B_W(E4) &= 6.285 \cdot 10^{-10} A^{8/3} e^2 \text{b}^4 \end{aligned}$$

So the transition strength given in single-particle units is a measure for the collectivity of a  $\gamma$  transition.

---

## 2.2 Angular Distributions

---

Ensembles of  $\gamma$  rays produced in the decay of excited nuclear states do not only possess an energy and an intensity, but also a spatial distribution of the intensity. This is obvious from the multipole decomposition of the electromagnetic field, where the multipole operators (cf. Equation (2.16)) are defined via integrals over the spherical harmonics. This leads to contributions of all non-vanishing multipole moments to the angular distribution of the  $\gamma$  rays. The following discussion is based on [21, 25].

---

### 2.2.1 Nuclear Orientation in the Case of Axial Symmetry

---

The deexcitation of an excited state  $|J_i\rangle$  to another nuclear state  $|J_f\rangle$  is constrained by the total angular momentum of the each state, respectively, but also by the projections  $m_i \in \{-J_i, \dots, J_i\}$  and  $m_f \in \{-J_f, \dots, J_f\}$  w.r.t. the chosen quantization axis, the so-called magnetic quantum numbers. The orientation of the nucleus is then completely characterized by the population  $a_m$  of the magnetic sub-states,

normalized to  $\sum_{m=-J_i}^{m=+J_i} a_m = 1$ .

From the populations  $a_{m_i}$  a set of  $2J_i$  independent functions  $f_k(J_i)$ , completely defined w.r.t. the axis of rotational symmetry, also called the *degree of orientation of order k*, can be defined via

$$f_k(J_i) = \binom{2k}{k}^{-1} J_i^{-k} \sum_{m_i} \sum_{\nu=0}^k (-1)^\nu \frac{(J_i - m_i)! (J_i + m_i)!}{(J_i - m_i - \nu)! (J_i + m_i - k + \nu)!} \binom{k}{\nu}^2 a_{m_i}, \quad (2.52)$$

with  $k \geq 0$ . However  $f_k$  vanishes for any  $k \geq 2J_i + 1$ . In the case of uniformly populated magnetic sub-states ( $a_{m_i} = (2J_i + 1)^{-1}$ ) the angular distribution of the  $\gamma$  rays emitted in the process of de-excitation will exhibit isotropic character. A state is called *aligned* if  $a_m = a_{-m}$ , leading to  $f_k(J) \neq 0$  for even  $k$  and  $f_k(J) = 0$  for odd  $k$ . The more general case of any  $f_k(J) \neq 0$ ,  $k$  odd, is called *nuclear polarization*. This situation may occur if  $a_m \neq a_{-m}$ . Hence the decay of a state with  $J_i = 0$  is always isotropic.

The alignment depends on the choice of a proper quantization axis, e.g., the direction of an incoming beam in a Coulomb-excitation experiment, or the velocity vector of the ion under investigation. The quantization axis should be chosen such that the experiment exhibits the highest possible symmetry w.r.t. this axis.

In general the magnetic sub-state population is influenced by the mechanism used to populate the state, in the case of direct excitation, as well as by the properties of preceding states if the state under investigation is part of a decay cascade.

The *degrees of orientation*  $f_k(J_i)$  are proportional to the statistical tensors  $\rho_k(J_i) = \rho_{k,\kappa=0}(J_i)$ , for the case of ensembles of nuclei with rotational symmetry

$$\rho_k(J_i) = \sum_{m_i} a_{m_i} (-1)^{J_i - m_i} \sqrt{2k+1} \begin{pmatrix} J_i & J_i & k \\ m_i & -m_i & 0 \end{pmatrix} \quad (2.53)$$

$$\Leftrightarrow \rho_k(J_i) = \underbrace{\binom{2k}{k} J_i^k \sqrt{\frac{(2k+1)(2J_i-k)!}{(2J_i+k+1)!}}}_{w_k(J_i)} f_k(J_i). \quad (2.54)$$

The formula is greatly reduced for the case of complete alignment, leading to

$$\rho_k(J_i) \equiv \begin{cases} (-1)^{J_i} \sqrt{(2J_i+1)(2k+1)} \begin{pmatrix} J_i & J_i & k \\ 0 & 0 & 0 \end{pmatrix} & \text{for integer spin,} \\ (-1)^{J_i-1/2} \sqrt{(2J_i+1)(2k+1)} \begin{pmatrix} J_i & J_i & k \\ 1/2 & -1/2 & 0 \end{pmatrix} & \text{for half-integer spin.} \end{cases} \quad (2.55)$$

Such rotational symmetry is, e.g., realized in a Coulomb-excitation experiment where the scattered particles are not detected.

If the state  $|J_i\rangle$  is solely populated by preceding  $\gamma$  radiation produced by the decay of the state  $|J_0\rangle$ , the population of the magnetic sub-states  $a_{m_i}$  can be determined from the populations  $a_{m_0}$  via

$$a_{m_i} = \sum_{m_0} a_{m_0} \left| (-1)^{J_i - \lambda + m_0} \sqrt{2J_0 + 1} \begin{pmatrix} J_i & \lambda & J_0 \\ m_i & m_0 - m_i & -m_0 \end{pmatrix} \right|^2. \quad (2.56)$$

The angular distribution of the emitted  $\gamma$  radiation, depending on the polar angle  $\theta$  measured w.r.t. the quantization axis, is described by

$$W(\theta) = \sum_k (-1)^{J_f + J_i - 1} \sqrt{\frac{2\lambda + 1}{2k + 1}} \begin{pmatrix} \lambda & k & \lambda \\ \lambda & 0 & 1 \end{pmatrix} \begin{Bmatrix} J_f & J_i & \lambda \\ k & \lambda & J_i \end{Bmatrix} \rho_k(J_i) Y_{k0}(\theta). \quad (2.57)$$

The spherical harmonics  $Y_{lm}(\phi, \theta)$  can also be given in terms of the associated Legendre polynomials  $P_{lm}(x)$  by

$$Y_{lm}(\phi, \theta) = \sqrt{\frac{2l + 1}{4\pi} \frac{(l - m)!}{(l + m)!}} P_{lm}(\cos(\theta)) e^{im\phi}. \quad (2.58)$$

In the special case of  $m = 0$  the associated Legendre polynomials  $P_{l0}(x)$  turn into Legendre Polynomials  $P_l(x)$  and the spherical harmonics are completely independent of  $\phi$ . In such cases, where the experimental setup exhibits rotational symmetry, the angular distribution can be rewritten in terms of Legendre polynomials

$$W(\theta) = \sum_k \underbrace{\rho_k(J_i) B_k(J_f \lambda \lambda' J_i)}_{A_k(J_f \lambda \lambda' J_i)} P_k(\cos(\theta)), \quad (2.59)$$

where  $B_k$  covers the angular momentum coupling. From a physical point of view (cf. Equation (2.41)) multiple multipole operators may connect the initial and final states of a nuclear decay. As stated in Section 2.1.2 the two multipolarities ( $\lambda$  and  $\lambda'$ ) with the smallest angular momenta mostly dominate the decay. This will also affect the shape of the angular distribution, making the distinction of two possible scenarios important, which may arise:

- $\lambda = \lambda'$  (Pure transition)

If the transition between two states is pure (e.g., for a  $2^+ \rightarrow 0^+$  transition),  $B_k(J_f \lambda \lambda' J_i)$  is identical to the F-coefficients [26]

$$F_k(J_f \lambda \lambda' J_i) = (-1)^{J_f + J_i - 1} \sqrt{(2\lambda + 1)(2\lambda' + 1)(2J_i + 1)} \cdot \sqrt{2k + 1} \begin{pmatrix} \lambda & \lambda' & k \\ 1 & -1 & 0 \end{pmatrix} \begin{Bmatrix} J_i & J_i & k \\ \lambda' & \lambda & J_f \end{Bmatrix}. \quad (2.60)$$

From symmetry considerations for the 3j symbol  $k$  becomes restricted to  $k \leq \lambda + \lambda'$ . In the case of a pure transition  $k \leq 2\lambda$ , thus,  $F_k$  can be given in a more compact way

$$F_k(J_f \lambda J_i) = (-1)^{J_f + J_i - 1} (2\lambda + 1) \sqrt{(2J_i + 1)(2k + 1)} \\ \times \begin{pmatrix} \lambda & \lambda & k \\ 1 & -1 & 0 \end{pmatrix} \begin{Bmatrix} J_i & J_i & k \\ \lambda & \lambda & J_f \end{Bmatrix}, \quad (2.61)$$

highlighting that the angular distribution of a pure transition is fully determined when the statistical tensor of the decaying state is known. On the other way round is it possible to determine the statistical tensor as soon as one can measure the angular distribution of such a transition.

- $\lambda' = \lambda + 1$  (Mixed transition)

The picture is more complex if the transition is not pure anymore, but rather a mixture of different multiplicities. This limits  $k$  to  $k \leq \lambda + \lambda' = 2\lambda + 1$ .  $B_k$  is not identical to  $F_k$  then, but it also incorporates a measure of the ratio of the strengths of the dominant multiplicities. This is achieved by employing the multipole-mixing ratio  $\delta$ , defined in Equation (2.43). Thus,  $\delta^2$  is proportional to the ratio of the reduced transition strengths. Using the preceding definition,  $B_k$  is described by

$$B_k(J_f \lambda \lambda' J_i) = \frac{1}{1 + \delta^2} \{F_k(J_f \lambda \lambda J_i) + 2\delta F_k(J_f \lambda \lambda' J_i) + \delta^2 F_k(J_f \lambda' \lambda' J_i)\}. \quad (2.62)$$

If neither the projectile ions nor the target atoms are polarized before a nuclear reaction, the excited states will be *aligned*, at most, limiting the non-vanishing contributions to the angular distribution to those with even  $k$ . This situation is often encountered in Coulomb-excitation experiments.

A common problem is the experimental deduction of multipole-mixing ratios of transitions between excited states. As outlined before this is quite straightforward for an experiment of Coulomb-excitation type, where excited states are populated from the ground-state. If the angular distributions of the ground-state transition from the excited state as well as to the other excited state were measured, the statistical-tensor components can be determined, allowing for the deduction of the multipole-mixing ratio from the angular distribution of the non-ground state-transition and the statistical tensor.

In some cases the ground-state transition may be too weak to be observed, or the peak-to-background ratio is too small to distinguish the transition in the spectrum. This can occur, if the transition strength holds only a few W.u. or even less. In

such situations the statistical tensor might be, at least for Coulomb excitation, calculated. As shown in Section 2.1.1, cross-sections can be deduced from reaction theory, but can also yield statistical tensors of excited states. This will be shortly outlined in the following paragraphs; it can again be found in great detail in [21]. In real experiments one always will have to deal with ensembles of nuclei, which can be described by a density matrix or a statistical tensor. The density matrix after the collision ( $t \rightarrow \infty$ ) is given by

$$\langle JM | \rho | JM' \rangle = \sum_{M_0 M'_0} a_{JM, J_0 M_0} \langle J_0 M_0 | \rho_i | J_0 M'_0 \rangle a_{JM', J_0 M'_0}^*, \quad (2.63)$$

where  $a$  is the excitation amplitude (cf. Section 2.1.1) and  $\langle n | \rho_i | n' \rangle$  is the initial density matrix. At  $t \rightarrow -\infty$  only the sub-matrix  $\langle 0 | \rho_i | 0' \rangle$  is non-vanishing, *i.e.*, all nuclei of the ensemble are in the ground state. If the nucleus under investigation is initially unpolarized, the initial density matrix is reduced to

$$\langle J_0 M_0 | \rho_i | J_0 M'_0 \rangle = \frac{1}{2J_0 + 1} \delta_{M_0 M'_0}. \quad (2.64)$$

$\delta_{M_0 M'_0}$  is here the Kronecker delta, which is only non-vanishing for  $M_0 = M'_0$ . The simplification of the initial density matrix leads to

$$\langle JM | \rho | JM' \rangle = \frac{1}{2J_0 + 1} \sum_{M_0} a_{JM, J_0 M_0} a_{JM', J_0 M_0}^*. \quad (2.65)$$

This form of the density matrix is closely related to the excitation probability  $P_J$  of a state of spin  $J$ , namely

$$P_J = \sum_M \langle JM | \rho | JM \rangle = \frac{1}{2J_0 + 1} \sum_{M_0 M} |a_{JM, J_0 M_0}|^2. \quad (2.66)$$

The statistical tensor, describing the state of polarization after the excitation reaction, can be expressed in terms of the density matrix via

$$\rho_{kk}(J) = \sqrt{2J+1} \sum_{MM'} (-1)^{J-M'} \begin{pmatrix} J & k & J \\ -M' & \kappa & M \end{pmatrix} \langle JM | \rho | JM' \rangle. \quad (2.67)$$

For unpolarized nuclei this results in

$$\rho_{kk}(J) = \frac{\sqrt{2J+1}}{2J_0+1} \sum_{M_0 MM'} (-1)^{J-M'} \begin{pmatrix} J & k & J \\ -M' & \kappa & M \end{pmatrix} a_{JM', J_0 M_0}^* a_{JM, J_0 M_0}. \quad (2.68)$$

These statistical tensors are not normalized, like the statistical tensors resulting from Equation (2.54), or the ones expected in Equation (2.59). In this context it should be noted that  $\rho_{00}(J) = P_J$  can be used to normalize the components of the statistical tensors via

$$\hat{\rho}_{kk}(J) = \frac{\rho_{kk}(J)}{\rho_{00}(J)}. \quad (2.69)$$

This is also called the polarization of the state of spin  $J$ , which is the quantity to be used in order to calculate the angular distributions.

If the beam axis is chosen to be the quantization axis, symmetry properties of the statistical tensors in Coulomb excitation yield purely real (imaginary)  $\rho_{kk}$  for  $k$  even (odd). In the case of backscattering ( $\theta = 180^\circ$ ) this leads to more strict  $\rho_{kk} = \delta_{k0}\rho_{k0}$ , real  $\rho_{kk}$  and even  $k$ .

The expressions mentioned above reduce the problem of calculating the statistical tensors to the calculation of the excitation amplitudes, which was already treated in Section 2.1.1. From this point of view the term for determining the statistical tensor does not change if first- or higher-order perturbation theory or even the full quantum-mechanical treatment is applied in order to solve the Coulomb-excitation problem. But this section is still only valid for the case of rotational symmetry.

---

### 2.2.2 Particle- $\gamma$ Angular Correlation

---

The preceding section was based on the assumption of rotational symmetry around the beam axis. This symmetry can be broken, in general, if an outgoing particle, neglecting the possible energy transfer and the accompanying velocity gain of target nuclei, as well as emitted  $\gamma$  radiation are detected. Even when the beam axis is chosen as the symmetry axis, the rotational symmetry is broken, giving rise to non-vanishing components of the statistical tensor with  $\kappa \neq 0$ . However, if the velocity vector of the incoming particle is chosen as axis, as well as the axis perpendicular to the plane spanned by the velocity vectors of the incoming and the outgoing particle are chosen as a set of axes, the angles of the outgoing particle are  $(\theta_p, \phi_b = 0)$ . The generalized expression of Equation (2.59) describing the particle- $\gamma$  angular correlation is then given by [27]

$$W(\theta_\gamma, \phi_\gamma) = 1 + \sum_{k \geq 2} \{A_{k0} P_k(\cos(\theta_\gamma)) + 2 \sum_{\kappa > 0} [\text{Re}(A_{k\kappa}) \cos(\kappa \phi_\gamma) - \text{Im}(A_{k\kappa}) \sin(\kappa \phi_\gamma)] C_{k\kappa}(\theta_\gamma, 0)\}. \quad (2.70)$$

Here  $A_{k\kappa}(J_f \lambda \lambda' J_i) = \rho_{k\kappa}(J_i) B_k(J_f \lambda \lambda' J_i)$ , the generalized expression of  $A_k(J_f \lambda \lambda' J_i) = A_{k,\kappa=0}(J_f \lambda \lambda' J_i)$ , and

$$C_{k\kappa}(\theta_\gamma, 0) = (-1)^\kappa \sqrt{\frac{(k-\kappa)!}{(k+\kappa)!}} P_{k\kappa}(\cos(\theta_\gamma)), \quad (2.71)$$

which is related to the associated Legendre polynomials  $P_{lm}(x)$ . The choice of axis implicates that  $\text{Im}(A_{k\kappa}) = 0$  [27]. Because only aligned nuclei are considered here, the terms of Equation (2.70) still are only finite for even  $k$ . Nevertheless, those restrictions do not apply for  $\kappa$ , it can also take odd values. This leads to a more compact form of Equation (2.70):

$$W(\theta_\gamma, \phi_\gamma) = 1 + \sum_{k \geq 2} \left\{ A_{k0} P_k(\cos(\theta_\gamma)) + 2 \sum_{\kappa > 0} A_{k\kappa} \cos(\kappa \phi_\gamma) C_{k\kappa}(\theta_\gamma, 0) \right\}. \quad (2.72)$$

---

## 2.3 Recoil in Vacuum

---

In free atoms or ions moving in vacuum, the hyperfine interaction between the hull electrons and the nucleus couples the total angular momentum of the electrons  $\vec{I}$  and the nuclear spin  $\vec{J}$  to a common angular momentum  $\vec{F}$ , causing precession of the whole system around  $\vec{F}$ . This is ultimately affecting the characteristic of angular distributions. It is discussed in detail in [28], the basis of the following short overview.

Not only the angular momenta are the origin of such a kind of precession of a free atom, but also the strength of the electromagnetic interaction between the electrons and the nucleus. Considering this fact, the angular distribution has to be modified in the following way

$$W(\theta) = \sum_k A_k G_k P_k(\cos(\theta)), \quad (2.73)$$

where  $G_k$  are attenuation coefficients measuring the precession and the subsequent rotation of the angular distribution. The rotation of the angular distribution is the combination of the precession and the nature of excited nuclear states: While the nucleus is precessing around  $\vec{F}$ , excited states are decaying. If the lifetime of such a state is short compared to the precession period, the angular distribution stays nearly unperturbed, as all decays take place before the precession begins to smear the angular distribution out. If otherwise the lifetime is in the order of or large



compared to the precession period, the nucleus may already have precessed a non-neglectable angle when decays take place. In the case where the lifetime is very long, several tens of ps, the angular distribution may be flattened out and, by experimental means, appear as flat, called the *nuclear deorientation effect*.

The Hamiltonian of the hyperfine interaction is predominantly of  $M1$  character, which can thus be considered as first order of a perturbation approach. In a non-relativistic way it can be written as

$$\mathcal{H} = \mu_N g \frac{H(0)}{J} \vec{I} \times \vec{J}. \quad (2.74)$$

$H(0)$  is the average magnetic field at the position of the nucleus. It is absolutely non-trivial to compute this field, commonly. One case, where the field strength can be evaluated is in the case of hydrogen-like ions, i.e., ions with only one 1s electron orbiting the nucleus. The field strength can then be estimated via [29]

$$B_{1s} \approx 16.7 Z^3 (1 + (Z/84)^{2.5}) \text{ T}. \quad (2.75)$$

For systems with more electrons this becomes more complex, as a number of additional effects arise: the electromagnetic interaction between the electrons has to be considered, but also the effect on the nucleus, as the total field strength increases. The latter scales not linear with the number of hull electrons, but inner electrons “shield” the field of the outer ones, resulting in a damped increase. Nevertheless it is possible to calculate systems involving few electrons, e.g., helium-, lithium- or boron-like ions, to an adequate precision. However, this situation is rarely encountered in heavy-ion experiments.

For more complex configurations with many electrons present in the electron hull, the attenuation coefficients may be approximated, from the field  $B$  the electrons produce at the location of the nucleus, by [30]

$$G_k(t) = \sum_{F,F'} C_{JI}^{FF'}(k) \cos(\omega_{FF'} t), \quad (2.76)$$

with

$$C_{JI}^{FF'}(k) = \frac{(2F+1)(2F'+1)}{2I+1} \left\{ \begin{matrix} F & F' & k \\ J & J & I \end{matrix} \right\}^2 \text{ and} \quad (2.77)$$

$$\omega_{FF'} = g \frac{\mu_N}{\hbar} B \frac{F(F+1) - F'(F'+1)}{2I}. \quad (2.78)$$

The equations hold true under the assumptions that the ensemble is isotropic and the hyperfine interaction is static. This is valid for s electrons, and a reasonable

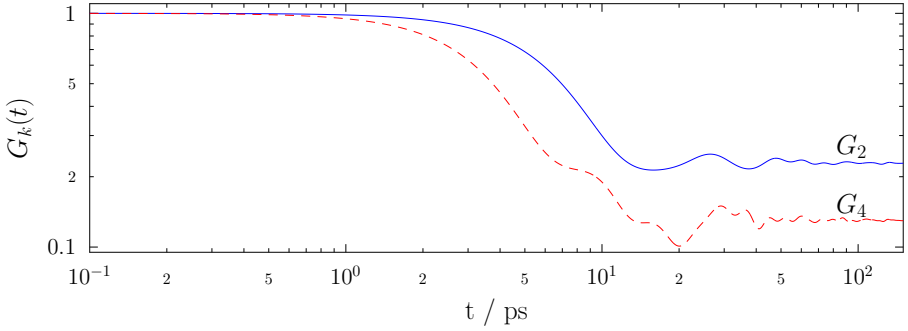


**Figure 2.4.:** Evolution of the averaged attenuation coefficients  $G_2(t)$  (blue, solid) and  $G_4(t)$  (red, dashed), calculated via Equation (2.79) for  $t_i = 0$  and  $t_f = t$ , for the case of the decay of the first excited nuclear  $2^+$  state in  $^{202}_{80}\text{Hg}_{122}$  with a lifetime  $\tau = 37.79$  ps [31–33] and a g-factor  $g = +0.41(3)$  [31]. The drop in the attenuation coefficients corresponds to a flattening of the angular distribution.

approximation for  $I > 1/2$ , if the ion is not polarized by any external field. If the nuclear decay is observed within a certain time window  $t_i \rightarrow t_f$ , the expectation values of the attenuation coefficients are given by

$$\langle G_k(t_i, t_f) \rangle = \frac{\int_{t_i}^{t_f} e^{-t/\tau} G_k(t) dt}{\int_{t_i}^{t_f} e^{-t/\tau} dt}, \quad (2.79)$$

where  $\tau$  is the lifetime of the excited nuclear state. The characteristic evolution of such averaged attenuation coefficients with time is exemplary depicted in Figure 2.4.

The hyperfine interaction, in the approximation of a static perturbation, exhibits a so-called “hard core” residual polarization, which is preserved for any interaction strength. The “hard core” attenuation coefficients are given by

$$G_k(hc) = \sum_F C_{JI}^{FF}(k). \quad (2.80)$$

This effect is the reason, that an angular distribution for states with long lifetimes will never be completely flat, but only may appear as such within experimental uncertainties. This is shown in Figure 2.5, where the angular distribution is less pronounced for advanced times. This calculation was based on a initially fully

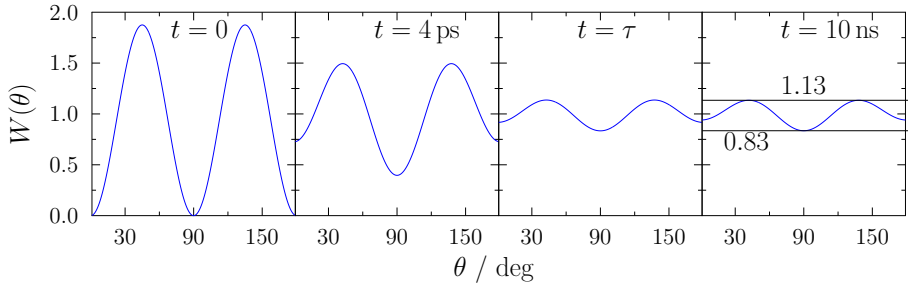


**Figure 2.5.:** Evolution of the angular distribution of the  $2_1^+ \rightarrow 0_1^+$  transition in  $^{202}\text{Hg}_{124}$  with time. Complete alignment of the  $2_1^+$  state at  $t = 0$  is assumed, i.e., the statistical tensor is given by Equation (2.55), leading to  $A_2 = 5/7$  and  $A_4 = -12/7$ . The attenuation coefficients used are the ones depicted in Figure 2.4. It is clearly visible that the angular distribution flattens for nuclear states exhibiting large lifetimes, like it is the case here for  $\tau(2_1^+) = 39.79$  ps. The rightmost graph ( $t = 10$  ns) shows the “hard core” polarization.

aligned  $2_1^+$  state, with a lifetime of 37.79 ps, of  $^{202}\text{Hg}_{124}$ , resulting in  $A_2 = 5/7$  and  $A_4 = -12/7$ . The average magnetic field at the location of the nucleus was for this calculation assumed to be 10 kT. This assumption was based on the value  $\bar{B} = 8.8$  kT in Te ions ( $Z = 52$ ) at an average velocity of  $0.062c$  [30], which is comparable to the experimental situation for  $^{202}\text{Hg}$  presented later within this work. The total angular momentum of the electrons was chosen to be  $I = 4$ , which is loosely based on [34], where for Platinum ions ( $Z = 78$ ) moving at  $v/c = 0.02$  the total angular momentum  $I > 3$  was deduced.

## 2.4 Inverse Kinematics

All of the relations given in the preceding sections refer to the center-of-mass system of the projectile-target system. In order to analyze experimental data taken using detectors with fixed-positions w.r.t. the laboratory system, it is necessary to transform angles and energies of the particles from the center-of-mass system to the laboratory system. These transformations are examined in [21] and in even more detail in [35]. The latter is the basis for the following short summary. The transformations are explicated in greater detail in Appendix D.

From a kinematics point-of-view the fixed-target experiments investigated within this work may be seen as particles moving inside the center-of-mass system while

the center-of-mass system itself moves - before and after the collision - with a constant speed w.r.t. the laboratory system. Thus the transformation to the center-of-mass system is given by the transformation from one system to the other one in a situation, where two systems move w.r.t. to each other. In addition, the case considered here is more simple as the beam axis is a natural choice for an axis in both systems.

In general the transformation from one system  $K$ , with coordinates  $x$ , to another system  $K'$ , with coordinates  $x'$ , can be seen as a rotation in 4-dimensional space time [36]

$$\begin{pmatrix} x'_1 \\ x'_2 \\ x'_3 \\ x'_4 \end{pmatrix} = \begin{pmatrix} \alpha_{11} & \alpha_{12} & \alpha_{13} & \alpha_{14} \\ \alpha_{21} & \alpha_{22} & \alpha_{23} & \alpha_{24} \\ \alpha_{31} & \alpha_{32} & \alpha_{33} & \alpha_{34} \\ \alpha_{41} & \alpha_{42} & \alpha_{43} & \alpha_{44} \end{pmatrix} \cdot \begin{pmatrix} x_1 \\ x_2 \\ x_3 \\ x_4 \end{pmatrix}. \quad (2.81)$$

The fourth coordinate represents time, i.e.,  $x_4 = ict$ . This is a consequence of the fact, that  $s^2 = x^2 + y^2 + z^2 - c^2 t^2 = x_1^2 + x_2^2 + x_3^2 + x_4^2$  is invariant. If  $K'$  moves with the velocity  $V$  w.r.t.  $K$  in direction of the  $x$  axis, which is parallel in both systems, then  $x'_2 = x_2$  and  $x'_3 = x_3$ . The transformation can be written in a covariant formulation by

$$x'^\mu = \sum_{\nu=0}^3 L^\mu{}_\nu x^\nu, \quad (2.82)$$

where the matrix  $L$  describes the Lorentz transformation of a four vector  $x^\nu = (ct, x, y, z)^T$ . For a relative motion solely parallel to the  $x$  axis,  $L$  is given by

$$L = \begin{pmatrix} \gamma & -\frac{V}{c}\gamma & 0 & 0 \\ -\frac{V}{c}\gamma & \gamma & 0 & 0 \\ 0 & 0 & 1 & 0 \\ 0 & 0 & 0 & 1 \end{pmatrix}, \quad (2.83)$$

where  $\gamma = 1/\sqrt{1-(\frac{V}{c})^2}$ . This gives the transformation between the systems for points being at rest in one system. The problem of the transformation from the laboratory system to the center-of-mass system, and vice versa, is reduced to the problem of determining the relative velocity  $V = \beta_c c$  and the Lorentz factor  $\gamma$ . The transformation (2.82) does not only apply for four vectors of spacetime, but also for four momenta  $p^\nu = (E/c, p_x, p_y, p_z)^T$ .

In the following paragraphs  $K'$  denotes the laboratory system and  $K$  is the center-of-mass system. For fixed target experiments, the velocity of the center-of-mass in

the laboratory system equals the velocity of the target nucleus in the center-of-mass system:

$$\gamma = \frac{E_T}{m_T c^2}. \quad (2.84)$$

A feature of the center-of-mass system is the fact, that the sum of momenta of all involved particles vanishes, *i.e.*,  $\sum_{i=1}^N \vec{p}_i = 0$ . For a system of two particles, *e.g.*, in a Coulomb-excitation experiment, this leads to  $|\vec{p}_P| = |\vec{p}_T|$ . This allows to determine the velocity of the center of mass for such a fixed-target experimental setup from the total energy of the projectile  $E_P = m_P c^2 + T$  and the mass of the target  $m_T$ :

$$\begin{aligned} |\vec{p}_T| &= \gamma m_P \beta_c c = \gamma \left( p'_P - \beta_c \frac{E'_P}{c} \right) = |\vec{p}_P| \\ \Rightarrow \beta_c &= \frac{\sqrt{E_P^2 - (m_P c^2)^2}}{E'_P + m_T c^2}. \end{aligned} \quad (2.85)$$

In addition, this allows to determine the energy of the projectile in the center-of-mass system from the Lorentz transformation of the four momentum to

$$\begin{aligned} E_P &= \gamma (E'_P - \beta_c c p'_P) \\ &= \gamma \left( \frac{E'_P m_T c^2 + (m_P c^2)^2}{m_T c^2 + E'_P} \right). \end{aligned} \quad (2.86)$$

All this information is valuable to determine the properties of scattering reactions in the center-of-mass frame, as the Coulomb-excitation theory (*cf.* Section 2.1) is formulated within the center-of-mass frame.

On the other hand, the measurement process after the scattering reaction is performed within the laboratory system, thus the necessity for transforming angles measured in the laboratory frame of reference back to the center-of-mass frame. This is particularly facilitated by the fact, that the center-of-mass itself will still move along the beam axis. Therefore, after the scattering reaction, the velocity vector of a nucleus moving under the angle  $\theta$  w.r.t. to the beam axis may be decomposed into a part parallel to the beam axis  $v_{\parallel} = \beta_{\parallel} c = \cos(\theta) \beta c$  and a part perpendicular to the beam axis  $v_{\perp} = \beta_{\perp} c = \sin(\theta) \beta c$ , which is not influenced by the transformation, *i.e.*,  $\beta'_{\perp} = \beta_{\perp}$ . The scattering angle in the laboratory system can be deduced via

$$\tan(\theta') = \frac{c \beta'_{\perp}}{c \beta'_{\parallel}} = \frac{1}{\gamma} \frac{\sin(\theta)}{\cos(\theta) + \tau}, \quad (2.87)$$

where  $\tau = \beta_c/\beta$ . If the kinetic energy is small, compared to the mass of the nuclei involved in the reaction, relativistic effects are negligible and  $\tau$  may be approximated by  $\tau \approx m_p/m_T$ . This transformation of the scattering angle of the projectile from the center-of-mass frame to the laboratory system exhibits different characteristics based on the value of  $\tau$ . Especially for  $\tau > 1$ , which is the case in inverse kinematics low-energy Coulomb-excitation experiments, the scattering angle in the laboratory frame-of-reference is limited to

$$\theta'_{\max} = \arctan\left(\frac{1}{\gamma \sqrt{\tau^2 - 1}}\right). \quad (2.88)$$

The limitation of the scattering angle also implicates that each measured angle  $\theta'$  corresponds to two angles  $\theta$  in the center-of-mass frame. The scattering angle of the target nuclei is also determined using Equation (2.87), though  $\tau = 1$ , *i.e.*,  $\beta = \beta_c$ , in that case, while the demand for  $\vec{p}_p = -\vec{p}_T$  in the center-of-mass frame implicates  $\theta_T = 180^\circ - \theta_p$ . Hence, any scattering angle of the projectile nucleus measured in the laboratory frame-of-reference corresponds to two scattering angles of target nuclei in the laboratory frame-of-reference.

---

## 3 Nuclear Structure Theory

This work is motivated by the prediction of the existence of isovector valence-shell excitations in the algebraic proton-neutron *Interacting Boson Model-2* [4]. Experimental results derived in this work shall be compared to calculations of the microscopic *Large-Scale Shell-Model* [37], a modern approach to Shell Model calculations involving an enhanced valence space, and to the *Quasiparticle-Phonon Model* [38], which is capable of predicting collective properties of nuclei near shell closures from a microscopic ansatz, providing microscopic justification for the *IBM-2*. The following sections present the *Shell Model*, the *QPM* and the *IBM-2*, alongside a description of nuclear surface excitations in the *Liquid-Drop Model*.

---

### 3.1 Surface Excitations

---

In a simple picture a nucleus can be seen as a homogeneous distribution of nucleons in space, similar to a drop of a liquid. This analogy leads to the name *Liquid-Drop Model*. The whole “drop” can be excited by some fundamental collective excitations, e.g., rotational motion or surface vibrations. Surface excitations can be described by a set of parameters  $\alpha_{\lambda\mu}$ , which emerge from the expansion of the surface in spherical harmonics. The distance of a particular point on the surface from the origin of the spherical nucleus is then given by [1]

$$R(\theta, \phi) = R_0 \left( 1 + \sum_{\lambda=0}^{\infty} \sum_{\mu=-\lambda}^{\lambda} \alpha_{\lambda\mu} Y_{\lambda\mu}^*(\theta, \phi) \right), \quad (3.1)$$

where  $R_0$  denotes the equilibrium radius. Near closed shells, the nucleon liquid takes a spherical form and can be excited to perform oscillations around the equilibrium shape, while in regions further from major shell closures deformed equilibrium shapes develop, which allow the nucleonic liquid to perform rotations. The collective model of Bohr and Mottelson allows for describing states undergoing vibrations, rotations or a superposition of both [1]. The corresponding Hamiltonian is given by [1, 39]

$$H = -\frac{\hbar^2}{2D} \left[ \frac{1}{\beta^4} \frac{\partial}{\partial \beta} \left[ \beta^4 \frac{\partial}{\partial \beta} + \frac{1}{\beta^2} \frac{1}{\sin(3\gamma)} \frac{\partial}{\partial \gamma} \left[ \sin(3\gamma) \frac{\partial}{\partial \gamma} \right] \right] \right] + \frac{\hbar^2}{2I} R^2 + V, \quad (3.2)$$

where  $D$  denotes a single mass parameter,  $V$  denotes the nuclear potential,  $I$  is the moment of inertia, and  $R$  is the rotational angular momentum.  $\beta$  and  $\gamma$  are the deformation parameters, which will be introduced below.

---

## Vibration

---

Magic nuclei exhibit spherical shapes. Moving away from these points of increased stability in the nuclear chart, nuclei will start to behave collective and exhibit vibrational behavior, close to shell closures. The description of the surface of a vibrating nucleus can be done employing Equation (3.1), though, the parameters  $\alpha_{\lambda\mu}$  have to be time dependent,  $\alpha_{\lambda\mu} = \alpha_{\lambda\mu}(t)$ . In that description of the shape,  $\lambda = 0$  represents a compression or expansion, the so-called “Breathing Mode”, of the nucleus at whole, without any change in the shape of the surface.  $\lambda = 1$  corresponds to a displacement of the nucleus. This corresponds to a harmonic oscillation around the origin, *e.g.*, of a spring in a classical picture, however, there is no restoring force present in the case of a nuclear excitation, prohibiting the formation of such excitations. Quadrupole modes ( $\lambda = 2$ ) are the lowest order at which collective excitations of the surface itself arise. In a geometrical picture this mode corresponds to oscillations between a flattening or an elongation of the nucleus followed by restoration of the spherical shape. However, on average, the nucleus is not of spherical shape anymore.  $\lambda = 3$  gives rise to pear-shaped octupole excitations, which are also commonly found in nuclei near shell closures.

This work focuses on fundamental quadrupole excitations, for which reason, the following paragraphs are restricted to those. For that class of excitations  $\alpha_{\lambda=2,\mu}$  vanish, for odd  $\mu$ , leaving  $\alpha_{22}$ ,  $\alpha_{20}$  and  $\alpha_{2-2}$ .

The Hamiltonian describing such a quadrupole vibrating behavior can be written as [39]

$$H = T + V = \frac{1}{2} B \sum_{\mu} \left| \frac{d\alpha_{2\mu}}{dt} \right|^2 + \frac{1}{2} C \sum_{\mu} |\alpha_{2\mu}|^2. \quad (3.3)$$

$H$  describes the motion of a harmonic oscillator and hence the  $\alpha_{2\mu}$  undergo oscillations of frequency

$$\omega = \sqrt{\frac{C}{B}}, \quad (3.4)$$

with a vibrational energy  $\hbar\omega$ . Therefore, excitations of a vibrational nucleus can be imagined as phonons with angular momentum  $\lambda$  and parity  $(-1)^\lambda$ , analog to oscillations in solid bodies. The lowest order of these phonons are, as described above, quadrupole phonons of  $J^\pi = 2^+$ . Creation and destruction of such phonons, *i.e.*,



excitation and decay of excited nuclear states, can be given in second quantization using quadrupole phonon creation and destruction operators  $\mathbf{b}^\dagger$  and  $\mathbf{b}$ , defined via

$$\mathbf{b} |n_b\rangle = \sqrt{n_b} |n_b - 1\rangle \quad (3.5)$$

$$\mathbf{b}^\dagger |n_b\rangle = \sqrt{n_b + 1} |n_b + 1\rangle . \quad (3.6)$$

Since phonons have integer spin, they are bosons and not affected by the Pauli principle. Therefore, excited  $N$ -phonon states can be constructed from the ground state  $|0\rangle$  by successively applying the creation operator:

$$|N_{\text{ph}}\rangle = (\mathbf{b}^\dagger)^N |0\rangle . \quad (3.7)$$

Apart from microscopic restrictions, imposed by the fermionic nature of the nucleons forming the phonons, no reasons opposing multi-phonon excitations exist. Contrary, excited nuclear states of multi-phonon nature are found throughout the nuclear chart. Allowed angular momenta for the coupling of  $N$  bosons can be derived via the  $m$  scheme. This leads to an angular momentum triplet of excited two phonon states of  $0^+$ ,  $2^+$  and  $4^+$ . For three phonon excitations a quintuplet of allowed angular momentum consisting of  $0^+$ ,  $2^+$ ,  $3^+$ ,  $4^+$  and  $6^+$  states is allowed. However, residual interactions between the phonons break the degeneracy of the multiplets, leading to small shifts in energy for the excited states, depending on the total angular momentum. For two phonon excitations, the value of  $R_{4/2} = E(2_1^+)/E(4_1^+)$  is expected to be 2, in the simple phonon picture. But the anharmonicities emerging from the residual interaction result in a value of  $\approx 2.2$ , which is observed in collective nuclei near closed shells.

---

## Shapes

---

The radius of a deformed nucleus is given by the expression Equation (3.1), which is the radius of the non-spherical shape relative to the radius of the spherical shape, modified by spherical harmonics and sets of parameters  $\alpha_{\lambda\mu}$  giving the deformation. In the case of quadrupole deformation these parameters are commonly expressed in terms of the deformation parameters  $\beta$  and  $\gamma$  [1] via

$$\alpha_{20} = \beta \cos(\gamma) \quad (3.8)$$

$$\alpha_{22} = \alpha_{2-2} = \frac{1}{\sqrt{2}} \beta \sin(\gamma). \quad (3.9)$$

The parameter  $\beta$  measures the extend of the quadrupole deformation, while  $\gamma$  represents the degree of axial symmetry. For small values of the parameters  $\alpha_{2\mu}$ , the deformed shape can also be characterized by the alteration of the axes

$$\delta R_\kappa = \sqrt{\frac{5}{4\pi}} \beta R_0 \cos\left(\gamma - \kappa \frac{2\pi}{3}\right), \quad (3.10)$$

where  $\kappa = 1, 2, 3$  denotes the intrinsic symmetry axes of the surface vibration. A common convention for the parameter ranges are  $\beta \geq 0$  and  $\gamma \in [0^\circ, 60^\circ]$ .  $\beta = 0$  corresponds to a spherical shape.  $\beta > 0$  and  $\gamma = 0^\circ$  represent an axially symmetric prolate deformed nucleus, while  $\beta > 0$  and  $\gamma = 60^\circ$  correspond to an axially symmetric oblate deformed nucleus. A value of  $\gamma$  in between the two limiting cases corresponds to a triaxial deformation, *i.e.*, all three principal axes exhibit different alterations in elongation.

---

### Rotation

---

With the onset of nuclear deformation, the mass distribution in the nucleus in the ground state begins to deviate statically from a spherical shape. This deviation is small near closed shells, but can be significant in midshell regions. In the description of the quadrupole deformation, two important quantities are the moment of inertia and the quadrupole moment, both can be formulated in dependence of  $\beta$  for axially symmetric nuclei. For an ellipsoid, the rigid body moment of inertia for a solid sphere of radius  $r$  rotating around an axis through the center is given by

$$I = \frac{2}{5} M r^2. \quad (3.11)$$

A deformed nucleus exhibits a quadrupole moment  $Q_0$ , which is related to the deformation parameter  $\beta$  via

$$Q_0 = \frac{3}{\sqrt{5\pi}} Z R_0^2 \beta (1 + 0.16\beta). \quad (3.12)$$

This quadrupole moment  $Q_0$  is an *intrinsic*, model-dependent quadrupole moment, which deviates from the experimentally observable *spectroscopic* quadrupole moment  $Q$ . Both are related, to second order in  $\beta$ , via

$$Q = \frac{3K^2 - J(J+1)}{(J+1)(2J+3)} Q_0, \quad (3.13)$$

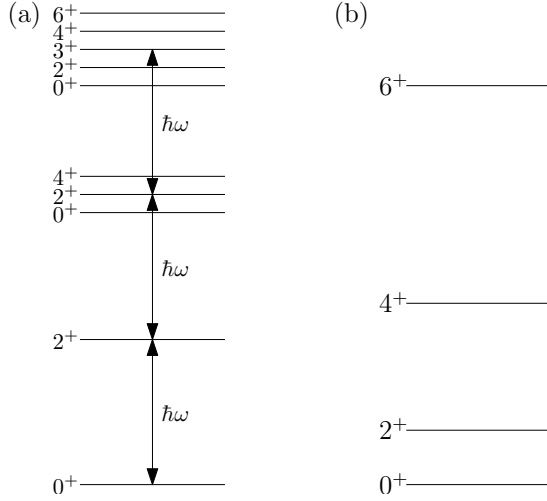


**Figure 3.1.:** Schematic low-lying level schemes of (a) quadrupole vibrational and (b) rotational behavior.

where  $K$  denotes the so-called *K-quantum number*, which is the projection of the angular momentum  $J$  onto the intrinsic symmetry axis of the nucleus, i.e.,  $K \leq J$ . Close inspection of Equation (3.13) reveals that the spectroscopic quadrupole moment has to vanish for states with  $J = 0$ . For the yrast  $2_1^+$  state ( $K = 0$ ),  $Q = -2/7 Q_0$ . In the limit of a rigid rotor, the intrinsic quadrupole moment  $Q_0(2_1^+)$  is related to the transition strength via

$$B(E2; 0_{1,\text{gs}}^+ \rightarrow 2_1^+) = \frac{5}{16\pi} e^2 Q_0(2_1^+)^2. \quad (3.14)$$

The energy of a rotational excitation with angular momentum  $J$ , based on a ground state of  $J^\pi = 0^+$ , is given by

$$E_{\text{rot}}(J) = \frac{\hbar^2}{2I} J(J+1). \quad (3.15)$$

A comparison of the low-energy level schemes of vibrational and rotational excitations is given in Figure 3.1. For rotational bands on top of a  $0^+$  ground state only even angular momenta  $J = 2, 4, 6, \dots$  can be found. From Equation (3.15), the excitation energy of non-vanishing rotations is  $E(2^+) = 6\hbar^2/2I$ ,  $E(4^+) = 20\hbar^2/2I$ ,

$E(6^+) = 42\hbar^2/2I, \dots$  Hence,  $R_{4/2} = 3.33$  for rotational bands.

As discussed above, superpositions of rotational and vibrational excitations of a deformed nucleus are also possible. Usually, vibrational excitations are the band heads rotational excitations are based on. However, vibrational excitations do not necessarily exhibit  $J = 0$ , thus, Equation (3.15) has to be generalized to

$$E_{\text{rot}} = \frac{\hbar^2}{2I} [J(J+1) - K(K+1)] . \quad (3.16)$$

For  $K = 0$  this results in a rotational band equivalent to the ground state band. Nevertheless, also rotational bands on top of  $K \neq 0$  states are allowed, featuring even and odd angular momenta, *i.e.*,  $J = K, K+1, K+2, \dots$  Low-lying levels of deformed nuclei often feature two rotational bands on top of a  $0^+$  and a  $2^+$  state, referred to as  $\beta$  and  $\gamma$  bands.

---

### 3.2 Shell Model

---

The existence of *magic numbers* was obvious from various experimental results as early as 1948. The abundance of a particular isotope relative to total natural abundance of the whole isotopic chain, the abundance of a particular isotone relative to the whole isotonic chain or the total natural abundance have already indicated the existence of particular stable nucleon configurations. *Goepfert-Mayer* [40] summarizes facts indicating the stability of shells of 50 and 82 protons and of 50, 82 and 126 neutrons. The nuclear shell model was developed independently by *Goepfert-Mayer* [41] and *Haxel, Jensen and Suess* [42] and published in 1949. It was a great success, as it was capable to theoretically justify the experimental findings. An increased stability was derived for particular *magic numbers* of protons and neutrons: 2, 8, 20, 28, 50, 82 and 126.

The starting point for microscopic investigations on nuclear structure is the interaction between the nucleons. Every nucleon, which is part of an atomic nucleus, possesses a particular kinetic energy and is subject to interactions with other nucleons. This force between nucleons is, for simplicity, assumed to be of 2-body nature. The Hamiltonian can then be given by

$$H = T + V = \sum_{i=1}^A \frac{\vec{p}_i^2}{2m_i} + \sum_{i>k=1}^A V_{ik}(\vec{r}_i - \vec{r}_k) . \quad (3.17)$$

The Hamiltonian has  $3A$  position coordinates, and is, consequently, extremely difficult to solve. The fundamental idea behind the independent particle model, which

is the basis of the shell model, is the independent motion of nucleons under the influence of a central potential. Other than in the electron hull surrounding the atomic nucleus, there is no external potential. Instead, the potential is formed by the nuclear force of  $A - 1$  nucleons acting on the  $A$ -th nucleon. The original Hamiltonian given in Equation (3.17), consisting of kinetic energy and two-body interaction terms, is modified by introduction of a 1-body potential  $U_i(\vec{r}_i)$ :

$$H = \underbrace{\sum_{i=1}^A \left[ \frac{\vec{p}_i^2}{2m_i} + U_i(\vec{r}_i) \right]}_{\equiv H_0} + \underbrace{\sum_{i>k=1}^A V_{ik}(\vec{r}_i - \vec{r}_k) - \sum_{i=1}^A U_i(\vec{r}_i)}_{\equiv H_{\text{residual}}} . \quad (3.18)$$

Using this Hamiltonian, the transformation from a *nucleon-nucleon* interaction potential to a common *central nuclear* potential can be achieved. The complex aim is to determine a mean-field potential  $U$ , which is experienced by all nucleons, and approximates the *nucleon-nucleon* interaction such that  $H_{\text{residual}}$  is a small perturbation of the Hamiltonian  $H_0$ . The residual interaction is, nevertheless, of uttermost importance in modern nuclear physics, as it gives rise to collective excitations. Taking the residual interaction into account widens the independent particle model out to the shell model.

An appropriate choice for the central potential is that of a harmonic oscillator, due to the attractive and short-range nature of the nuclear force. One of its flaws is the wrong asymptotic behavior (the potential is of infinite depth and width, in principle), though, it is sufficient as an approximation around the center and mathematically easy to handle. The potential is given by

$$V(\vec{r}) = \frac{1}{2} k \vec{r}^2 = \frac{1}{2} m \omega^2 \vec{r}^2, \quad (3.19)$$

where  $k$  is the spring constant in classic notion. For a 3-dimensional harmonic oscillator, the eigenvalues, *i.e.*, the excitation energies of modes of the oscillator,  $E_{nl}$  are given by  $E_{nl} = (2n + l + 1/2) \hbar \omega$ , where  $n \in \mathbb{N} \setminus \{0\}$  is the principal quantum number and  $l = 0, 1, 2, 3, \dots$  ( $s, p, d, f, \dots$ ) is the orbital angular momentum. However, different configurations can possess the same energy, producing degenerated energy levels for sets of the same oscillator shell number  $N = 2(n + 1) + l$ . This is depicted on the left side of Figure 3.2, where the energy of an excited state depends solely on  $N$ . However, it is also obvious that the magic numbers are not the ones found experimentally.

The degeneracy can be lifted by introducing additional terms which alter the potential. Nucleons in the center of a heavier nucleus should not experience any net force, because they are shielded from the asymmetric nucleon distribution at the

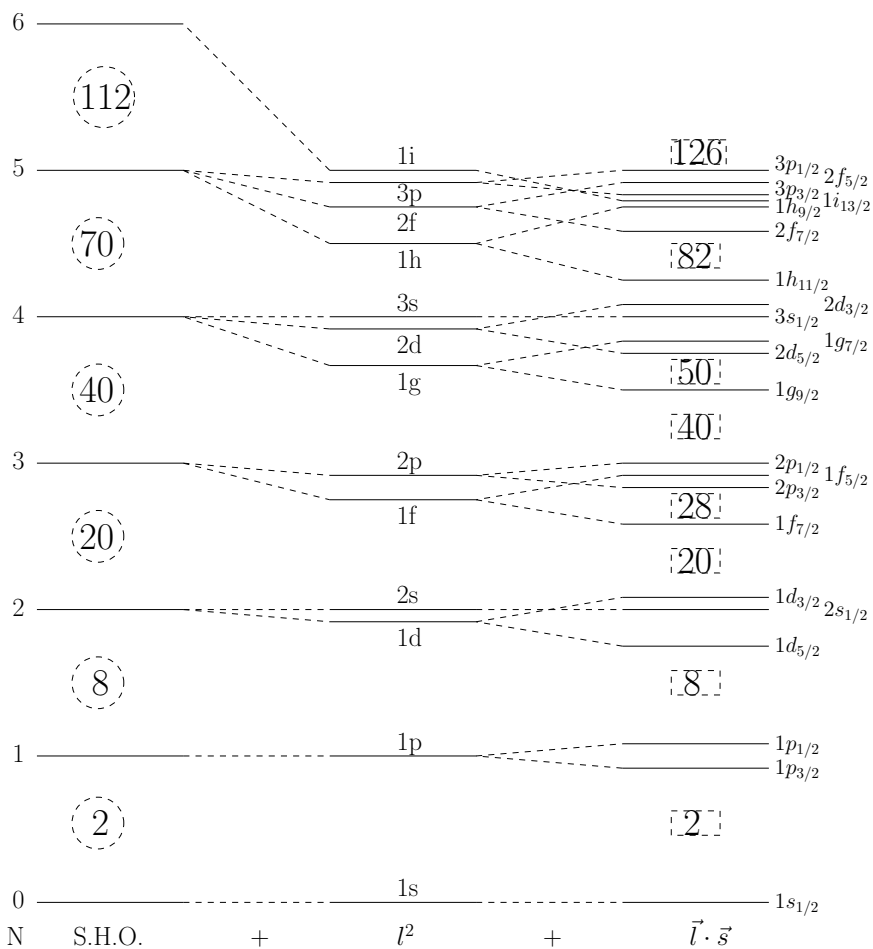


**Figure 3.2.:** Qualitative illustration of the orbitals emerging in the nuclear shell model. The model can be derived from a simple harmonic oscillator (S.H.O.) modified by a  $\vec{l}^2$  and a spin-orbit coupling  $\vec{l} \cdot \vec{s}$  term. Adapted from [39].

surface. Hence, the center of the nuclear potential shall be approximately flat. This can be achieved by changing the potential, but this will implicate more complex solutions. Another possibility is to include an attractive  $\vec{l}^2$  term in the potential, which splits the degeneracy in  $N$  and lowers levels of larger angular momentum  $l$ :

$$V_{l^2} = -V_l \vec{l}^2. \quad (3.20)$$

The combination of the harmonic oscillator potential and the  $\vec{l}^2$  term is shown in the middle of Figure 3.2. This is an improvement in comparison to the sole harmonic oscillator potential, but, nevertheless, does not generate the known magic numbers. Coupling the orbital angular momentum  $\vec{l}$  and the intrinsic nucleon spin  $|\vec{s}| = 1/2 \hbar$  yields another term, modifying the potential for a nucleon, depending on whether the spin is aligned parallel or antiparallel to the angular momentum. This leads to lowering of levels with  $j = l + s$  and raising of levels with  $j = l - s$ . The spin-orbit potential can be written as

$$V_{l \cdot s} = -V_{ls}(\vec{r}) \vec{l} \cdot \vec{s}. \quad (3.21)$$

The complete potential for the independent-particle model is then given by

$$U(\vec{r}) = \frac{1}{2} m \omega^2 \vec{r}^2 - V_l \vec{l}^2 - V_{ls} \vec{l} \cdot \vec{s}. \quad (3.22)$$

Inserting this rotation-symmetric central potential into the Hamiltonian  $H_0$  of Equation (3.18) yields the solution illustrated on the right side of Figure 3.2. The correct energy spacings resembling the empirically found *magic numbers* are clearly visible. An important additional property of an orbit is its parity quantum number  $\pi$ , which is related to the orbital angular momentum  $l$  via  $\pi_{nlm} = (-1)^l$ . Low-lying levels in between shell closures exhibit the same parity. This behavior emerges naturally from the degeneracy of the oscillator shell number, because an increase in angular momentum of two is equal to an increase in principal quantum number of one. However, this is not the case anymore in between higher-lying shells. The  $\vec{l}^2$  term at most, and a little less the spin-orbit coupling, lead to a substantial lowering of levels with large angular momentum, so they contribute to the next lower shell. Those levels are called *intruder* or *unique parity* orbits. In the independent-particle model they are necessary to resemble the correct magic numbers. In the presence of residual interactions, however, these orbits are mostly excluded from mixing with other nearby levels, due to their opposing parity.

As a consequence of the Pauli principle, the  $2j + 1$  nucleons of a completely filled orbit couple pairwise to  $J = 0$ . Hence, the properties of nuclei are determined by the nucleons in partially filled orbits, so-called *valence* nucleons. They are, in first

order, subject to the residual interaction, only. Valence nucleons of the same species in the same orbit can couple to different angular momenta  $J$ . The degeneracy of the various angular momenta, which is still present in the potential given in Equation (3.22), is broken by the residual interaction. An example of such a residual interaction is the  $\delta$  interaction

$$V_{\text{residual}} = -V_0 \delta(\vec{r}_1 - \vec{r}_2) \quad (3.23)$$

which models the short-range attractive part of the nuclear force. The  $\delta$  interaction is at maximum for two nucleons with maximum wave function overlap, which is the case for two antiparallel aligned nucleons, *i.e.*,  $M = m_1 + m_2 = 0$ . For this reason, nuclear configurations exhibiting  $J^\pi = 0^+$  are lowered most, followed by  $2^+, 4^+, \dots$  configurations. The number of pairs not coupled to  $0^+$  is measured by the *seniority*  $\nu$ . A prediction of this interaction is the  $0^+$  ground state of even-even nuclei. Another consequence is, that the properties of low-lying levels of even-odd or odd-even nuclei depend on the orbit of the last unpaired nucleon.

---

### 3.3 Interacting Boson Model

---

The *Interacting Boson Model* (IBM) [4] is an algebraic model describing low-energy collective excitations of atomic nuclei. The basic idea is, analog to the vibrational model of Bohr and Mottelson (cf. Section 3.1), to couple valence nucleons pairwise to bosons, drastically reducing the number of degrees of freedom. In the *IBM-1*, protons and neutrons are not distinguished.

In the *sd-IBM-1* a boson can carry an angular momentum of either  $L = 0$  ( $s$  boson) or  $L = 2$  ( $d$  boson). The bosons can mathematically be treated in terms of creation and destruction operators

$$s^\dagger, s, \quad \text{and} \quad d_\mu^\dagger, \tilde{d}_\mu, \quad (3.24)$$

respectively, with  $\mu = -2, \dots, 2$ . The operator  $\tilde{d}_\mu$  is related to the destruction operator  $d$  via  $\tilde{d}_\mu = (-1)^\mu d_{-\mu}$ . The components of the  $d$  boson and the  $s$  boson exhibit  $U(6)$  symmetry, which generators are given by  $s^\dagger s, s^\dagger \tilde{d}_\mu, d_\mu^\dagger s, [d_\mu^\dagger \tilde{d}_\mu]_J$ , with  $J = 0, 1, 2, 3, 4$  and  $|\mu| \leq J$ . This is analog for  $s$  and  $d$  bosons with projection  $\mu$  to the general boson operators introduced in Eqs. (3.5) and (3.6).

Among the set of generators, several subgroups can be found. Under the con-



straint, that that subgroups of  $U(6)$  have to include the rotational algebra  $O(3)$ , the following decompositions are found [4]:

$$U(6)_N \supset U(5)_{n_d} \supset O(5)_{\nu, \tilde{n}_\Delta} \supset O(3)_L \supset O(2)_M, \quad (3.25)$$

$$U(6)_N \supset SU(3)_{(\lambda, \mu), \tilde{\chi}} \supset O(3)_L \supset O(2)_M, \quad (3.26)$$

$$U(6)_N \supset O(6)_\sigma \supset O(5)_{\tau, \tilde{\nu}_\Delta} \supset O(3)_L \supset O(2)_M. \quad (3.27)$$

The subscripts correspond to the quantum numbers of the irreducible representations. For the subgroups  $U(5)$ ,  $SU(3)$  and  $O(6)$  analytic solutions exist. The subgroups represent vibrational, rotational and  $\gamma$ -soft behavior, respectively. A simple Hamiltonian is in the framework of the  $sd$ -IBM-1 given by [43]

$$H = \epsilon \hat{n}_d + \kappa Q^\chi Q^\chi, \quad (3.28)$$

where

$$\hat{n}_d = d_\mu^\dagger \cdot \tilde{d}_\mu, \quad (3.29)$$

$$Q^\chi = d^\dagger s + s^\dagger \tilde{d} + \chi [d^\dagger \tilde{d}]_2. \quad (3.30)$$

The operator  $\hat{n}_d$  is the  $d$  boson number operator and  $\chi$  is the quadrupole structure parameter.

Up to now, no distinction between protons and neutrons is made. The *Interacting Boson Model-2* [3, 4] has been introduced as an extension of the IBM-1, which is necessary in order to cover the proton-neutron interaction. In particular the IBM-2 is capable of describing excitations of proton-neutron mixed-symmetry, so-called *mixed-symmetry states* (MSS). An eye-catching innovation in the model is the introduction of separate creation and destruction operators of proton and neutron bosons. The extended Hamiltonian is given by [44]

$$H = \epsilon_\pi \hat{n}_{d_\pi} + \epsilon_\nu \hat{n}_{d_\nu} + \kappa_{\pi\pi} Q_\pi^{\chi_\pi} \cdot Q_\pi^{\chi_\pi} + 2\kappa_{\pi\nu} Q_\pi^{\chi_\pi} \cdot Q_\nu^{\chi_\nu} + \kappa_{\nu\nu} Q_\nu^{\chi_\nu} \cdot Q_\nu^{\chi_\nu} + \hat{M}(\xi_1, \xi_2, \xi_3), \quad (3.31)$$

where  $\pi$  and  $\nu$  denote proton and neutron parameters, respectively.  $\epsilon_\pi$  and  $\epsilon_\nu$  denote single  $d$  boson energies, while  $Q_\pi^{\chi_\pi}$  and  $Q_\nu^{\chi_\nu}$  are the quadrupole operators defined in Equation (3.30), for proton and neutron quadrupole phonons, respectively. The Majorana interaction  $\hat{M}$  is defined as [44]

$$\begin{aligned} \hat{M}(\xi_1, \xi_2, \xi_3) &= \frac{1}{2} \xi_2 (s_\pi^\dagger d_\nu^\dagger - d_\pi^\dagger s_\nu^\dagger) \cdot (s_\pi \tilde{d}_\nu - \tilde{d}_\pi s_\nu) \\ &\quad - \sum_{K=1,3} \xi_K ([d_\pi^\dagger d_\nu^\dagger]_K \cdot [\tilde{d}_\pi \tilde{d}_\nu]_K). \end{aligned} \quad (3.32)$$

In analogy to the isospin for formal discrimination of protons and neutrons, the  $F$ -spin quantum number is defined for proton and neutron bosons [3]. The concept of  $F$ -spin [45] is formally equivalent to the isospin, resulting in an assignment of an  $F$ -spin of  $F = 1/2$  with projections  $F_z = +1/2$  for proton and  $F_z = -1/2$  for neutron bosons. Thus, the total projection  $F_z$  for a nucleus is  $F_z = 1/2(N_\pi - N_\nu)$ , with the proton and neutron boson number  $N_\pi$  and  $N_\nu$ , respectively. The maximal  $F$ -Spin is given by  $F_{\max} = 1/2(N_\pi + N_\nu)$ . The  $F$ -spin quantifies the symmetry of a wave function under pairwise exchange of proton and neutron boson labels. States with maximum  $F$ -Spin exhibit a wave function which is symmetric under the exchange. This class of states is labeled *fully-symmetric states* (FSS) and correspond to the states emerging in the IBM-1. States exhibiting  $F < F_{\max}$  are labeled *mixed-symmetry states* (MSS) and their wave function is partially antisymmetric under the exchange of proton and neutron boson labels. So far, only MSS with  $F = F_{\max} - 1$  have been identified. Examples for such states are the  $1^+$  scissors mode [46] or  $2^+$  mixed-symmetry states in vibrational nuclei [44]. Excitations of lower  $F$ -spin have not been identified, yet.

A schematic level scheme is shown in Figure 3.3 using the Hamiltonian

$$H = \epsilon(n_{d_\pi} + n_{d_\nu}) + \lambda \hat{M} \quad (3.33)$$

for a nucleus exhibiting boson numbers  $N_\pi = N_\nu = 1$  and  $\epsilon = \epsilon_\pi = \epsilon_\nu$ . The Majorana operator takes the simple form  $\hat{M} = [F_{\max}(F_{\max} + 1) - \hat{F}^2]/2$ , in this case. Its structure is such, that it acts on MSSs only. This sensitivity results in the  $F = F_{\max} - 1$  states residing at higher energies w.r.t.  $F = F_{\max}$  states.

The experimental signature for such a configuration is a strong M1 decay of a MSS. This is due to the  $F$ -vector ( $\Delta F = 1$ ) nature of the M1 transition operator, which is given by [44]

$$T(M1) = \sqrt{\frac{3}{4\pi}} [g_\pi L_\pi + g_\nu L_\nu] \mu_N \quad (3.34)$$

$$= \sqrt{\frac{3}{4\pi}} \left[ \frac{N_\pi g_\pi + N_\nu g_\nu}{N} L_{\text{tot}} + (g_\pi - g_\nu) \frac{N_\pi N_\nu}{N} \left( \frac{L_\pi}{N_\pi} - \frac{L_\nu}{N_\nu} \right) \right] \mu_N, \quad (3.35)$$

where  $L_\rho = \sqrt{10} [d_\rho^\dagger \times \tilde{d}_\rho]_1$ ,  $\rho \in \{\pi, \nu\}$ , is the angular momentum operator for proton and neutron bosons, with the total angular momentum operator  $L_{\text{tot}} = L_\pi + L_\nu$ .  $L_{\text{tot}}$  is diagonal and, thus, not able to induce transitions between different states [45].  $g_\rho$  are the effective boson  $g$ -factors and  $N = N_\pi + N_\nu$  is the total number of bosons. For states of same  $F$ -Spin matrix elements for an operator  $T_\rho$  are proportional to  $N_\rho$ , i.e.,  $\langle \alpha; F \| T_\rho \| \alpha'; F \rangle = N_\rho c_{\alpha\alpha'}$  [45].  $c_{\alpha\alpha'}$  depends on the

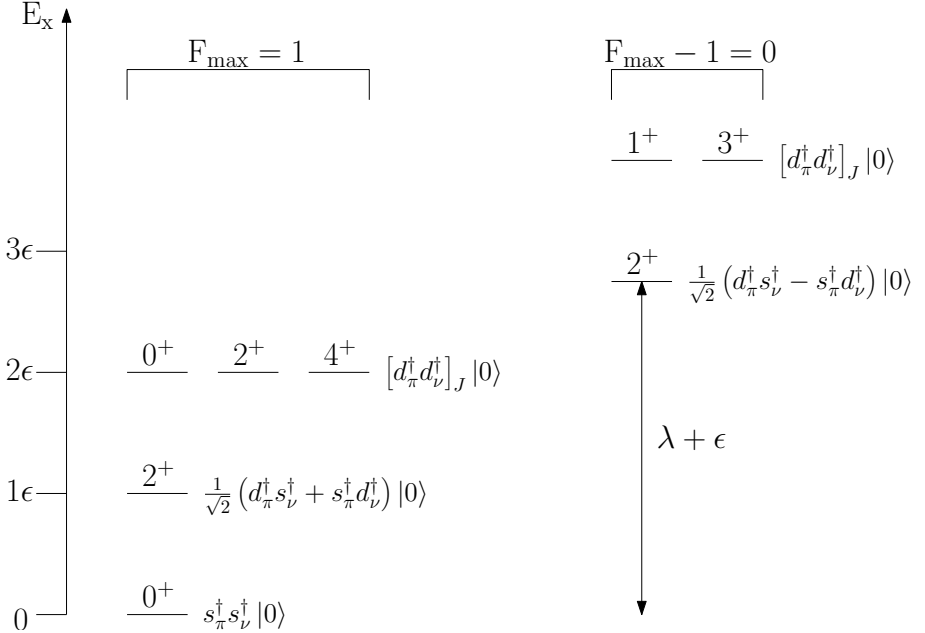


**Figure 3.3.:** Schematic low-lying level schemes of the IBM-2 Hamiltonian  $H = \epsilon (n_{d_\pi} + n_{d_\nu}) + \lambda \hat{M}$  for  $N_\pi = N_\nu = 1$ . The Majorana operator  $\hat{M}$  has an impact on MSSs, only. Adapted from [44].

initial and final states only, hence, it is the same for  $L_\pi$  and  $L_\nu$ . Ultimately, M1 transitions between FSSs are forbidden. M1 transition matrix elements connecting MSSs and FSSs are expected to be of the order of  $1 \mu_N^2$ . The M1 transition strength can be deduced in the  $U(5)$  dynamical symmetry limit from

$$B(M1; 2_{1,ms}^+ \rightarrow 2_1^+) = \frac{3}{4\pi} (g_\pi - g_\nu)^2 \frac{6}{N^2} N_\pi N_\nu. \quad (3.36)$$

The  $F$ -scalar ( $\Delta F = 0$ ) E2 transition operator

$$T(E2) = e_\pi Q_\pi^{\chi_\pi} + e_\nu Q_\nu^{\chi_\nu}, \quad (3.37)$$

where  $e_\pi$  and  $e_\nu$  are effective quadrupole boson charges, couples FSSs and FSSs or MSSs and MSSs, but is forbidden for transitions between MSSs and FSSs. Practically, the transition is never completely inhibited, but in most cases it is strongly

suppressed.

In order to be able to describe also  $3^-$  states, the  $sd$ -IBM-2 has to be expanded to include octupole  $f$  bosons, for which reason this enhanced model is dubbed the  $sdf$ -IBM-2 [47].  $f$  bosons exhibit an angular momentum of 3 and exhibit intrinsic negative parity. The  $sdf$ -IBM-2 does not only introduce FSSs and MSSs of  $J^\pi = 3^-$ , but it also couples  $f$ -boson spin-3 and  $d$ -boson spin-2 states. The corresponding E1 operator is also of  $F$ -vector character, resulting in enhanced transition strength between the fully-symmetric  $3_1^-$  and the mixed-symmetric  $2_{1,ms}^+$  state, yet, the transition between the fully-symmetric  $3_1^-$  and  $2_1^+$  states is suppressed.

---

### 3.4 Quasi-Particle Phonon Model

---

The quasiparticle-phonon model (QPM) [48] is a microscopic approach extending the quasiparticle random-phase approximation (QRPA) to a multiphonon basis. It is capable of describing collective excitations of nuclei. In the QPM, a Hamiltonian of general separable form is treated in a microscopic multiphonon approach. This allows for describing anharmonic features of collective modes as well as multiphonon states. The model incorporates a two-body Hamiltonian, which itself is composed of several multipole-multipole potentials, allowing the QPM to cover a large configuration space. The QPM can be seen as the microscopic approach to the nuclear structure phenomena described macroscopically by the IBM-2. A short summary of the basic principles, based on [48], is presented in the following.

The QPM works with a Hamiltonian of the form

$$H = H_{\text{sp}} + V_{\text{pair}} + V_{\text{M}}^{\text{ph}} + V_{\text{SM}}^{\text{ph}} + V_{\text{M}}^{\text{pp}}. \quad (3.38)$$

$H_{\text{sp}}$  is a single-particle Hamiltonian, including a mean-field Wood-Saxon potential,  $V_{\text{pair}}$  is the monopole pairing,  $V_{\text{M}}^{\text{ph}}$  and  $V_{\text{SM}}^{\text{ph}}$  include multipole and spin-multipole interactions of particles and holes, while  $V_{\text{M}}^{\text{pp}}$  represents the multipole interaction of particles. The definitions of the potentials can be found in Ref. [48].

Based on the particle and hole generation operators  $a_q^\dagger$  and  $a_q$ , the quasiparticle generation and elimination operators  $\alpha_q^\dagger$  and  $\alpha_q$  are derived. The separable Hamiltonian is then used to generate the QRPA phonons via

$$Q_\lambda^\dagger = \frac{1}{2} \sum_{qq'} \left\{ \psi_{qq'}^\lambda [\alpha_q^\dagger \alpha_{q'}^\dagger]_\lambda - \varphi_{qq'}^\lambda [\alpha_{q'} \alpha_q]_{\bar{\lambda}} \right\}. \quad (3.39)$$

The amplitudes  $\psi_{qq'}^\lambda$  and  $\varphi_{qq'}^\lambda$  are required to fulfill the conditions

$$\frac{1}{2} \sum_{qq'} [\psi_{qq'}^\lambda \psi_{qq'}^{\lambda'} - \varphi_{qq'}^\lambda \varphi_{qq'}^{\lambda'}] = \delta_{\lambda\lambda'}. \quad (3.40)$$

The QRPA phonons generated this way allow for expressing the Hamiltonian of quasiparticle separable form by phonons via

$$H_{\text{QPM}} = \sum_{\lambda} \omega_{\lambda} Q_{\lambda}^{\dagger} Q_{\lambda} + H_{\text{vq}}. \quad (3.41)$$

where  $\omega_{\lambda}$  is the QRPA phonon energy and  $H_{\text{vq}}$  is a phonon coupling part. The Hamiltonian transformed into the phonon form is diagonalized in a space spanned by states composed of one, two and three QRPA phonons. The wave functions are then given by

$$\begin{aligned} \Psi_{\nu JM} = & \sum_i R_i^{(\nu J)} Q_{iJM}^{\dagger} |0\rangle + \sum_{\lambda_1 \lambda_2} P_{\lambda_1 \lambda_2}^{(\nu J)} [Q_{\lambda_1}^{\dagger} \otimes Q_{\lambda_2}^{\dagger}]_{JM} |0\rangle \\ & + \sum_{\lambda_1 \lambda_2}^{\lambda_3 I} T_{\lambda_1 \lambda_2 \lambda_3}^{(\nu J)} [[Q_{\lambda_1}^{\dagger} \otimes Q_{\lambda_2}^{\dagger}]_I \otimes Q_{\lambda_3}^{\dagger}]_{JM} |0\rangle. \end{aligned} \quad (3.42)$$

They have to be normalized and antisymmetrized according to a particular procedure outlined in Ref. [48] and Refs. therein.

In the QPM, one-body transition operators  $\mathfrak{M}(\sigma\lambda)$  can be separated into two pieces, leading to the expression

$$\mathfrak{M}(\sigma\lambda) = \mathcal{M}_{\text{ph}}(\sigma\lambda) + \mathcal{M}_{\text{sc}}(\sigma\lambda). \quad (3.43)$$

The first term connects states differing by one phonon. It is the leading term and is responsible for the *boson-allowed* transitions. It is given by

$$\mathcal{M}_{\text{ph}}(\sigma\lambda\mu) = \frac{1}{\sqrt{2\lambda+1}} \sum_{qq'} \langle q \| \mathfrak{M}(\sigma\lambda) \| q' \rangle (u_q v_{q'} \pm v_q u_{q'}) (\Psi_{qq'}^{\lambda} + \Phi_{qq'}^{\lambda}) (Q_{\lambda}^{\dagger} + Q_{\bar{\lambda}}) \quad (3.44)$$

The second term is the quasiparticle scattering term, which is given by

$$\mathcal{M}_{\text{sc}}(\sigma\lambda) = \frac{1}{\sqrt{2\lambda+1}} \sum_{qq'} \langle q \| \mathfrak{M}(\sigma\lambda) \| q' \rangle (u_q u_{q'} \mp v_q v_{q'}) [\alpha_q^{\dagger} \times \alpha_{q'}]_{\lambda}. \quad (3.45)$$

This term links states with the same number of phonons, or with phonon counts differing by two, and is responsible for the *boson-forbidden* transitions.

A problem in the application of the QPM is the determination of the parameters. The parameters of the Wood-Saxon potential are deduced in order to resemble single-particle spectra. The single-particle space includes shells below and bound

states above the Fermi energy, to maximize the energy range available for investigation of nuclear structure. The large model space allows for the use of effective charges, which can be close to the bare values. A constant monopole pairing interaction is used, which amplitude is determined from odd-even mass differences. The coupling parameters for the quadrupole-quadrupole and octupole-octupole particle-hole potentials are fixed from fits to the energies of the  $2_1^+$  and  $3_1^-$  states. The coupling parameters of other multipolarities are chosen such, that the energy of the lowest two-quasiparticle states remains unchanged.

The quadrupole pairing is the only particle-particle interaction relevant to low-energy spectra, and is assumed to be equal for protons and neutrons. It is crucial for the properties of low-energy quadrupole modes determined using the QPM. Sets of parameters are always determined for a particular mass region, and used for calculations of the full energy range. In the QPM, a problem underlying the QRPA persists: The particle number is only conserved on average. However, the violation for one species of nucleons is smaller than 10%, in common.

Another issue is the selection of the phonons to include in the multiphonon basis used for diagonalization. The choice is restricted by the states to be investigated. For low-lying states of positive parity, only phonons exhibiting positive parity are considered, but in multipolarities  $\lambda = 1 - 6$ . For each  $\lambda$ , phonons up to a certain cutoff energy, which depends on the species of states to be investigated, are included. The structure of the QPM is subject to changes, when increasing the number of two-phonon basis states, until a saturation value is reached. The onset of this saturation regime determines the dimensions of the multiphonon basis to use.

The close relation between IBM-2 and QPM can be seen, when identifying  $d$  bosons in the IBM-2 as  $Q_{\lambda=2}^\dagger$  QRPA phonons.

---

## 4 Experimental Setup

The experiments presented in this work were conducted at different facilities. The measurement of the transition strength and the quadrupole moment of the exotic nucleus  $^{142}\text{Sm}$ , exhibiting a half-life of 72.49(5) min, was performed at CERN, the European Organization for Nuclear Research, in Geneva, Switzerland. The experiments for the investigation of stable  $^{202,204}\text{Hg}$  were conducted at Argonne National Laboratory, in Chicago, USA. Nuclear structure investigations of atomic nuclei, no matter whether the nuclei of interest are stable or unstable, make certain demands on the design of a facility. Although the basic principle is the same for all experiments performed within this work, differences exist when working with stable or exotic nuclei.

---

### 4.1 REX-ISOLDE & Miniball

---

The ISOLDE<sup>1</sup> facility is dedicated to the investigation of nuclear structure physics of exotic nuclei and is one of the oldest and most successful experiments present at CERN. The ISOLDE experiment was initially located nearby and connected to the Synchrocyclotron, which delivered protons exclusively for this experiment for over two decades. The Synchrocyclotron was shut down in 1990, leading to a relocation of the ISOLDE experiment, which is since 1992 supplied with protons by the Proton Synchrotron Booster [50]. The ISOLDE facility, in the configuration before the remodeling towards HIE-ISOLDE started in 2013, is shown in Figure 4.1.

---

#### 4.1.1 Isotope Production

---

The ISOLDE facility makes use of the ISOL technique for the production of exotic nuclei. The ISOL technique – in general – consists of a high power source providing ionizing radiation, e.g., protons, electrons or photons, impinging on suitable so-called primary “targets”. These “targets” are conveniently made from material which in first place has to fulfill two conditions: It needs to exhibit nuclei of large mass as well as a high boiling point, so that it stays solid over a large temperature range, simplifying handling under everyday conditions. Nevertheless it has also

---

<sup>1</sup> Isotope Separator Online Device

been possible to operate using molten targets. The primary target containers are heated, in addition, in order to increase vapor pressure and to optimize evaporation of the produced ions. The electrical heating of the targets may cause them to exceed temperatures of 2000 °C.

In the case of the current ISOLDE facility the high power radiation source is the PSB<sup>2</sup>, providing protons with an kinetic energy of about 1.4 GeV. The PSB consists, in fact, of four vertically stacked identical synchrotrons, which deliver about 2  $\mu$ s long pulses of about  $10^{13}$  protons per pulse at a low repetition rate grouped in a so-called supercycle. About one third to one half of the pulses of such a supercycle are dedicated to isotope production at ISOLDE, equaling a DC proton current of about 2  $\mu$ A [51]. The remaining pulses are delivered to the Proton Synchrotron, which is amongst others used as pre-accelerator for the Large Hadron Collider. The protons

---

<sup>2</sup> Proton Synchrotron Booster

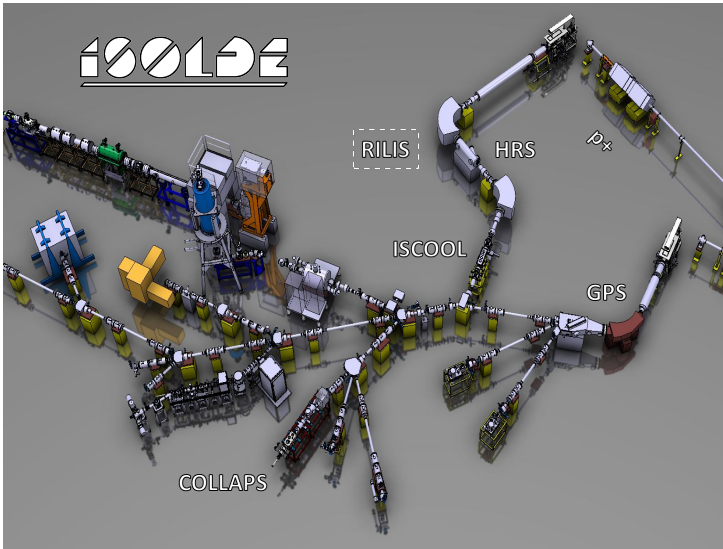


**Figure 4.1.:** Schematic view of the ISOLDE facility ground floor. The proton beams are impinging from the middle right side onto the primary targets, separate for GPS and HRS, which afterwards are used to select the species of interest. The beam is then guided towards the experiments or post-acceleration. The REX section is located within the top left beamline. Image taken from [49].



---

can be redirected towards two target stations containing a primary target, each. The energy of the protons allows for spallation, fragmentation and fission processes of the primary target material. This allows for production of a wide range of nuclei, notably also of proton-rich nuclei, in contrast to spontaneous-fission sources, which favor neutron-rich nuclei within certain mass regions. The range of nuclei produced can be controlled by choosing an appropriate primary target material. Produced nuclei will afterwards leave the primary target via evaporating through a transfer line, consisting of selected metals or quartz glass, mounted on top of the target container, directing the nuclei towards the ion source.

The ISOLDE facility offers a rich bouquet of ion sources, suitable for various kinds of atomic species:

- **Surface Ion Source**

The Surface Ion Source consists of a tube of metal connected to the transfer line, heated up up to 2000 °C, exhibiting a higher work function than the atom to ionize, stripping single valence electrons.

- **Plasma Ion Source**

Atoms emerging from the primary target, which cannot be ionized via surface ionization, may be directed into a Plasma Ion Source, holding a electron beam induced plasma of a noble gas mixture. In addition, an external magnetic field is applied. For the ionization of noble gas isotopes a water cooled transfer line is available, in order to suppress contamination.

- **Laser Ion Source**

The Laser Ion Source RILIS<sup>3</sup> allows for selective ionization of specific elements. A combination of several laser beams at various wavelength is directed into the surface ionization tube to interact with the vaporized atoms. The lasers' wavelengths are precisely tuned to a sequence of successive electronic transfer energies, leading to the ionization of atoms of a specific element. This allows for greatly enhancing the amount of ions of a selected element.

The primary target container is on 30–60 kV potential, while behind the ion source ground potential is present, resulting in the extraction of accelerated isotopes [51].

---

<sup>3</sup> Resonance Ionization Laser Ion Source

---

### 4.1.2 Purification

---

The purification of the cocktail beam is performed by using two mass separation arrangements, the GPS<sup>4</sup> and the HRS<sup>5</sup> [51]:

- The GPS consists of a single 70°, edge focusing bending magnet with a radius of 1.5 m followed by an electrostatic “switchyard”. This device allows for extracting three different masses, within  $\pm 15\%$  around the central mass, and directing each to an experiment. Without making use of the “switchyard” the beam can be guided to other experiments, which are also reachable from the HRS. This mass separator exhibits a resolving power  $\Delta M/M$  of 2400.
- The HRS is composed of two C-yoke magnets of bending radii of 1 m, each, and angles of 90° and 60°. The former one also exhibits edge focusing. Using the combination of these magnets, as well as electrostatic ion optics surrounding the magnets, a mass resolving power of 11000 – 15000 is achievable.

The continuous ion beam is afterwards delivered to the low-energy experiments, *e.g.*, COLLAPS [52] or ISOLTRAP [53], but can also be guided towards the post-acceleration section.

---

### 4.1.3 Post Acceleration

---

The REX-ISOLDE [54] post-acceleration section (*cf.* Figure 4.2) starts with a preparatory arrangement, shown in detail in Figure 4.3, providing a beam for most efficient acceleration and improved signal-to-background ratio. The process starts with bunching the continuous beam of singly charged ions. This is done by guiding the beam into a Penning trap (REXTRAP). The trap itself consists of a 1 m tube, using a 3 T magnetic field. The tube is filled with an inert buffer gas, *e.g.*, Argon at  $10^{-3}$  mbar. The ions under investigation collide multiple times with the atoms of the buffer gas, and are phase-space cooled in the process. In order to achieve a suitable speed to decelerate the ions in the trap, the trap resides on a 60 kV high voltage platform, so the 60 keV ions coming from the primary target are slowed down to few eV before entering the trap. In addition, sideband cooling can be used to further cool and purify the beam. In this mode a RF field is used to drive the ions towards orbits, which are larger than the opening of the trap, and back to small

---

<sup>4</sup> General Purpose Separator

<sup>5</sup> High Resolution Separator

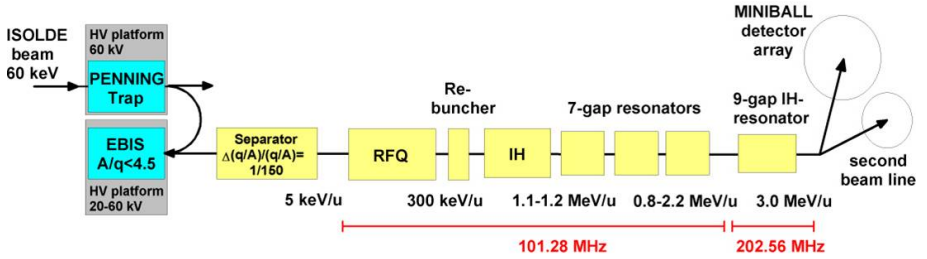


**Figure 4.2.:** Schematic view of the REX beam preparation and acceleration setup. The beam coming from either GPS or HRS is guided into REXTRAP for bunching, charge bred in REXEBIS and afterwards separated and accelerated. Image taken from [55].

orbits of low diameter. This procedure depends on the  $A/q$  ratio of the ions and is thus suited to remove unwanted contamination from the beam. At the end of the cooling process the potential is lowered and the ion bunch is extracted towards the REXEBIS for charge breeding.

The ions of interest are bunched and exhibit low emittance behind the REXTRAP, but still are singly charged, whereas multiply charged ions offer higher acceleration effectiveness. This is the purpose of the “charge breeding”, where ions are getting stripped of hull electrons, *i.e.*, acquire a higher positive charge. Bunched ions from the Penning trap are injected into the EBIS<sup>6</sup>. The ion source is composed of a 1.5 m solenoid, drift tubes and an electron source. The electrons released from the source are accelerated to 3 – 6 keV by drift tubes outside the solenoid, while the drift tubes inside the solenoid slow the electrons down for better collection at the electron collector in front of the injection/extraction window, and focused by a magnetic field of about 2 T. The source is capable of providing electron currents of up to 0.4 A, yielding, in combination with the strong magnetic field, current densities of about  $150 A/cm^2$ . The ions are trapped longitudinally via cylindrical electrodes around the electron beam and radially by the space charge of the electrons. They are “charge bred” stepwise via collisions with beam electrons, where the desired mass-to-charge ratio for the successive separation and acceleration is centered around  $A/q \approx 4.5$ . The efficiency of this process scales with the phase space overlap of the beam electrons and the bunched ions. The ionization process generates a charge-state distribution, which center and width is defined by the breeding time. After the breeding, the potential confining the ions in the longitudinal direc-

<sup>6</sup> Electron Breeder Ion Source

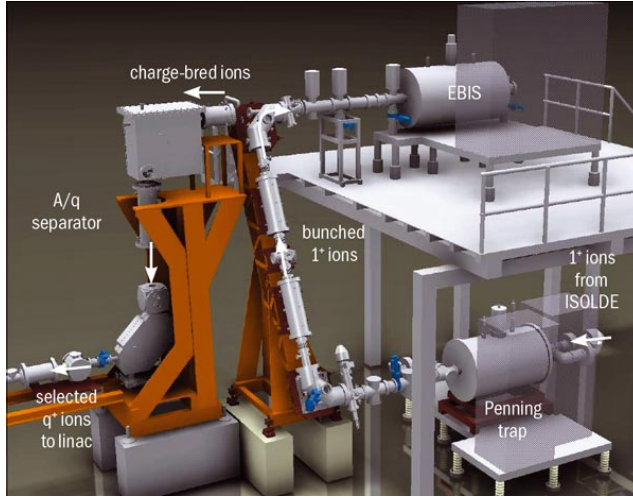


**Figure 4.3.:** Schematic view of the REX beam preparation section. The ions coming from the ISOLDE mass separators are cooled down in first placed, followed by charge breeding as well as additional mass separation, to get rid of buffer gas remains. Image taken from [55].

tion is continuously lowered, so the ions can be extracted with an arbitrary bunch length.

After the “charge breeding” another separation process occurs. At this point the beam consists of various species, *i.e.*, isobaric ions from the mass separation as well as buffer gas ions, which outnumber the ions under investigation, stemming from the REXTRAP in multiple charge states, which necessitates an additional step of separation. The ions exhibit, in addition, a large energy spread, rendering the use of magnetic mass separation impracticable. A solution offers a so-called Nier-spectrometer consisting of a  $90^\circ$  electrostatic, energy-filtering deflector and a subsequent  $90^\circ$  dipole magnet, arranged in an S-shape, featuring a  $A/q$  resolution of 150. Using the aforementioned way of separation, by selecting a single ion species of a certain charge state, limits the breeding efficiency to a maximum of 30%. The ions leave the REXEBIS at around 5 keV/u, and are at this point sufficiently purged of contamination and prepared for efficient acceleration. The complete temporal shaping of the continuous ion beam towards accelerator compatible bunches is depicted in Figure 4.5.

Subsequently is the acceleration section located. This section is depicted in Fig-

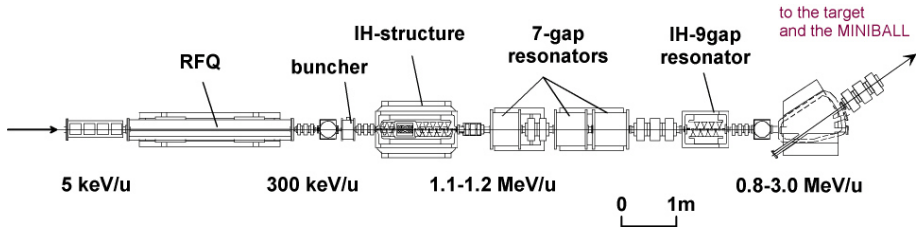


**Figure 4.4.:** Schematic view of the REX acceleration section. The ions leaving the REXEBIS at about 5 keV/u are subsequently accelerated to up to 3 MeV/u using different, velocity adjusted accelerating structures. Image taken from [55].

ure 4.4. It allows for the post-acceleration of the RIB<sup>7</sup> to up to 0.8 – 3.0 MeV/u. The first stage of acceleration is a RFQ<sup>8</sup>, a structure exhibiting a special RF field, which is not only suited for acceleration, but at the same time features longitudinal and transversal focusing of the beam, providing the temporal micro-structure necessary for the following resonators. The beam structure is further shaped, in order to match the longitudinal phase space and the acceptance of the following IH structure. The IH structure consists of specifically shaped drift tubes, permitting acceleration to 1.1 – 1.2 MeV/u. In order to achieve kinetic energies of 0.8 – 3.0 MeV/u, three 7-gap split-ring resonators as well as a 9-gap Interdigital-H structure follow. The ions are then guided towards the experimental setups.

#### 4.1.4 Gamma Spectroscopy

In this work the experimental setup used was surrounded by the Miniball detector array [56]. The Miniball array consists of eight triple-cluster HPGe<sup>9</sup> detectors, summing up to a total number of crystals of 24, and was designed for the detection of  $\gamma$  radiation. Miniball was located downstream the REX post-accelerator (cf. Figure 4.4) and complemented by a particle detector.

The HPGe triple-clusters are located around a common axis within a shared housing, and, together with the pre-amplifiers, connected to a collective dewar for cooling. The Miniball detectors stem from a first generation of segmented detectors, featuring a six-fold segmentation of the front face of each germanium

<sup>7</sup> Rare Ion Beam

<sup>8</sup> Radio Frequency Quadrupole

<sup>9</sup> High Purity Germanium

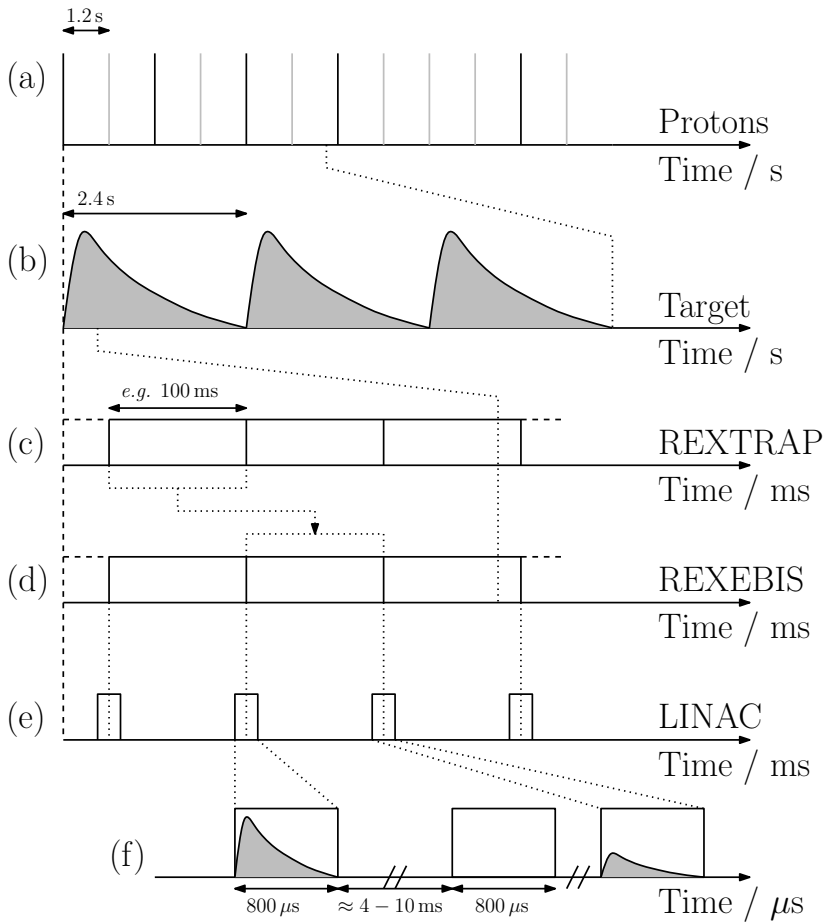


**Figure 4.5.:** Time structure of the ISOLDE facility through all steps. (a) shows the "supercycle" structure with proton beams 1.2s apart. Black are bunches delivered to ISOLDE, grey are bunches delivered to other experiments. (b) shows the release of the produced nuclei. The slope of the curve depends on the properties of the primary target and the ion source as well as on the chemical properties of the produced species. (c) shows the trapping process in the REXTRAP, whereas (d) shows the "charge breeding" in the REXEBIS. (e) depicts the macro-bunch structure of the REX-LINAC after extraction from the REXEBIS, while (f) shows the micro-bunch structure delivered to the experimental setup.

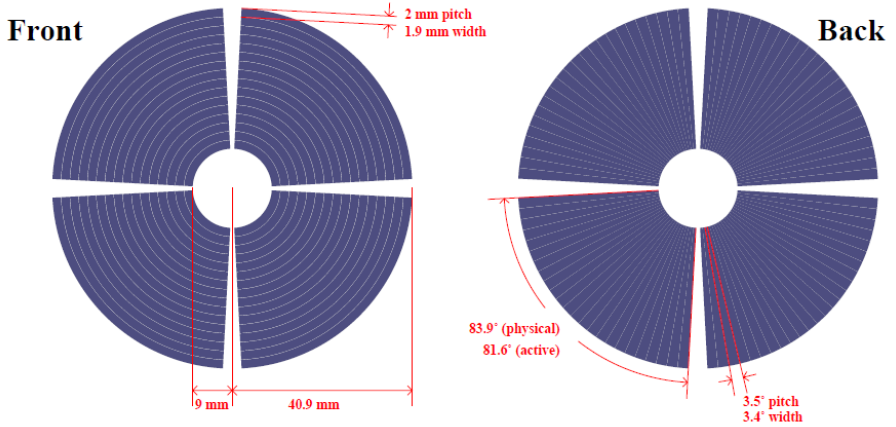


**Figure 4.6.:** Schematic view of the DSSSD used in the  $^{142}\text{Sm}$  Coulomb-excitation experiment at ISOLDE. The left image shows the front layer segmented in the polar angle, whereas the right image shows the back layer segmented in the azimuthal angle. Image taken from [58].

crystal. This permits an improved angular resolution, resulting in an improved Doppler-correction of the  $\gamma$  rays. For example, the 2167.5-keV,  $2_1^+ \rightarrow 0_{1,gs}^+$  transition of  $^{38}\text{Ar}$  was observed using Miniball. The Doppler-correction using the position information of the core contact yielded a FWHM of 35 keV, whereas using the signal from the segments for determining the position, the FWHM was reduced to 15 keV [57]. In the measured events only the core connection is used to determine the energy of the incoming radiation, while the segments solely serve for enhancing the angular resolution. This adds up to a total of seven signals emerging from a single crystal. The front faces of the triple clusters are located about 10 cm away from the center of the target chamber, manifesting in a solid angle coverage of about 60%.

The Coulomb-excitation target-chamber inside the Miniball array was made from a single piece, exhibiting two half-spheres at an inner radius of about 8 cm. Inside the target chamber a particle detector is located. This is usually a single DSSSD<sup>10</sup> (shown schematically in Figure 4.6). Besides the setup using a single DSSSD detector, more complicated approaches have been developed, e.g., the T-REX arrangement [59] for investigation of transfer reactions, which consists of several DSSSD

<sup>10</sup> Double-Sided Silicon Strip Detector

---

detectors of circular and rectangular shape, covering most of the solid angle. The single DSSSD detectors used inside Miniball for Coulomb-excitation experiments exhibit a radius of about 41 mm to the outer edge of the active surface. The detector consists of two layers of silicon, which are segmented in the polar angle on the front and in the azimuthal angle on the back. The active surfaces are partitioned into four quadrants, each. The front layer is made of 16 rings of a width of 1.9 mm with spacing of 2 mm in between rings, where the innermost ring possesses a radius of 9 mm. For the measurement of  $^{142}\text{Sm}$ , a distance between the Coulomb-excitation target and the DSSSD of 25.2 mm was chosen, resulting in an angular coverage of  $19.7^\circ - 58.4^\circ$ .

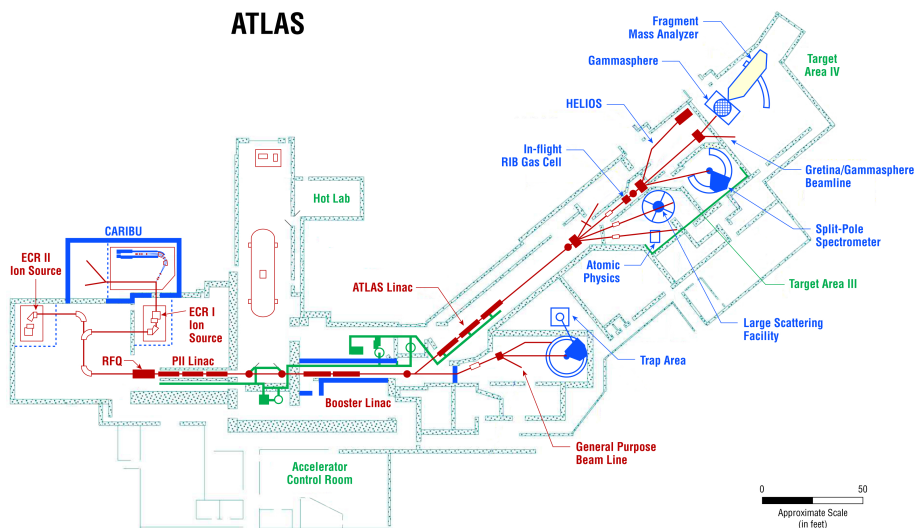
The back layer of the DSSSD is parted into 24 sectors of  $3.4^\circ$ , each, per quadrant. For most cases it is sufficient to electrically combine two sectors, so an effective strip width of  $7.8^\circ$  is achieved. 93 % of the silicon surface are active, combined to a total of effective 192 pixels per quadrant or 768 discriminable pixels in total. The thickness of the active layers depends on the ion species under investigation and on the penetration depth into the silicon layers, and is chosen such that the ions are completely stopped in the back layer. The energy resolution of such a type of detector is around 100 keV at 5 MeV kinetic energy of the impinging particle. Besides the DSSSD, a target wheel is located inside the target chamber. A maximum of six targets can be mounted onto the target wheel, which afterwards can be manipulated from outside without breaking the vacuum. In the case of  $^{142}\text{Sm}$  experiment the target wheel was equipped with different targets, namely:

- Two targets for determining the position of the incoming RIB,
- One unused  $^{64}\text{Zn}$  target,
- One  $^{48}\text{Ti}$  target of an area density of  $1.4 \text{ mg/cm}^2$ ,
- One  $^{94}\text{Mo}$  target of an area density of  $2.0 \text{ mg/cm}^2$ ,
- One thick copper target for beam contamination analysis.

For the projectile Coulomb-excitation analysis the stable  $^{48}\text{Ti}$  and  $^{94}\text{Mo}$  targets were, in combination with Miniball and the DSSSD, employed, whereas the thick  $^{\text{nat}}\text{Cu}$  target was used for determining the beam composition via detection of  $\gamma$  rays after implantation.



# ATLAS



RP081301

**Figure 4.7.:** Schematic view of the ATLAS facility. The ion beams are created in either one of two ECR ion sources and bunched and accelerated afterwards. From the linear accelerator they are guided directly to the experiments. Image taken from [60].

## 4.2 ATLAS & Gammasphere

The ATLAS<sup>11</sup> facility [61], shown in Figure 4.7, was erected in the 1970s and is dedicated to the investigation of nuclear structure physics. The accelerator system is capable of producing and accelerating stable and exotic beams. It employs the first superconducting accelerator for ions, providing a wide range of kinetic energy.

### 4.2.1 Beam Production

The ATLAS facility can provide beams of stable nuclei as well as exotic beams. However, for production of the exotic beams a technique different to the one used at the ISOLDE facility (cf. Section 4.1.1), namely a fission source. This is a small source of radioactive  $^{252}\text{Cf}$  in vacuum, decaying via spontaneous fission. The decay

<sup>11</sup> Argonne Tandem Linear Accelerator System

---

products leaving the source itself are subsequently prepared to be injected into the accelerators. In contrast to ISOLDE, the decay favors neutron-rich nuclei as decay products, with intensities of the daughter nuclei centered around  $A \approx 100$  and  $A \approx 150$ , roughly preserving the  $N/Z$  ratio of the mother nucleus.

In addition, the ATLAS facility is also capable of producing exotic nuclei via the *In-Flight Fragmentation* technique, where an accelerated beam of heavy ions hits a production target located inside a straight section of the beam pipe, leading to a spallation reaction. The reaction products are afterwards (mass) separated and re-accelerated. In contrast to the ISOL-technique, both, the beam impinging on the primary target and the cocktail beam of reaction products, are guided towards the separation stage.

Stable as well as exotic nuclei, produced via the fission decay, are fed into an ECR<sup>12</sup> ion source. An ECR ion source – in the most general way – consists of a plasma inside a magnetic bottle confining ions within a complex arrangement of magnetic fields. As the ions diverge from the center of the source, they are reflected by the increasing magnetic field, depending on their energy. An external source of microwave radiation, with its frequency matched to the cyclotron frequency of the plasma's electrons, provides heating of the plasma. The accelerated electrons subsequently strip electrons from the outer shells of the atoms, increasing the charge state stepwise. The ions can be extracted from the source by attaching the plasma cage to a high voltage source, followed by a ground electrode outside the magnetic coil arrangement.

---

#### 4.2.2 Acceleration

---

After being multiply ionized in the ECR, the continuous ion beam is directed towards the first stage of acceleration, an RFQ. The temporal structure and the emittance are matched to the bunch length and acceptance, respectively, of the PII<sup>13</sup> Linac, where they are further accelerated. The PII Linac, as well as the ATLAS Linac further downstream, are composed of similar quarter-wave resonator cavities, but optimized for different values of  $\beta$ . The Booster Linac, in the middle between the PII and the ATLAS Linac, consists of quarter-wave as well as split-ring resonators. This acceleration system allows for velocities of up to 21 MeV/u for light ions and up to 17 MeV/u for heavy ions. In a nutshell, the ATLAS facility provides accelerated beams for a wide range of ions all over the nuclear chart up to uranium.

---

<sup>12</sup> Electron Cyclotron Resonance

<sup>13</sup> Positive Ion Injector

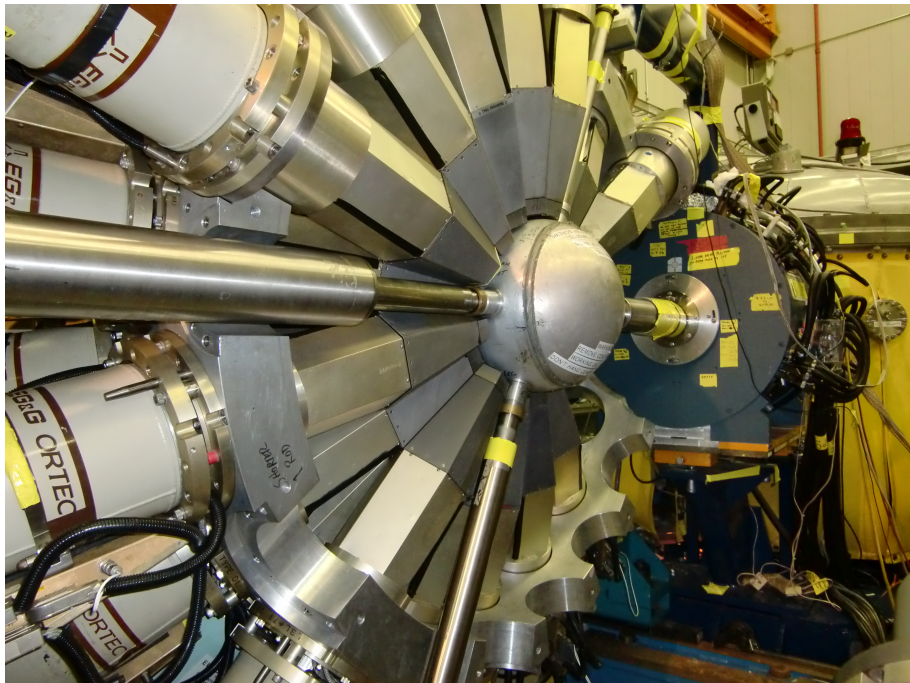


**Figure 4.8.:** Photography of one hemisphere of the Gammasphere HPGe detector array. In the center of the array the target chamber, containing the Coulomb-excitation targets, is located. The beam comes from the left and leaves to the right, towards the FMA (not used within this work). The tilted tube beneath the target chamber contains the target ladder.

---

#### 4.2.3 Target Chamber & Detectors

---

After passing the Linacs, the accelerated ions are delivered to the experimental sites. For the experiments conducted within this work, the  $^{202,204}\text{Hg}$  ions were guided to the Gammasphere HPGe detector array [62]. The Gammasphere array consists of up to 110 HPGe detectors. A picture of the array is shown in Figure 4.8. Any of the detectors is about 84 mm long at a diameter of about 72 mm, features an efficiency of 78 % w.r.t. the NaI standard [63]. Every detector is equipped with an individual BGO<sup>14</sup> Compton-suppression shield. The pair of detectors – HPGe

---

<sup>14</sup> Bismuth Germanium Oxide

**Table 4.1.:** Polar angles  $\theta$  of the rings of the Gammasphere array. In the setup at ANL, ring # 1 is permanently removed.

Ring #	$\theta$	Ring #	$\theta$	Ring #	$\theta$
1	17.3°	7	79.2°	13	121.7°
2	31.7°	8	80.7°	14	129.9°
3	37.4°	9	90.0°	15	142.6°
4	50.1°	10	99.2°	16	148.3°
5	58.3°	11	100.8°	17	162.7°
6	69.8°	12	110.2°		

and BGO – are connected to form a so-called anti-veto trigger. If  $\gamma$  radiation is detected in both detectors at the same time, both events may stem from at least one Compton-scattering event in the HPGe detector. This means the other way round, that not the full  $\gamma$  energy was deposited in the HPGe detector, but the event increases the background. Thus if both detectors register an event, it gets refused. The HPGe crystals are in – in contrast to Miniball – single housings. A single crystals offers an opening angle of 14.8°. The pure germanium surface of the total array of 110 detectors covers about 46% of the solid angle. In its full configuration, the Gammasphere array offers a symmetric quasi- $4\pi$  coverage, with a total photopeak efficiency of about 9.4% at 1332 keV. A profile view of a HPGe detector is shown in Figure 4.9. The detectors are grouped in up to 17 rings of 5 to 10 detectors, each. The polar angles are summarized in Table 4.1. This allows for angular resolved measurements. In its configuration at the Argonne National Laboratory, Gammasphere is placed in front of the FMA<sup>15</sup>, requiring permanent removal of the ring with the smallest angle in forward direction. This reduces the number of available detectors by 5. In addition, not all detectors were usable during the experiments, resulting in 100 detectors being present in the data.

The Gammasphere array was intentionally build for high-spin experiments, exhibiting  $\gamma$  ray multiplicities  $\gg 1$ . For the measurements performed within this work, an event was recorded, when at least one of the HPGe detectors detected  $\gamma$  radiation. This led to an increase in recorded background and Compton events. The background was further raised by not using a particle detector, in order to be able to cope with a higher beam current.

<sup>15</sup> Fragment Mass Analyzer

**Table 4.2.:** List of experiments conducted, which data was analyzed within this work. The column “Coulomb barrier” gives the beam energy relative to the approximated height of the Coulomb barrier.

Projectile	Target		Energy / MeV	Coulomb barrier	Aim
	Isotope	Thickness / mg/cm <sup>2</sup>			
<sup>142</sup> Sm	<sup>48</sup> Ti	1.4	405	66 %	Det. of $B(E2)$
	<sup>94</sup> Mo	2.0	405	60 %	Det. of $B(E2)$
<sup>202</sup> Hg	<sup>12</sup> C	1	890	85 %	Ident. of MSS
<sup>204</sup> Hg	<sup>12</sup> C	1	890	84 %	Ident. of MSS
	<sup>27</sup> Al	1 mm	890	89 %	compl. DSAM

An overview of the experiments conducted for this work, including their aims, is given in Table 4.2.



**Figure 4.9.:** Schematic transverse section of a Gammasphere HPGe detector, together with the BGO anti-Compton shield and the liquid nitrogen dewar. Image taken from [64].

---

## 5 Data Analysis and Results

Within this section, the preparation and analysis of the data taken in the ISOLDE experiment IS496 regarding  $^{142}\text{Sm}$  and the ATLAS/Gammasphere experiment GSFMA311 regarding  $^{202,204}\text{Hg}$  is presented. In Section 5.1 the preparation of the data for the analysis is introduced, while in Sections 5.2 and 5.3 the basic analysis principles are summarized. Finally, in Sections 5.4 and 5.5 the results are presented.

---

### 5.1 Data Preparation

---

The data is recorded in raw format, where the  $\gamma$  ray and particle information are stored in a continuous data stream, subdivided into so-called “events”, where ionizing radiation was detected within a certain time window. In order to analyze the nuclear structure properties, this data stream has to be converted to a more appropriate format, a process dubbed “sorting”. This task is complex, especially for the particle- $\gamma$  data stream of the ISOLDE experiment. The sorting of that data was performed using the software “Miniball Offline MED to Root Converter” [65]. In the case of the pure  $\gamma$ -ray events taken at ATLAS, a new sorting software, leaned on the sorting code GSSort [60], was developed. This software is described in greater detail in Section 5.1.1.

Further processing of the data also requires correction for relativistic effects as well as for the finite size of the detectors. Furthermore,  $\gamma$  rays from sources outside the desired experimental ones will also be recorded by the HPGe detectors.

In the beginning, energy and timing calibration have to be checked. Both  $\gamma$ -ray detector systems were energy calibrated in the beginning, which was additionally confirmed during the analysis, where shifts from the desired transition energies were in the sub-percentage regime. The temporal alignment of the detectors w.r.t. the RF signal was also tested and corrected for deviations, which in most cases were in the range of a single timing bin, corresponding to few nanoseconds. This is usually done by sorting simple spectra of timing and energy. Particularly the energy alignment, and the succeeding Doppler-correction, presuppose each other, for which reason the steps cannot be performed independent of each other.

---

### 5.1.1 Sorting Gammasphere Data

---

The experiment conducted at ATLAS within this work relied solely on the detection of  $\gamma$  rays by the Gammasphere array. These information are recorded by the analogue Gammasphere DAQ<sup>1</sup>, which saves the data in the Gammasphere raw data format depicted in Figure 5.1. This raw format is used for online as well as offline analysis of the information collected by Gammasphere; the data recorded for offline analysis may either be stored on magnetic tape data storage or on common hard-disk drives. In the case of the former, the headers possess rather short lengths of 112 and 90 Bytes, respectively, while for hard-disk drives they are fixed to 16384 Bytes. The raw data format was intentionally designed for compatibility to computer systems of arbitrary byte order, which was the cause for storing the Byte order in the “tape header”. For convenience the experiment title, as well as run and file number are stored within the headers. Storing the data on hard-disk drives blurs the difference between “tape” and “file headers”, as these appear in any file.

The headers are succeeded by an arbitrary number of “data records”, holding a “buffer header” as well as an arbitrary number of events. The “buffer header” not only stores the length, which is fixed to 16384 Bytes, but, besides information for handling auxiliary detectors, also the conditions under which the data was recorded, *i.e.*, the switches set in the DAQ for storing information. It is important to note, that each “data record” includes, in common, more than one event. Event information is stored in the “event data” structure. This structure holds all the information about what was in the DAQ properties defined as an event. Besides a header, containing information about the timing - the absolute run time of the DAQ as well as timing information relative to the RF master trigger - and the number of  $\gamma$  rays recorded, each  $\gamma$ -ray detector is stored separate, discriminated between “clean” and “dirty” signals recorded by the HPGe detectors and signals recorded by the BGO anti-Compton shields. A single entry is created for each detector in which a signal occurred, which is identified via its ID. The energy corresponding to the signal amplitude is stored as well, alongside, for segmented detectors, the energy detected by the second channel. While the energy is in general stored with a resolution of 14 Bit, the energy of the second – or “side” – channel is only stored using 12 Bit. Storage of additional information is betokened by the “mode flags” in the preceding “buffer header”. This may be additional timing, or information about the BGO events. An event may also store data stemming from auxiliary detectors, which possess an individual data format, each. Types of such auxiliary detector are, *e.g.*, DSSSD particle detectors.

In addition to the discrimination in “clean” and “dirty” HPGe events, one has to

---

<sup>1</sup> Data Acquisition System



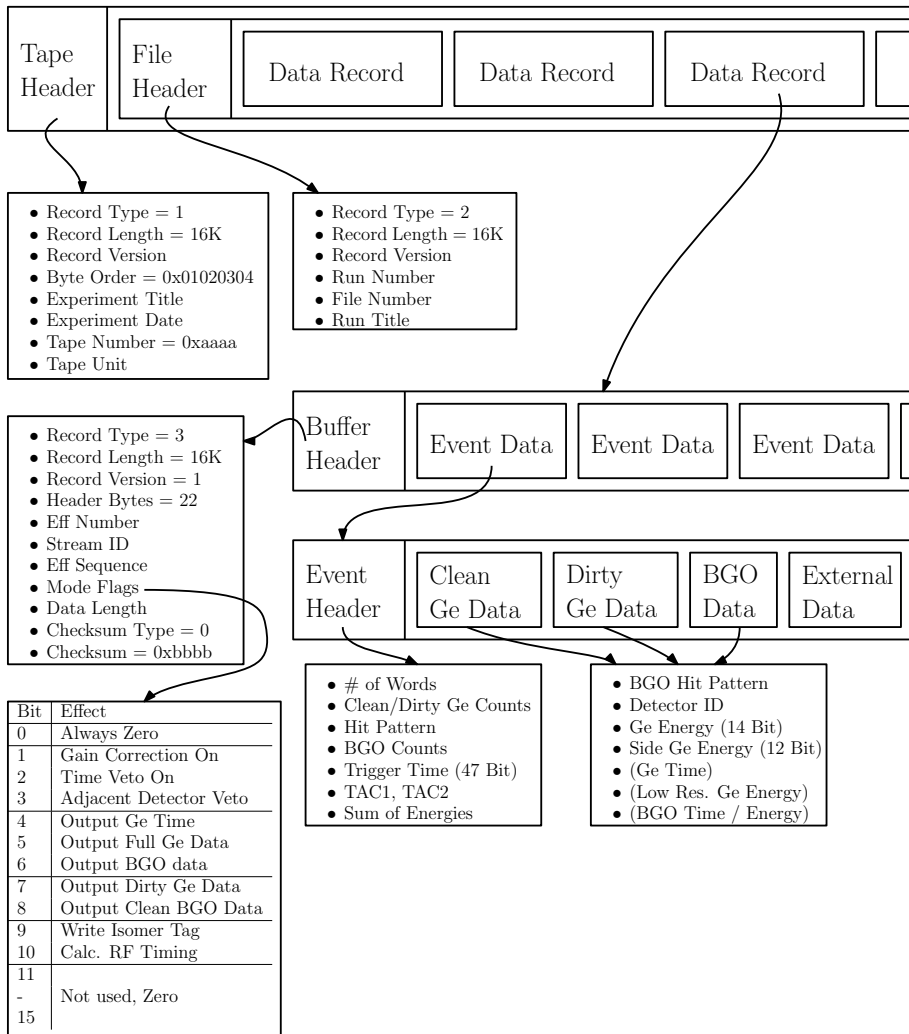


**Figure 5.1.:** Gammasphere raw data format in a nutshell. Each file starts with a “tape” and a “run header”, giving general information about the entire file. They appear exclusively at the beginning. Afterwards an arbitrary number of “data records” occur. Each of those “data records”, limited to  $2^{14}$  Bytes, starts with a header giving general information, followed by an arbitrary number of “events”. Each “event” begins with a header, succeeded by the information about the detected  $\gamma$  radiation.

check carefully the multiplicity of the  $\gamma$  rays recorded. An event in one of the Germanium detectors may be counted as a “clean” event with a very low  $\gamma$ -ray energy, with only a few keV. Such events may also be caused by electric noise, for which reason the  $\gamma$  ray is discarded. The same situation may also appear in “dirty” Germanium events, but the noise may also appear in one of the BGO scintillators, why there the same conditions are applied. Of course, this may also happen for events, in which only the BGOs detected  $\gamma$  radiation. Appearance of such cases decreases the number of “real” detected  $\gamma$  rays. It may also appear, that events are saved as “clean”, but the “Honeycomb Suppression” flag is set, thus these events are actual “dirty” events. All these conditions are necessary to be checked, in order to determine the actual multiplicity of “clean” detected  $\gamma$  rays. This can also result in events, where in the end, no “clean”  $\gamma$  ray is left and the event is discarded, although the opposite was indicated in first place.

After the aforementioned multiplicity checks, valid events are sorted into various spectra.

A novel feature of the sorting software developed within this work is the capability to sort a complete run at once, without the need for manually restarting the sort for every file of the run. It provides the capability to not only sort singles spectra, but also various types of matrices, e.g.,  $\gamma$ - $\gamma$  matrices,  $\gamma$  energy vs. time w.r.t. RF,  $\gamma$  energy vs. absolute time, events per detector vs. absolute time, and so forth.

---

### 5.1.2 Kinematics and Doppler Correction

---

A crucial point in the analysis of Coulomb-excitation experiments is the knowledge of the reaction kinematics and the associated Doppler-correction. This is of uttermost importance when dealing with inverse kinematics and the two-fold solution arising when transforming back from the center-of-mass system of the reaction to the laboratory frame of reference, where the measurement takes place. In the following, this will be illustrated using the  $^{142}\text{Sm} + ^{94}\text{Mo}$  reaction of the experiment IS496 conducted in 2012, where a particle detector was part of the setup.

The velocities in low-energy Coulomb excitation are low w.r.t. the speed of light, so that the transformation between the laboratory and the center-of-mass frame of references can be handled in a non-relativistic manner [21]. The excitation energies of the levels populated in such kind of experiment are usually small w.r.t. to the kinetic energy, so the scattering process is not completely elastic, but disturbed by a small deviation  $\Delta E$ , which is the excitation energy. The projectile energy in the laboratory system is thus modified to be [21]

$$\tilde{E}' = E_p - \Delta E \left( 1 + \frac{A_p}{A_T} \right). \quad (5.1)$$

The scattering process causes substantial transfer of kinetic energy to the recoiling target nucleus, thus it is necessary to transform the disturbance caused by the excitation to the laboratory frame of reference. However, this solely holds true for a target material of infinitesimal thickness, where the nuclei are not slowed down by stopping processes. Nevertheless, this is approximately still valid in the case of thin targets, *i.e.*, for targets of few  $\text{mg}/\text{cm}^2$  for low-energy Coulomb excitation.  $\tau$  (cf. Section 2.4) can be defined in a non-relativistic way, but while incorporating the energy loss, via [21]

$$\tau = \frac{A_P}{A_T} \sqrt{\underbrace{\frac{E_P}{\tilde{E}'}}_{\tilde{\tau}}}, \quad (5.2)$$

where  $\tilde{\tau}$  measures the degree of “elasticity” of the collision, *i.e.*,  $\tilde{\tau} = 1$  is the case of pure elastic scattering. In the non-relativistic approximation, the scattering angles after the collision are given by

$$\frac{\sin(\vartheta_P - \theta_P)}{\sin(\theta_P)} = \tau, \text{ and} \quad (5.3)$$

$$\frac{\sin(\vartheta_T - \theta_T)}{\sin(\theta_T)} = \tilde{\tau}. \quad (5.4)$$

The indices  $P$  and  $T$  denote projectile and target nuclei, respectively, while  $\vartheta$  and  $\theta$  denote scattering angles in the center-of-mass and the laboratory frame of reference, respectively. In the center-of-mass system applies  $\vartheta_P = \pi - \vartheta_T$ , otherwise the direction of movement of the center of mass itself would change. In the case of completely elastic scattering, the correlation between the target scattering angles, *i.e.*,  $\tilde{\tau} = 1$ , is  $\theta_T = \frac{1}{2}(\pi - \vartheta_P)$ .

The reconstruction of the scattering angle of one collision partner, when the other one is detected, is of utter importance. The Coulomb-excitation cross section as well as the energy distribution after the collision depend both on the scattering angle. In order to ensure clean spectra, knowledge of the scattering angles and velocities is essential for a sophisticated Doppler correction. Low-energy Coulomb excitation results in excitations of states with only few MeV, which permits to assume  $\tilde{E}' \approx E_P$ , *i.e.*, the scattering process takes place in an elastic manner. The

particle scattering angles may then be expressed in terms of the scattering angle of the respective other particle via [66]

$$\tan(\theta_p) = \frac{\sin(2\theta_T)}{\frac{A_p}{A_T} - \cos(2\theta_T)}, \quad (5.5)$$

$$\cos(\theta_T) = \frac{\cos(\theta_p)}{A_T} \sqrt{\frac{1}{2} \left[ A_T^2 + A_T(A_p + A_T) \tan^2(\theta_p) - \sqrt{A_T^4 + (A_T^4 - A_p^2 A_T^2) \tan^2(\theta_p)} \right]}. \quad (5.6)$$

Combining the information discussed above, the velocity of projectile and recoiling target nuclei after the collision can be determined. Formulating the velocities in dependence of the scattering angle of the recoiling nucleus  $\theta_T$ , effaces the ambiguity in the projectile scattering angle  $\theta_p$ . The velocity in the laboratory system is then given by [66]

$$v'_p = \sqrt{\frac{2\tilde{E}'}{m_p}} \sqrt{1 - \frac{4A_T/A_p}{(1 + A_T/A_p)^2} \cos^2(\theta_T)}, \quad (5.7)$$

$$v'_T = \sqrt{\frac{2\tilde{E}'}{m_p}} \frac{2A_p}{A_p + A_T} \cos(\theta_T). \quad (5.8)$$

$\gamma$  rays following the decay of excited nuclear levels will appear shifted in energy, if the emitting nucleus moves at a non-negligible fraction of the speed of light. The photons are emitted in the rest frame of reference of the emitting nucleus, but due to the motion of that frame of rest relative to the laboratory system, the frequency of the photons is increased in the direction of motion, and decreased in the opposing direction. This effect scales with the photon energy / frequency as well as with the velocity of the emitting nucleus. The relation of shifted and unshifted energy is given by

$$E_u = \frac{1 - \beta \cos(\vartheta)}{\sqrt{1 - \beta^2}} E_s, \quad (5.9)$$

where  $E_u$  is the unshifted energy,  $E_s$  is the shifted, detected energy,  $\beta$  is the speed of the emitting nucleus relative to the speed of light, while  $\vartheta$  is the angle between the direction of motion of the emitting nucleus and the direction of motion of the emitted photon. From the angles of the moving nucleus ( $\theta_n, \phi_n$ ) and the detected  $\gamma$  ray ( $\theta_\gamma, \phi_\gamma$ ),  $\vartheta$  is given by [66]

$$\cos(\vartheta) = \cos(\theta_n) \cos(\theta_\gamma) + \cos(\phi_n - \phi_\gamma) \sin(\theta_n) \sin(\theta_\gamma). \quad (5.10)$$

The Doppler correction strongly supports the correct identification of transitions, but the uncertainties of the quantities, it depends on, limit the achievable correction. However, if the uncertainties are known, the uncertainty of the Doppler correction can be determined and can be used to identify overlapping peaks from the width of the resulting peak. The width of a single peak can then be determined to be

$$\begin{aligned}\Delta E_u &= \sqrt{\left(\frac{dE_u}{d\beta} \Delta\beta\right)^2 + \left(\frac{dE_u}{d\vartheta} \Delta\vartheta\right)^2 + \left(\frac{dE_u}{dE_s} \Delta E_s\right)^2} \\ &= \sqrt{\left(E_s \frac{\beta - \cos(\vartheta)}{(\sqrt{1-\beta^2})^3} \Delta\beta\right)^2 + \left(E_s \frac{\beta \cdot \sin(\vartheta)}{\sqrt{1-\beta^2}} \Delta\vartheta\right)^2 + \left(\frac{1 - \beta \cos(\vartheta)}{\sqrt{1-\beta^2}} \Delta E_s\right)^2},\end{aligned}\tag{5.11}$$

where  $\Delta\beta$  is determined by the quality of the experimental deduction of the velocity of the emitting nucleus. The opening angle of one detector is denoted as  $\Delta\vartheta$  and  $\Delta E_s$  denotes the intrinsic resolution of the  $\gamma$ -ray detector. The latter is material dependent, *e.g.*, the Gammasphere detectors feature an intrinsic resolution of about 0.2%. It has to be noted, that the solid angle of the detector is, of course, not Gaussian distributed, however, the relation is more used as a guide to be able to distinguish single peaks from multiplets of peaks. Equation (5.11) results in a linear relation between the uncertainty of the Doppler correction, *i.e.*, the width of a single peak in the spectrum, and the unshifted energy of a transition. Thus, a width calibration can also be performed from determining the widths of a set of peaks in the spectrum and fitting a linear function. This yields a good hint for identifying and disentangling multiplets in spectra.

---

### 5.1.3 Background Subtraction

---

Besides  $\gamma$  rays stemming from the decay of excited states populated via Coulomb excitation in projectile and recoiling target nuclei,  $\gamma$  rays also occur in the decay of natural radionuclides, *e.g.*,  $^{40}\text{K}$  incorporated in concrete. All  $\gamma$  rays are detected by the HPGe detectors, as they are not able to discriminate the origin of the radiation. This might change in the future using position-sensitive detectors in combination with  $\gamma$ -ray tracking algorithms.

However, the radiation originating from outside the experimental setup causes debasement of the peak-to-total ratio of the transitions of interest. Therefore, it is desirable to subtract the  $\gamma$  rays originating from so-called “background” decays

---

from the total spectrum. Different methods exist to overcome this issue, e.g., timing correlations or coincidence analysis. This section will focus on the former, while the latter is covered in Section 5.1.5.

The usage of timing correlations, in order to reduce the background, relies on the fact, that the nuclear decays not related to the experiment itself also appear when there is no beam impinging onto the target, whereas, in the case of non-isomeric excited states, decays originating from Coulomb excitation are distributed closely in time around the arrival of the beam pulse at the target position. The background events, in contrast, are distributed randomly in time. Clearance of the background events is also aided by the long half-life of the radionuclides. This allows for assuming that the distribution of the decay activity is flat, i.e., the intensity can be assumed to be constant over, at least, the course of the experiment.

The conditions for timing correlations are different for the ISOLDE and the ATLAS experiments. While Miniball is configured for decay lifetimes of up to a few nanoseconds, Gammasphere was constructed for high-spin experiments, involving isomeric states and long decay cascades.

The data taking process of Miniball is activated by a trigger coming from the REX section, signaling an incoming beam pulse. The Miniball DAQ is, in principle, a triggerless system, meaning that all the signals detected by any detector are written to disk. The data rate is reduced by opening a time window for recording when a RF trigger signal is pending. While sorting the data, the output can be restricted to events, where, at least, either two  $\gamma$  rays or a particle and a  $\gamma$  ray were detected in coincidence. This reduces the amount of data as well as suppresses background of signals restricted to a sole detector. A timing spectrum taken with Miniball is shown in Figure 5.2. The times are not given relative to the beam trigger, but the point of origin is defined via coincidence of two simultaneously emitted and detected  $\gamma$  rays. For this spectrum only events involving particle- $\gamma$  coincidences were taken into account during the sorting process. A nearly constant *background* of random coincidences is apparent. These events are not correlated to the Coulomb excitation of projectile and target nuclei, but are events, where the particle detector recorded a signal and one of the HPGe detectors measured a  $\gamma$  ray, which were not necessarily correlated to each other. However, the sharp peak centered on  $-800$  ns stems from decays after Coulomb excitation. The excited states giving rise to this peak exhibit lifetimes in the picosecond regime, which width is narrow w.r.t. the full time window of 6 ms. The clipping of the data to the full time window causes the sharp borders of the time difference spectrum. As stated before, the temporal point of origin is given from  $\gamma$ - $\gamma$  coincidences, but the electronics handling the signals generated by the particle detector is slower than the one handling signals from the HPGe detectors, causing an offset of 800 ns.

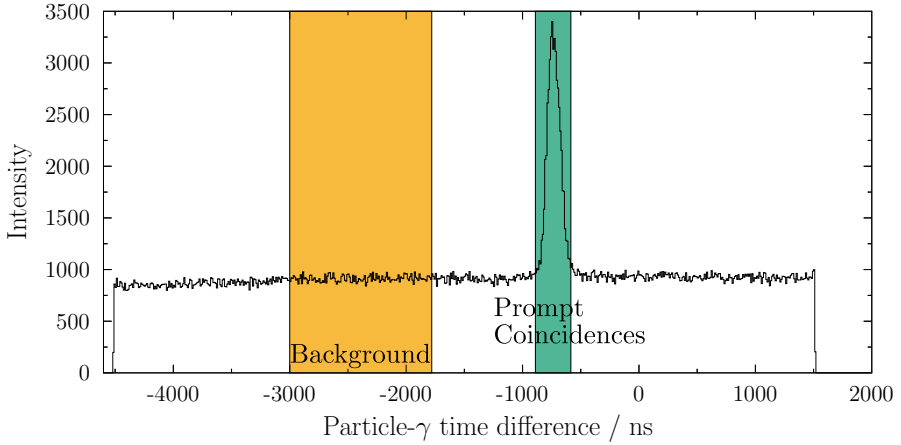


**Figure 5.2.:** Particle- $\gamma$  time difference spectrum for the events recorded by Miniball. Data taking is triggered by a RF master trigger and successive detection of at least either two  $\gamma$  rays or a particle and a  $\gamma$  ray in coincidence. This is subsequently restricted, during sorting of the raw data, to particle- $\gamma$  coincidences. *Prompt Coincidences* stem from decays after Coulomb excitation, while *Background* labels random coincidences. The abscissa is reversed, i.e., time evolves from right to left.

The background subtraction is performed by generating separate spectra for events, which are exclusively within the *prompt coincidences* window, and events, which are solely within the *background* time window. As statistics per time interval for the *background* are usually low, but not negligible, w.r.t. the intensity within an equal time interval within the *prompt coincidences* window, the *background* window is chosen broader than the *prompt coincidences* window. In order to correct for random coincidences, the *background* spectrum is scaled and subtracted from the *prompt coincidences* spectrum.

This process, in a general manner, also applies for the data taken using the Gammasphere array, although, the time difference and the respective windows are treated a bit different. Again, the DAQ relies on an RF trigger from the accelerator system, but in this case data is taken vs. the RF pulse, while the high-spin detection design goal of the Gammasphere system is achieved by opening the data recording window for ten successive beam pulses. The resulting time distribution is depicted in Figure 5.3. The timing is aligned such that  $\gamma$  rays emitted during decays of excited states, exhibiting lifetimes that are short w.r.t. the intrinsic time resolu-

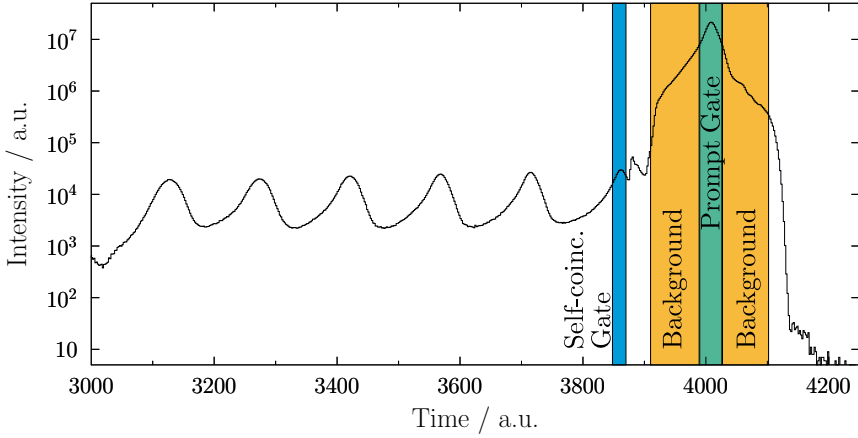


**Figure 5.3.:** Time difference spectrum for events recorded by Gammasphere. Timing information are taken w.r.t. the RF trigger signal, which is centered at 4000. *Prompt Coincidences* stem from decays after Coulomb excitation, while *Background* labels events probably not correlated to the beam. In order to aid high-spin detection nature of Gammasphere, data is taken for ten subsequent beam pulses after the RF trigger signal. The *self-coincidences gate* was used to disentangle events, where two concurrent Coulomb-excitation events took place. The abscissa is reversed, i.e., time evolves from right to left.

tion of the HPGe detector, after Coulomb excitation, are centered around 4000 (in a.u.). Like in the case of Miniball, separate spectra are generated for in-beam as well as off-beam detected  $\gamma$  rays. The spectra are subsequently subtracted from each other, in order to clear up the contamination from uncorrelated decays. The procedure, starting with the raw spectrum, is depicted in Figure 5.4.

---

### 5.1.4 Efficiency Calibration

---

Germanium semiconductor detectors provide only limited efficiency in detecting the full energy of an impinging  $\gamma$  ray. This is caused by the limited finite size of the detector itself. The photo-peak detection efficiency scales with the material specific total interaction cross-section, which itself scales reciprocally with the energy of the photon. In most case, for high-energy photons only Compton-scattering events



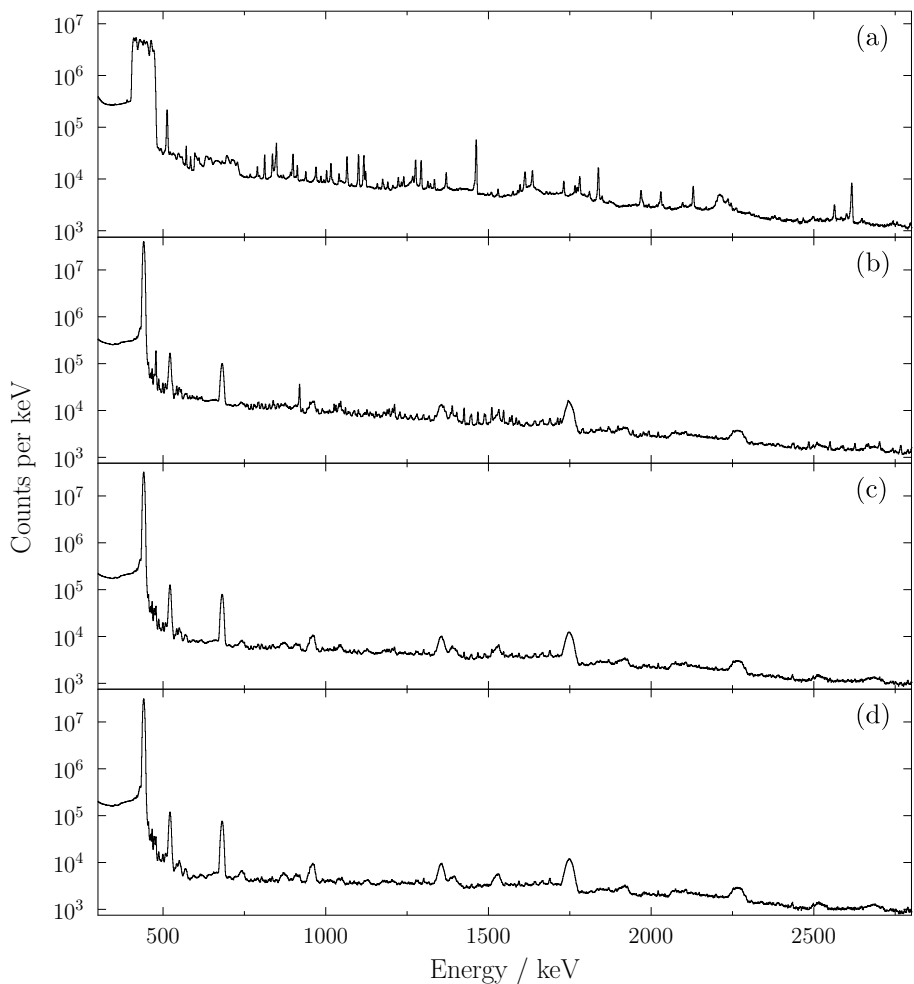


**Figure 5.4.:** Illustrative steps of the background subtraction procedure. (a) shows the raw  $\gamma$ -ray singles spectrum, without any corrections. (b) depicts the situation after applying Doppler correction. (c) shows the spectrum of  $\gamma$  rays present in the “Prompt Gate”, only, while (d) is after subtracting contributions of  $\gamma$  rays present in the “Background Gate”. The spectra are not corrected for efficiency. It is clearly visible, how the fraction of background  $\gamma$  rays in the spectrum is decreased with each step, while the intensity of transitions emitted from the nucleus under investigation is rarely influenced.

occur. But in order to compare the intensity of different nuclear transitions, the measured intensities have to be corrected for this finite detection efficiency. The detection efficiency can also be manipulated using filter materials in front of the detectors.

For the ISOLDE experiments, HPGe photon detectors as well as Silicon particle detectors have been employed. The nuclei impinging on the Silicon detector exhibit only low penetration depths, leading to full energy deposition for almost every event. The total number of events is solely subdivided by the particle angles of the CD, thus a efficiency calibration for the total Miniball array is sufficient.

The experiments conducted using Gammasphere did not employ a particle detector, but the analysis of angular distributions was designated. For that reason, not only the sum efficiency had to be determined, but also the efficiency for every polar angle group. Not only that the efficiency slightly differs between different detectors, but in addition different rings exhibit different numbers of detectors. On this account, every ring has to be calibrated for efficiency individually.

For the analysis of Coulomb-excitation experiments, relative intensities are sufficient, as this kind of experiment is based on normalization to known transition strengths, either to the nucleus itself, or to transitions in the partner nucleus. A standard source for detector calibration is  $^{152}\text{Eu}$ , which decays into  $^{152}\text{Sm}$ , exhibiting transitions covering the range from 100 keV to 1.4 MeV. The relative intensities of these decay transitions are known to a small uncertainty, which, alongside the half-life of 13.5 years, renders  $^{152}\text{Eu}$  suitable for this scenario.

The relative efficiency is determined by the ratio  $\epsilon = A/I$  of the measured peak area  $A$  and the known relative intensity  $I$  of the transition in an ensemble of decaying nuclei. The efficiency depends on the energy  $E_\gamma$  of the  $\gamma$  ray emitted and can, in the energy range above 200 keV, be described using a set of three parameters  $a$ ,  $b$ , and  $c$ :

$$\epsilon(E_\gamma) = a \cdot (E_\gamma - c)^{-b}. \quad (5.12)$$

The resulting curve is depicted in Figure 5.5, as dashed line. In the ISOLDE experiments, only  $\gamma$ -ray energies above 200 keV were relevant for the desired analysis, so that this formula was sufficient to determine the true intensities of the transitions. Nevertheless, besides the  $^{152}\text{Eu}$  source, also a  $^{133}\text{Ba}$  source was employed, in order to gain efficiency data in the event of low-energy  $\gamma$  or x rays. The efficiency for the full energy range can be described using a formula with five parameters:

$$\epsilon(E_\gamma) = a \cdot \exp(-b \cdot \ln(E_\gamma - c + d \cdot \exp(e \cdot E_\gamma))), \quad (5.13)$$

where  $a$ - $e$  label the set of free parameters. The full curve is shown as solid line in Figure 5.5.

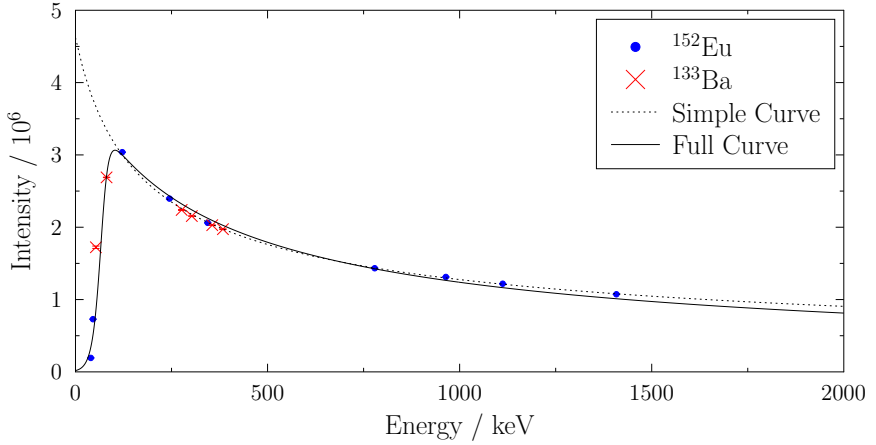


**Figure 5.5.:** Efficiency calibration used for the analysis of Miniball experiments. Calibration sources made from  $^{152}\text{Eu}$  and  $^{133}\text{Ba}$  were used to determine the efficiency. The dashed curve is given by the simplified equation (5.12), valid for energies above 200 keV, while the solid line is given by the full equation (5.13).

The experiments conducted using Gammasphere also employed a  $^{152}\text{Eu}$  source, which data was taken in a two hour run at the end of the experimental runs. It was also desired to measure using  $^{56}\text{Co}$  and  $^{182}\text{Ta}$  sources, in order to enlarge the regime where the efficiency can be determined. Unfortunately both sources were not present at ATLAS at the time of the experiment, why an older dataset recorded under the same experimental conditions was used for the analysis. The Ta source provided additional data in the low-energy regime below 200 keV, while the Co source provided additional information up to 3.3 MeV. This was necessary, as transitions with energies well above 1408 keV were expected. In order to suppress x rays to be able to cope with higher particle currents, x-ray absorbers made from Tantalum and Copper were mounted in front of the HPGe detectors. This has to be taken into account, because these filters modify the efficiency for detecting low-energy  $\gamma$  rays. The transmission curve is given by [60]

$$t(E) = \frac{1}{1 + e^{-\frac{E-B}{C}}}, \quad (5.14)$$

where the material constants  $B$  and  $C$  for the absorbers used, are 78.9(6) keV and 38.7(8) keV, respectively. The simplified curve, valid for energies above 200 keV,

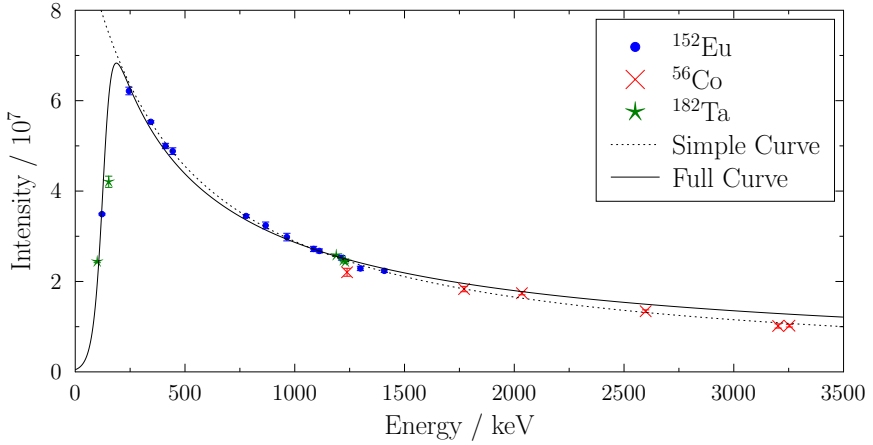


**Figure 5.6.:** Efficiency calibration used for the analysis of Gammasphere experiments. The  $^{152}\text{Eu}$  source (blue) data was taken at the end of the experiment. Data from  $^{56}\text{Co}$  (red) and  $^{182}\text{Ta}$  sources was taken during a previous experiment, which employed the same experimental setup. The Co and Ta datasets were scaled in terms of intensity in order to match the Eu dataset. This was done by fitting Equation (5.12) the Eu dataset, and succeeding to the Co and Ta datasets, while the parameter values for  $b$  and  $c$  were fixed to the ones obtained for the Eu dataset. The ratio of the parameters  $a$  was afterwards used as an normalization constant.

as well as the full curve are shown in Figure 5.6 for the case of the Gammasphere experiments. This formalism was employed not only to determine the efficiency for the total array, but also ringwise to be able to compare the intensities from different polar angle groups.

---

### 5.1.5 Coincidences

---

The  $\gamma$  rays have not been analyzed isolated, but also in coincidence to other  $\gamma$  rays or particles. The former was the case for the  $^{202,204}\text{Hg}$  experiments, while the latter was used for  $^{142}\text{Sm}$ .

---

## Particle- $\gamma$ Coincidences

---

The radioactive nature of  $^{142}\text{Sm}$  and its daughter and mother nuclei requires the use of particle- $\gamma$  coincidences. All of the nuclei, until reaching a stable endpoint, emit  $\gamma$  rays during their decay. All these  $\gamma$  rays are detected by the Germanium semiconductor detectors and will generate a vast background in the spectra. In order to clean up and restrict the spectra to the nucleus under investigation, every energy deposition in any of the Germanium  $\gamma$ -ray detectors requires energy deposition in the particle detector to form a valid event. Radioactive nuclei implanted into the particle detector, and decaying while implanted, will generate only a negligible signal. Thus, the demand of particle- $\gamma$  coincidence is suitable to distinguish between the population of excited nuclear states via radioactive decay or via Coulomb excitation, if the half-life of the nucleus under investigation is long enough w.r.t. the time required to pass the accelerator system. The kinematics aspect of particle- $\gamma$  coincidences is discussed above in Section 5.1.2, while the impact on the Coulomb-excitation cross section is described in Section 2.1. The beam energy was suitable to exclusively populate the  $2_1^+$  state, which was aimed to be investigated, in projectile and target-like nuclei, resulting in events of  $\gamma$ -ray multiplicity of two at most, or  $\gamma$ -ray multiplicity of one if restricting to one species of nucleus, rendering  $\gamma$ - $\gamma$  coincidence analysis neither necessary nor applicable.

---

## $\gamma$ - $\gamma$ Coincidences

---

The beam energy used for investigating the nuclei  $^{202,204}\text{Hg}$  permitted Coulomb excitation of higher-lying excited nuclear states. Although one-step excitation dominates in the  $^{12}\text{C} \left( ^{202,204}\text{Hg}, ^{202,204}\text{Hg}^* \right) ^{12}\text{C}^*$  scattering, most of these states decay also through cascades. The choice of the target material, however, strongly prefers excitation of the  $2_1^+$  state of  $^{202,204}\text{Hg}$ . In the data this is visible from the low fraction of events with  $\gamma$  multiplicity  $\geq 2$  of 1–2 % (cf. Figure 5.7). These events containing multiple  $\gamma$  rays are of importance in the analysis. They reveal correlations between the  $\gamma$  transitions, and allow for investigation of  $\gamma$  rays, which intensity is too weak in the singles spectrum to be distinguished from the background. These information also permit reconstruction of the experimental (partial) level scheme.

The raw data of events with multiplicity  $\geq 2$  is sorted into so-called  $\gamma$ - $\gamma$  matrices, which allows for evaluation of the correlations. The matrices are 2D-histograms, which are filled with tuples  $(E_{\gamma,1}, E_{\gamma,2})$  and  $(E_{\gamma,2}, E_{\gamma,1})$  of  $\gamma$ -ray energies  $E_{\gamma,1}$  and  $E_{\gamma,2}$  detected within the same event. Sorting into the  $\gamma$ - $\gamma$  matrix is performed pairwise, in case the multiplicity is  $\geq 3$ , permitting the investigation of cascades exceeding the length of two succeeding transitions. An exemplary matrix is shown in Fig. 5.8.

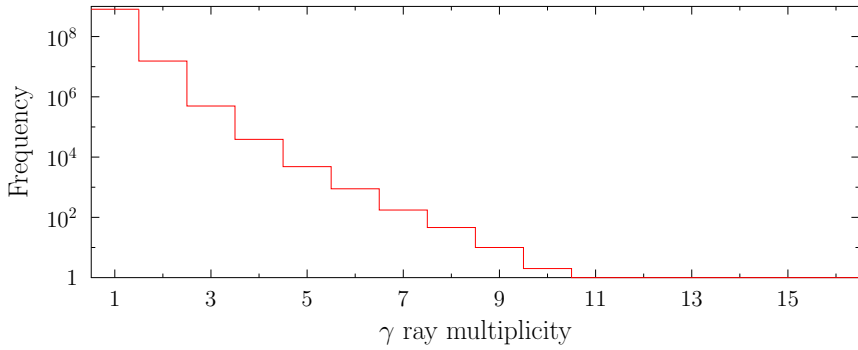


**Figure 5.7.:** Multiplicity distribution of the  $^{202}\text{Hg}$  experiment at Gammasphere. The trigger condition was set to the detection of at least one  $\gamma$  ray. No further corrections have been applied.

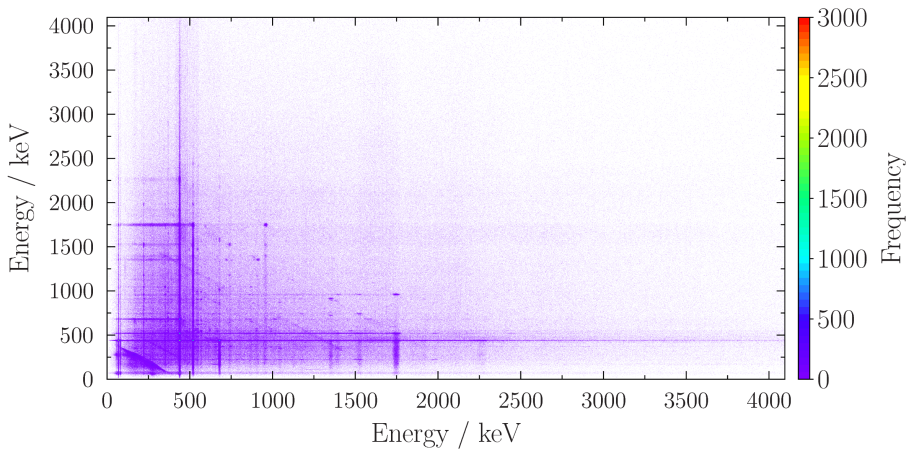


**Figure 5.8.:** The bare  $\gamma$ - $\gamma$  coincidence matrix of the  $^{202}\text{Hg}$  experiment, after Doppler-correction on the projectile nuclei and background subtraction.

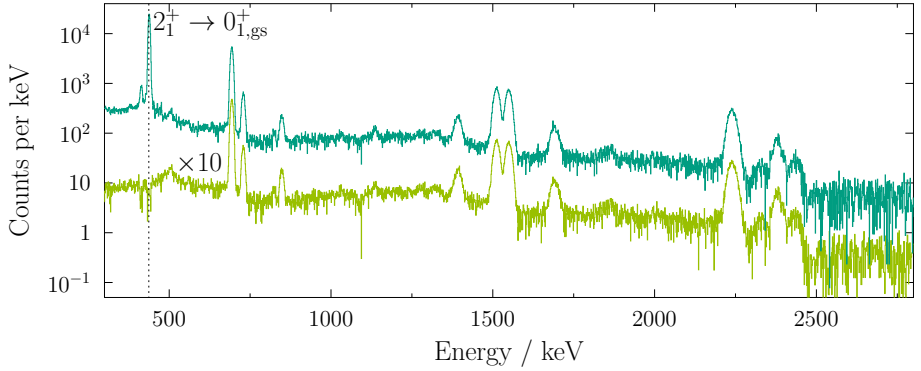


**Figure 5.9.:** Spectra of  $\gamma$  rays in coincidence to the  $2_1^+ \rightarrow 0_{1,gs}^+$  transition of  $^{204}\text{Hg}$ . The upper spectrum is without subtraction of *self-coincidences*, while in the lower spectrum such events are subtracted. The lower spectrum is shifted down by one order of magnitude to increase perceptibility. The peak areas of other transitions remain unaltered by this procedure.

The bare matrices get also filled by random coincidence events. Within these events  $\gamma$  rays appear as coincident to each other, in spite of them lacking any physical correlation. For a proper analysis, such coincidences should be removed from the corresponding matrix.

Random coincidences may not solely originate from detecting any  $\gamma$  ray from an excited nucleus and a  $\gamma$  ray from background radiation, but also from two nuclei of the same species getting Coulomb-excited at the same time. Coincidences of two physically uncorrelated decays of Coulomb-excited states in uncorrelated nuclei at the same time can be treated in a manner related to the one outlined in Section 5.1.3. It is assumed that the probability, that two Coulomb excitations take place within the same beam bunch, is roughly as large as the probability, that two Coulomb excitations take place in two succeeding beam bunches. This is referenced by the *self-coincidence gate* indicated in Figure 5.3. It is used to create a second  $\gamma$ - $\gamma$  matrix under the condition, that one  $\gamma$  is detected in the *prompt coincidence window*, while the other one is detected in the *self-coincidence window*. The spectrum generated by gating on the *self-coincidence window* is afterwards subtracted from the one generated by gating on the *prompt coincidence window*, using an adequate scaling factor. A comparison of  $\gamma$ -ray spectra in coincidence with the  $2_1^+ \rightarrow 0_{1,gs}^+$  transition of  $^{204}\text{Hg}$ , with and without subtraction of *self-coincidences*, is shown in Figure 5.9.

## 5.2 Angular Distribution Analysis

In order to identify mixed-symmetry states, the absolute matrix elements have to be known and have to fulfill the requirements of low E2 and enhanced M1 strengths. The low-energy Coulomb-excitation process is not sensitive to M1 matrix elements, *i.e.*, they yield negligible excitation cross-sections. Therefore, the M1 transition strength has to be determined in another manner. This is facilitated by determining first the E2/M1 multipole-mixing ratio (cf. Equation (2.43)) and second, the excitation cross-section for the corresponding E2 transitions. This section focuses on the measurement of multipole-mixing ratios, while Section 5.3 covers the determination of the absolute matrix elements. Determination of multipole-mixing ratios is only applicable for the case of the investigation of  $^{202,204}\text{Hg}$ , since the spin-parity assignment for the state under investigation of  $^{142}\text{Sm}$  was already fixed to  $2^+$  [67–71], allowing solely for decaying via an E2 transition.

The impact of the angular distribution on the measured intensities can be quite small, depending on kind and lifetime of the excited nuclear state, and range from about 20 % to less than 10 %. For this reason, the efficiencies of the detectors, relative to each other, have to be calibrated carefully. Furthermore, sufficient intensity in each of the polar angle groups is necessary, limiting this kind of analysis to the most intense ones. Nevertheless, the intensities, subdivided by the polar angle, are mostly so low, that assumptions on the level and the shape of the background can have a significant impact on the measured angular distribution curve.

The intensities and efficiency curves have to be determined per polar angle group, corresponding to a ring in Gammasphere terminology. According to the beam energy, relativistic effects have to be taken into account. In the case of the Hg isotopes  $\beta$  is about 8 %. For the analysis of angular distributions, relativistic corrections affect the transformation of angles between the laboratory and the center-of-mass frame of reference. The polar angles  $\theta_{lab}$  of the detectors in the laboratory system are not the same in the center-of-mass system, but they are related via the velocity, w.r.t. the speed of light,  $\beta$ , of the emitting nucleus [72]

$$\cos(\theta_{nuc}) = \frac{\cos(\theta_{lab}) - \beta}{1 - \beta \cos(\theta_{lab})}. \quad (5.15)$$

This relation solely alters the angles in the center-of-mass frame of reference, but does not have any other consequence. Nevertheless, this change of polar angles applies to all angles, *i.e.*, also the angles of the edges of the detector have to be transformed, ultimately resulting in a modification of all solid angles

$$d\Omega_{nuc} = \frac{1 - \beta^2}{(1 - \beta \cos(\theta_{lab}))^2} d\Omega_{lab}. \quad (5.16)$$



Thus, the Lorentz boost results in detectors of the same kind exhibiting various solid angles in the rest frame of reference of the emitting nucleus, *i.e.*, detectors in forward direction exhibiting larger solid angles compared to those located in backward direction. This ultimately shifts the intensity distribution towards smaller polar angles in the laboratory frame of reference.

As soon as both of the relativistic implications have been corrected for, the experimental angular distribution - in terms of the analysis - is fully determined.

The experimental setups covered within this work all exhibit rotational symmetry, hence, the context given in Section 2.2.1 can be applied. In order to deduce the multipole-mixing ratio, as a first step,

$$\begin{aligned}
 W(\theta) &= A_0 + A_2 P_2(\cos(\theta)) + A_4 P_4(\cos(\theta)) \\
 &= A_0 \left( 1 + \underbrace{A_2/A_0}_{a_2} P_2(\cos(\theta)) + \underbrace{A_4/A_0}_{a_4} P_4(\cos(\theta)) \right) \quad (5.17)
 \end{aligned}$$

is fitted to the experimental angular distribution. The normalization is necessary to match the theoretical description, which is given in Equation (2.59) in its normalized variant. The  $a_k$  here correspond to the  $A_k$  in Section 2.2.1. They are determined by a product of the statistical tensor  $\rho_k(J_i)$  and a geometrical factor  $B_k(J_f \lambda \lambda' J_i)$  (cf. Equation (2.62)). There exist ambiguities when attempting to determine the multipole-mixing ratio from measuring  $a_2$  and  $a_4$  coefficients for the transition under investigation (as long as it is not a ground-state transition), as the contribution of the statistical tensor cannot be disentangled from the contribution of the mixing ratio, *e.g.*, when identifying a mixed-symmetry state. Therefore, it is desirable to measure the angular distribution of the corresponding ground-state decay. This transition is pure, thus, the geometrical factor is fully determined by the angular momenta of the states involved, *i.e.*, the only free parameters are the components of the statistical tensor. Thereby, the statistical tensor can be measured using the angular distribution of the ground-state transition.

---

### 5.3 Coulomb-Excitation Calculations

---

The angular-distribution analysis presented in the preceding section only allows for deduction of transition strength ratios. However, it is not capable of measuring absolute transition strengths. However, Coulomb-excitation theory (cf. Section 2.1.1) can link experimental information to the desired absolute transition strengths. The procedure is outlined in the following paragraphs.

---

## General Procedure

---

Coulomb-excitation theory is capable of predicting excitation probabilities, and thus, excitation cross sections (cf. Eqs. (2.6) and (2.7)), of nuclear states. The experimentally accessible counterpart to the excitation cross section of a nuclear state is the *yield* of a state. The yield measures the population, via Coulomb excitation from the ground state, of a state. It can be computed by subtracting the efficiency corrected intensities of feeding  $\gamma$  rays from the ones of depopulating  $\gamma$  rays, taking also into account corrections for decays via conversion electrons. The link between the yield and the cross section is the beam intensity. If it is not measured, Coulomb-excitation measurements can be performed as relative measurements, where yields are normalized to the yield of a state with known depopulating transition strength. Depending on the structure of the experiment, two different cases of normalization may occur:

- Self-normalization

At least one transition strength of the nucleus under investigation has to be known previously. In the most common case, for even-even nuclei, the  $B(E2; 2_1^+ \rightarrow 0_1^+)$  is known and can be used for normalization. This information permits for calculating the excitation cross section of this excited state. The cross sections for other excited states can be retrieved via

$$\sigma_i = \frac{Y_i}{Y_n} \frac{W_n(\theta)}{W_i(\theta)} \sigma_n, \quad (5.18)$$

where  $Y$  and  $\sigma$  denote the yield and the cross section, respectively, while  $i$  and  $n$  label the state of investigation and the state used for normalization, respectively. The angular distribution  $W$  of the decay, which has to be taken into account, if the  $\gamma$ -ray detector array does not cover the full solid angle.

- Normalization to partner nucleus

This method closely resembles the self-normalization method, although the normalization is performed to a state in the reaction partner nucleus. But in contrast to the self-normalization arise, both, beam and target may contain contaminations by other nuclei. They exhibit different excitation cross sections and can lead to erroneous results. Therefore, this has to be taken into account. The normalization is then given by

$$\sigma_i = \frac{Y_i}{Y_n} \frac{W_n(\theta)}{W_i(\theta)} \frac{1 - Q_n}{1 - Q_i} \sigma_n. \quad (5.19)$$

This is similar to the formula for self-normalization, although it contains an additional factor, to take the contamination  $Q$  into account.  $Q_i$  and  $Q_n$  label the purity of beam and target, respectively.

---

The aforementioned procedures allow for determination of the Coulomb-excitation cross section from measured and literature values. But, as pointed out in Section 2.1.1, the excitation cross section is given by the matrix elements connecting the state under investigation to other excited states. In order to infer these matrix elements from the cross sections, computer codes like CLX [73] or GOSIA [74], which are both based on the original code of Winther and de Boer [75], have been used. These softwares compute the cross sections from given sets of matrix elements. By varying the matrix elements until all relative cross sections are matched, a set of solutions can be extracted.

Each of this computer codes needs a specific input file. A sample input file for CLX is presented in Appendix A. The file consists of three parts. In the beginning, the output as well as the working precision of the calculation are controlled. Next, projectile and target charge and mass, respectively, have to be declared. In the second block all states, which shall be considered in the calculation have to be declared, including their energy, spin and parity. The states need to be numbered by a running index for use in the last block, where all the transition matrix elements are given. This includes diagonal as well as non-diagonal matrix elements. Initial and final state are referred to by their respective index, where the initial index always has to be smaller than or as large as the final index. Also, the transition character has to be given. Note, that CLX performs all the calculations within the center-of-mass frame of reference.

This is different when dealing with GOSIA(2). There, input and output expect and contain, respectively, particle angles in the laboratory frame of reference. This can lead to implications when dealing with experimental setups without a particle detector. An example input is given in Appendix B. The main difference, in comparison to CLX, is, that GOSIA is capable of performing a least-squares fit of the matrix elements to given experimental intensities and to literature values for various observables.

For the CLX calculations, this has to be performed manually. The distribution of intensity among different electromagnetic transitions depopulating specific excited nuclear levels, is governed by the ratios, called branching ratios, of the partial decay widths (cf. Equation (2.49)). These ratios are equivalent to the ratios of the

measured transition intensities, ultimately allowing to deduce the ratios of matrix elements connecting the specific level to other levels:

$$\begin{aligned} \frac{I'}{I} &= \frac{\Gamma'(\sigma'\lambda')}{\Gamma(\sigma\lambda)} = \frac{c_{\sigma'\lambda'} \cdot \left(\frac{E'_\gamma}{\text{MeV}}\right)^{2\lambda'+1} \cdot B(\sigma'\lambda'; J_i \rightarrow J_f)_\downarrow}{c_{\sigma\lambda} \cdot \left(\frac{E_\gamma}{\text{MeV}}\right)^{2\lambda+1} \cdot B(\sigma\lambda; J_i \rightarrow J_f)_\downarrow} \\ &= \frac{c_{\sigma'\lambda'} \cdot \left(\frac{E'_\gamma}{\text{MeV}}\right)^{2\lambda'+1} \cdot |\langle J_i \| \mathfrak{M}(\sigma'\lambda') \| J_f \rangle|^2}{c_{\sigma\lambda} \cdot \left(\frac{E_\gamma}{\text{MeV}}\right)^{2\lambda+1} \cdot |\langle J_i \| \mathfrak{M}(\sigma\lambda) \| J_f \rangle|^2}. \end{aligned} \quad (5.20)$$

However, this is only valid for the case of pure transitions. If the specific initial and any final state are connected by more than one electromagnetic transition operator, the ratio of their partial decay widths has to be considered in addition. This can be facilitated by using the multipole-mixing ratio  $\delta^2$  (cf. Eq (2.43)). The most important superposition within this work is the superposition of M1 and E2 transitions, for which reason the approach is described using this as an example. In low-energy Coulomb excitation the excitation process itself is not sensitive to M1 transitions. Although cross sections for E1 excitations are largest if considering different multiplicities of the same transition strength,  $B(E1)$  values are of the order of  $10^{-3} \dots 10^{-4}$  W.u., in general, exhibiting negligible excitation cross section. Nevertheless, the M1 transition strength is essential in identifying states of mixed-symmetric character. Thus, the M1/E2 multipole-mixing ratio is used to connect the respective matrix elements, via

$$\delta^2 = \frac{\Gamma(E2)}{\Gamma(M1)} \Rightarrow \Gamma = \Gamma(E2) + \Gamma(M1) = \Gamma(E2) \cdot \left(1 + \frac{1}{\delta^2}\right), \quad (5.21)$$

where  $\Gamma$  denotes the sum of the partial decay widths of transitions sharing the same transition energy, *i.e.*, what appears in spectra as a single peak. Combining Equations (5.20) and (5.21) finally allows for determining relations of all transitions depopulating a level. Argumentum e contrario, all matrix elements from a state can be given in dependence of a single matrix element, *e.g.*, the matrix elements of unstretched transitions depopulating a state can be given, from the knowledge of the intensities and the multipole-mixing ratios, as a function of the matrix element of the stretched transition.

Using the relations above, a fit of the excitation cross section can be performed. The cross section relative to the cross section of a particular level is fitted to the relative experimental yield. This is done by varying the stretched matrix element,

and therewith the unstretched ones, until the relative yield is matched. Besides non-diagonal matrix elements interconnecting different levels, also diagonal matrix elements play a role. If literature values for these matrix elements existed, they were taken into account. However, in experiments, where particle detectors were not part of the setup, measurement of diagonal matrix elements was not possible. In such cases, unknown diagonal matrix elements are assumed to be zero. Another natural appraisal are the rotational limits, though they were not taken into account. It was shown before, that the uncertainty of the non-diagonal matrix elements, induced by the rotational limits for the diagonal ones, are  $\leq 3\%$  [76], which is small w.r.t. to the uncertainty imposed by the uncertainties of the relative yields.

The use of a Carbon target for the  $^{202,204}\text{Hg}$  experiments aids the Coulomb-excitation analysis. Higher-order excitation amplitudes scale with  $Z^n$ , where  $n$  is the order, resulting in mainly population of excited levels via one-step excitation from the ground state. However, this keeps the influence of matrix elements, not directly connected to the state under investigation, small, allowing for dividing the whole data into different subsets, containing only few or even solely individual levels. For each of these subsets the Coulomb-excitation fits of matrix elements is performed individually. This was the only way to treat the extensive (partial) level schemes the data of  $^{202,204}\text{Hg}$  exhibits. Recombination of the results obtained from the subsets imposes only slight changes on the matrix elements found before. This also legitimates the separate treatment of the subsets, and was continuously monitored during the analysis.

In the analysis of excited levels, various sources inducing uncertainties exist and have to be taken into account when determining the uncertainty of matrix elements depopulating a level under investigation, *e.g.*, the uncertainty of the transition strength used for normalization, of diagonal matrix elements, of the relative yield, as well as those of branching and multipole-mixing ratios.

---

### Sign of the Matrix Elements

---

When reproducing the relative population of excited levels, the excitation path has to be taken into account. If levels are excited exclusively either via one-step or multi-step excitation, no additional constraints apply. However, as soon as the level under investigation is not the lowest excited level, this scenario is rarely given. In most cases, both excitation paths contribute a non-vanishing fraction of the levels population.

Visible from second-order perturbation theory, having one- and two-step excitation paths present at the same time imposes some difficulties on the analysis. Taking

a look at Equation (2.35), this manifests in the factor  $\chi_{0 \rightarrow f}^{(\lambda)} \chi_{0 \rightarrow z}^{(\lambda')} \chi_{z \rightarrow f}^{(\lambda'')} (\chi_{i \rightarrow j} \propto \langle J_i \| \mathfrak{M}(\sigma\lambda) \| J_j \rangle)$ . The sign generated by this  $|0\rangle \rightarrow |z\rangle \rightarrow |f\rangle \rightarrow |0\rangle$  loop can either be positive (constructive interference) or negative (destructive interference). Either way, the loop will influence the excitation cross section.

Using Coulomb-excitation experiments, there are no means to measure the sign of each matrix element independently: In first- and second-order terms, the matrix elements appear only squared. This results either in additional uncertainties of the measured mean transition strength, or in two valid solutions.

Knowledge of the influence of interference on excitation cross sections, renders providing valid matrix elements, for some states with non-vanishing excitations from the ground state, impossible. This is the case, e.g., for the  $4_1^+$  state of  $^{202}\text{Hg}$ , where the  $B(E4; 0_{1,gs}^+ \rightarrow 4_1^+)$  value was not measured before, and  $\gamma$  spectroscopy is not sensitive to such transitions. Although, this E4 strength is finite in  $^{204}\text{Hg}$ , indicating that disregarding this value in the calculations for  $^{202}\text{Hg}$  is improper. Not only, that this renders deduced  $B(E4; 2_1^+ \rightarrow 4_1^+)$  values, calculated using pure two-step excitation, invalid, but also the interference of the loop is impossible to deduce. The  $B(E4; 4_1^+ \rightarrow 0_{1,gs}^+) = 5.5(7)\text{W.u.}$  of  $^{204}\text{Hg}$  and the unknown sign of the loop increase the uncertainty of the  $B(E2; 4_1^+ \rightarrow 2_1^+) = 14.9\text{W.u.}$  from  $0.9\text{W.u.}$  to  $4.7\text{W.u.}$

---

## Energy Loss in the Target

---

The Coulomb excitation cross section depends on the energy of the beam. Ions will experience several electronic interactions when passing through material of finite size, leading to a loss of kinetic energy. The amount of energy deposited in the target depends on the energy of the beam, as well as on the species of projectile and target nuclei. In the experiments conducted within this work, the energy loss can exceed  $120\text{MeV}$  during the passage. Therefore, the Coulomb excitation cross section will vary, while the projectile nuclei travel through the extended target material. In order to cope with the energy loss, several calculations using CLX for  $^{204}\text{Hg} + ^{12}\text{C}$  have been carried out. The target was virtually subdivided into slices. This was modeled by supplying the calculation for each slice with an individual beam energy, representing the integrated energy loss in the preceding slices. It can be shown, that the average of the cross section deduced using this slicing, yields only minor deviations from performing the calculations of the cross section for the center of the target.

The disadvantage of the latter is the determination of the uncertainty of the energy loss, which contributes to the uncertainties of all matrix elements. Taking the difference of entry or exit energy and kinetic energy in the center of the target, drives

---

unrealistically large uncertainties for the matrix elements. For this reason,  $\pm 10\%$  of the difference of entry and center kinetic energy were chosen as appropriate, still contributing the largest fraction of the overall uncertainty of the matrix elements.

---

## 5.4 Radioactive $^{142}\text{Sm}$

---

The analysis of this dataset was previously started as part of a master's thesis [77]. However, during the preparation of [78], concerns in the contamination analysis arose, for which reason the data was partially reanalyzed within this work. The data preparation as well as determined experimental intensities were kept, but the succeeding steps were redone.

In the second part of the experiment IS496,  $^{142}\text{Sm}$  was produced using a 1.4-GeV proton beam impinging on a tantalum primary target. The laser ion source RILIS was employed to increase the amount of Sm extracted from the target. In a preceding thesis [66], laser on/laser off runs were used in order to get rid of isobaric contamination. However, in the beginning of the  $^{142}\text{Sm}$  experiment, it was seen that isobaric contamination is not present in the  $\gamma$ -ray spectrum, for which reason RILIS was used for the whole experiment. The cocktail beam was post-accelerated to 2.85 MeV/u. Foils of  $1.4 \text{ mg/cm}^2$   $^{48}_{22}\text{Ti}_{26}$  and  $2.0 \text{ mg/cm}^2$   $^{94}_{42}\text{Mo}_{52}$  were used as Coulomb excitation secondary targets. Data was taken for 24 h and 8 h using the Ti and Mo targets, respectively.

The particle detector exhibited an opening angle of  $19.7^\circ - 58.4^\circ$ . The maximum scattering angle of the projectile scattered of the  $^{48}\text{Ti}$  target is  $19.8^\circ$ , while in the case of the  $^{94}\text{Mo}$  target the maximum angle is  $41.5^\circ$ . The recorded particle spectra are depicted in Figure 5.10. In the rings exhibiting slightly larger angles, discrimination of scattered projectile as well as recoiling target-like nuclei is possible, allowing for analyzing the data exploiting the reorientation technique (cf. Section 2.1.1).

By using different time windows (cf. Section 5.1.3),  $\gamma$  rays emitted from background decays are eliminated from the particle- $\gamma$  coincidence  $\gamma$ -ray spectra. Nevertheless, Doppler correction for either projectile or target-like nuclei is necessary in order to obtain sharp peaks. The resulting spectra are shown in Figure 5.11. The only  $\gamma$  rays present in the spectra are from the decays of the  $2_1^+$  states of  $^{142}\text{Sm}$  (768 keV),  $^{48}\text{Ti}$  (984 keV), and  $^{94}\text{Mo}$  (984 keV), as well as the decay of the  $\left(\frac{3}{2}\right)_1^+$  state of  $^{95}\text{Mo}$  (204 keV).

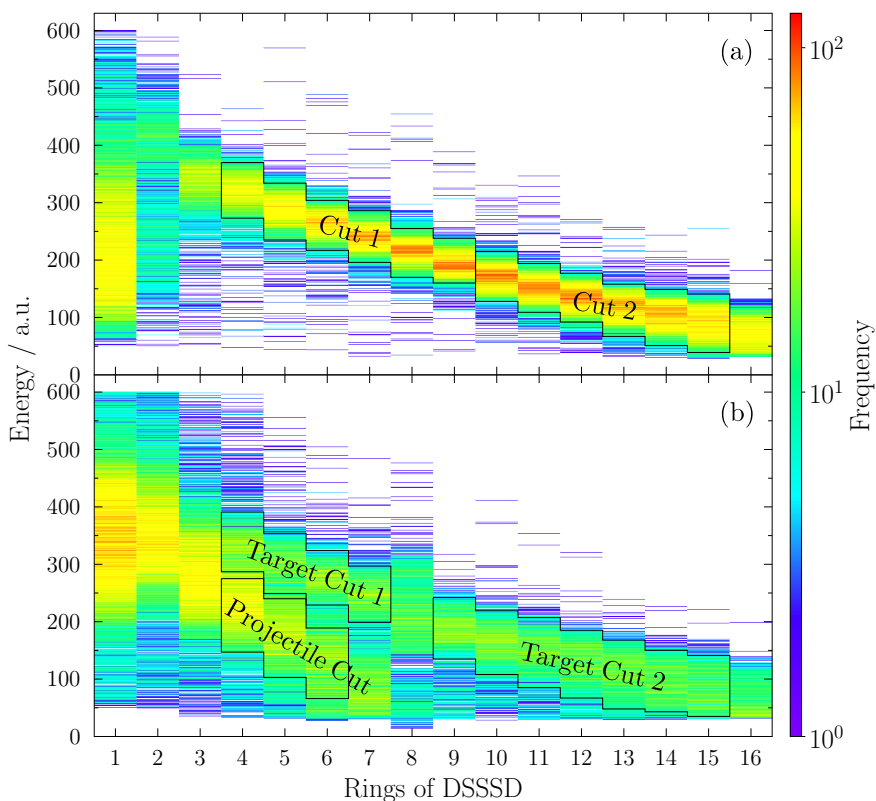


**Figure 5.10.:** Particle- $\gamma$  coincidence particle spectra. (a) shows the data recorded with the  $^{48}\text{Ti}$  target. Only the recoiling target-like nuclei are clearly visible, while the scattered projectile nuclei are solely located in the innermost ring (ring 1), where both species cannot be distinguished. (b) shows the data recorded with the  $^{94}\text{Mo}$  target. The innermost rings (rings 1-3) do still not allow for distinguishing both species, but because of the larger maximum scattering angle of the projectile both species can be discriminated in rings exhibiting larger angles.

---

### Contamination Analysis

---

Two types of contamination have to be distinguished: Beam and target contamination. While the Ti target was isotopically pure, the Mo was enriched to 94.2 (30) %.



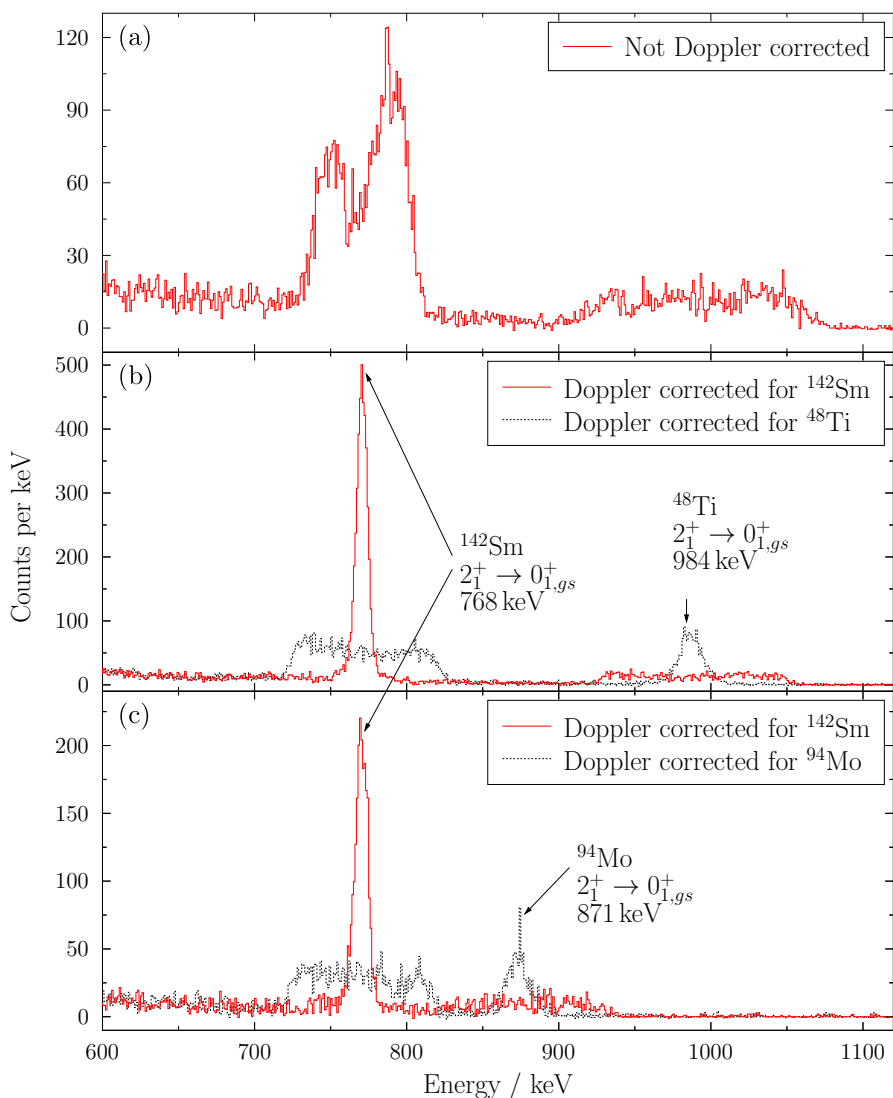


**Figure 5.11.:** Background-subtracted particle- $\gamma$  coincidence spectra without any particle angular range restrictions, not Doppler corrected in (a) and Doppler corrected in (b, c) for projectile (red, solid line) and target-like recoils (black, dashed line). (a, b) show spectra obtained using a  $^{48}\text{Ti}$  target, while (c) shows spectra obtained using a  $^{94}\text{Mo}$  target.

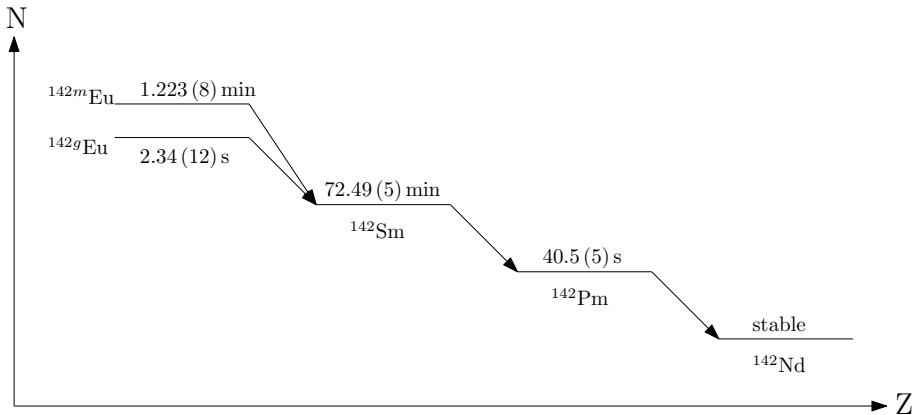


**Figure 5.12.:** Illustrative decay scheme of the isobars investigated in decay spectroscopy. The times indicate the half-lives of the respective nuclide or isomer.

In the excitation spectra obtained with the latter,  $\gamma$  rays stemming from the decay of excited levels in  $^{95}\text{Mo}$  are present. The Coulomb excitation intensities of the projectile are corrected by  $Q_i = 5.8(30)\%$ . The intensities, which are in this case of exclusive excitation of the lowest-lying level equivalent to the yields, are thus only from interaction with the  $^{94}\text{Mo}$  target nuclei.

One challenge in measuring the Coulomb excitation cross section of the  $2_1^+$  state is the determination of the beam composition. Although there are no  $\gamma$  rays from decays of projectile nuclei other than  $^{142}\text{Sm}$  present in the spectra, yet beam contaminants still excite target nuclei, tampering the measured intensities. In order to cope with possible contaminants, a Bragg ionization chamber was connected downstream Miniball, but the recorded spectra are not conclusive. However, during the experiment, it qualitatively indicated a slight presence of isobaric contaminants in the beam (cf. Figure 5.12). In order to evaluate the beam composition quantitatively, a more detailed decay spectroscopy had to be performed. A thick copper target was placed inside Miniball, at the position of the Ti and Mo targets, and irradiated for 30 minutes.  $\gamma$  rays emitted in radioactive decays during the irradiation time as well as up to 1 h afterwards, were collected in singles mode. Excerpts of the collected data are presented in Figure 5.13.

Electromagnetic transitions following  $\beta^+$  / electron capture (EC) decays of  $^{142g,m}_{63}\text{Eu}_{79}$ ,  $^{142}_{62}\text{Sm}_{80}$  and  $^{142}_{61}\text{Pm}_{81}$  are visible in the spectra, rendering at least the first two possible components of the beam. Although the harvested activity in-

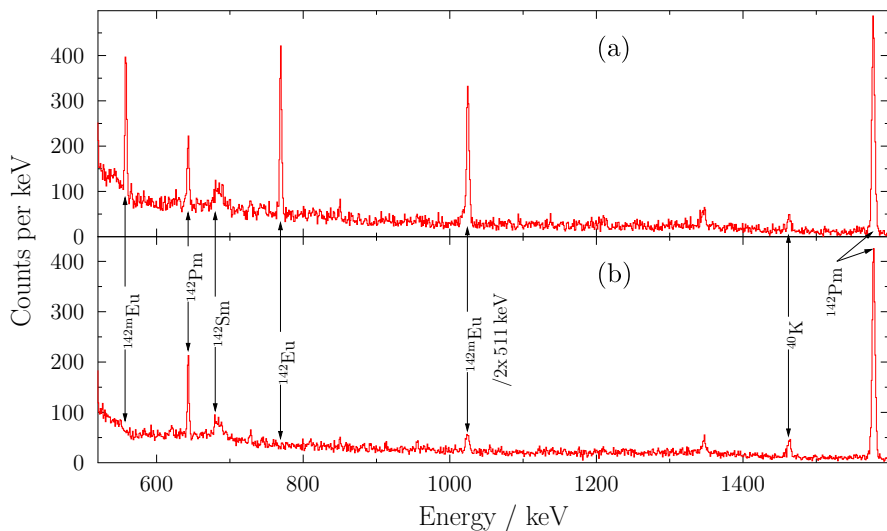


**Figure 5.13.:** Singles spectra showing the decay of radioactive projectile nuclei implanted into the thick copper target for 30 minutes. The spectra show intervals of 3 minutes beginning in the (a) 1<sup>st</sup> and (b) 40<sup>th</sup> minute after ending the irradiation. Next to each of the most intense  $\gamma$ -ray transitions the corresponding parent nuclide is indicated. The beam contamination by  $^{142g,m}_{63}\text{Eu}_{79}$  are obvious from their decays. Despite the short half-life of 40.5(5)s [71, 79], the intensity of  $^{142}_{61}\text{Pm}_{81}$  stays nearly constants during the course of the decay spectroscopy, indicating that it stems only from decays of  $^{142}_{62}\text{Sm}_{80}$ .

indicates an isobaric contamination of the beam  $\leq 10\%$ , an analysis of the beam composition was performed and is presented in the following paragraphs.

The 1576-keV transition originates from  $^{142}_{60}\text{Nd}_{82}$ , which excited levels are populated in the decay of  $^{142}\text{Pm}$ . Despite the half-life of 40.5(5)s of  $^{142}\text{Pm}$ , the activity from its decay stays nearly constant over the course of the decay spectroscopy of 1 h (cf. Figure 5.13). This allows for concluding, that  $^{142}\text{Pm}$  is not part of the beam produced in the primary target, but solely originates from the decay of long-lived  $^{142}\text{Sm}$  ( $T_{1/2} = 72.49(5)\text{ min}$  [71, 80]). Thus, from the radioactive side, the beam consists of  $^{142g,m}\text{Eu}$  and  $^{142}\text{Sm}$ . The latter is not only produced in the primary target, but additionally in the  $\beta^+$  decay of  $^{142}\text{Eu}$ , indicated by the presence of the 768-keV  $2^+_1 \rightarrow 0^+_{1,gs}$  transition of  $^{142}\text{Sm}$  in the decay spectra. However, the decay

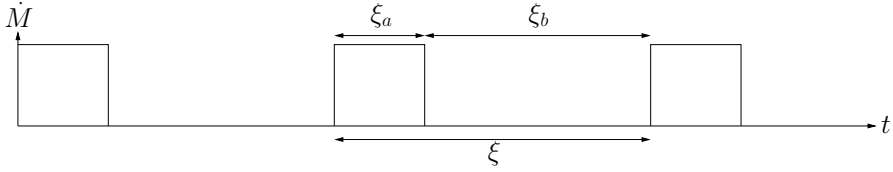


**Figure 5.14.:** Bunch structure of the beam impinging on the secondary target mounted inside the Miniball target chamber. The temporal structure is slightly different from the one shown in Figure 4.5, but the approximation is sufficient for the analysis. The bunch length  $\xi_a = 5$  ms as well as the time in between bunches  $\xi_b = 145$  ms were determined from recorded data.

lines at 1023 and 556 keV hint at the presence of  $^{142m}\text{Eu}$  in the beam, as these transitions do not occur in the ground-state decay of  $^{142g}\text{Eu}$ .

The first step is assessing the ratio of  $^{142m}\text{Eu}$  and  $^{142}\text{Sm}$ . The half-lives differ by two orders of magnitude, rendering decay spectroscopy after implantation unsuitable, as most of the Eu has already decayed at this point, while most of Sm has not. Employing decay spectroscopy after implantation despite this finding, yields a ratio of  $\approx 10^{-3} : 1$  of  $^{142}\text{Eu}$  to  $^{142}\text{Sm}$ , rendering an appearance of Eu in the Bragg chamber measurement almost impossible. In order to cope with this situation, a more sophisticated approach has to be chosen.

REX operates in a pulsed mode, with bunch lengths of  $\xi_a = 5$  ms and time in between bunches of  $\xi_b = 145$  ms, as deduced from the recorded data. In between pulses, solely nuclear decay of implanted radioactive ions takes place

$$\frac{dN_a(t)}{dt} = -\lambda N_a(t), \quad (5.22)$$

where  $\lambda = -\ln(2)/T_{1/2}$  denotes the decay constant. When a beam pulse approaches the target, nuclear decay still takes place, but also not yet decayed nuclides are implanted at a rate  $\dot{M}$

$$\frac{dN_b(t)}{dt} = \dot{M} - \lambda N_b(t). \quad (5.23)$$

The solutions for this set of equations are

$$N_a(t) = \frac{\dot{M}}{\lambda} (1 - e^{-\lambda t}) + N_0 e^{-\lambda t} \quad (5.24)$$

$$N_b(t) = N_0 e^{-\lambda t}. \quad (5.25)$$

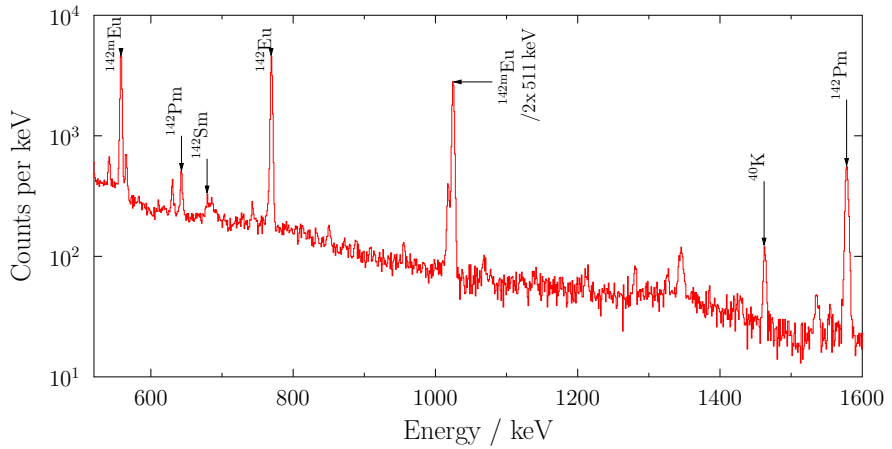


**Figure 5.15.:** Summed  $\gamma$  rays recorded over the period of 30 minutes of irradiation of the thick copper target, in order to deduce the beam composition. Not all transitions are marked, but only the most intense ones for each decaying radioactive beam component. Besides every peak the decaying parent nucleus is noted.

Applying a recursive ansatz, the number of implanted nuclei  $N$  after  $k$  periods  $\xi = \xi_a + \xi_b$  can be determined to be

$$N_k(k\xi) = \frac{\dot{M}}{\lambda} (1 - e^{-\lambda\xi_a}) e^{-\lambda\xi_b} \frac{1 - e^{-\lambda k\xi}}{1 - e^{-\lambda\xi}}. \quad (5.26)$$

For large irradiation times  $t \gg \xi$  is  $k \gg 1$ , implying that the difference between periods with and without a beam pulse impinging vanishes in terms of count rate, leading to  $k\xi \approx t$ . This allows for representing the activity through

$$A(t) = \lambda N(t) \approx \dot{M} (1 - e^{-\lambda\xi_a}) e^{-\lambda\xi_b} \frac{1 - e^{-\lambda t}}{1 - e^{-\lambda\xi}}. \quad (5.27)$$

Although this equation already allows for disentangling the beam composition, the activity per time is rather low. A more handy approach is to compare the integrated

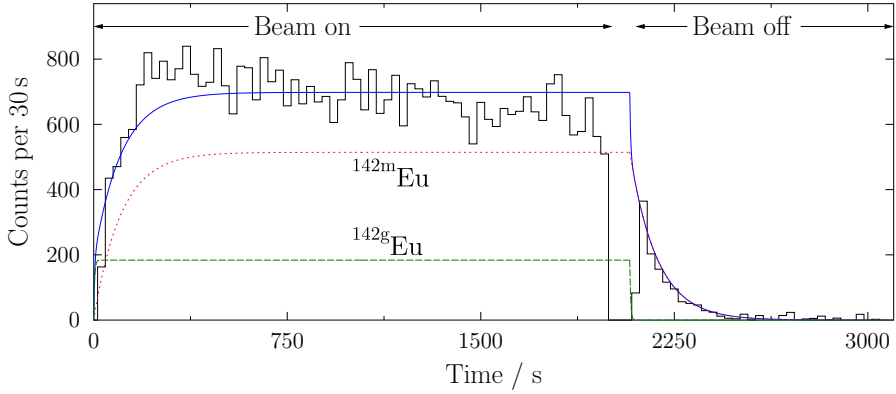


**Figure 5.16.:** Temporal evolution of detected 768-keV  $\gamma$  rays emitted after the decay of  $^{142g,m}\text{Eu}$ . The activity after implantation is used to determine the isomeric ratio. The orders of magnitude difference in half-lives of  $^{142g}\text{Eu}$  ( $T_{1/2} = 2.34(12)\text{s}$  [70, 71]) and  $^{142m}\text{Eu}$  ( $T_{1/2} = 1.223(8)\text{min}$  [71, 81]) allows for fitting the slope at the beginning of the decay spectroscopy in order to deduce the ratio. The red, dotted line depicts the decay of  $^{142m}\text{Eu}$ , while the green, dashed line represents  $^{142g}\text{Eu}$ . The gap between 1980 and 2130 s is caused by stopping the accelerator and switching to a different trigger source.

activity over the full course of the 30 minutes of irradiation and to deduce the implantation rate, *i.e.*, the incoming beam intensity:

$$\begin{aligned}
 N_{\gamma}(T) &= \int_0^T A(t) dt = \dot{M} \frac{(1 - e^{-\lambda \xi_a}) e^{-\lambda \xi_b}}{1 - e^{-\lambda \xi}} \left[ T + \frac{1}{\lambda} (e^{-\lambda T} - 1) \right] \\
 \Rightarrow \dot{M} &= \frac{N_{\gamma}(T) (1 - e^{-\lambda \xi})}{(1 - e^{-\lambda \xi_a}) e^{-\lambda \xi_b} \left[ T + \frac{1}{\lambda} (e^{-\lambda T} - 1) \right]}.
 \end{aligned} \tag{5.28}$$

The ratio of the isomeric and the ground state decay has to be determined first, because both will cause 768-keV  $\gamma$  rays to be emitted. Because the half-lives of  $^{142g}\text{Eu}$  ( $T_{1/2} = 2.34(12)\text{s}$  [70, 71]) and  $^{142m}\text{Eu}$  ( $T_{1/2} = 1.223(8)\text{min}$  [71, 81]) differ also by two orders of magnitude, the ratio of isomeric and ground state Eu can be estimated by fitting the intensity of detected  $\gamma$  rays to the data, *i.e.*, the activity given by Equation (5.27), in dependence of the time after starting

**Table 5.1.:** Total  $\gamma$  ray intensity, following the radioactive decay of  $^{142m}\text{Eu}$ ,  $^{142g}\text{Eu}$  and  $^{142}\text{Sm}$ , recorded during irradiation of the thick copper target. The intensities of  $^{142m}\text{Eu}$  and  $^{142g}\text{Eu}$  were deduced by employing the isomeric ratio.

Nuclide	Half-life $T_{1/2}$	Energy / keV	$N_\gamma(30\text{min})$
$^{142g}\text{Eu}$	2.34 (12) s	768.0(2)	$2.5(10) \cdot 10^4$
$^{142m}\text{Eu}$	1.223 (8) min	768.0(2)	$7.2(10) \cdot 10^3$
$^{142}\text{Sm}$	72.49 (5) min	679(1)	$5.5(44) \cdot 10^4$

to implant radioactive ions into the copper target. The resulting slopes, besides the recorded data, are given in Figure 5.16. From the curves, an isomeric ratio of  $N(^{142m}\text{Eu})/N(^{142g}\text{Eu}) = 23.5(94)\%$  is deduced. The  $\approx 40\%$  uncertainty is caused by the low sensitivity of the measurement to the slope of the decay curve of  $^{142g}\text{Eu}$ .

From the total  $\gamma$ -ray spectrum taken over the whole 30 minutes of irradiation (cf. Figure 5.15), in combination with the isomeric ratio, the intensities given in Table 5.1 are determined. Inserting these intensities into Equation (5.28) for  $^{142m}\text{Eu}$  as well as for  $^{142}\text{Sm}$  allows for expressing the ratio of both isobaric components in the beam. Because the beam period is small compared to the half-lives, even compared to the half-life of  $^{142g}\text{Eu}$ , only few nuclei decay within this period. Thus, the ratio can be approximated by

$$\frac{\dot{M}_{\text{mEu}}}{\dot{M}_{\text{Sm}}} \approx \frac{N_{\gamma, \text{mEu}}}{N_{\gamma, \text{Sm}}} \cdot \frac{T + \frac{1}{\lambda_{\text{Sm}}}(e^{-\lambda_{\text{Sm}}T} - 1)}{T + \frac{1}{\lambda_{\text{mEu}}}(e^{-\lambda_{\text{mEu}}T} - 1)} = 2.0(16)\%. \quad (5.29)$$

The large uncertainty of the ratio is caused by the large uncertainty of the 679-keV transition intensity. Applying the same procedure as outlined towards Equation (5.29), in combination with the isobaric ratio, yields  $\frac{\dot{M}_{\text{mEu}}}{\dot{M}_{\text{Sm}}} \approx 6.7(60)\%$ . The uncertainty of the ratio induced from the uncertainties of the intensities is much larger than the uncertainty from applying the approximation, which accounts to about 5%. Despite the substantial uncertainty, it is obvious, that the isobaric beam contamination by  $^{142g, \text{m}}\text{Eu}$  is less than 15%.

However, the decay spectroscopy is not sensitive to stable beam contaminants, which are also produced when bombarding the primary target. In order to estimate the amount of stable  $^{142}\text{Nd}$  and  $^{142}\text{Ce}$ , intensities from Coulomb-excitation runs on the  $^{48}\text{Ti}$  target are used. Using CLX and DCY [73] the expected number

**Table 5.2.:** Recorded  $\gamma$ -ray intensities from particle- $\gamma$  coincidence for the  $^{48}\text{Ti}$  target, corrected for relative efficiency and beam impurities.

$\theta_{\text{lab}}$ range	Ring (DSSSD)	Detected	$^{142}\text{Sm}$	$^{48}\text{Ti}$
$30.8^\circ - 46.9^\circ$	4 - 9	Target	1591 (35)	535 (32)
$47.0^\circ - 57.1^\circ$	10 - 15	Target	1406 (33)	558 (33)

**Table 5.3.:** Recorded  $\gamma$ -ray intensities from particle- $\gamma$  coincidence for the  $^{94}\text{Mo}$  target, corrected for relative efficiency, beam and target impurities.

$\theta_{\text{lab}}$ range	Ring (DSSSD)	Detected	$^{142}\text{Sm}$	$^{94}\text{Mo}$
$30.8^\circ - 39.7^\circ$	4 - 6	Projectile	640 (29)	233 (20)
$30.8^\circ - 42.3^\circ$	4 - 7	Target	387 (21)	139 (14)
$44.8^\circ - 57.1^\circ$	9 - 15	Target	386 (21)	138 (14)

of counts per ion are calculated and fitted to the spectra via a G-test approximation [82]. This yields an upper limit of 1 % of  $^{142}\text{Nd}$  and 0.6 % of  $^{142}\text{Ce}$  in the beam, respectively. The total isobaric contamination is 8.8 (62) %.

## Data Analysis

As outlined before, particle- $\gamma$  coincidence is required for events to be valid. Those events are selected for further analysis, where projectile nuclei or target-like recoils can be assigned unambiguously. The data is subdivided into several particle angular ranges in order to increase sensitivity for the  $\langle 0_{1,\text{gs}}^+ \parallel \mathcal{M}(E2) \parallel 2_1^+ \rangle (M_{20})$  and  $\langle 2_1^+ \parallel \mathcal{M}(E2) \parallel 2_1^+ \rangle (M_{22})$  matrix elements. The difference in kinematics requires different particle gates for scattering off  $^{48}\text{Ti}$  and  $^{94}\text{Mo}$ . The angular ranges and the resulting experimental intensities for  $^{48}\text{Ti}$  and  $^{94}\text{Mo}$  are presented in Tables 5.2 and 5.3, respectively.

The targets were chosen because there is no overlap in energy of the  $2_1^+ \rightarrow 0_{1,\text{gs}}^+$  transitions, but also because both matrix elements are well-known, rendering them suitable for normalization of cross sections. The spectroscopic observables as well as the derived matrix elements are given in Table 5.4. The projectile-excitation cross section is derived for every particle gate separately.

As already mentioned before, from the computed cross section of the target and



**Table 5.4.:** Reduced matrix elements of the  $2_1^+ \rightarrow 0_{1,gs}^+$  transitions and the quadrupole moments of the  $2_1^+$  states of  $^{48}\text{Ti}$  and  $^{94}\text{Mo}$ , used for calculation of the Coulomb-excitation cross-sections.

Nuclide	$B(E2) \downarrow$ / W.u.	$M_{20}$ / eb	$Q(2_1^+) / \text{eb}$	$M_{22} / \text{eb}$
$^{48}\text{Ti}$	13, 9 (8) [83]	0, 268 (7)	-0, 177 (8) [84]	-0, 234 (11)
$^{64}\text{Zn}$	20, 0 (6) [85]	0, 390 (6)	-0, 26 (6) [86]	-0, 34 (8)
$^{94}\text{Mo}$	16, 0 (3) [83]	0, 451 (4)	-0, 13 (8) [87]	-0, 17 (11)

the ratio of the yields, the cross section of the projectile can be retrieved. All of the observables just mentioned exhibit uncertainties, propagating to the uncertainty of the projectile cross section. By varying transition and quadrupole matrix elements a map of projectile-excitation cross sections is computed, using the computer codes CLX and DCY [73]. This is done for the angular range of each individual particle gate separately. Comparison to the cross section derived from normalization yields sets of consistent matrix elements, which are, including their uncertainties, derived in the same manner, as the bands visible in Figure 5.17. Each of these bands represents a Gaussian distribution around the normalized cross section. Superposition of these distributions yields a maximum-likelihood mean value as well as a  $1\sigma$  area, highlighting the most probable range of the matrix elements. The maximum-likelihood analysis is explained in great detail and a more general manner in Ref. [88].

Unfortunately, for this particular dataset, very large quadrupole moments  $\geq 3 \text{ eb}$  cannot be excluded from the level of statistical significance. However, this excess is not covered by phenomenological experience, for which reason the result was slightly constrained. Matrix elements outside the rigid rotor limit are not impossible, but nevertheless, highly unlikely for a nucleus of near vibrational behavior. Thus, the likelihood is reduced exponentially for sets of matrix elements exhibiting quadrupole moments outside the rigid rotor limits. However, this approach does not allow anymore for making a statement about the quadrupole moment of the  $2_1^+$  state of  $^{142}\text{Sm}$ .

The analysis ultimately yields  $M_{20} = 0.83(4) \text{ eb}$  for the case of the  $^{48}\text{Ti}$  target and  $M_{20} = 0.88(10) \text{ eb}$  for the  $^{94}\text{Mo}$  target, respectively. The uncertainty-weighted average of both results in  $B(E2; 0_{1,gs}^+ \rightarrow 2_1^+) = 0.70(9) \text{ e}^2 \text{ b}^2$ , corresponding to  $B(E2; 2_1^+ \rightarrow 0_{1,gs}^+) = 32(4) \text{ W.u.}$

The complete analysis is also repeated using GOSIA2, which performs a fit of the hypersurface spanned by all degrees of freedom, yielding consistent results. How-

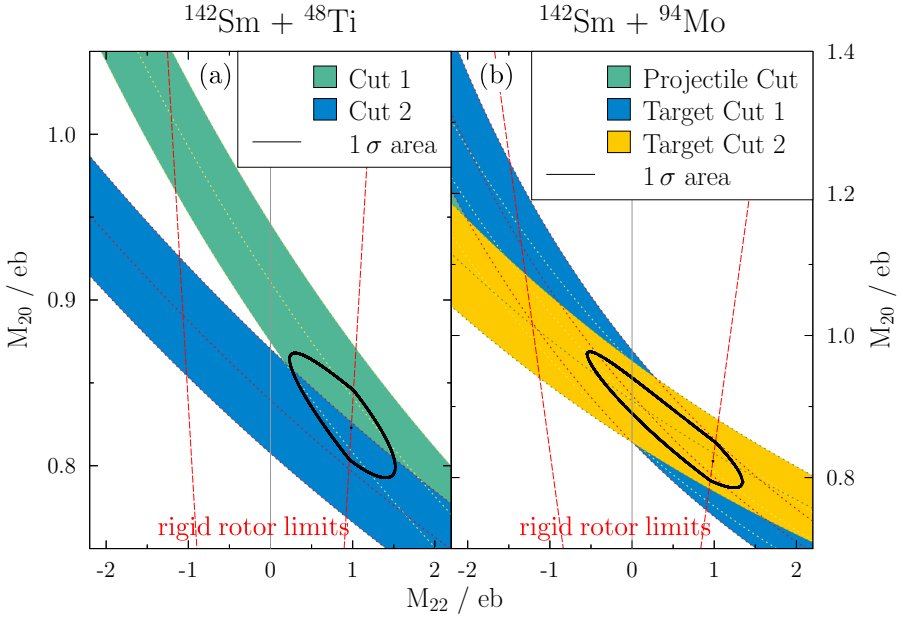


**Figure 5.17.:** Result of the maximum-likelihood analysis from the data taken using (a)  $^{48}\text{Ti}$  and (b)  $^{94}\text{Mo}$  as targets. The bands are modeled as Gaussian distributions. Folding of the bands results in the  $1\sigma$  area highlighted.

ever, these calculations also exhibit large quadrupole moments, hence, the same restrictions outside the rigid rotor limits have to be applied.

---

## 5.5 Stable $^{202,204}\text{Hg}$

---

The analysis of the  $^{202}\text{Hg}$  and  $^{204}\text{Hg}$  datasets is presented in this section. Beams of both isotopes were produced using plasma-ion sources, and accelerated to 890 MeV in a 12 MHz pulsed-beam scheme. Both experiments shared the same  $^{12}\text{C}$  target. In addition,  $^{204}\text{Hg}$  was also impinging on a  $^{27}\text{Al}$  target, in order to perform complementary DSAM lifetime measurements. The analysis was not performed within this work, however, the outcome [89] is consistent with the results of this work, thus, both are presented alongside. The conjunction of both experiments, and a short description of the DSAM analysis, are presented in Ref. [90].

In contrast to the experiment of  $^{142}\text{Sm}$ , the analysis of these nuclei is based on self-normalization. Both experiments did not employ a particle detector. The analysis is based on singles level intensities, however, not all transitions can be analyzed on this stage, highlighting the necessity of investigating  $\gamma$ - $\gamma$  correlations.

---

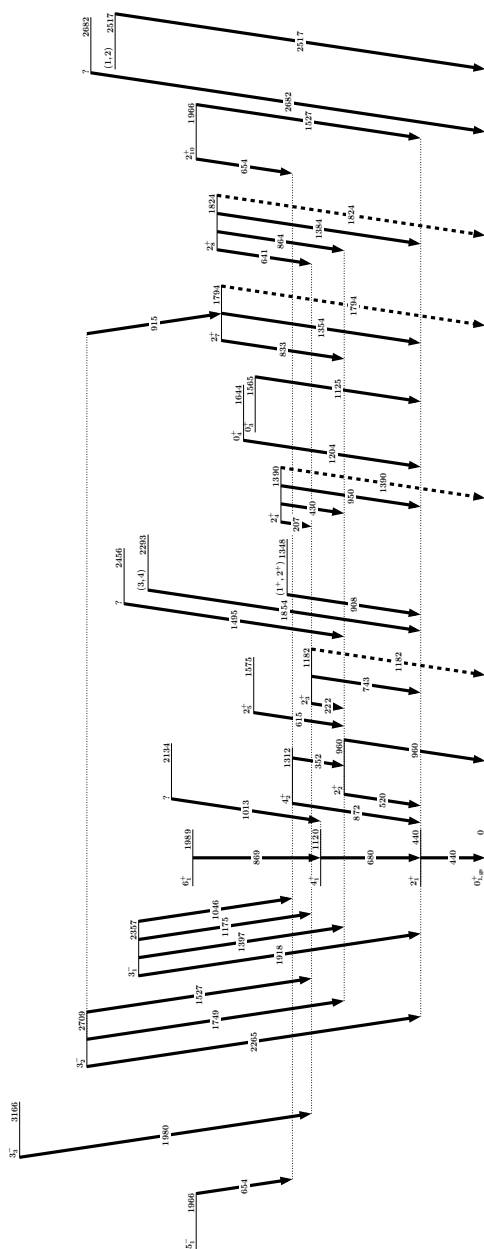
### 5.5.1 $^{202}\text{Hg}$ Analysis

---

In the  $^{202}\text{Hg}$  experiment, a total of  $8.2 \times 10^8$  events of  $\gamma$ -ray fold  $\geq 1$  were collected over a period of 19 h of beam on the  $^{12}\text{C}$  target, corresponding to 12100 counts-per-second.  $1.5 \times 10^7$  of those events even exhibited  $\gamma$  multiplicities  $\geq 2$ , thus qualified for building  $\gamma$ - $\gamma$  matrices. Spectra were corrected for the Doppler shift, adopting a projectile velocity of  $\beta \approx 8.3\%$ . The Doppler corrected, background-subtracted sum spectrum of the  $^{202}\text{Hg}$  experiment, as well as the spectrum of  $\gamma$  rays coincident with the  $2_1^+ \rightarrow 0_{1,\text{gs}}^+$  transition are presented in Figure 5.18. The background subtraction was performed like explained in Section 5.1.3, including correction for *self-coincidences*. Reconstruction of the level scheme, besides determination of the experimental yields, was a big challenge of this dataset. The combination of both experimental conditions ( $\gamma$ -ray singles and events of  $\gamma$ -ray multiplicity  $\geq 2$ ) was necessary to improve the level of statistics for this qualitative part of the analysis. The resulting level scheme is shown in Figure 5.19.

The spectrum is dominated by the 440-keV,  $2_1^+ \rightarrow 0_{1,\text{gs}}^+$  transition of  $^{202}\text{Hg}$  with  $2.1 \times 10^8$  counts. All other strong transitions originate from excited levels of  $^{202}\text{Hg}$  [32, 91–108]. Besides these transitions, the spectrum (cf. Figure 5.18 (a)) also contains numerous weak transitions from fusion-evaporation reactions of recoiling target-like nuclei and the walls of the target chamber and the beam pipe. These transitions are smeared out by the Doppler correction, as they are also corrected for the velocity of the excited beam nuclei, although emitted by nuclei of differing speeds. Hence, they only contribute to an increase in background, resulting in partially larger statistical uncertainties.





The Coulomb-excitation experiment of  $^{202}\text{Hg}$  shows the power of Coulomb excitation in terms of investigation of quadrupole collectivity: The spectrum exhibits numerous transitions following the decay of excited  $2^+$  and  $4^+$  states. The lowest of the spin-2 levels and the lowest at all is the  $2_1^+$  state at 440 keV, which only decays to the  $0_{1,\text{gs}}$  ground state. The literature-value  $B(E2; 2_1^+ \rightarrow 0_{1,\text{gs}}) = 17.34(14) \text{ W.u.}$  [31–33] is used as normalization for the CLX calculations. The quadrupole moment  $Q = 1.01(13) \text{ eb}$  [33] was also taken into account when evaluating the excitation cross-section.

The next-to-lowest state of this group, and thus, the lowest state for which the calculations will yield new transition strengths, is the  $2_2^+$  state at 960 keV, which exhibits a strong decay to the  $2_1^+$  state, but also about 15 % of this decay intensity to the ground state. The multipole-mixing ratio of the  $2_2^+ \rightarrow 2_1^+$  transition is known to be  $+0.9(1)$  [109], providing a complete set of transition strengths.

Above those two spin-2 states, additional levels fixed in spin and parity to  $2^+$ , at 1182 keV, 1390 keV, 1794 keV, 1824 keV and 1966 keV are populated in the experiment. These decay predominantly to other  $2^+$  levels. Besides the ground-state decays of the  $2_1^+$  and  $2_2^+$  levels, ground-state decays of other excited  $2^+$  levels are not observed. Nevertheless, the branching ratios  $I_{2_3^+ \rightarrow 0_1^+} / I_{2_3^+ \rightarrow 2_2^+} < 14\%$  [31]  $I_{2_4^+ \rightarrow 0_1^+} / I_{2_4^+ \rightarrow 2_1^+} = 11(4)\%$  [31],  $I_{2_7^+ \rightarrow 0_1^+} / I_{2_7^+ \rightarrow 2_1^+} = 2.8(13)\%$  [31],  $I_{2_8^+ \rightarrow 0_1^+} / I_{2_8^+ \rightarrow 2_1^+} = 8(3)\%$  [31] are known from literature and allow for determining the ground-state decay intensity.

There also exist additional candidates for  $2^+$ , i.e., the level at 1348 keV and 2517 keV. The former holds the tentative spin-parity assignment  $(1^+, 2^+)$ , while for the latter only tentative spin assignments  $(1, 2)$  exist. For neither of those, the analysis was able to yield former information on either spin or parity assignments. However, Coulomb excitation is more in favor for exciting spin-2 states, as electric dipole matrix elements are small, hence, they do not contribute to the excitation process. Magnetic dipole excitation is also not strong in low-energy Coulomb excitation. Despite those constraints, further statements about these states are not possible, why transition strengths are not given.

In addition, two  $4^+$  levels, at 1120 and 1312 keV were populated, decaying predominantly to the  $2^+$  levels at 440 and 960 keV, respectively. The 1120-keV,  $4_1^+$  level does not feature a transition to the 960-keV,  $2_2^+$  level, in contrast to the  $4_2^+$  level, which decays with about 20 % of the intensity of the decay to the  $2_2^+$  level to the 440-keV,  $2_1^+$  state. Unfortunately, the  $B(E4; 4_i^+ \rightarrow 0_{1,\text{gs}})$  is unknown for both states. Hence, only two-step excitation via  $2_i^+$  levels of these  $4_i^+$  levels can be taken into account, although it can be estimated from the non-negligible  $B(E4; 0_1^+ \rightarrow 4_1^+) = 0.045(6) \text{ e}^2 \text{ b}^4$  of  $^{204}\text{Hg}$  [110], that sizable E4 strengths are also present in  $^{202}\text{Hg}$ . This does not allow for statements about the E2 decay strengths.

Furthermore, two levels with fixed  $J^\pi = 0^+$  at 1565 and 1644 keV were populated, both decaying exclusively to the  $2_1^+$  state. Decay of the  $6^+$  level is also visible in the spectra, although, it was only populated very weakly.

Two additional  $3^-$  levels, at 2357 and 2709 keV, and a  $5^-$  level, at 1966 keV, are observed as well. A 2293-keV level with tentative spin assignment (3, 4) was also populated, but the level of statistics did not allow for conclusions about the nature of this level, for which reason, also no matrix element connecting this level to others is given.

The high overall statistics and the predominant one-step excitation process permitted also population of hitherto unknown levels at 2134 and 2682 keV. As no information are available about these states, only the energy and decay intensities are determined.

The CLX calculations are carried out, as outlined in Section 5.3, normalized to the Coulomb excitation cross section of the  $2_1^+$  state, based on the literature  $B(E2; 2_1^+ \rightarrow 0_{1,gs}^+)$  and quadrupole moment.

The high statistics nature of the experiment permitted measurements of the angular distributions of transitions sufficiently intense (cf. Figure 5.20), allowing for extraction of the  $A_2/A_0$  and  $A_4/A_0$  coefficients given in Table 5.5. The  $3_2^- \rightarrow 2_2^+$  transition serves as benchmark, exhibiting dipole character with small  $A_4/A_0$  and negative  $A_2/A_0$ . The angular distributions of the  $4_1^+ \rightarrow 2_1^+$ ,  $2_2^+ \rightarrow 2_1^+$  and  $2_1^+ \rightarrow 0_{1,gs}^+$  transitions are damped, most likely due to the long lifetimes of 2.96(9) [31, 32, 104], 20(4) [31, 32, 104] and 39.33(32) ps [31–33] of the  $4_1^+$ ,  $2_2^+$  and  $2_1^+$  states, respectively. The 440 keV  $2_1^+ \rightarrow 0_{1,gs}^+$  transition is not completely flat, but features a “hard core” residual polarization (cf. Section 2.3), which is preserved despite the lifetime. It was possible to extract the  $A_2/A_0$  and  $A_4/A_0$  coefficients for the 222 keV  $2_3^+ \rightarrow 2_2^+$ , the 743 keV  $2_3^+ \rightarrow 2_1^+$  and the 1354 keV  $2_7^+ \rightarrow 2_1^+$  transitions (cf. Table 5.5). However, this was only possible to extract from the ringwise spectra, when a coincidence to the  $2_1^+ \rightarrow 0_{1,gs}^+$  transition was required, because the level of statistics, w.r.t. the background level, in rings with few detectors is otherwise not sufficient for this kind of analysis.

In general, the angular distribution permits to extract multipole-mixing ratios of transitions between excited states. For excited  $2^+$  levels, which angular distribution coefficients of the transitions to the  $2_1^+$  state and the ground state are known, this method was shown to be valid in Ref. [12]. In this situation, the  $2_i^+ \rightarrow 0_{1,gs}^+$  transition is limited to E2 character, hence, the only unknowns are the components of the statistical tensor, which can be determined from the angular distribution. However, the data does not permit that kind of analysis, as ground-state transitions of  $2_i^+$ ,  $i \geq 3$ , are not observed, even in the sum spectra. From this lack of information, the issue arises, that in order to deduce the multipole-mixing ratio,

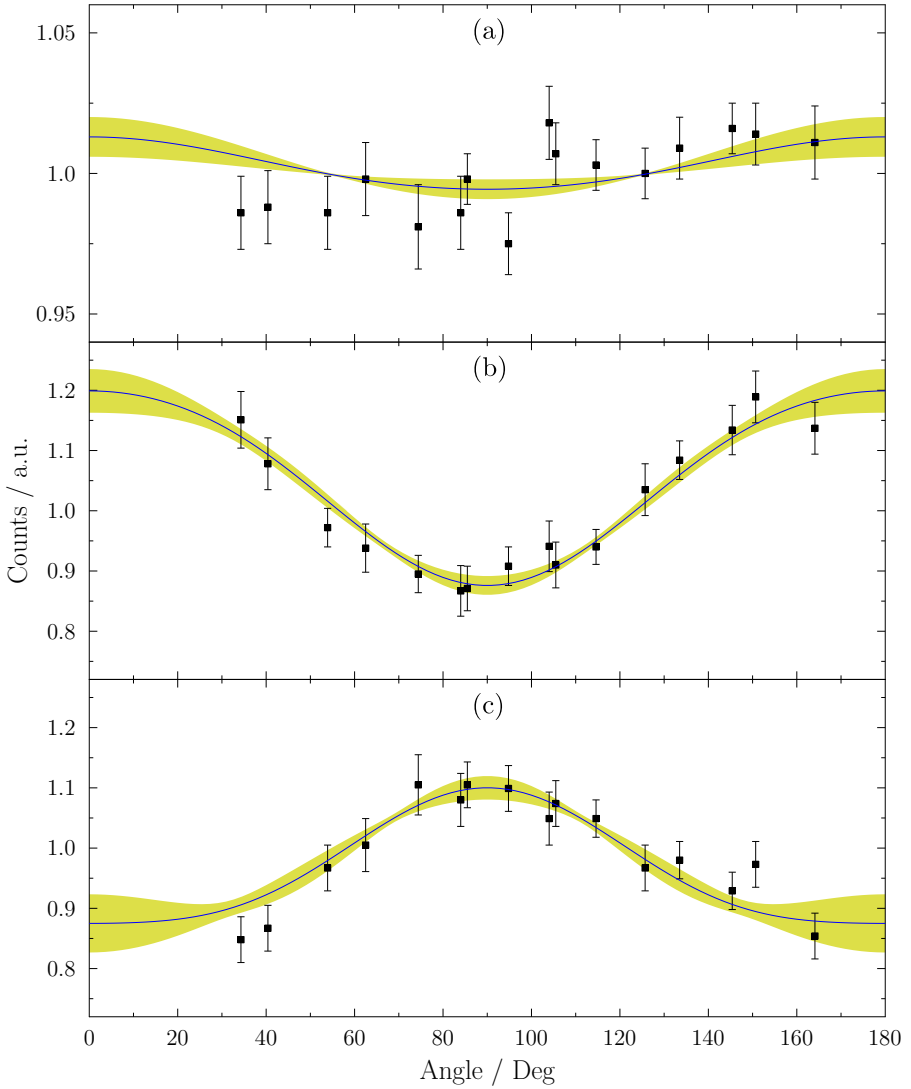


**Figure 5.20.:** Results of the angular distribution analyses of the (a)  $2_1^+ \rightarrow 0_{1,gs}^+$ , (b)  $2_7^+ \rightarrow 2_1^+$ , and (c)  $3_2^- \rightarrow 2_2^-$  transitions of  $^{202}\text{Hg}$ . The colored areas indicate the uncertainties from the fit of Equation (2.59) to the experimental data.



the statistical tensor is necessary. The statistical tensor itself can be calculated, but the matrix elements connecting the state under investigation are necessary, which depend on the multipole-mixing ratio. To cope with those issue, the approach chosen tries to bypass the need for the angular distribution of stretched transitions. This is performed by an iterative cycle. In the first step, the relative population of the state under investigation is reproduced by E2 excitation from the ground state, while the  $2_1^+ \rightarrow 2_i^+$  transition was assumed to be of pure dipole character, coupled via the branching ratio known from literature. As the employed low-Z target, *i.e.*,  $^{12}\text{C}$ , favors one-step excitation, the state is effectively populated exclusive directly from the ground state. This yields a good estimate for the  $\langle 0_{1,\text{gs}}^+ \parallel \mathfrak{M}(E2) \parallel 2_i^+ \rangle$  matrix element as well as for the m-substate distribution. Based on this set of matrix elements, the components of the statistical tensor are calculated.

In the next step, the multipole-mixing ratio is estimated using that statistical tensor in combination with the  $A_2/A_0$  and  $A_4/A_0$  coefficients deduced from the experimental angular distribution. Afterwards, based on the matrix element retrieved in the first step, the branching ratio, and multipole-mixing ratio retrieved in the second step, a  $\langle 2_1^+ \parallel \mathfrak{M}(E2) \parallel 2_i^+ \rangle$  matrix element is introduced, and the  $\langle 2_1^+ \parallel \mathfrak{M}(M1) \parallel 2_i^+ \rangle$  matrix element is modified accordingly. The multipole-mixing ratio must be taken into account, as it modifies the ratio of the unstretched M1 and stretched E2 strengths. The set of matrix elements is fitted to the measured relative population and the components of the statistical tensor are calculated, taking into account one-step E2 and two-step E2 and M1 excitation. From this, the multipole-mixing ratio is deduced, allowing for refining the unstretched matrix elements. This iterative procedure is repeated, until the multipole-mixing ratio, as well as the matrix elements, converge. In this way, different multipole-mixing ratios can be determined; the results are given in Table 5.5. A mixing ratio  $\delta = -0.13(3)$  for the  $2_3^+ \rightarrow 2_2^+$  transition is deduced, indicating predominant M1 character. For the  $2_3^+ \rightarrow 2_1^+$ , the result is ambiguous, as  $\delta = 0.02(7)$  and  $\delta = 2.1(4)$  are both solutions, where the former indicates predominant M1 character, while the latter hints to predominant E2 character. The analysis yields for the  $2_7^+ \rightarrow 2_1^+$  also an ambiguous set of valid solutions,  $\delta = 0.06(4)$  and  $\delta = 1.9(2)$ .

**Table 5.5.:** Measured properties of the levels and  $\gamma$ -ray transitions in  $^{202}\text{Hg}$ . The  $\gamma$ -ray intensities are corrected for relative efficiencies and scaled down to improve readability.

$E_{\text{level}}$ (keV)	$J^\pi$	$E_\gamma$ (keV)	$J_f^\pi$	$I_\gamma$	$A_2/A_0$	$A_4/A_0$	$\delta$	$\pi\lambda$	$B(\pi\lambda) \downarrow^a$	$B(\pi\lambda)_{\text{lit}}^{a,b}$
440	$2_1^+$	440	$0_1^{\text{gs}}$	$1.92(2) \cdot 10^5$	0.012(7)	0.001(10)		E2		17.34(14) [32, 33]
960	$2_2^+$	520	$2_1^+$	853(8)	0.11(1)	0.012(16)	+0.9(1) [109]	M1	0.0042(5)	0.0091(23) [109]
								E2	2.6(3)	5.6(15) [109]
1120	$4_1^+$	960	$0_1^{\text{gs}}$	119(2)				E2	0.037(2)	0.087(21) [32]
1182	$2_3^+$	680	$2_1^{\text{gs}}$	770(8)	0.16(2)	-0.010(28)		E2	23.8(8) <sup>c</sup>	26.5(8) [32, 104]
		222	$2_2^+$	68(3)	0.12(2)	-0.007(22)	-0.13(3)	M1	< 0.17(9)	
								E2	< 12(7)	
		743	$2_1^+$	35(1)	0.21(4)	-0.039(54)	2.1(4)	M1	< 0.0005(2)	
								E2	< 0.7(4)	
1312	$4_2^+$	1182	$0_1^{\text{gs}}$	< 11 <sup>d</sup>				E2	< 0.002	
		352	$2_2^+$	43(2)				E2	89(12)	
		872	$2_1^+$	22(3)				E2	0.48(6)	
1348	$(1^+, 2^+)$	908	$2_1^+$	14(1)				E2		
1390	$2_4^+$	207	$2_1^+$	4(1)				E2		
		430	$2_2^+$	8(1)				E2		
		950	$2_2^+$	26(1)				E2		
		1390	$0_1^{\text{gs}}$	3(1) <sup>d</sup>				E2	210(78)	
1565	$0_3^+$	1125	$2_1^+$	22(1)				E2	11(3)	
1575	$2_5^+$	615	$2_1^+$	5(1)				E2	0.7(2)	
1644	$0_4^+$	1204	$2_1^+$	9(1)				E2	0.011(2)	
1794	$2_7^+$	833	$2_1^+$	6(1)				E2	5.4(4)	
		1354	$2_1^+$	209(3)				E2	15(5)	
								E2	2.4(3)	
								E2	6(5)	
					0.23(2)	-0.028(32)	0.06(4)/1.9(2)	M1	0.16(7)	
1824	$2_8^+$	1794	$0_1^{\text{gs}}$	6(3) <sup>d</sup>				E2	0.1(1)	
		641	$2_3^+$	7(1)				E2	0.12(1)	
								E2	18(8)	

<sup>a</sup>  $B(M1)$  values are given in  $\mu_N^2$ ,  $B(E1)$  values are given in  $\text{mW.u.}$ ,  $B(E2)$ ,  $B(E3)$  and  $B(E4)$  values are given in  $\text{W.u.}$  ( $1 \text{ W.u.}(E1) = 2.22 \text{ e}^2 \text{fm}^2$ ,  $1 \text{ W.u.}(E2) = 70.4 \text{ e}^2 \text{fm}^4$ ,  $1 \text{ W.u.}(E3) = 2.42 \times 10^3 \text{ e}^2 \text{fm}^6$ ,  $1 \text{ W.u.}(E4) = 8.83 \times 10^4 \text{ e}^2 \text{fm}^8$ ).

<sup>b</sup> The values in this column are the ones given within [31], converted to single-particle units.

<sup>c</sup> Assuming pure two-step excitation

<sup>d</sup> Calculated via literature branching ratios.

1966	5 <sup>-</sup> <sub>1</sub>	864	2 <sup>+</sup> <sub>2</sub>	17(1)	E2	10(5)
1966	2 <sup>+</sup> <sub>10</sub>	1384	2 <sup>+</sup> <sub>1</sub>	42(2)	E2	2(1)
		1824	0 <sup>+</sup> <sub>1,gs</sub>	3(1) <sup>d</sup>	E2	0.047(4)
		654	4 <sup>+</sup> <sub>2</sub>	7(1)		
		654	4 <sup>+</sup> <sub>2</sub>	3(1)		
		1527	2 <sup>+</sup> <sub>1</sub>	41(3)	E2	63(30)
1989	6 <sup>+</sup> <sub>1</sub>	869	4 <sup>+</sup> <sub>1</sub>	4(1)	E2	11(1)
2134	? <sub>1</sub>	1013	4 <sup>+</sup> <sub>1</sub>	18(1)		
2293	(3, 4)	1854	2 <sup>+</sup> <sub>1</sub>	23(2)		
2357	3 <sup>-</sup> <sub>1</sub>	1046	4 <sup>+</sup> <sub>1</sub>	19(2)		
		1175	2 <sup>+</sup> <sub>3</sub>	19(2)		
		1397	2 <sup>+</sup> <sub>2</sub>	47(3)		
		1918	2 <sup>+</sup> <sub>2</sub>	63(2)		
		2357	0 <sup>+</sup> <sub>1,gs</sub>		E3	1.7(1)
2456	? <sub>2</sub>	1495	2 <sup>+</sup> <sub>2</sub>	8(3)		
2517	(1, 2)	2517	0 <sup>+</sup> <sub>1,gs</sub>	35(2)		
2682	? <sub>3</sub>	2682	0 <sup>+</sup> <sub>1,gs</sub>	43(3)		
2709	3 <sup>-</sup> <sub>2</sub>	915	2 <sup>+</sup> <sub>2</sub>	24(3)		
		1527	2 <sup>+</sup> <sub>3</sub>	36(2)		
		1749	2 <sup>+</sup> <sub>2</sub>	467(10)		
		2265	2 <sup>+</sup> <sub>1</sub>	117(4)		
		2709	0 <sup>+</sup> <sub>1,gs</sub>		E3	18.5(11)
3166	3 <sup>-</sup> <sub>3</sub>	1980	2 <sup>+</sup> <sub>3</sub>	14(7)	E3	0.70(39)
		3166	0 <sup>+</sup> <sub>1,gs</sub>			

24.9(21) [104]

-0.17(2) 0.048(30)

---

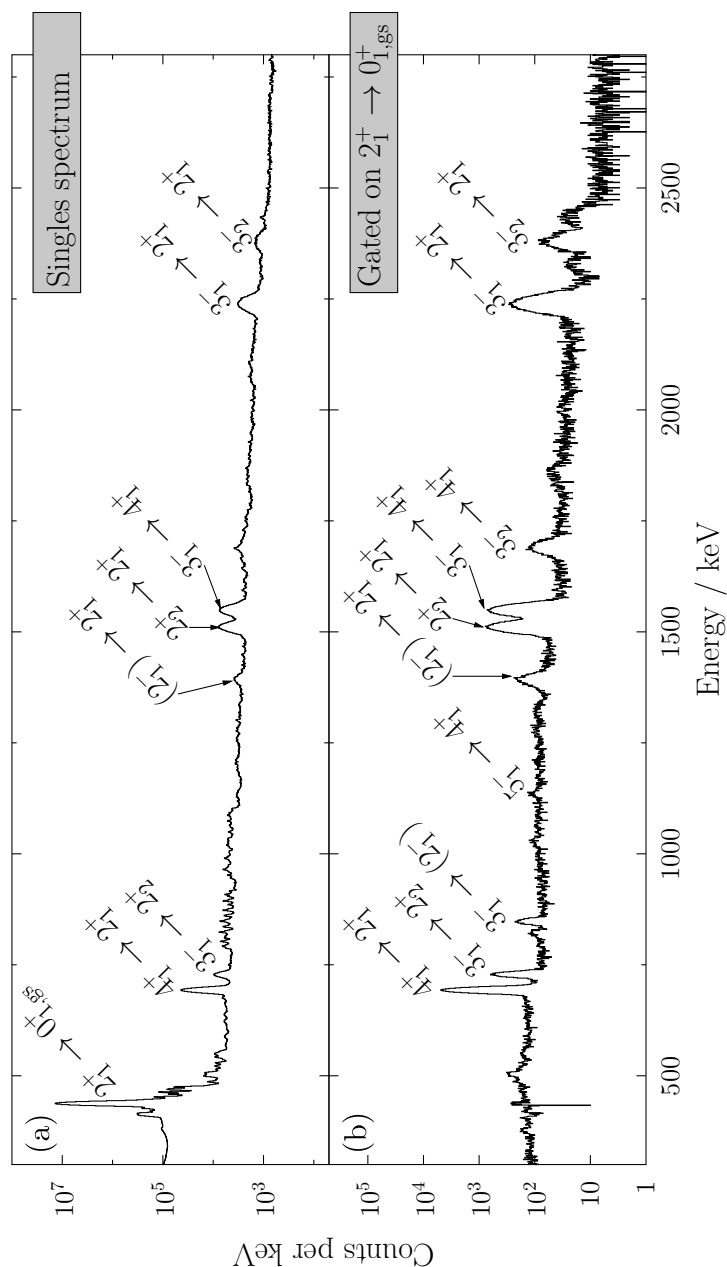
### 5.5.2 $^{204}\text{Hg}$ Analysis

---

In the  $^{204}\text{Hg}$  experiment, a total of  $4.4 \times 10^8$  events of  $\gamma$ -ray fold  $\geq 1$  were collected over a period of 13 h of beam on the  $^{12}\text{C}$  target, corresponding to 6800 counts-per-second. About 1.4% of those events exhibited  $\gamma$  multiplicities  $\geq 2$ , thus qualified for building  $\gamma$ - $\gamma$  matrices. Spectra were corrected for the Doppler shift, adopting a projectile velocity of  $\beta \approx 8.4\%$ . The Doppler corrected, background-subtracted sum spectrum of the  $^{204}\text{Hg}$  experiment, as well as the spectrum of  $\gamma$  rays coincident with the  $2_1^+ \rightarrow 0_{1,\text{gs}}^+$  transition are presented in Figure 5.21. The background subtraction was performed like explained in Section 5.1.3, including correction for *self-coincidences*. Although fewer transition w.r.t. the  $^{202}\text{Hg}$  measurement are present in the data, reconstruction of the level scheme and determination of the experimental yields was as ambitious. The combination of both experimental conditions ( $\gamma$ -ray singles and events of  $\gamma$ -ray multiplicity  $\geq 2$ ) was necessary to improve the level of statistics for this qualitative part of the analysis. The resulting level scheme is shown in Figure 5.19. The spectrum is dominated by 437-keV,  $2_1^+ \rightarrow 0_{1,\text{gs}}^+$ , transition of  $^{204}\text{Hg}$ , which features  $\approx 9.5 \times 10^7$  counts in the Doppler-corrected, background-subtracted spectra, but not corrected for efficiency. The  $^{204}\text{Hg}$  dataset exhibits a similar situation to the one found in the  $^{202}\text{Hg}$  dataset: All strong  $\gamma$  ray transitions, present in the spectra, originate from excited levels of  $^{204}\text{Hg}$  [91, 101–107, 110–117]. Besides the transitions originating from the decay of excited levels of  $^{204}\text{Hg}$ , numerous weak transitions stemming from fusion-evaporation reactions of recoiling target-like nuclei and the walls of the target chamber and the beam pipe populate the spectrum. But they are smeared out by the Doppler correction and, hence, contribute only by an increase of the background level.

The partial level scheme, including solely levels of  $^{204}\text{Hg}$  populated in the experiment analyzed within this work, is shown in Figure 5.22. Few candidates for spin-2 states are populated. The lowest one is the  $2_1^+$  state at 437 keV, which solely decays to the ground state. The literature value  $B(E2; 2_1^+ \rightarrow 0_{1,\text{gs}}^+) = 11.96(9)\text{W.u.}$  [32, 110, 113, 118], together with the known quadrupole moment  $Q = 0.40(20)\text{eb}$  [113], is taken into account for evaluation of the Coulomb-excitation cross-section used for normalization.

The next-to-lowest of this group of states is the level at 1829 keV. For this state, negative parity is favored [118]. It decays exclusively via the 1392-keV,  $(2^-) \rightarrow 2_1^+$  transition, exhibiting a sizable intensity. The next level of this spin-2 group is located at 1852 keV, with demonstrated positive parity, but the tentative spin assignment is ambiguous: The suggested spin is either 2 or 3 [118]. This state decays exclusively to the  $4_1^+$  state, no decay to the  $2_1^+$  state is observed, but the branching



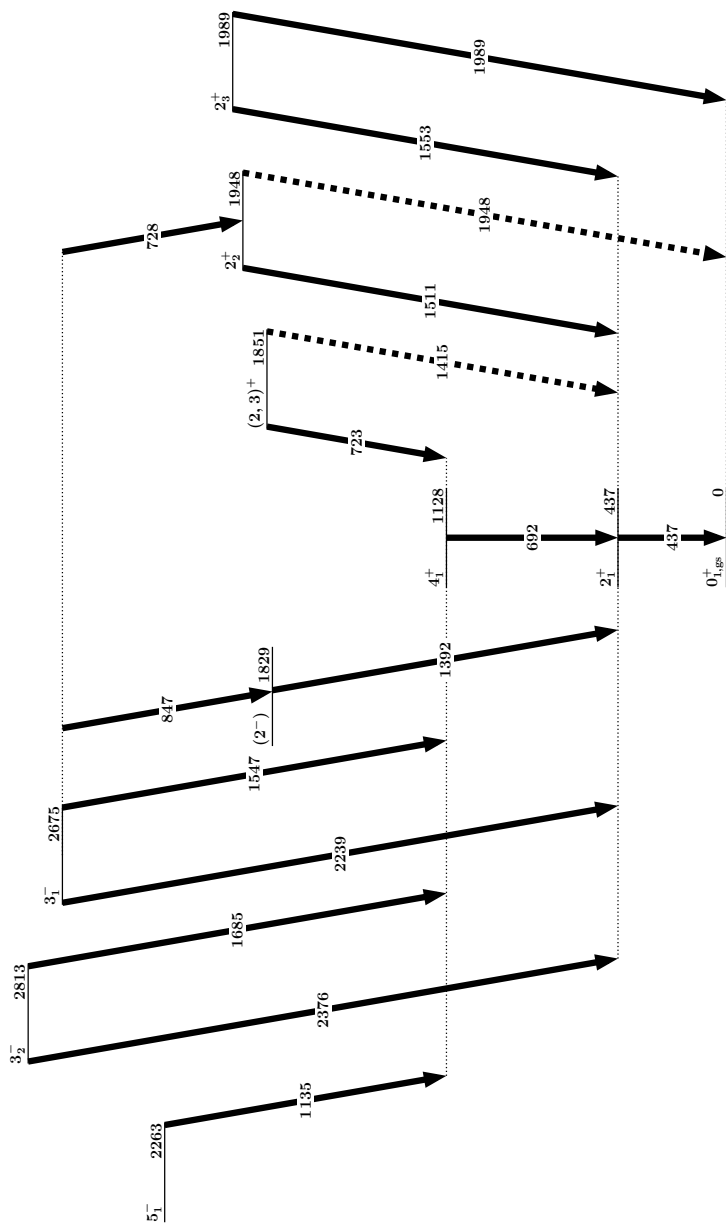


**Figure 5.22.:** The partial experimental level scheme extracted from the  $^{204}\text{Hg}$  dataset, showing levels for which at least one transition is observed. Dashed lines indicate transitions unobserved in this work, but where literature branching ratios exist.

ratio is known [91]. The level of statistics does not permit for an angular distribution analysis of the  $(2^-) \rightarrow 2_1^+$  or the  $(2,3)^+ \rightarrow 2_1^+$  transition, hence, this experiment is not capable of further fixing the spin and/or parity assignments of the  $(2^-)$  and  $(2,3)^+$  states.

From literature, another state of  $J^\pi = (2^+)$  at 1717 keV is known in the literature [102,106]. However, this state was obviously not populated in the experiment presented here, as no 1280-keV,  $(2^+) \rightarrow 2_1^+$   $\gamma$  ray was observed, neither in the single nor in any coincidence spectrum, which is the only decay transition known [118]. Additional levels, fixed in spin and parity to  $2^+$  [118], at 1948 and 1989 keV were populated as well. In contrast to the spin-2 states mentioned before, the assignment of the quantum number is neither tentative nor ambiguous, but several measurements favor the assignment [118]. While the ground-state decay of the 1948-keV level is not observed, the branching ratio is known to be  $I_{2_2^+ \rightarrow 2_1^+} / I_{2_2^+ \rightarrow 0_{1,gs}^+} = 5.3(4)\%$  [91], allowing for determining the intensity of the stretched transition. The level at 1989 keV decays to the  $2_1^+$  as well as to the  $0_{1,gs}^+$  states. Besides the ground-state decays of the 437 and 1989-keV levels, no other ground-state transitions are observed. As the 1948 and 1989-keV levels are the only higher-lying levels with spin and parity quantum numbers unambiguously fixed to  $2^+$ , they are labeled  $2_2^+$  and  $2_3^+$ , accordingly.

Furthermore, two  $3^-$  levels at 2675 and 2813 keV were populated in the experiment. Both decay predominantly to the  $4_1^+$  and  $2_1^+$  levels, while the  $3_1^-$  decays to the  $2_2^+$  and  $(2^-)$  levels, in addition. Furthermore, the population of  $5^-$  level at 2263 keV was observed, which decays exclusively to the  $4_1^+$  state.

The analysis is performed in the same manner, as the one of the  $^{202}\text{Hg}$  dataset (cf. Section 5.3). The relative population of the states excited in the experiment are determined from the measured, efficiency corrected, transition intensities. The low level of statistics, w.r.t. the background level, of some weaker transitions, made it necessary, to estimate some of the intensities from the  $\gamma$ - $\gamma$  matrices. However, this does not cause any side effects, except intensities extracted this way exhibit slightly larger statistical uncertainties, w.r.t. to those determined from the singles spectrum. In the analysis, the quadrupole moment of the  $2_2^+$  level was varied within the limits of the quadrupole moment of the fully-symmetric  $2_1^+$  state, i.e., from 0.20 - 0.60 eb, introducing additional uncertainties of  $\approx 1\%$ .

Angular distribution analyses are also possible for  $^{204}\text{Hg}$ , hence,  $A_2/A_0$  and  $A_4/A_0$  coefficients can be extracted for transitions of sufficient intensity (cf. Figure 5.23). The deduced coefficients are given in Table 5.6. The  $3_1^- \rightarrow 2_1^+$  transition at 2239 keV can serve as a benchmark, exhibiting clear dipole character with negative  $A_2/A_0$  and vanishing  $A_4/A_0$ . The angular distributions of the  $4_1^+ \rightarrow 2_1^+$  and  $2_1^+ \rightarrow 0_{1,gs}^+$  transitions are damped, probably due to the long lifetimes of 4.20(30) and 58.1(4)ps

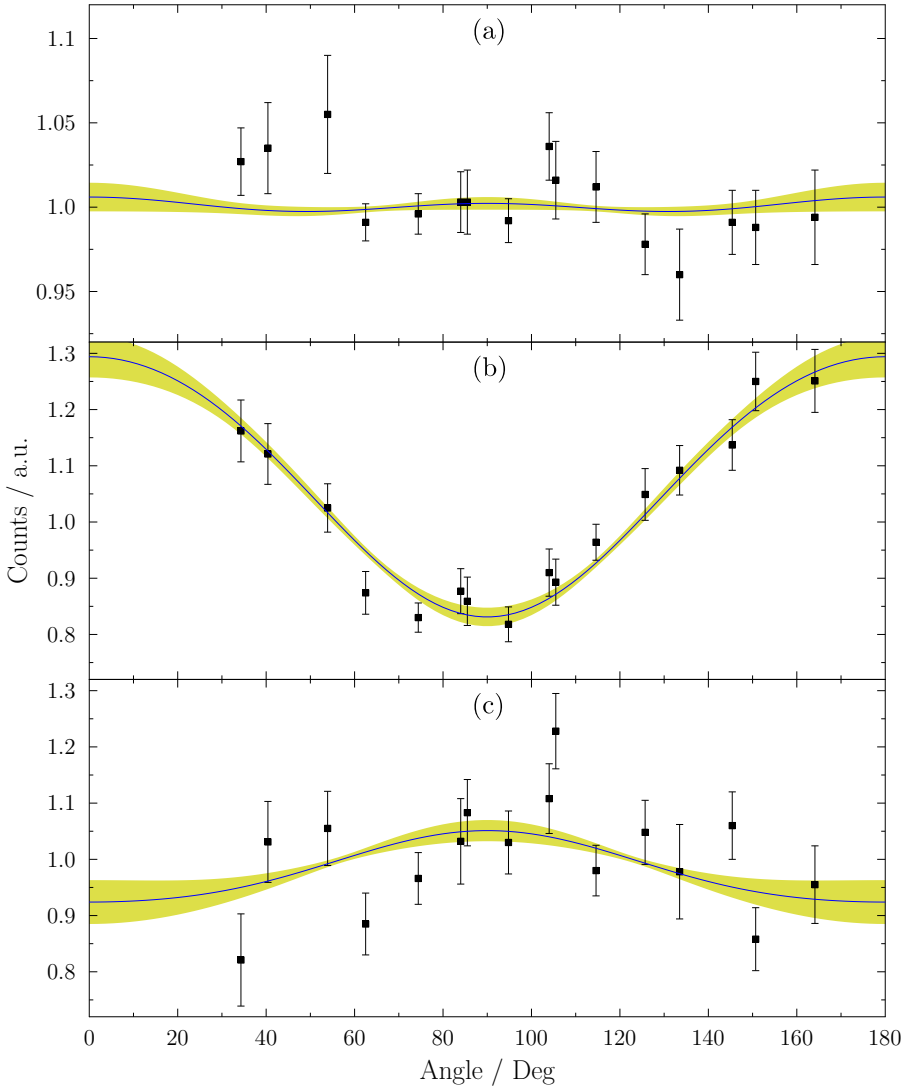


**Figure 5.23.:** Results of the angular distribution analyses of the (a)  $2_1^+ \rightarrow 0_{1,gs}^+$ , (b)  $2_2^+ \rightarrow 2_1^+$ , and (c)  $3_1^- \rightarrow 2_1^+$  transitions of  $^{204}\text{Hg}$ . The colored areas indicate the uncertainties from the fit of Equation (2.59) to the experimental data.



---

of the  $4_1^+$  and  $2_1^+$  states of  $^{204}\text{Hg}$ , respectively (cf. Section 2.3). Nevertheless, extraction of the angular distribution coefficients for the 1392-keV  $(2^-) \rightarrow 2_1^+$  and 1511-keV  $2_2^+ \rightarrow 2_1^+$  transitions is possible (cf. Table 5.6).

However, neither the extracted angular distribution coefficients nor the matrix elements allow for confirming or refusing the tentative spin-parity assignment of the level at 1829 keV. In contrast, the angular distribution coefficients for the 1511-keV transition allow for determination of a multipole-mixing ratio. The ground-state transition is not observed, inducing the same issue reported for the 1354-keV,  $2_7^+ \rightarrow 2_1^+$ , transition of  $^{202}\text{Hg}$ , hence, the same iterative procedure to overcome this is applied, yielding a multipole mixing ratio of  $\delta = 0.26(8)$ , indicating predominant M1 character.

The results retrieved from the Coulomb excitation analysis are consistent with the lifetime of the  $2_2^+$  level retrieved from a DSAM measurement of a  $^{204}\text{Hg}$  beam impinging on a  $^{27}\text{Al}$  target [89, 90]. In addition, the lifetime of the  $3_1^-$  state can be determined. The combination of both measurements, the lifetime of the  $3_1^-$  state, and the branching ratios of the transitions depopulating this particular state, allowed for the extraction of various transition strength. However, as no multipole-mixing ratios for these transitions can be deduced, they are assumed to be of pure electric character with the lowest allowed multipolarity. In this way, the matrix elements for all decay transitions of the  $3_1^-$  state can be estimated.

The analysis of the  $^{204}\text{Hg}$  dataset is also repeated using GOSIA. However, through the course of the analysis issues from the lack of a particle detector in the experiment arise, as GOSIA expects angular ranges given in the laboratory system, but these ranges are depending on the energy loss in the excitation process. It was not possible to achieve consistent results, the M1 strength computed by GOSIA is about twice as large as the one derived in the CLX analysis. The issue of the transformation of the angles renders the result from the GOSIA fit less trustworthy in relation to those retrieved using CLX.

**Table 5.6.:** Measured properties of the levels and  $\gamma$ -ray transitions in  $^{204}\text{Hg}$ . The  $\gamma$ -ray intensities are corrected for relative efficiencies and scaled down to improve readability.

$E_{\text{level}}$ (keV)	$J^\pi$	$E_\gamma$ (keV)	$J_f^\pi$	$I_\gamma$	$A_{2i}/A_0$	$A_4/A_0$	$\delta$	$\tau^a$ (fs)	$\pi\lambda$	$B(\pi\lambda)^{\downarrow bc}$	$B(\pi\lambda)_{\text{lit}}^{cd}$
437	$2_1^+$	437	$0^+$	$1.73(2) \cdot 10^5$	0.000(12)	0.006(18)			E2		11.96(9) [118]
1128	$4_1^+$	692	$2_1^+$	935(13)	0.119(16)	-0.006(23)	E2 <sup>e</sup>		E2	14.9(47)	17.0(13) [104]
		1128	$0^+$						E4		5.5(7) [110]
1829	$(2^-)$	1392	$2_1^+$	97(2)	0.218(53)	0.088(72)					
1851	$(2,3)^+$	723	$4_1^+$	15(2)							
		1415	$2_1^+$	5.8(8) <sup>f</sup>							
1948	$2_2^+$	1511	$2_1^+$	461(9)	0.319(27)	-0.025(38)	0.260(81)	$84.6_{-7.4}^{+14.2}$ [89]	M1	0.200(23)	
		1948	$0^+$	24(2) <sup>f</sup>					E2	1.19(71)	
1989	$2_3^+$	1553	$2_1^+$	88(6)					E2	0.280(21)	
		1989	$0^+$	20(2)			E2 [106]		E2	1.55(38)	
2263	$5^-$	1135	$4_1^+$	29(2)					E2	0.099(24)	
2675	$3_1^-$	728	$2_1^+$	111(3)							
		847	$(2^-)$	38(2)				232(30) [89]	E1	0.413(56)	
		1547	$4_1^+$	375(11)	0.072(26)	-0.006(37)			E2	5.10(72)	
		2239	$2_1^+$	324(15)	-0.091(36)	0.015(54)			E1	0.145(19)	
		2675	$0^+$	< 1.1					E1	0.0412(56)	
2813	$3_2^-$	1685	$4_1^+$	85(4)					E3	20.5(17)	23(2) [118]
		2376	$2_1^+$	80(4)							
		2813	$0^+$	< 9.3					E3	5.14(40)	8.03(92) [110]

<sup>a</sup> Extracted via DSAM analysis.

<sup>b</sup> Extracted via Coulomb excitation analysis in the present experiment.

<sup>c</sup>  $B(M1)$  values are given in  $\mu_N^2$ ,  $B(E1)$  values are given in  $\text{mW.u.}$ ,  $B(E2)$ ,  $B(E3)$  and  $B(E4)$  values are given in  $\text{W.u.}$  ( $1 \text{ W.u.}(E1) = 2.23 \text{ e}^2 \text{fm}^2$ ,  $1 \text{ W.u.}(E2) = 71.3 \text{ e}^2 \text{fm}^4$ ,  $1 \text{ W.u.}(E3) = 2.47 \times 10^3 \text{ e}^2 \text{fm}^6$ ,  $1 \text{ W.u.}(E4) = 9.06 \times 10^4 \text{ e}^2 \text{fm}^8$ ).

<sup>d</sup> The values in this column are the ones given within [118], converted to single-particle units.

<sup>e</sup> Treated as a pure-E2 transition. The angular distribution is washed out because of deorientation effects.

<sup>f</sup> Calculated via literature branching ratios.

---

## 6 Discussion

The results presented in Chapter 5 are to be compared to several theoretical models. The impact of the subshell closure on the  $N = 80$  isotones is investigated by the evolution of the  $B(E2; 2_1^+ \rightarrow 0_{1,gs}^+)$  values towards  $^{142}_{60}\text{Sm}$ .

Furthermore, some levels of  $^{202,204}\text{Hg}$  are candidates for fragments of their  $2_{1,ms}^+$  states. The levels are investigated in terms of their ability to exhibit sizable M1 decay strength, and, in the case of  $^{204}\text{Hg}$ , are compared to theoretical calculations.

---

### 6.1 Shell Stabilization in the $N = 80$ Isotones

---

The campaign at ISOLDE to investigate the  $N = 80$  isotones beyond the subshell closure at  $^{138}_{58}\text{Ce}$  was motivated by the finding of the *lack of shell stabilization* [12] arising at  $^{138}_{58}\text{Ce}$ . This manifests in the change from a single, isolated one quadrupole-phonon mixed-symmetry state (MSS) [119] to the fragmentation of the  $2_{1,ms}^+$  state over several  $2^+$  levels with reduced total strength, indicated by the distribution of the M1 transition strength. In  $^{132}\text{Te}$  [16],  $^{134}\text{Xe}$  [13] and  $^{136}\text{Ba}$  [120], single isolated  $2_{1,ms}^+$  states have been found. This can be motivated by the fact, that excitations to the not completely filled  $\pi(g_{7/2})$  subshell are possible and favored in energy. However, in  $^{138}\text{Ce}$  the  $2_2^+$ ,  $2_3^+$ ,  $2_4^+$ ,  $2_5^+$  and  $2_6^+$  levels exhibit sizable M1 components in the decay to the  $2_1^+$  state. Hence, the  $2_{1,ms}^+$  state mixes with nearby fully-symmetric  $2^+$  states (FSS), distributing the M1 strength among several  $2^+$  levels. This requires promotion of the protons from the completely filled  $\pi(g_{7/2})$  subshell to the completely unfilled  $\pi(d_{5/2})$  subshell [12]. The situation is illustrated in Figure 6.1.

From this finding, the question arises whether the underlying mechanism, resulting in the *lack of shell stabilization*, also affects the quadrupole collectivity of the fully-symmetric states. This question is further investigated by surveying the  $N = 80$  isotones with  $Z > 58$ , i.e.,  $^{140}\text{Nd}$  and  $^{142}\text{Sm}$ . In these isotones, the  $\pi(d_{5/2})$  subshell is partially filled, exposing a similar situation to the one found in the  $N = 80$  isotones with  $Z < 58$ : Promotion of protons towards partially filled subshells are possible again. When taking a look at the evolution of the  $B(E2; 2_1^+ \rightarrow 0_{1,gs}^+)$  values along the  $N = 80$  isotonic chain, a reduced growth of the  $B(E2)$  value when approaching the  $Z = 58$  subshell closure is apparent. Recent investigations [121]

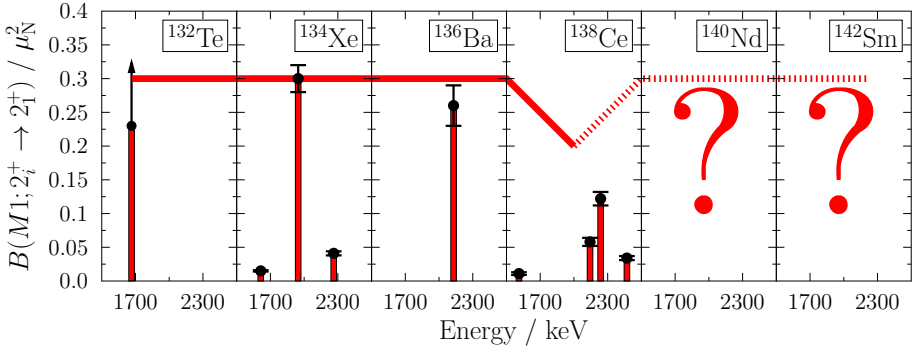


**Figure 6.1.:** Evolution of the  $B(M1; 2_i^+ \rightarrow 2_1^+)$  strength in the  $N = 80$  isotones. The isotones  $^{132}\text{Te}$  [16],  $^{134}\text{Xe}$  [13] and  $^{136}\text{Ba}$  [120] exhibit concentration of the M1 strength in the decay of one particular state, each, while in  $^{138}\text{Ce}$  [12] the  $2_{1,\text{ms}}^+$  state is fragmented among several  $2^+$  levels. Up to now it is not clear, how the evolution continues in  $^{140}\text{Nd}$  and  $^{142}\text{Sm}$ .

of  $^{140}\text{Nd}$  show a clear deviation of the  $B(E2; 2_1^+ \rightarrow 0_{1,\text{gs}})$  strength of  $^{138}\text{Ce}$  from the collective trend, which is continued [121] in  $^{140}\text{Nd}$ . The result obtained in this work for  $^{142}\text{Sm}$  confirms the restoration of the collective trend.

The *lack of shell stabilization* when approaching the  $\pi(g_{7/2})$  subshell closure is not reflected by basic properties, like the energy of the  $2_1^+$  state or the  $R_{4/2}$  ratio: Both exhibit a smooth trend. The  $2_1^+$  energy is slowly decreasing, like it is expected when going from near doubly-magic nuclei to the midshell region for protons. The  $R_{4/2}$  ratio, however, indicates a smooth evolution from spherical to near-spherical, vibrational behavior, showing a nearly constant ratio from  $Z = 56$  on. In a phenomenological approach, the energy of the  $2_1^+$  state and the  $B(E2; 2_1^+ \rightarrow 0_{1,\text{gs}}^+)$  strength can be correlated via Grodzin's rule [122]:

$$E(2_1^+)[\text{keV}] \cdot B(E2; 0_{1,\text{gs}}^+ \rightarrow 2_1^+)[\text{e}^2\text{b}^2] = 2.57 \cdot Z^2 \cdot A^{-2/3} \cdot [1.288 - 0.088 \cdot (N - \bar{N})], \quad (6.1)$$

where  $\bar{N}$  is the number of neutrons in an isobaric chain, for which the nuclear mass reaches its minimum. The uncertainty of the resulting reduced E2 transitions strengths accounts for about 30%. Grodzin's rule predicts a smooth trend for the evolution, but the large uncertainties cover the most of the  $B(E2)$  values found in the  $N = 80$  isotonic chain. However, when taking only a look at the mean values, Grodzin's rule is not able to reproduce the small increase in the  $B(E2)$  from 19.3(2) W.u. in  $^{136}\text{Ba}$  [120] to 21.2(14) W.u. in  $^{138}\text{Ce}$  [83, 123] and the steep rise

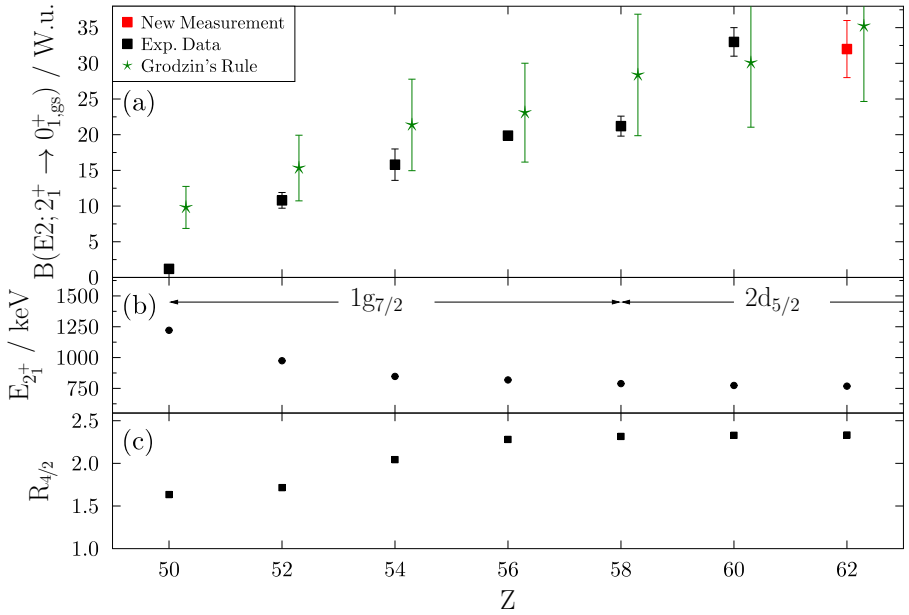


**Figure 6.2.:** (a) Evolution of the  $B(E2; 2_1^+ \rightarrow 0_{1,gs}^+)$  values in the  $N = 80$  isotonic chain. The measured values exhibit a reduced growth when approaching the  $Z = 58$  subshell closure, and a steep increase afterwards. The empiric Grodzin's rule is not capable of reproducing this trend, but instead predicts a smooth evolution. The experimental values are, nevertheless, covered by the large uncertainties. (b) Evolution of the energy of the  $2_1^+$  state. The *lack of shell stabilization* is not reflected in these values. (c) Evolution of the  $R_{4/2} = E_{4_1^+}/E_{2_1^+}$  values, showing a smooth changeover from spherical to near-spherical, vibrational behavior. There is no impact of the *lack of shell stabilization* observable.

from  $^{138}\text{Ce}$  towards 33 (2) W.u. in  $^{140}\text{Nd}$  [121] (cf. Figure 6.2).

State-of-the-art microscopic calculations may provide an insight into the underlying mechanism. For this reason, calculations in the quasiparticle-phonon model (QPM) and the large-scale shell-model (LSSM) were carried out.

In the QPM approach, a microscopic multiphonon basis is constructed from phonons generated in quasiparticle-random-phase approximation (QRPA) and used

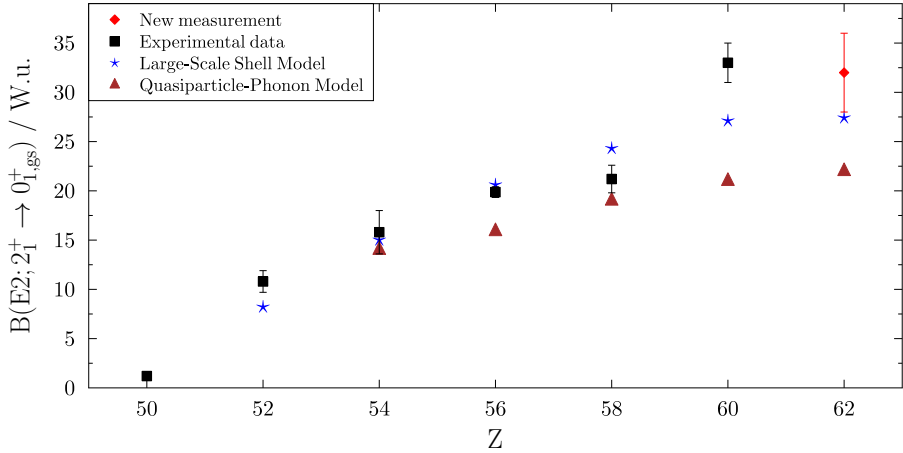


**Figure 6.3.:** Evolution of the  $B(E2; 2_1^+ \rightarrow 0_1^{gs+})$  values in the  $N = 80$  isotonic chain. Between  $Z = 50$  and  $Z = 62$  the proton  $1g_{7/2}$  and  $2d_{5/2}$  orbitals are consecutively filled. The experimental values are taken from [16, 83, 121, 123, 127–129]. The values are shown in comparison to calculations performed with the Large-Scale Shell Model and Quasiparticle-Phonon Model. Both feature a smooth trend, not resembling the steep rise towards  $^{140}\text{Nd}$  and  $^{142}\text{Sm}$ .

to treat a Hamiltonian of separable form [48]. The QPM is capable of describing anharmonic features of collective modes as well as multiphonon excitations. For the calculations performed for  $N = 80$  isotones, the set of parameters used for the Wood Saxon potential was adopted to fit the single-particle energy spectra of  $A = 141$  nuclei, on average. The set of parameters was first used to investigate  $^{136}\text{Ba}$  [124], with increased energy difference of the  $\pi(g_{7/2})$  and  $\pi(d_{5/2})$  orbitals. The strength of the quadrupole-quadrupole interaction was determined from excitation energies and E2 decay transition strength of  $2^+$  states. The nature of the QPM allows for covering a large model space resulting in effective charges close to the bare values, which were chosen to  $e_\pi = 1.05$  and  $e_\nu = 0.05$ . A spin-gyromagnetic quenching factor  $g_s = 0.8$  was also employed. The value calculated for  $^{142}\text{Sm}$  is  $B(E2; 2_1^+ \rightarrow 0_1^{gs+}) = 22 \text{ W.u.}$  [125, 126].

The large-scale shell model (LSSM) is based on the conventional shell model (cf. Section 3.2), but usage of the  $m$  scheme in combination with a recently developed iterative algorithm allows for consideration of large model spaces, compared to other shell model approaches. The calculations include the shells

$\{2d_{5/2}, 1g_{7/2}, 2d_{3/2}, 3s_{1/2}, 1h_{11/2}\}$  for protons and neutrons relative to a  $^{132}_{50}\text{Sn}_{82}$  core. Protons are treated as valence particles, while neutrons are considered as holes with regard to the core. One and two body properties are modeled using a renormalized G-Matrix derived from the CD-Bonn potential [130]. Effective charges  $e_\pi = 1.6$  and  $e_\nu = 0.7$  as well as a spin-gyromagnetic quenching factor  $g_s = 0.5$  are applied. Levels of  $^{135}\text{Xe}$  are used to fix neutron single-hole energies, while proton single-particle energies are fixed from the spectra of  $^{108}\text{Sn}$  and  $^{133}\text{Xe}$  [37]. The value calculated for  $^{142}\text{Sm}$  is  $B(E2; 2_1^+ \rightarrow 0_{1,gs}^+) = 27.4 \text{ W.u.}$  [131, 132]. The results of QPM and the LSSM calculations, besides measured values, are shown in Figure 6.3. Both models are able to reproduce the transition strength of  $^{130}\text{Sn}$ ,  $^{132}\text{Te}$  and  $^{134}\text{Xe}$ , but both cannot resemble the reduced growth towards the  $g_{7/2}$  subshell closure. While the LSSM matches the experimental E2 transition strength of  $^{136}\text{Ba}$ , it is underestimated by the QPM. However, the deviation is rather small and does not alter the power of the statements of the QPM, if only comparing the  $N = 80$  isotones up to  $Z = 56$ . The situation for  $^{138}\text{Ce}$  is somehow reversed, as the QPM matches the E2 strength, while it is overestimated by the LSSM. Nevertheless, both models fail to reproduced the steep rise in E2 strength when exceeding the  $Z = 58$  subshell closure, as both models considerably underestimate the  $B(E2)$  of  $^{140}\text{Nd}$ . When approaching  $^{142}\text{Sm}$ , the situation somehow settles in the case of the LSSM, but this is also due to the experimental uncertainties. Both models predict a smooth trend, whereas evolution of the experimental values quite significantly deviates from such a course. LSSM and QPM seem to not be able to reproduce the underlying mechanism modifying the quadrupole transition strength.

Inspecting the evolution of the E2 strength in the  $N = 80$  isotones, a linear trend in superposition with an additional, subshell specific, modification is apparent. The  $N_\pi N_\nu$  scaling [133] can give a hint for the general trend between the major shells.  $N_\pi$  and  $N_\nu$  are the number of valence protons and neutrons, respectively, and  $N_\pi$  and  $N_\nu$  are counted relative to the respective next major shell closure, independent whether this counts valence particles or holes. The  $N_\pi N_\nu$  scaling emerges from residual proton-neutron interaction, if it dominates the pairing interaction. Integration of the residual proton-neutron interaction results in the simple proportionality of the total strength approximately to  $N_\pi \cdot N_\nu$ , albeit the interaction differs for different pairs of protons and neutrons. This scheme can be applied in even-even nuclei with  $P = \frac{N_\pi \cdot N_\nu}{N_\pi + N_\nu} \lesssim 5$ . In  $N = 80$  isotones, two neutron holes are constantly existent ( $N_\nu = 2$ ). Thus, the only parameter varying is the number of protons, which increases in steps of two when advancing in valence-proton number from  $^{130}\text{Sn}$  ( $N_\pi = 2, 4, 6, \dots$ ). Most valence nucleons exist in  $^{142}\text{Sm}$  with  $N_\nu = 2$  and  $N_\pi = 14$ , resulting in  $P = 1.75$ , thus the scheme is applicable. The result is a linear dependence of the transition strength on the product of the num-

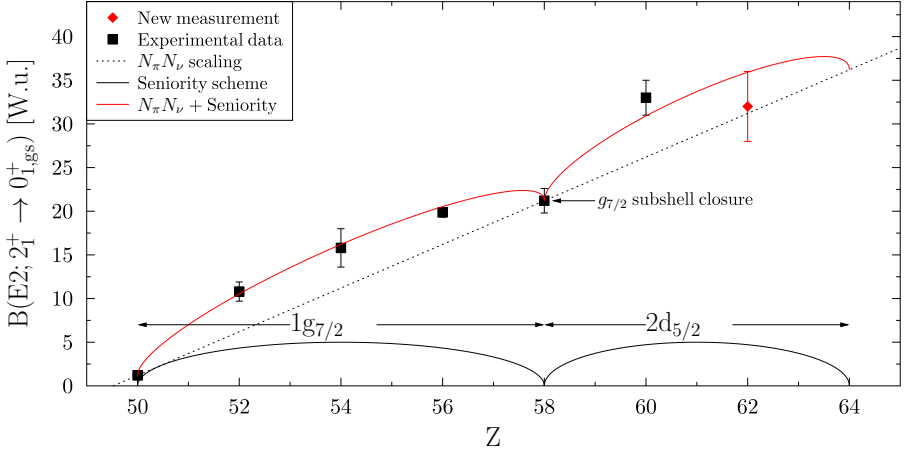


**Figure 6.4.:** Evolution of the  $B(E2; 2_1^+ \rightarrow 0_1^+)$  values in the  $N = 80$  isotonic chain. Between  $Z = 50$  and  $Z = 62$  the proton  $1g_{7/2}$  and  $2d_{5/2}$  orbitals are consecutively filled. The experimental data are taken from [16, 83, 121, 123, 127–129]. A linear  $N_\pi N_\nu$  dependence (dashed) and an extreme shell model case (solid) are indicated schematically.

ber of valence nucleons, depicted as a dashed line in Figure 6.4. Although the measured points are not completely matched, the general trend is resembled. The  $N_\pi N_\nu$  scaling is matched to the E2 strengths of  $^{130}\text{Sn}$  and  $^{138}\text{Ce}$ . All other transition strengths, besides  $^{142}\text{Sm}$ , are underestimated. However, it is obvious, that this is an effect related to the filling of the subshell, as the deviation seems to scale to the filling of the subshell, again without distinction of particles and holes.

A candidate concept for describing the subshell behavior might be the seniority scheme. In this scheme, all particles in the ground state of an even-even nucleus are coupled to 0, described by the seniority of this state of  $\nu = 0$ . The  $2_1^+$  state is formed by breaking a pair of like nucleons, which couples to  $J = 2$ , while all other pairs are still coupled to  $J = 0$ , giving it a seniority of  $\nu = 2$ . The number of pairs available to break increases with increasing number of valence nucleons. This allows for a description of the resulting E2 strength approximately by  $\sqrt{f(1-f)}$  [133], where  $f$  is the fractional filling of the subshell. For the  $2_1^+ \rightarrow 0_{1,gs}^+$  transitions this relation is depicted as solid, black lines in Figure 6.4. The combination of the integrated residual proton-neutron interaction and the seniority scheme, shown as solid, red line in Figure 6.4, reproduce the evolution of the E2 strength between  $^{130}\text{Sn}$  and  $^{142}\text{Sm}$  quite well. Yet, the situation is not as satisfactory, when



proceeding towards the  $Z = 64$  subshell closure. The superposition of both effects is not exactly capable of describing the steep rise of the  $B(E2)$  value from  $^{138}\text{Ce}$  to  $^{140}\text{Nd}$ . Either the seniority interaction is scaled to match the sudden jump towards  $^{140}\text{Nd}$ , but then the strength of  $^{142}\text{Sm}$  is a little bit overestimated, or the E2 strength of  $^{142}\text{Sm}$  is matched, but then the one of  $^{140}\text{Nd}$  is a little bit underestimated. Either way, it is not exactly capable of reproducing the steep rise and the following plateau when advancing from  $^{138}\text{Ce}$  on. Still, the superposition of  $N_\pi N_\nu$  scaling and the seniority scheme allows for conceptually resembling the E2 strength in the  $N = 80$  isotones, for which the  $g_{7/2}$  subshell is the highest valence orbital in the ground state.

At least, there is a qualitative agreement with the hypotheses, that the general trend of quadrupole collective properties is modulated by the underlying subshell structure. However, Both microscopic models are solely able to reproduce the general trend, but are not able to account for the observed modulation. This makes further experimental and theoretical efforts on the understanding of the microscopic structure necessary.

---

## 6.2 Mixed-Symmetry States of $^{202,204}\text{Hg}$

---

The experimental campaign for the investigation of  $^{202,204}\text{Hg}$  was motivated by the search for one-quadrupole-phonon mixed-symmetry states, *i.e.*, the  $2^+_{1,ms}$  state, in the region about doubly-magic  $^{208}\text{Pb}$ . This collective excitation emerges in the framework of the Interacting Boson Model-2. The wave function of this particular state is, unlike the wave function of low-lying collective states, like the fully-symmetric one-quadrupole-phonon  $2^+_1$  state, not symmetric under the exchange of proton and neutron labels. It was demonstrated [134], that these phonon excitations are the fundamental building blocks of nuclear structure in vibrational nuclei. Unique experimental signature of such a configuration is an enhanced M1 strength of the  $2^+_{1,ms} \rightarrow 2^+_1$  transition, with matrix elements in the order of about  $1 \mu_N$ . The E2 component of that transition, on the contrary, is suppressed, to the order of  $\approx 1 \text{ W.u.}$  The  $2^+_{1,ms} \rightarrow 0^+_{1,gs}$  transition exhibits low collectivity in the order of tens of a W.u. to few W.u. [44].

In addition, E1 transition rates from the decay of the one-octupole-phonon fully-symmetric state to the one-quadrupole-phonon mixed-symmetric state are enhanced w.r.t. the E1 transition rates between the one-octupole-phonon and the one-quadrupole-phonon fully-symmetric states. This is caused by the predominant *F-vector* character of the dipole transition operators [135] in the *sdf*-IBM-2 [47].

$2^+_{1,ms}$  states are the lowest states of mixed-symmetric character in vibrational nuclei. Therefore, the most pronounced examples of these states are found in the proxim-

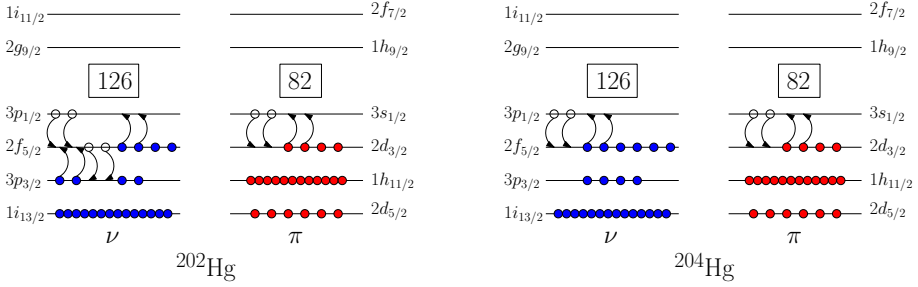


**Figure 6.5.:** Valence orbital configuration of  $^{202}\text{Hg}$  (left) and  $^{204}\text{Hg}$  (right). The sequence of the orbitals for the neutrons is deduced from the ground-state spin-parity configurations of the even-odd Pb isotopes and for the protons from the ground and excited states of odd-even At, Bi, Tl and Au isotopes and predictions of the independent particle model. The excitations of the valence neutron and proton boson holes to  $d$  and  $f$  orbitals, exhibiting non-vanishing angular momentum, sizable M1 strength can be expected.

ity of doubly-magic nuclei. The textbook example of such a state is the  $2^+_{1,\text{ms}}$  state of  $^{94}\text{Mo}$  with  $B(M1; 2^+_{1,\text{ms}} \rightarrow 2^+_1) = 0.56(5) \mu_N^2$  [9, 136], with one valence neutron boson and one valence proton boson relative to magic  $^{90}\text{Zr}$ . The  $A \approx 90$  region was intensively explored and featured additional nuclei exhibiting mixed-symmetric excitations, e.g.,  $^{96}\text{Ru}$  [10] and  $^{92}\text{Zr}$  [11]. The identification of the  $2^+_{1,\text{ms}}$  state of  $^{96}\text{Ru}$  was also the first one to employ projectile Coulomb excitation for this purpose. Furthermore, several examples of MSSs have been identified in the mass  $A \approx 130$  region, e.g., in the  $N = 80$  isotones, as outlined in Section 6.1. The identification of isovector valence shell excitations of  $^{132}\text{Te}$  [16] and  $^{138}\text{Ce}$  [12] made also use of the same technique. More examples of MSSs are found in the Barium isotopic chain, e.g., in  $^{130}\text{Ba}$  [76] or  $^{136}\text{Ba}$  [120].

In the vicinity of doubly-magic  $^{208}\text{Pb}$ , still two years ago, there was no MSS discovered. Only recently a single low-lying isovector state has been identified in  $^{212}_{84}\text{Po}_{128}$  [137], a nucleus with two valence protons and two valence neutrons with respect to  $^{208}\text{Pb}$ . The region shall be investigated further, starting with the particle-hole mirror of  $^{212}\text{Po}$  relative to  $^{208}\text{Pb}$ , i.e.,  $^{204}\text{Hg}$ . In order to resolve whether this feature is unique to  $^{212}\text{Po}$  or to nuclei exhibiting one valence boson of each kind, only, or whether isovector valence excitations are a general feature in the proximity of doubly-magic  $^{208}\text{Pb}$ ,  $^{202}\text{Hg}$  is included in the investigation. From all the information on MSSs gathered, pronounced one-phonon MSSs can be expected when

protons and neutrons occupy orbitals with high angular momenta. However, the angular momenta defined by the valence structure are smaller w.r.t. those of  $^{212}\text{Po}$ . Nevertheless, MSSs can be expected to occur, but with smaller M1 strength. The valence configuration of the Hg isotopes, together with possible excitations, are shown in Figure 6.5.

---

### 6.2.1 $^{204}\text{Hg}$

---

$^{204}\text{Hg}$  is presented first, because it has a simpler valence space structure. It exhibits two valence-proton and two valence-neutron holes with respect to  $^{208}\text{Pb}$ , leading to domination of the low-lying excitations by a  $\pi(2d_{3/2})^{-2} \nu(2f_{5/2})^{-2}$  valence structure. The  $R_{4/2} = 2.58$  [118] suggests a vibrational character of the nucleus, corresponding to the regime of the  $U(5)$  dynamical symmetry of the  $sd$ -IBM-2 [4] with anharmonicities. In the  $U(5)$  limit for nuclei of vibrational character, the M1 transition strength can be deduced from [44]

$$B(M1; 2_{1,\text{ms}}^+ \rightarrow 2_1^+) = \frac{3}{4\pi} (g_\pi - g_\nu)^2 \frac{6}{(N_\pi + N_\nu)^2} N_\pi N_\nu. \quad (6.2)$$

The difference of the boson  $g$ -factors  $g_\pi - g_\nu$  can be assumed to be about  $1 \mu_N$ . For  $^{204}\text{Hg}$ , the number of proton bosons  $N_\pi$  and the number of neutron bosons  $N_\nu$  are both unity, resulting in a  $B(M1)$  value of  $\approx 0.36 \mu_N^2$ , given this nucleus would exhibit strict  $U(5)$  dynamical symmetry. This value gives a suitable estimate for the M1 strength to expect for  $^{204}\text{Hg}$ .

Although the orbital momenta are smaller in comparison to  $^{212}\text{Po}$ , the absolute transition strength  $B(M1; 2_2^+ \rightarrow 2_1^+) = 0.200(23) \mu_N^2$  is measured, which is substantially larger than the expected  $10^{-2} \mu_N^2$  for transitions between FSSs. This allows to consider the  $2_2^+$  level at 1948 keV at least a fragment of the  $2_{1,\text{ms}}^+$  state. The weakly-collective transition strength  $B(E2; 2_2^+ \rightarrow 0_{1,\text{gs}}^+) = 0.28(2) \text{ W.u.}$  supports this conclusion.

The result for the M1 strength in the decay of the MSS of  $^{204}\text{Hg}$  is similar to the situation in the  $A \approx 90$  and  $A \approx 130$  mass regions, where transition matrix elements of single isolated MSS of the order of  $1 \mu_N^2$  were found. The M1 strength in the decay of the  $2_2^+$  level of  $^{204}\text{Hg}$  holds about one third of the strength of  $^{94}\text{Mo}$ . The M1 strength exceeds even the transition strength  $B(M1; 2_2^+ \rightarrow 2_1^+) = 0.126(16) \mu_N^2$  of  $^{212}\text{Po}$  [137], although the suggested valence shell configurations of protons and neutrons exhibit larger angular momenta for which the contributions to orbital M1 transition strength is expected to be larger.

The combination of DSAM lifetime values [89, 90] and branching ratios, deduced

from the Coulomb excitation measurements, allow for determining E1 transition strengths, to which Coulomb excitation measurements alone are not sensitive. This provides another mean in the investigation of the  $2_2^+$  level. The  $B(E1; 3_1^- \rightarrow 2_2^+) = 0.41(6)$  mW.u. is ten times larger than the  $B(E1; 3_1^- \rightarrow 2_1^+) = 0.041(6)$  mW.u. From the predominant isovector character of the dipole transition operator and the enhancement of the E1 transition strength, together with the suppression of the isoscalar transition to the FSS, underlines the isovector character of the  $2_2^+$  level of  $^{204}\text{Hg}$ . The ratio of the E1 transition strength of the decay from the isoscalar one-octupole-phonon fully-symmetric state to the isovector one-quadrupole-phonon mixed-symmetric state to the E1 transition rate between isoscalar octupole and quadrupole fully-symmetric states of 10 is similar to the ratios of these transition strengths found in  $^{92}\text{Zr}$  and  $^{94}\text{Mo}$  [44], which feature distinct isovector valence excitations.

In order to back this finding, microscopic calculations using the QPM [48] have been performed. The approach is similar to the one used in the  $N = 80$  isotones (cf. Section 6.1). The effective charges and the spin-gyromagnetic factor are the same, i.e.,  $e_\pi = 1.05$ ,  $e_\nu = 0.05$  and  $g_s = 0.8$ . The strength of the quadrupole-quadrupole and octupole-octupole interaction are chosen according to the properties of the  $2_1^+$  and  $3_1^-$  states, respectively [48, 138]. The *RPA* states generated in the calculations can be analyzed regarding their symmetric or mixed-symmetric structure by their response to isovector/-scalar external fields, e.g., using the quantity [139]

$$B(2^+) = \frac{|\langle 2^+ || \sum_k r_k^2 Y_{2\mu}(\Omega k) - \sum_k r_k^2 Y_{2\mu}(\Omega k) || g.s. \rangle|^2}{|\langle 2^+ || \sum_k r_k^2 Y_{2\mu}(\Omega k) + \sum_k r_k^2 Y_{2\mu}(\Omega k) || g.s. \rangle|^2}. \quad (6.3)$$

This ratio is sensitive to the isoscalar ( $B(2^+) < 1$ ) or isovector ( $B(2^+) > 1$ ) character of the state under investigation. The value of  $B(2^+)$  for the lowest-lying  $[2_1^+]_{\text{RPA}}$  state is 0.016, indicating nearly pure isoscalar structure of the state. For the  $[2_2^+]_{\text{RPA}}$ , in contrast, the value is 1.06, and, hence, 60 times larger, hinting at an isovector character of the *RPA* state.

The results of the calculation are presented in Table 6.1, together with either the experimental values deduced within this work, or, where this is not available, with literature values. This is, for example, the case for the  $B(E4; 4_1^+ \rightarrow 0_{1,gs}^+)$  strength, which was measured in  $(e, e')$  measurements, because this decay path is strongly suppressed in  $\gamma$ -decays. The structure of the  $2_1^+$  state consists predominantly of the  $[2_1^+]_{\text{RPA}}$ , which is of isoscalar nature, whereas the main component of the  $2_2^+$  level is the  $[2_2^+]_{\text{RPA}}$ , which is of isovector character. The isovector nature of the  $[2_2^+]_{\text{RPA}}$ , and, hence, of the  $2_2^+$  level is highlighted by the large  $B(M1; [2_2^+]_{\text{RPA}} \rightarrow [2_1^+]_{\text{RPA}})$  of  $0.48 \mu_N^2$ .

The QPM calculations describe the data quite well. The excitation energies of

**Table 6.1.:** Results of QPM calculations for  $^{204}\text{Hg}$  and comparison to experimental and literature values.

$E_{\text{level}}$ QPM	(keV) Exp.	$J^\pi$	Structure	$J_f^\pi$	$\pi\lambda$	QPM	$B(\pi\lambda) \downarrow^a$ Exp.
581	436	$2_1^+$	$69\%[2_1^+]_{RPA} + 14\%[2_1^+ \times 2_1^+]_{RPA}$	$0^+$	$E2$	8.6	11.96(9) [118]
1078	1128	$4_1^+$	$59\%[2_1^+ \times 2_1^+]_{RPA}$	$2_1^+$	$E2$	16	14.9(47)
				$0^+$	$E4$	1.2	5.5(7) [110]
1751	1948	$2_2^+$	$79\%[2_2^+]_{RPA}$	$2_1^+$	$M1$	0.26	0.20(2)
					$E2$	1.3	1.2(7)
				$0^+$	$E2$	1.7	0.28(2)
2099	1989	$2_3^+$	$96\%[2_3^+]_{RPA}$	$2_1^+$	$M1$	0.004	0
					$E2$	0.15	1.55(38)
				$0^+$	$E2$	0.13	0.099(24)
2771	2675	$3_1^-$	$87\%[3_1^-]_{RPA}$	$2_2^+$	$E1$	$2 \times 10^{-3}$	$0.41(6) \times 10^{-3}$
				$4_1^+$	$E1$	$0.06 \times 10^{-3}$	$0.15(2) \times 10^{-3}$
				$2_1^+$	$E1$	$1 \times 10^{-3}$	$0.041(6) \times 10^{-3}$
				$0^+$	$E3$	28	20.5(17)

<sup>a</sup>  $B(M1)$  values are given in  $\mu_N^2$ ,  $B(E\lambda)$  values in W.u. (1 W.u.(E1) =  $2.23 \text{ e}^2 \text{ fm}^2$ , 1 W.u.(E2) =  $71.3 \text{ e}^2 \text{ fm}^4$ , 1 W.u.(E3) =  $2.47 \times 10^3 \text{ e}^2 \text{ fm}^6$ , 1 W.u.(E4) =  $9.06 \times 10^4 \text{ e}^2 \text{ fm}^8$ ).

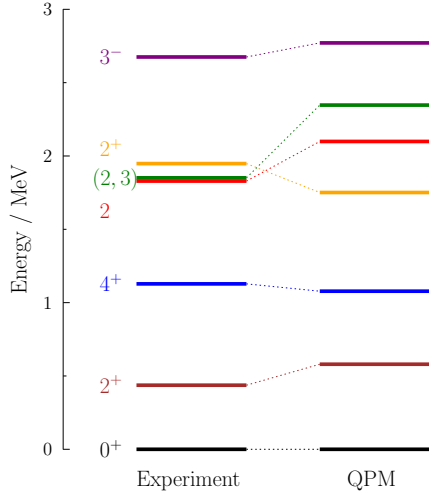


**Figure 6.6.:** The partial experimental level scheme of the states included in the QPM calculations, next to the states calculated using the QPM.

the  $2_1^+$ ,  $4_1^+$  and  $3_1^-$  levels are in agreement to the ones determined experimentally (cf. Fig 6.6). The calculated  $B(E2; 2_1^+ \rightarrow 0_{1,gs}^+)$  of 8.6 W.u. is in satisfactory agreement with the literature value of 11.96(9) W.u. [118], which is used for normalization in the Coulomb excitation analysis. Hence, the analysis does not provide a new independent  $B(E2)$  value for the  $2_1^+ \rightarrow 0_{1,gs}^+$  transition. This is of course a general deficiency of such relative measurements, but the value is deduced from several experiments, where it was confirmed [118]. In addition, both, the analysis performed within this work as well as the QPM calculation, yield E3 strengths similar to the literature value: While the adopted literature value is  $B(E3; 3_1^- \rightarrow 0_{1,gs}^+) = 23(2)$  W.u., the value extracted within this work is 21(2) W.u., and the QPM value is 28 W.u.. This underlines the validity of the calculations and the Coulomb excitation analysis. In addition, the experimental results and the QPM calculations match the literature  $B(E2; 4_1^+ \rightarrow 2_1^+)$  value of 17.0(13) W.u. [104, 113, 118]. The value deduced within this work is 14.9(47) W.u., which mean value is a bit lower w.r.t. the literature value, but with a larger uncertainty. This might appear strange to the reader, but the literature value does not take the  $B(E4; 4_1^+ \rightarrow 0_{1,gs}^+) = 5.5(7)$  W.u. [110] into account. The E4 transition lowers the E2 strength, but it also generates a  $0_{1,gs}^+ \rightarrow 4_1^+ \rightarrow 2_1^+ \rightarrow 0_{1,gs}^+$  loop, which increases the uncertainty of the measured E2 transition strength, due

to the unknown signs of the matrix elements.

The calculated E1 transition strengths are small but differ from the experimental ones, as the QPM results strongly depend on the numerous components weakly contributing to the structure of the  $2_1^+$  and  $3_1^-$  states. The collectivity of these states makes it impossible to separate the main components contributing to the E1 transitions. However, the QPM confirms the measured ratio of E1 strength, although by a smaller ratio of 2 only. Besides the comparison in Table 6.1, a graphical comparison, to the experimental and the literature values, is depicted in Figure 6.7. The agreement of the QPM results with experimental and literature values, underlines its predictive power even in mass regions where it is applied for the first time for the description of MSSs.

From the experimental level of statistics, it is not possible to exclude that weaker fragments of the  $2_{1,ms}^+$  state exist. Only another  $2^+$  level is present in the spectra, which level of statistics is not sufficient for an angular distribution analysis. Fortunately, it was shown before that its decay is of pure E2 character [106]. Nevertheless, weak fragments might be present, although not visible in the spectra, e.g., due to the background level. However, the QPM predicts higher-lying excited  $2^+$  levels and is capable of providing M1 transition strength. Overall, it predicts negligible M1 transition strengths for almost all  $2_i^+ \rightarrow 2_1^+$ , with the sole exception being the  $2_2^+ \rightarrow 2_1^+$  transition for which  $B(M1) = 0.26 \mu_N^2$  is calculated. This closely resembles the experimentally deduced M1 transition strength of  $0.20(2) \mu_N^2$ . The overall good agreement between the QPM calculations, the literature values and the values deduced in the Coulomb excitation analysis allows for concluding, that the  $2_2^+$  level is not only a fragment of the  $2_{1,ms}^+$  state, but at least the main fragment, if not even a single, isolated MSSs.

---

### 6.2.2 $^{202}\text{Hg}$

---

The analysis of the  $^{202}\text{Hg}$  dataset is similar to the one of the  $^{204}\text{Hg}$  and so is the discussion. The nucleus  $^{202}\text{Hg}$  exhibits a larger variety of possible valence excitations, caused by its two valence proton-holes and four valence neutron-holes. Low-lying nuclear structure can be formed from excitations of the holes to  $\pi(2d_{3/2})^{-2} \nu(2f_{5/2})^{-2}(3p_{3/2})^{-2}$  orbitals. This nucleus features  $R_{4/2} = 2.55$  [31], which is even a bit less compared to  $^{204}\text{Hg}$ , suggesting vibrational character. The M1 transition strength in the  $U(5)$  dynamical symmetry limit of the  $sd$ -IBM-2 [4] yields for this nucleus exhibiting one proton-hole boson ( $N_\pi = 1$ ) and two neutron-hole bosons ( $N_\nu = 2$ ) a reduced M1 transition strength of  $0.32 \mu_N^2$ , which is similar to the result of  $^{204}\text{Hg}$ .  $E_{2_1^+} = 439.512(8)\text{keV}$  and  $E_{4_1^+} = 1119.84(10)\text{keV}$  of  $^{202}\text{Hg}$  [31] are also close to  $E_{2_1^+} = 436.552(8)\text{keV}$  and  $E_{4_1^+} = 1128.13(11)\text{keV}$  of

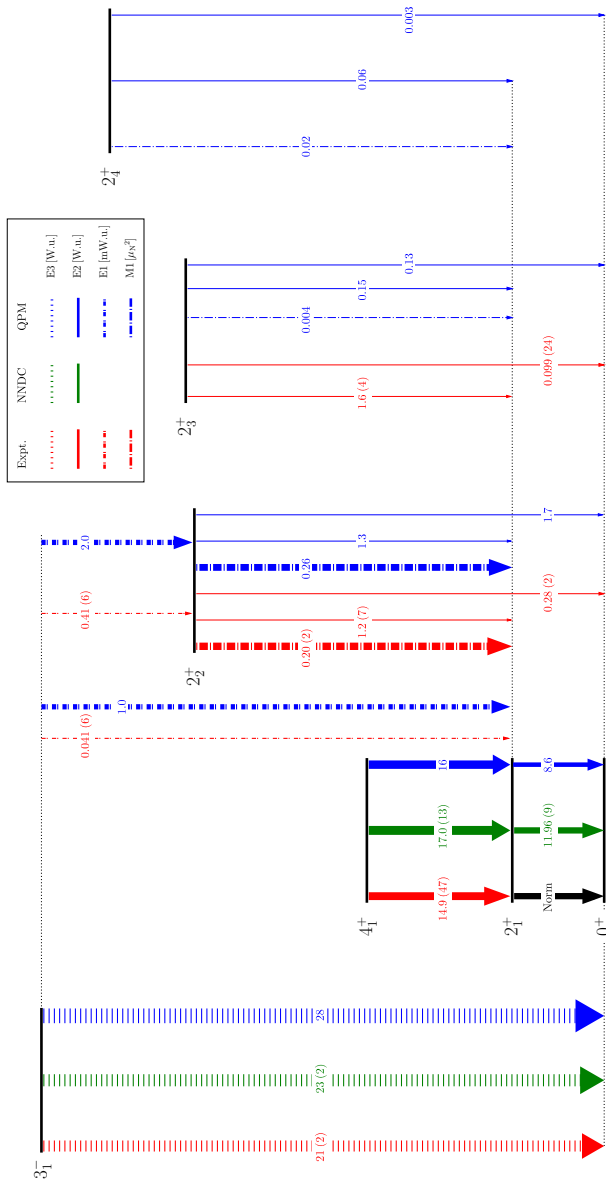


**Figure 6.7.:** Comparison of the result of the  $^{204}\text{Hg}$  analysis with the literature values and the results of a QPM calculation. The width of the arrows, indicating  $\gamma$  ray transitions, is scaled to the respective transition strength, for each transition character and multipolarity separate. From the experiment it can be concluded, that the  $2_2^+$  level is at least the dominant fragment of the  $2_{1,ms}^+$  state. The QPM calculations further support this assumption and allow for extending it, due to the small M1 decay strength of the other  $2^+$  levels, labeling the  $2_2^+$  level an single, isolated mixed-symmetry state. This is further backed by the one order larger E1 strength in the decay of the  $3_1^-$  state to the  $2_2^+$  level w.r.t. the decay to the  $2_1^+$  state.



$^{204}\text{Hg}$  [118]. This information allows to expect a similar situation in  $^{202}\text{Hg}$  like the one found in  $^{204}\text{Hg}$ . The additional neutron-hole boson does not seem to influence the energies of the one and two quadrupole-phonon fully-symmetric states, *i.e.*, the  $2_1^+$  and  $4_1^+$  states.

Nevertheless, more higher-lying  $2^+$  levels of  $^{202}\text{Hg}$  are excited during the Coulomb-excitation reactions, namely the  $2_{2,3,4,5,7,8,10}$  levels, each a possible fragment of the  $2_{1,\text{ms}}^+$  state. The  $2_2^+$  level at 960 keV is not a fragment of the  $2_{1,\text{ms}}^+$  state, due to its relative long lifetime of 20(4)ps, which is too long for a pronounced M1 decay. Besides this first indicator, the complete set of E2 and M1 transition strengths is already known, featuring  $B(M1; 2_2^+ \rightarrow 2_1^+) = 9.1(23) \text{ m}\mu_N^2$  and a E2 strength of the same transition in the order of 6 W.u. This rules out, that the  $2_2^+$  level is a fragment of the  $2_{1,\text{ms}}^+$ . However, in the analysis, the transition strengths retrieved are in good qualitative agreement with the literature values [109], although they are about a factor of 2 too small. The situation is a bit relaxed in the  $4_1^+ \rightarrow 2_1^+$  transition: The literature value of 26.5(8) W.u. [31, 32, 104] is resembled by the value retrieved within this work of 23.8(8) W.u. It has to be noted, that the  $B(E4; 4_1^+ \rightarrow 0_{1,\text{gs}}^+)$  value of  $^{202}\text{Hg}$  was never measured, hence, the  $4_1^+$  level is assumed to be excited exclusively via two-step excitation. The matches of the literature values and the values extracted within this work allows for investigating the manifold of  $2^+$  levels excited during the scattering process, for (at least fragments of) the one quadrupole-phonon mixed-symmetry state.

The next candidate for a fragment of the  $2_{1,\text{ms}}^+$  state is the  $2_3^+$  level at 1182 keV. The ground-state decay of this level is neither observed nor is its branching ratio, besides an upper limit, known, allowing only for limits of the decay strengths. The multipole-mixing ratio  $\delta = 2.1(4)$  indicates predominant quadrupole character of the  $2_3^+ \rightarrow 2_1^+$  transition, and consequently the upper limit of the reduced M1 strength is  $5(2) \text{ m}\mu_N^2$ , in the extreme case of a vanishing stretched transition, too low to be a fragment of the  $2_{1,\text{ms}}^+$  state. In addition, the decay intensity to the fully-symmetric  $2_1^+$  state holds only about half the intensity of the decay to the  $2_2^+$  level, suggesting that the  $2_2^+$  and  $2_3^+$  levels belong to a differing nuclear structure configuration. This is further underlined, as the decay to the  $2_2^+$  level holds remarkable  $B(M1; 2_3^+ \rightarrow 2_2^+) < 0.17(9) \mu_N^2$ , together with an upper limit of the E2 strength of 12(7) W.u. for the same transition.

The  $2_4^+$  level at 1390 keV might be a possible candidate for a fragment of the MSS, indicated by its intense transition to the  $2_1^+$  state, in comparison to the other decay transitions of this state, and a known branching ratio for the stretched transition [31]. However, the level of statistics does not permit for an angular distribution analysis, but even in the extreme case, where  $\delta = 0.01$  is assumed, the analysis yields a reduced M1 strength of  $3 \text{ m}\mu_N^2$  at maximum. So, also this level can be

ruled out to be a fragment of the MSS. The  $2_5^+$  level at 1575 keV does not decay to the  $2_1^+$  state at all, but exclusively to the  $2_2^+$  level.

The  $2_8^+$  level at 1824 keV exhibits similar properties like the  $2_4^+$  level, *e.g.*, an intense decay to the  $2_1^+$  state and a known branching ratio for the ground-state decay. Both, the  $2_4^+$  and the  $2_8^+$  level, hold sizable transition intensities in the decay to the  $2_2^+$  level, about one half to one third of the transition to the  $2_1^+$ . This condition may be a hint towards a structure, which is different to that of a MSS or a fragment of it. Nevertheless, the M1 strength is probed with a multipole-mixing ratio of 0.01, leading to a maximum M1 strength of  $0.02 \mu_N^2$ . The  $2_{10}^+$  level at 1966 keV does neither feature a measured ground-state transition nor a known branching ratio. In addition, the level of statistics is not sufficient to perform an angular distribution analysis. However, the intensity of the decay to the  $2_1^+$  state is similar to the one of the  $2_8^+ \rightarrow 2_1^+$  transition, for which reason, the quantities of the  $2_8^+$  level are assumed, resulting in similar M1 transition strengths.

The most promising candidate for a fragment of the  $2_{1,ms}^+$  state is the  $2_7^+$  level at 1794 keV. Although the stretched transition is not observed, its intensity can be derived by using the known branching ratio [31]. In addition, the level of statistics is sufficient to perform an angular distribution analysis, which yields E2/M1 multipole-mixing ratios of 0.06(4) or 1.9(4). The former is statistically the favored solution, while the latter cannot be completely ruled out, but it is only compatible with a  $2\sigma$  uncertainty of the angular distribution coefficients. However, in the case of the latter, this level is also not a fragment of the MSS, hence, the  $2_{1,ms}^+$  state of  $^{202}\text{Hg}$  will be located above the excitation limit for this experiment of about 3 MeV. On the other hand,  $\delta = 0.06(4)$  indicates a predominant dipole character of the  $2_7^+ \rightarrow 2_1^+$  transition, resulting in an enhanced M1 component of  $B(M1; 2_7^+ \rightarrow 2_1^+) = 0.16(7) \mu_N^2$ , which is about the same size as the M1 transition strength found in  $^{204}\text{Hg}$ , and a suppressed E2 component of  $B(E2) = 0.1(1) \text{W.u.}$  Favoring the smaller mixing ratio is further supported by the transition from the  $3_2^-$  level to the  $2_7^+$  level. In contrast to  $^{204}\text{Hg}$ , lifetime information on the  $3_2^-$  level is not available, hence, the E1 transition strength cannot be derived. Nevertheless, it is possible to deduce the ratio of the E1 matrix elements from the measured  $I_{3_2^- \rightarrow 2_7^+} / I_{3_2^- \rightarrow 2_1^+} = 0.21(3)$  to

$$R_{E1} = \frac{I_{3_2^- \rightarrow 2_7^+}}{I_{3_2^- \rightarrow 2_1^+}} \left( \frac{E_{3_2^- \rightarrow 2_1^+}}{E_{3_2^- \rightarrow 2_7^+}} \right)^3 = 3.11(40). \quad (6.4)$$

This is comparable to the ratio found in  $^{92}\text{Zr}$  for its  $2_{1,ms}^+$  state [136]. The knowledge about the isovector character of the E1 transition operator further supports the assignment of a predominant isovector character to the  $2_7^+$  level, rendering this

level at least a fragment of the  $2_{1,\text{ms}}^+$  state.

From systematics the assignment of the E2/M1 multipole-mixing ratio of the  $2_7^+ \rightarrow 2_1^+$  transition of 0.06(4) is further backed. The additional neutron-hole boson does not qualitatively alter the excitation energies of the low-energy  $2_1^+ = Q_s \left| 0_{1,\text{gs}}^+ \right\rangle$  and  $4_1^+ = [Q_s Q_s]^{(4)} \left| 0_{1,\text{gs}}^+ \right\rangle$ , although the  $B(E2; 4_1^+ \rightarrow 2_1^+)$  and  $B(E2; 2_1^+ \rightarrow 0_{1,\text{gs}}^+)$  values are increased by a factor of  $\approx 1.5$  w.r.t.  $^{204}\text{Hg}$ . From this, the MSS ought to be located in the same energy regime like the MSS of  $^{204}\text{Hg}$ , which main fragment is located at 1948 keV, rendering the  $2_7^+$  level at 1794 keV of  $^{202}\text{Hg}$  a suitable candidate.

In conclusion, the good agreement of the literature values and the values retrieved in the Coulomb excitation analysis within this work, allows for concluding, that with the  $2_7^+$  at least a major fragment of the  $2_{1,\text{ms}}^+$  state of  $^{202}\text{Hg}$  is identified.

---

### 6.2.3 Mixed-Symmetry States in the Proximity of $^{208}\text{Pb}$

---

The M1 strengths of  $B(M1; 2_7^+ \rightarrow 2_1^+) = 0.16(7) \mu_N^2$  of  $^{202}\text{Hg}$  and  $B(M1; 2_2^+ \rightarrow 2_1^+) = 0.200(23) \mu_N^2$  of  $^{204}\text{Hg}$  allow for expanding the map of fragments of MSSs found in the region around doubly-magic  $^{208}\text{Pb}$  further towards the side of boson holes. Ultimately, fragments of MSSs are identified in few boson systems, on the side of particles and of holes only. An overview is shown in Figure 6.8. Combinations of particles of one kind and holes of the other, *i.e.*, proton particles and neutron holes, *e.g.*, in  $^{208}\text{Po}$ , or proton holes and neutron particles, *e.g.*, in  $^{208}\text{Hg}$ , have not been investigated, yet, due to the experimental challenges related to their production. However, the situation is similar to the one found around  $^{90}\text{Zr}$ , where lots of distinct mixed-symmetry states have been identified. The results from this work further show the applicability of the *Interacting Boson Model* in this region of heavy nuclei.

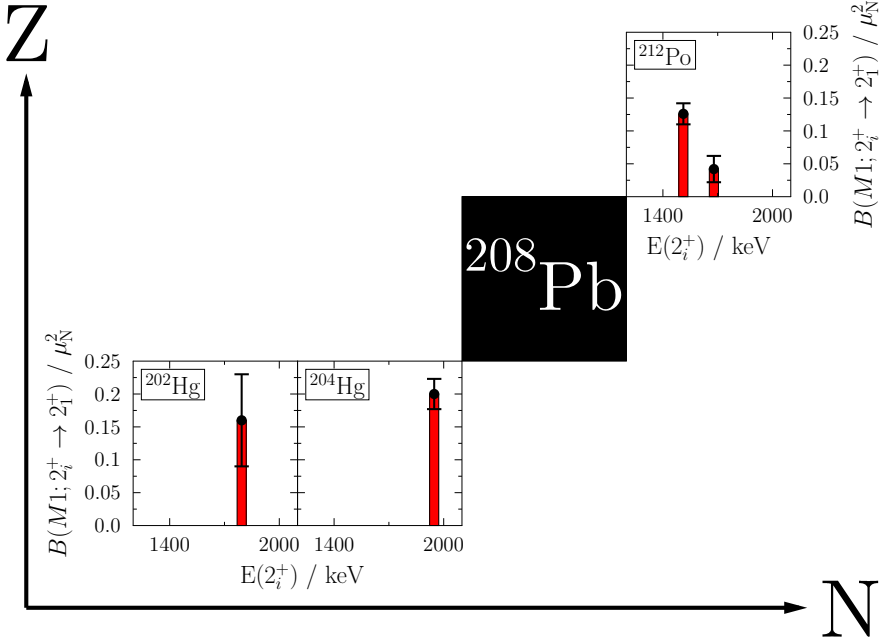


**Figure 6.8.:** Overview over the current status of the investigation of mixed-symmetry states via M1 strengths in the vicinity of the doubly-magic nucleus  $^{208}\text{Pb}$ . The M1 strengths of  $^{212}\text{Po}$  are taken from [137], while the M1 strengths of the Hg isotopes are derived within this work.

---

## 7 Summary and Outlook

In this work, data taken in two different experimental campaigns utilizing projectile Coulomb-excitation reactions are presented. The analysis of the datasets as well as their results are presented and discussed. The power of projectile-Coulomb excitation for the investigation of quadrupole collectivity is demonstrated. Highly selective excitation of quadrupole and octupole levels renders this method an ideal tool in the search for one quadrupole-phonon mixed-symmetry states, which are expected to occur in near-spherical, vibrational nuclei.

Both steps of the identification process are presented within this work: Determination of the E2 transition strength of the transition between the one quadrupole-phonon fully-symmetric  $2_1^+$  state and the  $0_{1,gs}^+$  ground state, as well as the extraction of a full set of matrix elements and the resulting identification of the one quadrupole-phonon mixed-symmetric  $2_{1,ms}^+$  state.

The first step was demonstrated for  $^{142}\text{Sm}$ , where projectile Coulomb-excitation cross sections, normalized to  $^{48}\text{Ti}$  and  $^{94}\text{Mo}$  excitation cross sections, are employed to determine

$$B(E2; 2_1^+ \rightarrow 0_{1,gs}^+) = 32(4) \text{ W.u.}$$

The second step, the identification of the  $2_{1,ms}^+$  state is demonstrated, using the literature value of the  $B(E2; 2_1^+ \rightarrow 0_{1,gs}^+)$ , for  $^{202,204}\text{Hg}$  scattered off a  $^{12}\text{C}$  target. The high statistics of the experiment, in combination with the selectivity of the method, allows for measurement of angular distributions and  $\gamma$  ray intensities, enabling to extract multipole-mixing ratios and full sets of matrix elements. Hence, the  $2_{1,ms}^+$  state is identified in each Hg isotope, and the M1 transition strengths are determined to be

$$\begin{aligned} ^{202}\text{Hg} : \quad & B(M1; 2_7^+ \rightarrow 2_1^+) = 0.16(7) \mu_N^2 \\ ^{204}\text{Hg} : \quad & B(M1; 2_2^+ \rightarrow 2_1^+) = 0.20(2) \mu_N^2. \end{aligned}$$

The ability to perform both steps is a premise in order to continue the investigation of the *shell stabilization* in the  $N = 80$  isotones, which next steps are the identification of the  $2_{1,ms}^+$  states in the radioactive nuclei  $^{140}\text{Nd}$  and  $^{142}\text{Sm}$ . Within this work, the power of the designated experimental method of projectile Coulomb excitation for the investigation of quadrupole collectivity is proven.

---

The method is not restricted to the  $N = 80$  isotones, but on the contrary the eligibility of this method for the mass  $A \approx 208$  region is highlighted by the results of this work. Additionally, the results underline the applicability of concepts of the algebraic *IBM-2* in heavy nuclei, justified by microscopic *QPM* calculations. Hence, the door for surveying this particular region of the nuclear chart with regard to isovector valence-shell excitations is opened.

# A CLX Input

The listing A.1 shows a CLX input file for the analysis of  $^{204}\text{Hg}$ . It features a subset of states, taking only the  $0_{1,gs}^+$ ,  $2_1^+$ ,  $2_{1,ms}^+$  and  $3_1^-$  states into account. The input file is divided into three sections:

- The first part are switches to control CLX as well as different parameters of the experiment. **Carefully pay attention**, as between different versions of CLX the declaration of projectile, respective target excitation, are different!
- The second block gives the states which are to be considered in the calculation. Information to give includes level energy, spin and parity.
- The last part consists of matrix elements connecting the states declared in the second block. Besides the indices of initial and final state, the matrix element (including sign) and the character of the transition have to be given.

**Listing A.1:** CLX input for analyzing a subset of states of  $^{204}\text{Hg}$

```
1 204Hg -> C @890 MeV
2 11101111
3 4      3      2.
4 0.      0.      0.
5 6      204
6 80      12
7 828.
8 0.00001 180. 5
9
10
11 1 0 0.0      1 0
12 2 2 0.437    1 0
13 3 2 1.948    1 0
14 4 3 2.675    -1 0
15
16
17 1      1      0.0      2
18
19 1      2      0.653    2
20 2      2      -0.53    2
21
22 1      3      0.09986 2
23 2      3      -0.206168      2
24 2      3      -0.998621      -1
25 3      3      -0.53      2
26
27 1      4      0.59513 3
28 2      4      1.0e-04 1
29 3      4      1.0e-04 1
```





---

## B GOSIA Input

GOSIA is able to perform fit of the matrix elements to given transition intensities, resulting in a much more extensive input. The normalization is performed onto a selected state of the same nucleus. Here is again shown the input for analyzing a subset of states of  $^{204}\text{Hg}$ . There are much more options and switches w.r.t. the CLX input, for details refer to [22]. GOSIA calculations need several runs of GOSIA, using different executive options. The input can be coarsely divided into several sections:

- OP, FILE Declaration of several files for temporary storage of results
- OP, TITL The title of the experiment
- OP, GOSI Here the nuclear levels are given, as well as the matrix elements, beam energy, and the angular range in the center-of-mass frame to cover. This section ends with a control section containing several switches to manipulate calculations and output.
- OP, GDET Arrangement and properties of the  $\gamma$ -ray detectors have to be given here.
- OP, YIEL This section covers details of the arrangement of the intensities in the yield files. Also at this point, a possible subdivision by scattering angles of projectile or target can be conducted. At the end of this section, literature values for matrix elements and branching ratios can be given, which will be considered in the matrix element's fit.
- OP, INTI The integration over energy and angles is done here. The angles have to be given in the laboratory frame of reference, at which the user can chose either particle or target detection, and the respective angles.
- OP, MINI Controls the least-squares fit of the matrix elements.

A sample file containing intensities is given Listing B.1, while a sample input file controlling a full GOSIA analysis is presented in Listing B.2. When comparing to the CLX input, beware that the GOSIA input covers a larger subset of states.

### Listing B.1: Yield input for GOSIA for analyzing $^{204}\text{Hg}$

```

1 1, 1, 80, 204, 890, 14, 1.0
2 2, 1, 13411900., 159500.
3 3, 2, 92179., 1305.
4 4, 2, 10282., 218.
5 5, 3, 1512., 178.
6 6, 2, 46231., 913.
7 7, 3, 3034., 218.
8 8, 1, 50., 49.
9 8, 2, 33510., 1537.
10 8, 3, 46231., 969.
11 8, 4, 4049., 154.
12 8, 6, 10592., 229.
13 9, 1, 50., 49.
14 9, 2, 8245., 453.
15 9, 3, 9268., 344.

```

### Listing B.2: GOSIA input for analyzing a subset of states of $^{204}\text{Hg}$

```

1 OP, FILE
2 22,3,1
3 204Hg_subset.out
4 25,3,1
5 204Hg_subset.inp
6 3,3,1
7 204Hg_cor_subset.yld
8 4,3,1
9 204Hg_subset.cor
10 7,3,1
11 204Hg_subset.map
12 8,3,1
13 204Hg_subset.raw
14 9,3,1
15 204Hg_subset.gdt
16 12,3,1
17 204Hg_subset.bst
18 15,3,1
19 204Hg_subset.err
20 29,3,1
21 conv.icc
22 11,3,2
23 crf.dat
24 23,3,1
25 204Hg_op_subset.raw
26 13,3,1
27 cnor.dat
28 99,3,1
29 204Hg_subset.amp
30 0,0,0
31 OP, TITL
32 Projectile excitation of reaction 204Hg -> 12C
33 OP, GOSI
34 LEVE
35 1 1 0.0 0.0
36 2 1 2.0 0.4366
37 3 1 4.0 1.1282
38 4 1 2.0 1.8287
39 5 1 2.0 1.8513
40 6 1 2.0 1.9477
41 7 -1 5.0 2.263
42 8 -1 3.0 2.6753
43 9 -1 3.0 2.8128
44 0 0 0 0
45 ME
46 1 0 0 0 0
47 2 8 0.11 -3.0 3.0

```

---

```

48 2 9 0.1 -3.0 3.0
49 3 7 0.1 -3.0 3.0
50 3 8 0.3 -3.0 3.0
51 3 9 0.2 -3.0 3.0
52 4 8 0.2 -3.0 3.0
53 6 8 0.43 -3.0 3.0
54 2 0 0 0 0
55 1 2 0.653 0.643 0.663
56 1 5 0.01 1e-05 3.0
57 1 6 0.3 0.001 3.0
58 2 2 0.53 -0.77 1.83
59 2 3 1.044 0.854 1.234
60 2 4 1.16 -3.0 3.0
61 2 5 0.07 -3.0 3.0
62 2 6 -0.16 -1.5 1.5
63 3 5 0.6 -3.0 3.0
64 3 0 0 0 0
65 1 8 0.63 0.53 1.1
66 1 9 0.373 0.268 0.478
67 5 0 0 0 0
68 1 7 0.202 0.092 0.312
69 7 0 0 0 0
70 2 6 0.5 0.001 5.0
71 0 0 0 0 0
72 EXPT
73 1 80 204
74 -6, 12, 828., -1.8, 6, 1, 0, 0.0, 360.0, 0, 1
75 CONT
76 INT,1.
77 1,1000
78 SPL,1.
79 PRT,
80 1,1
81 2,1
82 3,1
83 4,-2
84 5,1
85 6,1
86 7,1
87 8,1
88 10,1
89 11,1
90 12,1
91 13,1
92 14,1
93 15,1
94 16,1
95 17,3
96 18,1
97 19,1
98 20,1
99 0,0
100 END,
101
102 OP, BRIC
103 /home/robert/GOSIA/BrIccFOV22.idx
104 /home/robert/GOSIA/BrIccFOV22.icc
105
106 OP, GDET
107 1
108 0.01, 3.5, 8.4, 24.97
109 0, 0, 0, 0, 0, 0, 0
110
111 OP, YIEL
112 1
113 -1,-1
114 0.01
115 1

```

```

116| 1
117| 90
118| 90
119| 2,1
120| 1
121| 1000
122| 1.0
123| 4 13, NTAP
124| 3, 1
125| 6, 1, 6, 2, 0.053, 0.0043
126| 5, 2, 5, 3, 0.393, 0.0168
127| 5, 1, 5, 3, 0.012, 0.012
128| 0, 0
129| 1, 1
130| 6, 2, 0.5, 0.05
131| 6, 1
132| 2, 1, 2, 0.653, 0.002
133| 2, 2, 2, 0.53, 0.26
134| 2, 2, 3, 1.044, 0.038
135| 3, 1, 8, 0.63, 0.02
136| 3, 1, 9, 0.373, 0.021
137| 5, 1, 7, 0.202, 0.022
138|
139| OP,INTI
140| 15, 24, 768.2, 890.2, 0.01, 84.1
141| 900., 890., 880., 870., 860., 850., 840., 830., 820., 810., 800., 790., 780., 770., 760.
142| 0.009, 0.01, 0.02, 0.03, 0.04, 0.05, 0.075, 0.1, 0.25, 0.5, 0.75, 1.0, 2.0, 5.0, 7.5, 10., 20., 30.,
    40., 50., 60., 70., 80., 84.1
143| 3
144| 700., 800., 900.
145| 114.54, 114.11, 113.39
146| 20, 20
147| OP,CORR
148| OP,EXIT
149|
150| OP,MAP
151| OP,EXIT
152|
153| OP,MINI
154| 2100, 5000, 1e-10, 1e-08, 0.9, 1, 20, 1, 1, 1e-08
155| OP,EXIT
156|
157| OP,REST
158| 0, 0
159| OP,RE,F
160| OP,ERRO
161| 1,0,0,1,1,1e+308
162| OP,EXIT
163|
164| OP,REST
165| 0, 0
166| OP,RE,F
167| OP,ERRO
168| 0,0,0,0,1,1e+308
169| OP,EXIT

```

## C GOSIA2 Input

GOSIA2 performs fits of matrix elements, but in contrast to GOSIA, GOSIA2 is designed to normalize input to the scattering partner. Hence, the input is quite similar to the GOSIA input (cf. Appendix B), but two input files, one for each involved nucleus, are necessary. Two exemplary input files from the analysis of the  $^{142}\text{Sm} \rightarrow ^{48}\text{Ti}$  reaction are given, together with the respective yield files

**Listing C.1:** Yield input for GOSIA2 for  $^{48}\text{Ti}$ , subdivided into three particle scattering angular ranges, where target-like recoils were detected

```
1 1, 1, 62, 142, 404.7, 1, 1
2 2, 1, 152.120, 11.104
3 2, 1, 62, 142, 404.7, 1, 1
4 2, 1, 488.147, 22.381
5 3, 1, 62, 142, 404.7, 1, 1
6 2, 1, 332.999, 17.479
```

**Listing C.2:** GOSIA2 input for  $^{48}\text{Ti}$ , subdivided into three particle scattering angular ranges, where target-like recoils were detected

```
1 2
2 OP, FILE
3 22,3,1
4 48Ti.out
5 25,3,1
6 142Sm_48Ti.inp
7 26,3,1
8 48Ti.inp
9 3,3,1
10 48Ti_cor.yld
11 4,3,1
12 48Ti_cor
13 7,3,1
14 142Sm_48Ti.map
15 27,3,1
16 48Ti.map
17 8,3,1
18 48Ti.raw
19 9,3,1
20 48Ti.gdt
21 12,3,1
22 142Sm_48Ti.bst
23 32,3,1
24 48Ti.bst
25 15,3,1
26 48Ti.err
27 29,3,1
28 conv.icc
29 11,3,2
30 crf.dat
31 23,3,1
```

```

32 48Ti_op.raw
33 13,3,1
34 cnor.dat
35 99,3,1
36 48Ti_amp
37 0,0,0
38 OP,TITL
39 Target excitation of reaction 142Sm -> 48Ti
40 OP,GOSI
41 LEVE
42 1 1 0.0 0.0
43 2 1 2.0 0.983539
44 3 1 4.0 2.295654
45 0 0 0 0
46 ME
47 2 0 0 0 0
48 1 2 0.268 0.01 5.0
49 2 2 -0.234 -5.0 5.0
50 2 3 0.4142 0.01 5.0
51 3 3 0.01 1 1
52 0 0 0 0 0
53 EXPT
54 3 22 48
55 62, 142, 362.36, -19.242, 3, 1, 0, 0.0, 360.0, 0, 1
56 62, 142, 362.36, -18.637, 3, 1, 0, 0.0, 360.0, 1, 2
57 62, 142, 362.36, -16.334, 3, 1, 0, 0.0, 360.0, 1, 3
58 CONT
59 INT,3.
60 1,1000
61 2,1000
62 3,1000
63 SPL,1.
64 PRT,
65 1,1
66 2,1
67 3,1
68 4,-2
69 5,1
70 6,1
71 7,1
72 8,1
73 10,1
74 11,1
75 12,1
76 13,1
77 14,1
78 15,1
79 16,1
80 17,3
81 18,1
82 19,1
83 20,1
84 0,0
85 END,
86
87 OP,GDET
88 -21
89 0.1, 5.0, 7.8, 12.0 !clu1a
90 0.2, 0, 0, 0, 0, 0, 0
91 0.1, 5.0, 7.8, 12.0 !clu1b
92 0.2, 0, 0, 0, 0, 0, 0
93 0.1, 5.0, 7.8, 12.0 !clu1c
94 0.2, 0, 0, 0, 0, 0, 0
95 0.1, 5.0, 7.8, 12.0 !clu2a
96 0.2, 0, 0, 0, 0, 0, 0
97 0.1, 5.0, 7.8, 12.0 !clu2b
98 0.2, 0, 0, 0, 0, 0, 0
99 0.1, 5.0, 7.8, 12.0 !clu2c

```



```
100 0.2, 0, 0, 0, 0, 0, 0
101 0.1, 5.0, 7.8, 12.0          !clu3a
102 0.2, 0, 0, 0, 0, 0, 0
103 0.1, 5.0, 7.8, 12.0          !clu3b
104 0.2, 0, 0, 0, 0, 0, 0
105 0.1, 5.0, 7.8, 12.0          !clu3c
106 0.2, 0, 0, 0, 0, 0, 0
107 0.1, 5.0, 7.8, 12.0          !clu4a
108 0.2, 0, 0, 0, 0, 0, 0
109 0.1, 5.0, 7.8, 12.0          !clu4b
110 0.2, 0, 0, 0, 0, 0, 0
111 0.1, 5.0, 7.8, 12.0          !clu4c
112 0.2, 0, 0, 0, 0, 0, 0
113 0.1, 5.0, 7.8, 12.0          !clu6a
114 0.2, 0, 0, 0, 0, 0, 0
115 0.1, 5.0, 7.8, 12.0          !clu6b
116 0.2, 0, 0, 0, 0, 0, 0
117 0.1, 5.0, 7.8, 12.0          !clu6c
118 0.2, 0, 0, 0, 0, 0, 0
119 0.1, 5.0, 7.8, 12.2          !clu7a
120 0.2, 0, 0, 0, 0, 0, 0
121 0.1, 5.0, 7.8, 12.2          !clu7b
122 0.2, 0, 0, 0, 0, 0, 0
123 0.1, 5.0, 7.8, 12.2          !clu7c
124 0.2, 0, 0, 0, 0, 0, 0
125 0.1, 5.0, 7.8, 12.0          !clu8a
126 0.2, 0, 0, 0, 0, 0, 0
127 0.1, 5.0, 7.8, 12.0          !clu8b
128 0.2, 0, 0, 0, 0, 0, 0
129 0.1, 5.0, 7.8, 12.0          !clu8c
130 0.2, 0, 0, 0, 0, 0, 0
131 OP, YIEL
132 1
133 12,1
134 0.05, 0.075, 0.1, 0.2, 0.375, 0.5, 0.75, 1.0, 1.25, 1.5, 1.75, 2.0
135 2
136 5.1, 1.057, 0.343, 0.0232, 0.00228, 0.000866, 0.000256, 0.0001211, 9.01E-5, 0.0001369, 0.000231,
    0.000342
137 21, 21, 21
138 1, 2, 3, 4, 5, 6, 7, 8, 9, 10, 11, 12, 13, 14, 15, 16, 17, 18, 19, 20, 21
139 108.5,126.6,134.0, 60.1, 71.4, 44.1, 65.7, 38.5, 57.2,111.2,126.2,137.9, 42.4, 67.5,
    49.0,123.5,132.1,106.4, 43.2, 69.3, 52.6
140 133.7,157.0,122.2, 58.9, 31.6, 30.4,117.7,120.0,147.4, 36.8, 63.1,
    29.4,242.0,228.5,204.6,339.9,307.4,316.8,341.0,330.9,306.0
141 1, 2, 3, 4, 5, 6, 7, 8, 9, 10, 11, 12, 13, 14, 15, 16, 17, 18, 19, 20, 21
142 108.5,126.6,134.0, 60.1, 71.4, 44.1, 65.7, 38.5, 57.2,111.2,126.2,137.9, 42.4, 67.5,
    49.0,123.5,132.1,106.4, 43.2, 69.3, 52.6
143 133.7,157.0,122.2, 58.9, 31.6, 30.4,117.7,120.0,147.4, 36.8, 63.1,
    29.4,242.0,228.5,204.6,339.9,307.4,316.8,341.0,330.9,306.0
144 1, 2, 3, 4, 5, 6, 7, 8, 9, 10, 11, 12, 13, 14, 15, 16, 17, 18, 19, 20, 21
145 108.5,126.6,134.0, 60.1, 71.4, 44.1, 65.7, 38.5, 57.2,111.2,126.2,137.9, 42.4, 67.5,
    49.0,123.5,132.1,106.4, 43.2, 69.3, 52.6
146 133.7,157.0,122.2, 58.9, 31.6, 30.4,117.7,120.0,147.4, 36.8, 63.1,
    29.4,242.0,228.5,204.6,339.9,307.4,316.8,341.0,330.9,306.0
147 2,1
148 1
149 1000
150 1.0
151 1
152 1000
153 1.0
154 1
155 1000
156 1.0
157 3 !NTAP
158 0, 0
159 1, 1
160 2, 5.8285, 0.1443
```

[illegible]



```

229 0, 0, 0, 0, 0, 0, -50, 0      !0.89362, -0.29051, -0.00044825, -0.0083302, 0, 0, 0, 0
230 0, 0, 0, 0, 0, 0, -50, 0      !0.89362, -0.29051, -0.00044825, -0.0083302, 0, 0, 0, 0
231 0, 0, 0, 0, 0, 0, -50, 0      !0.89362, -0.29051, -0.00044825, -0.0083302, 0, 0, 0, 0
232 0, 0, 0, 0, 0, 0, -50, 0      !0.89362, -0.29051, -0.00044825, -0.0083302, 0, 0, 0, 0
233 0, 0, 0, 0, 0, 0, -50, 0      !0.89362, -0.29051, -0.00044825, -0.0083302, 0, 0, 0, 0
234 0, 0, 0, 0, 0, 0, -50, 0      !0.89362, -0.29051, -0.00044825, -0.0083302, 0, 0, 0, 0
235 0, 0, 0, 0, 0, 0, -50, 0      !0.89362, -0.29051, -0.00044825, -0.0083302, 0, 0, 0, 0
236 0, 0, 0, 0, 0, 0, -50, 0      !0.89362, -0.29051, -0.00044825, -0.0083302, 0, 0, 0, 0
237 0, 0, 0, 0, 0, 0, -50, 0      !0.89362, -0.29051, -0.00044825, -0.0083302, 0, 0, 0, 0
238 0, 0, 0, 0, 0, 0, -50, 0      !0.89362, -0.29051, -0.00044825, -0.0083302, 0, 0, 0, 0
239 1
240 21
241 1,2,3,4,5,6,7,8,9,10,11,12,13,14,15,16,17,18,19,20,21
242 0
243 OP,INTI
244 7, 8, 320.5985, 404.7, 27.29, 33.85
245 410., 395., 380., 365., 350., 335., 320.
246 27., 28., 29., 30., 31., 32., 33., 34.
247 7, 13, 320.5985, 404.7, 37.02, 48.91
248 410., 395., 380., 365., 350., 335., 320.
249 37., 38., 39., 40., 41., 42., 43., 44., 45., 46., 47., 48., 49.
250 7, 10, 320.5985, 404.7, 49.01, 57.06
251 410., 395., 380., 365., 350., 335., 320.
252 49., 50., 51., 52., 53., 54., 55., 56., 57., 58.
253 6
254 300., 325., 350., 375., 400., 425.
255 52.56, 53.62, 54.41, 55.28, 56.08, 56.77
256 20, 20
257 6
258 300., 325., 350., 375., 400., 425.
259 52.56, 53.62, 54.41, 55.28, 56.08, 56.77
260 20, 20
261 6
262 300., 325., 350., 375., 400., 425.
263 52.56, 53.62, 54.41, 55.28, 56.08, 56.77
264 20, 20
265 OP,CORR
266 OP,EXIT
267
268 OP,MAP
269 OP,EXIT
270
271 OP,MINI
272 2100, 20, 1.0E-06, 1.0E-04, 1.1, 1, 5, 1, 1, 1.0E-04
273 OP,EXIT

```

**Listing C.3:** Yield input for GOSIA2 for  $^{142}\text{Sm}$ , subdivided into three particle scattering angular ranges, where target-like recoils were detected

```

1 1, 1, 62, 142, 404.7, 1, 1
2 2, 1, 450.506, 18.197
3 2, 1, 62, 142, 404.7, 1, 1
4 2, 1, 1227.146, 30.740
5 3, 1, 62, 142, 404.7, 1, 1
6 2, 1, 795.987, 24.043

```

**Listing C.4:** GOSIA2 input for  $^{142}\text{Sm}$ , subdivided into three particle scattering angular ranges, where target-like recoils were detected

```

1 1
2 OP, FILE
3 22,3,1
4 142Sm_48Ti.out

```

```

5 | 25,3,1
6 | 142Sm_48Ti.inp
7 | 26,3,1
8 | 48Ti.inp
9 | 3,3,1
10 | 142Sm_48Ti_cor.yld
11 | 4,3,1
12 | 142Sm_48Ti.cor
13 | 7,3,1
14 | 142Sm_48Ti.map
15 | 27,3,1
16 | 48Ti.map
17 | 8,3,1
18 | 142Sm_48Ti.raw
19 | 9,3,1
20 | 142Sm_48Ti.gdt
21 | 12,3,1
22 | 142Sm_48Ti.bst
23 | 32,3,1
24 | 48Ti.bst
25 | 15,3,1
26 | 142Sm_48Ti.err
27 | 29,3,1
28 | conv.icc
29 | 11,3,2
30 | crf.dat
31 | 23,3,1
32 | 142Sm_48Ti_op.raw
33 | 13,3,1
34 | cnor.dat
35 | 99,3,1
36 | 142Sm_48Ti.amp
37 | 0,0,0
38 | OP,TITL
39 | Projectile excitation of reaction 142Sm -> 48Ti
40 | OP,GOSI
41 | LEVE
42 | 1 1 0.0 0.0
43 | 2 1 2.0 0.76808
44 | 3 1 4.0 1.7914
45 | 0 0 0 0
46 | ME
47 | 2 0 0 0 0
48 | 1 2 1.0 0.6 0.9
49 | 2 2 -3.0 -1.5 4.5
50 | 2 3 0.5 0.01 5.0
51 | 3 3 0.01 1 1
52 | 0 0 0 0 0
53 | EXPT
54 | 3 62 142
55 | -22, 48, 362.36, -19.242, 3, 1, 0, 0.0, 360.0, 0, 1
56 | -22, 48, 362.36, -18.637, 3, 1, 0, 0.0, 360.0, 1, 2
57 | -22, 48, 362.36, -16.334, 3, 1, 0, 0.0, 360.0, 1, 3
58 | CONT
59 | INT,3.
60 | 1,1000
61 | 2,1000
62 | 3,1000
63 | SPL,1.
64 | PRT,
65 | 1,1
66 | 2,1
67 | 3,1
68 | 4,-2
69 | 5,1
70 | 6,1
71 | 7,1
72 | 8,1

```

```

73 10,1
74 11,1
75 12,1
76 13,1
77 14,1
78 15,1
79 16,1
80 17,3
81 18,1
82 19,1
83 20,1
84 0,0
85 END,
86
87 OP, GDET
88 -21
89 0.1, 5.0, 7.8, 12.0 !clu1a
90 0.2, 0, 0, 0, 0, 0, 0
91 0.1, 5.0, 7.8, 12.0 !clu1b
92 0.2, 0, 0, 0, 0, 0, 0
93 0.1, 5.0, 7.8, 12.0 !clu1c
94 0.2, 0, 0, 0, 0, 0, 0
95 0.1, 5.0, 7.8, 12.0 !clu2a
96 0.2, 0, 0, 0, 0, 0, 0
97 0.1, 5.0, 7.8, 12.0 !clu2b
98 0.2, 0, 0, 0, 0, 0, 0
99 0.1, 5.0, 7.8, 12.0 !clu2c
100 0.2, 0, 0, 0, 0, 0, 0
101 0.1, 5.0, 7.8, 12.0 !clu3a
102 0.2, 0, 0, 0, 0, 0, 0
103 0.1, 5.0, 7.8, 12.0 !clu3b
104 0.2, 0, 0, 0, 0, 0, 0
105 0.1, 5.0, 7.8, 12.0 !clu3c
106 0.2, 0, 0, 0, 0, 0, 0
107 0.1, 5.0, 7.8, 12.0 !clu4a
108 0.2, 0, 0, 0, 0, 0, 0
109 0.1, 5.0, 7.8, 12.0 !clu4b
110 0.2, 0, 0, 0, 0, 0, 0
111 0.1, 5.0, 7.8, 12.0 !clu4c
112 0.2, 0, 0, 0, 0, 0, 0
113 0.1, 5.0, 7.8, 12.0 !clu6a
114 0.2, 0, 0, 0, 0, 0, 0
115 0.1, 5.0, 7.8, 12.0 !clu6b
116 0.2, 0, 0, 0, 0, 0, 0
117 0.1, 5.0, 7.8, 12.0 !clu6c
118 0.2, 0, 0, 0, 0, 0, 0
119 0.1, 5.0, 7.8, 12.2 !clu7a
120 0.2, 0, 0, 0, 0, 0, 0
121 0.1, 5.0, 7.8, 12.2 !clu7b
122 0.2, 0, 0, 0, 0, 0, 0
123 0.1, 5.0, 7.8, 12.2 !clu7c
124 0.2, 0, 0, 0, 0, 0, 0
125 0.1, 5.0, 7.8, 12.0 !clu8a
126 0.2, 0, 0, 0, 0, 0, 0
127 0.1, 5.0, 7.8, 12.0 !clu8b
128 0.2, 0, 0, 0, 0, 0, 0
129 0.1, 5.0, 7.8, 12.0 !clu8c
130 0.2, 0, 0, 0, 0, 0, 0
131 OP, YIEL
132 1
133 12,1
134 0.05, 0.075, 0.1, 0.2, 0.375, 0.5, 0.75, 1.0, 1.25, 1.5, 1.75, 2.0
135 2
136 34.1, 6.8, 2.34, 0.209, 0.0287, 0.01283, 0.00469, 0.00249, 0.001586, 0.001177, 0.000997, 0.000932
137 21, 21, 21
138 1, 2, 3, 4, 5, 6, 7, 8, 9, 10, 11, 12, 13, 14, 15, 16, 17, 18, 19, 20, 21
139 108.5,126.6,134.0, 60.1, 71.4, 44.1, 65.7, 38.5, 57.2,111.2,126.2,137.9, 42.4, 67.5,
    49.0,123.5,132.1,106.4, 43.2, 69.3, 52.6

```

```

140 133.7,157.0,122.2, 58.9, 31.6, 30.4,117.7,120.0,147.4, 36.8, 63.1,
    29.4,242.0,228.5,204.6,339.9,307.4,316.8,341.0,330.9,306.0
141 1, 2, 3, 4, 5, 6, 7, 8, 9, 10, 11, 12, 13, 14, 15, 16, 17, 18, 19, 20, 21
142 108.5,126.6,134.0, 60.1, 71.4, 44.1, 65.7, 38.5, 57.2,111.2,126.2,137.9, 42.4, 67.5,
    49.0,123.5,132.1,106.4, 43.2, 69.3, 52.6
143 133.7,157.0,122.2, 58.9, 31.6, 30.4,117.7,120.0,147.4, 36.8, 63.1,
    29.4,242.0,228.5,204.6,339.9,307.4,316.8,341.0,330.9,306.0
144 1, 2, 3, 4, 5, 6, 7, 8, 9, 10, 11, 12, 13, 14, 15, 16, 17, 18, 19, 20, 21
145 108.5,126.6,134.0, 60.1, 71.4, 44.1, 65.7, 38.5, 57.2,111.2,126.2,137.9, 42.4, 67.5,
    49.0,123.5,132.1,106.4, 43.2, 69.3, 52.6
146 133.7,157.0,122.2, 58.9, 31.6, 30.4,117.7,120.0,147.4, 36.8, 63.1,
    29.4,242.0,228.5,204.6,339.9,307.4,316.8,341.0,330.9,306.0
147 2,1
148 1
149 1000
150 1.0
151 1
152 1000
153 1.0
154 1
155 1000
156 1.0
157 3 INTAP
158 0, 0
159 0, 0
160 0, 0
161 0, 0
162 OP,RAW
163 1
164 0, 0, 0, 0, 0, 0, -50, 0 !0.89362, -0.29051, -0.00044825, -0.0083302, 0, 0, 0, 0
165 0, 0, 0, 0, 0, 0, -50, 0 !0.89362, -0.29051, -0.00044825, -0.0083302, 0, 0, 0, 0
166 0, 0, 0, 0, 0, 0, -50, 0 !0.89362, -0.29051, -0.00044825, -0.0083302, 0, 0, 0, 0
167 0, 0, 0, 0, 0, 0, -50, 0 !0.89362, -0.29051, -0.00044825, -0.0083302, 0, 0, 0, 0
168 0, 0, 0, 0, 0, 0, -50, 0 !0.89362, -0.29051, -0.00044825, -0.0083302, 0, 0, 0, 0
169 0, 0, 0, 0, 0, 0, -50, 0 !0.89362, -0.29051, -0.00044825, -0.0083302, 0, 0, 0, 0
170 0, 0, 0, 0, 0, 0, -50, 0 !0.89362, -0.29051, -0.00044825, -0.0083302, 0, 0, 0, 0
171 0, 0, 0, 0, 0, 0, -50, 0 !0.89362, -0.29051, -0.00044825, -0.0083302, 0, 0, 0, 0
172 0, 0, 0, 0, 0, 0, -50, 0 !0.89362, -0.29051, -0.00044825, -0.0083302, 0, 0, 0, 0
173 0, 0, 0, 0, 0, 0, -50, 0 !0.89362, -0.29051, -0.00044825, -0.0083302, 0, 0, 0, 0
174 0, 0, 0, 0, 0, 0, -50, 0 !0.89362, -0.29051, -0.00044825, -0.0083302, 0, 0, 0, 0
175 0, 0, 0, 0, 0, 0, -50, 0 !0.89362, -0.29051, -0.00044825, -0.0083302, 0, 0, 0, 0
176 0, 0, 0, 0, 0, 0, -50, 0 !0.89362, -0.29051, -0.00044825, -0.0083302, 0, 0, 0, 0
177 0, 0, 0, 0, 0, 0, -50, 0 !0.89362, -0.29051, -0.00044825, -0.0083302, 0, 0, 0, 0
178 0, 0, 0, 0, 0, 0, -50, 0 !0.89362, -0.29051, -0.00044825, -0.0083302, 0, 0, 0, 0
179 0, 0, 0, 0, 0, 0, -50, 0 !0.89362, -0.29051, -0.00044825, -0.0083302, 0, 0, 0, 0
180 0, 0, 0, 0, 0, 0, -50, 0 !0.89362, -0.29051, -0.00044825, -0.0083302, 0, 0, 0, 0
181 0, 0, 0, 0, 0, 0, -50, 0 !0.89362, -0.29051, -0.00044825, -0.0083302, 0, 0, 0, 0
182 0, 0, 0, 0, 0, 0, -50, 0 !0.89362, -0.29051, -0.00044825, -0.0083302, 0, 0, 0, 0
183 0, 0, 0, 0, 0, 0, -50, 0 !0.89362, -0.29051, -0.00044825, -0.0083302, 0, 0, 0, 0
184 0, 0, 0, 0, 0, 0, -50, 0 !0.89362, -0.29051, -0.00044825, -0.0083302, 0, 0, 0, 0
185 1
186 21
187 1,2,3,4,5,6,7,8,9,10,11,12,13,14,15,16,17,18,19,20,21
188 2
189 0, 0, 0, 0, 0, 0, -50, 0 !0.89362, -0.29051, -0.00044825, -0.0083302, 0, 0, 0, 0
190 0, 0, 0, 0, 0, 0, -50, 0 !0.89362, -0.29051, -0.00044825, -0.0083302, 0, 0, 0, 0
191 0, 0, 0, 0, 0, 0, -50, 0 !0.89362, -0.29051, -0.00044825, -0.0083302, 0, 0, 0, 0
192 0, 0, 0, 0, 0, 0, -50, 0 !0.89362, -0.29051, -0.00044825, -0.0083302, 0, 0, 0, 0
193 0, 0, 0, 0, 0, 0, -50, 0 !0.89362, -0.29051, -0.00044825, -0.0083302, 0, 0, 0, 0
194 0, 0, 0, 0, 0, 0, -50, 0 !0.89362, -0.29051, -0.00044825, -0.0083302, 0, 0, 0, 0
195 0, 0, 0, 0, 0, 0, -50, 0 !0.89362, -0.29051, -0.00044825, -0.0083302, 0, 0, 0, 0
196 0, 0, 0, 0, 0, 0, -50, 0 !0.89362, -0.29051, -0.00044825, -0.0083302, 0, 0, 0, 0
197 0, 0, 0, 0, 0, 0, -50, 0 !0.89362, -0.29051, -0.00044825, -0.0083302, 0, 0, 0, 0
198 0, 0, 0, 0, 0, 0, -50, 0 !0.89362, -0.29051, -0.00044825, -0.0083302, 0, 0, 0, 0
199 0, 0, 0, 0, 0, 0, -50, 0 !0.89362, -0.29051, -0.00044825, -0.0083302, 0, 0, 0, 0
200 0, 0, 0, 0, 0, 0, -50, 0 !0.89362, -0.29051, -0.00044825, -0.0083302, 0, 0, 0, 0
201 0, 0, 0, 0, 0, 0, -50, 0 !0.89362, -0.29051, -0.00044825, -0.0083302, 0, 0, 0, 0
202 0, 0, 0, 0, 0, 0, -50, 0 !0.89362, -0.29051, -0.00044825, -0.0083302, 0, 0, 0, 0

```



203	0, 0, 0, 0, 0, 0, -50, 0	!0.89362, -0.29051, -0.00044825, -0.0083302, 0, 0, 0, 0
204	0, 0, 0, 0, 0, 0, -50, 0	!0.89362, -0.29051, -0.00044825, -0.0083302, 0, 0, 0, 0
205	0, 0, 0, 0, 0, 0, -50, 0	!0.89362, -0.29051, -0.00044825, -0.0083302, 0, 0, 0, 0
206	0, 0, 0, 0, 0, 0, -50, 0	!0.89362, -0.29051, -0.00044825, -0.0083302, 0, 0, 0, 0
207	0, 0, 0, 0, 0, 0, -50, 0	!0.89362, -0.29051, -0.00044825, -0.0083302, 0, 0, 0, 0
208	0, 0, 0, 0, 0, 0, -50, 0	!0.89362, -0.29051, -0.00044825, -0.0083302, 0, 0, 0, 0
209	0, 0, 0, 0, 0, 0, -50, 0	!0.89362, -0.29051, -0.00044825, -0.0083302, 0, 0, 0, 0
210	1	
211	21	
212	1,2,3,4,5,6,7,8,9,10,11,12,13,14,15,16,17,18,19,20,21	
213	3	
214	0, 0, 0, 0, 0, 0, -50, 0	!0.89362, -0.29051, -0.00044825, -0.0083302, 0, 0, 0, 0
215	0, 0, 0, 0, 0, 0, -50, 0	!0.89362, -0.29051, -0.00044825, -0.0083302, 0, 0, 0, 0
216	0, 0, 0, 0, 0, 0, -50, 0	!0.89362, -0.29051, -0.00044825, -0.0083302, 0, 0, 0, 0
217	0, 0, 0, 0, 0, 0, -50, 0	!0.89362, -0.29051, -0.00044825, -0.0083302, 0, 0, 0, 0
218	0, 0, 0, 0, 0, 0, -50, 0	!0.89362, -0.29051, -0.00044825, -0.0083302, 0, 0, 0, 0
219	0, 0, 0, 0, 0, 0, -50, 0	!0.89362, -0.29051, -0.00044825, -0.0083302, 0, 0, 0, 0
220	0, 0, 0, 0, 0, 0, -50, 0	!0.89362, -0.29051, -0.00044825, -0.0083302, 0, 0, 0, 0
221	0, 0, 0, 0, 0, 0, -50, 0	!0.89362, -0.29051, -0.00044825, -0.0083302, 0, 0, 0, 0
222	0, 0, 0, 0, 0, 0, -50, 0	!0.89362, -0.29051, -0.00044825, -0.0083302, 0, 0, 0, 0
223	0, 0, 0, 0, 0, 0, -50, 0	!0.89362, -0.29051, -0.00044825, -0.0083302, 0, 0, 0, 0
224	0, 0, 0, 0, 0, 0, -50, 0	!0.89362, -0.29051, -0.00044825, -0.0083302, 0, 0, 0, 0
225	0, 0, 0, 0, 0, 0, -50, 0	!0.89362, -0.29051, -0.00044825, -0.0083302, 0, 0, 0, 0
226	0, 0, 0, 0, 0, 0, -50, 0	!0.89362, -0.29051, -0.00044825, -0.0083302, 0, 0, 0, 0
227	0, 0, 0, 0, 0, 0, -50, 0	!0.89362, -0.29051, -0.00044825, -0.0083302, 0, 0, 0, 0
228	0, 0, 0, 0, 0, 0, -50, 0	!0.89362, -0.29051, -0.00044825, -0.0083302, 0, 0, 0, 0
229	0, 0, 0, 0, 0, 0, -50, 0	!0.89362, -0.29051, -0.00044825, -0.0083302, 0, 0, 0, 0
230	0, 0, 0, 0, 0, 0, -50, 0	!0.89362, -0.29051, -0.00044825, -0.0083302, 0, 0, 0, 0
231	0, 0, 0, 0, 0, 0, -50, 0	!0.89362, -0.29051, -0.00044825, -0.0083302, 0, 0, 0, 0
232	0, 0, 0, 0, 0, 0, -50, 0	!0.89362, -0.29051, -0.00044825, -0.0083302, 0, 0, 0, 0
233	0, 0, 0, 0, 0, 0, -50, 0	!0.89362, -0.29051, -0.00044825, -0.0083302, 0, 0, 0, 0
234	0, 0, 0, 0, 0, 0, -50, 0	!0.89362, -0.29051, -0.00044825, -0.0083302, 0, 0, 0, 0
235	1	
236	21	
237	1,2,3,4,5,6,7,8,9,10,11,12,13,14,15,16,17,18,19,20,21	
238	0	
239	OP,INTI	
240	7, 8, 320.5985, 404.7, 27.29, 33.85	
241	410., 395., 380., 365., 350., 335., 320.	
242	27., 28., 29., 30., 31., 32., 33., 34.	
243	7, 13, 320.5985, 404.7, 37.02, 48.91	
244	410., 395., 380., 365., 350., 335., 320.	
245	37., 38., 39., 40., 41., 42., 43., 44., 45., 46., 47., 48., 49.	
246	7, 10, 320.5985, 404.7, 49.01, 57.06	
247	410., 395., 380., 365., 350., 335., 320.	
248	49., 50., 51., 52., 53., 54., 55., 56., 57., 58.	
249	6	
250	300., 325., 350., 375., 400., 425.	
251	52.56, 53.62, 54.41, 55.28, 56.08, 56.77	
252	20, 20	
253	6	
254	300., 325., 350., 375., 400., 425.	
255	52.56, 53.62, 54.41, 55.28, 56.08, 56.77	
256	20, 20	
257	6	
258	300., 325., 350., 375., 400., 425.	
259	52.56, 53.62, 54.41, 55.28, 56.08, 56.77	
260	20, 20	
261	OP,CORR	
262	OP,EXIT	
263		
264	OP,MAP	
265	OP,EXIT	
266		
267	OP,MINI	
268	2100, 20, 1.0E-06, 1.0E-04, 1.1, 1, 5, 1, 1, 1.0E-04	
269	OP,EXIT	



## D Relativistic Transformations

From considerations about electromagnetic fields it follows that these propagate with the speed of light, independent of the choice of the inertial frame of reference. This leads to

$$c^2 t^2 - \vec{x}^2 = 0, \quad (\text{D.1})$$

which is invariant under transformation of the frame of reference. In a more general covariant formulation:

$$s^2 \equiv c^2 t^2 - \vec{x}^2 = x_\nu x^\nu, \quad (\text{D.2})$$

with the contra-variant four-vector defined as  $x^\nu = (ct, x, y, z)^T$  and the covariant one as  $x_\nu = (ct, -x, -y, -z)^T$ . This invariance can be understood when compared to the rotation of a vector, where its length is invariant under this rotational transformation. Analogous the change of the frame of reference can be thought of as a rotation of the four-vector in space-time.

In a slightly different approach the transformation of a point  $x$  in a coordinate system  $K$  into a coordinate system  $K'$ , which is moving relative to  $K$  with velocity  $V$ , may be described via [36]

$$\begin{pmatrix} x' \\ y' \\ z' \\ ict' \end{pmatrix} = \underbrace{\begin{pmatrix} \alpha_{11} & \alpha_{12} & \alpha_{13} & \alpha_{14} \\ \alpha_{21} & \alpha_{22} & \alpha_{23} & \alpha_{24} \\ \alpha_{31} & \alpha_{32} & \alpha_{33} & \alpha_{34} \\ \alpha_{41} & \alpha_{42} & \alpha_{43} & \alpha_{44} \end{pmatrix}}_{\alpha} \cdot \begin{pmatrix} x \\ y \\ z \\ ict \end{pmatrix}. \quad (\text{D.3})$$

The transformation is restricted to a linear character. This is required by the fact that a straight line in  $K$  has to stay straight in  $K'$ . A transformation of at least quadratic order would result in points following accelerated movement in  $K'$ . Assuming relative movement parallel to the  $x$  axis, the  $y$  and  $z$  coordinates have stay independent of  $x$  and  $t$ , and thus  $y' = y$  and  $z' = z$ . The transformation can thus be written in a compacter way:

$$\begin{pmatrix} x' \\ ict' \end{pmatrix} = \begin{pmatrix} \alpha_{11} & \alpha_{14} \\ \alpha_{41} & \alpha_{44} \end{pmatrix} \cdot \begin{pmatrix} x \\ ict \end{pmatrix}. \quad (\text{D.4})$$

For such kind of linear transformations of a set of orthonormal basis vectors applies  $\sum_{k=1}^4 \alpha_{ik} \alpha_{jk} = \delta_{ij}$  (orthonormality of matrix row vectors) and  $\sum_{k=1}^4 \alpha_{ki} \alpha_{kj} = \delta_{ij}$  (orthonormality of matrix column vectors). These orthonormal relations also result in length unity of the respective vectors, imposing additional constraints for determination of the matrix elements. The relative motion of the origin of both coordinate systems yields for the movement of the origin of  $K'$  in  $K$   $x' = 0 = \alpha_{11} \left( x + \frac{\alpha_{14}}{\alpha_{11}} ict \right) \Rightarrow x = -\frac{\alpha_{14}}{\alpha_{11}} ict$  [36]. The relative velocity of the systems is the velocity of one of the origins in the respective other system  $\beta_x = \frac{1}{c} \frac{\partial x}{\partial t} = -i \frac{\alpha_{14}}{\alpha_{11}}$ . The orthonormality of row vectors, in combination with the condition that in the case of  $\beta \rightarrow 0$   $x' = x$  is required, leads to [36]

$$1 = \alpha_{11}^2 + \alpha_{14}^2 = \alpha_{11}^2 \cdot \left( 1 + \left( \frac{\alpha_{14}}{\alpha_{11}} \right)^2 \right) = \alpha_{11}^2 \cdot (1 + (i\beta_x)^2) = \alpha_{11}^2 \cdot (1 - \beta_x^2)$$

$$\Rightarrow \alpha_{11} = \frac{1}{\sqrt{1 - \beta_x^2}} = \gamma \quad (D.5)$$

$$\Rightarrow \alpha_{14} = i\beta_x \alpha_{11} = \frac{i\beta_x}{\sqrt{1 - \beta_x^2}} = i\beta_x \gamma \quad (D.6)$$

The orthonormality of column vectors imposes  $\alpha_{11}^2 + \alpha_{14}^2 = 1 = \alpha_{11}^2 + \alpha_{41}^2 \Rightarrow \alpha_{14} = \pm \alpha_{41}$ . This allows to determine also  $\alpha_{44}$  from the relation  $\alpha_{11}\alpha_{41} + \alpha_{14}\alpha_{44} = 0$  to be [36]

$$\alpha_{44} = -\frac{\alpha_{11}\alpha_{41}}{\alpha_{14}} = \mp \alpha_{11} = \mp \gamma. \quad (D.7)$$

Because the Lorentz transformation has to turn into the Galileo transformation for  $\beta_x \rightarrow 0$ , only the positive sign is left, i.e.,  $\alpha_{44} = \alpha_{11}$ , leading to  $\alpha_{14} = -\alpha_{41}$ . Summarizing all the findings for the various  $\alpha_{ij}$ ,  $i, j \in \{1, 4\}$ , and inserting into equation (D.4) yields [36]

$$x' = \gamma (x - \beta_x ct), \quad (D.8)$$

$$t' = \gamma \left( t - \beta_x \frac{x}{c} \right). \quad (D.9)$$

Using co- and contra-variant four-vectors allows for writing the Lorentz transformation as

$$x'^{\mu} = \sum_{\nu=0}^3 L^{\mu}_{\nu} x^{\nu}, \quad (D.10)$$



where  $L$  denotes the transformation matrix. Equation (D.10) is valid for any Lorentz transformation. In the special case of relative movement of the frames of reference exclusively parallel to the  $x$ -axis, with relative velocity  $\beta_x$ ,  $L$  is given by

$$L = \begin{pmatrix} \gamma & -\beta_x \gamma & 0 & 0 \\ -\beta_x \gamma & \gamma & 0 & 0 \\ 0 & 0 & 1 & 0 \\ 0 & 0 & 0 & 1 \end{pmatrix}. \quad (\text{D.11})$$

The Lorentz transformation holds not only true for four vectors, but in the covariant notation also for four momenta  $p^\nu = (E/c, p_x, p_y, p_z)^T = (E/c, \vec{p})^T$ , where  $E$  denotes the relativistic energy, i.e.,  $E = E_0 + T = \sqrt{\vec{p}^2 c^2 + E_0^2}$ , where  $E_0 = mc^2$  is the rest energy and  $T$  denotes the kinetic energy. The relativistic energy allows for rewriting  $\gamma = \frac{1}{\sqrt{1-\beta_x^2}}$  as  $\gamma = \frac{E}{E_0}$ .

The most important transformation between frames of references for this work are the transformation from the laboratory to the center-of-mass frame of reference, and vice versa. Therefore, the following paragraphs will focus on these relations. Prime values refer to values in the laboratory system, while such without refer to the center-of-mass system. In the latter, the sum of momenta of all particles involved vanishes by definition, i.e.,  $\sum_{i=1}^N \vec{p}_i = 0$ . If only two particles are involved into the transformation, e.g., in a Coulomb-excitation experiment,  $|\vec{p}_P| = |\vec{p}_T|$ , where indices  $P$  and  $T$  indicate projectile and target-like recoiling nuclei, respectively. In fixed-target experimental setup, the target particle is immobile in the laboratory frame of reference before the scattering event, while the projectile is moving towards it. Thus, in the center-of-mass frame of reference, the target has to move with the velocity of the center of mass itself, but in the opposite direction [35]. The Lorentz transformation (D.10) allows for determining the momentum  $|\vec{p}_P|$  of the projectile in the center-of-mass frame of reference, and consequential, the relative velocity of the systems

$$\begin{aligned} \gamma_c \left( |\vec{p}_P'| - \beta_c \frac{E'_P}{c} \right) &= |\vec{p}_P| = |\vec{p}_T| = \gamma_c m_T \beta_c c \\ &\Leftrightarrow \beta_c \left( m_T + \frac{E'_P}{c^2} \right) = \frac{|\vec{p}_P'|}{c} \\ &\Leftrightarrow \beta_c = \frac{|\vec{p}_P'|}{m_T c + \frac{E'_P}{c}} = \frac{\sqrt{\left(\frac{E'_P}{c}\right)^2 - (m_P c)^2}}{m_T c + \frac{E'_P}{c}} = \frac{\sqrt{E_P'^2 - (m_P c^2)^2}}{m_T c^2 + E'_P}, \end{aligned} \quad (\text{D.12})$$

where an index  $c$  indicates values related to the motion of the center of mass itself. Determination of the velocity of the center of mass allows for transforming between the frames of reference. From the Lorentz transformation of the four momenta, the energy of the projectile in the center-of-mass system can be determined to be

$$\begin{aligned} E_p &= \gamma_c (E'_p - \beta_c c p'_p) \\ &= \gamma_c \left( \frac{E'_p m_T c^2 + (m_p c^2)^2}{m_T c^2 + E'_p} \right). \end{aligned} \quad (D.13)$$

These transformations are valid, as long as the center of mass moves parallel to the  $x$  axis. In fixed-target experiments, this is given by the immobility of the target and the definition of the direction of the movement vector of the impinging projectile as the  $x$  direction. The vanishing sum of momenta in the center-of-mass frame of reference, which persists during and after the scattering process, ensures that the direction of motion of the center of mass is not altered. Nevertheless, if scattering occurs, projectile and target-like recoiling particles will exhibit velocity components perpendicular to the  $x$ -axis. Velocity components parallel to the  $x$  axis, *i.e.*,  $\beta_{||}$ , are transformed via

$$\begin{aligned} \beta'_{||} &= \frac{1}{c} \frac{\partial x'}{\partial t'} = \frac{1}{c} \frac{\partial}{\partial t'} [\gamma_c (x + \beta_c c t)] = \frac{1}{c} \frac{1}{1 + \beta_c \beta_{||}} \frac{\partial}{\partial t} (x + \beta_c c t) \\ &= \frac{1}{c} \frac{1}{1 + \beta_c \beta_{||}} \left( \frac{\partial x}{\partial t} + \beta_c c \frac{\partial t}{\partial t} \right) = \frac{\beta_{||} + \beta_c}{1 + \beta_c \beta_{||}}, \end{aligned} \quad (D.14)$$

employing

$$\begin{aligned} \frac{\partial t'}{\partial t} &= \frac{\partial}{\partial t} \left[ \gamma_c \left( t + \beta_c \frac{x}{c} \right) \right] = \gamma_c \left[ \frac{\partial t}{\partial t} + \frac{\partial}{\partial t} \left( \beta_c \frac{x}{c} \right) \right] = \gamma_c \left( 1 + \frac{\beta_c}{c} \frac{\partial x}{\partial t} \right) \\ &= \gamma_c (1 + \beta_c \beta_{||}). \end{aligned} \quad (D.15)$$

The components of the velocity vector perpendicular to the  $x$  axis, *i.e.*,  $\beta_{\perp}$ , are transformed in a similar manner, however, coordinates of perpendicular axis are not transformed, leaving

$$\beta'_{\perp} = \frac{1}{c} \frac{\partial y'}{\partial t'} = \frac{1}{c} \frac{\partial y}{\partial t'} = \frac{1}{c} \frac{1}{\gamma_c \cdot (1 + \beta_c \beta_{||})} \frac{\partial y}{\partial t} = \frac{\beta_{\perp}}{\gamma_c \cdot (1 + \beta_c \beta_{||})}. \quad (D.16)$$

A scattering angle given in the center-of-mass frame of reference by  $\tan(\theta) = \frac{c\beta_{\perp}}{c\beta_{||}}$  can be transformed to the laboratory frame of reference via

$$\tan(\theta') = \frac{c\beta'_{\perp}}{c\beta'_{||}} = \frac{\beta_{\perp}}{\gamma_c \cdot (1 + \beta_c \beta_{||})} \frac{1 + \beta_c \beta_{||}}{\beta_{||} + \beta_c} = \frac{1}{\gamma_c} \frac{\beta_{\perp}}{\beta_{||} + \beta_c}. \quad (D.17)$$

In a case, where not the components of the velocity vector are known, but the scattering angle  $\theta$  as well as the absolute value of the velocity  $\beta$ , the parallel component of the is given by  $\beta_{\parallel} = \beta \cdot \cos(\theta)$ , and the perpendicular component is given by  $\beta_{\perp} = \beta \cdot \sin(\theta)$ . Equation (D.17) can thus be rewritten to

$$\tan(\theta') = \frac{1}{\gamma_c} \frac{\beta_{\perp}}{\beta_{\parallel} + \beta_c} = \frac{1}{\gamma_c} \frac{\beta \cdot \sin(\theta)}{\beta \cdot \cos(\theta) + \beta_c} = \frac{1}{\gamma_c} \frac{\sin(\theta)}{\cos(\theta) + \underbrace{\beta_c/\beta}_{\tau}}. \quad (\text{D.18})$$

It has to be noted, that for both, projectile as well as target particles,  $\beta$  is different, although,  $\beta_c$  is identical. In the case of fixed-target experiments, the projectile  $\beta$  has explicitly to be calculated, while target  $\beta = -\beta_c$ .

On closer inspection, the limitation of  $\tan(\theta')$  for  $0 \leq \theta \leq 180^\circ$ , and  $\tau > 1$ , is obvious:  $\gamma_c \geq 1$ ,  $0 \leq \sin(\theta) \leq 1$ , and  $-1 \leq \cos(\theta) \leq 1$ . Thus, a maximum scattering angle  $\theta'$  in the laboratory frame of reference exists:

$$\begin{aligned} 0 &= \frac{\partial \theta'}{\partial \theta} = \frac{\partial}{\partial \theta} \arctan\left(\frac{1}{\gamma_c} \frac{\sin(\theta)}{\cos(\theta) + \tau}\right) = \frac{\gamma_c + \gamma_c \tau \cos(\theta)}{\gamma_c^2 [\tau + \cos(\theta)]^2 + \sin^2(\theta)} \\ &\Rightarrow \gamma_c + \gamma_c \tau \cos(\theta) = 0 \\ &\Leftrightarrow \cos(\theta) = -\frac{1}{\tau} \Rightarrow \sin^2(\theta) = 1 - \frac{1}{\tau^2} \\ &\Rightarrow \theta'_{\max} = \arctan\left(\frac{1}{\gamma_c} \frac{\sqrt{1 - \frac{1}{\tau^2}}}{\tau - \frac{1}{\tau}}\right) = \arctan\left(\frac{1}{\gamma_c \sqrt{\tau^2 - 1}}\right). \end{aligned} \quad (\text{D.19})$$

This ultimately implies an ambiguity when transforming vice versa, from the laboratory to the center-of-mass frame of reference, as every angle  $\theta'$  corresponds to two angles  $\theta$ .



# E Spectra

## E.1 $^{142}\text{Sm}$

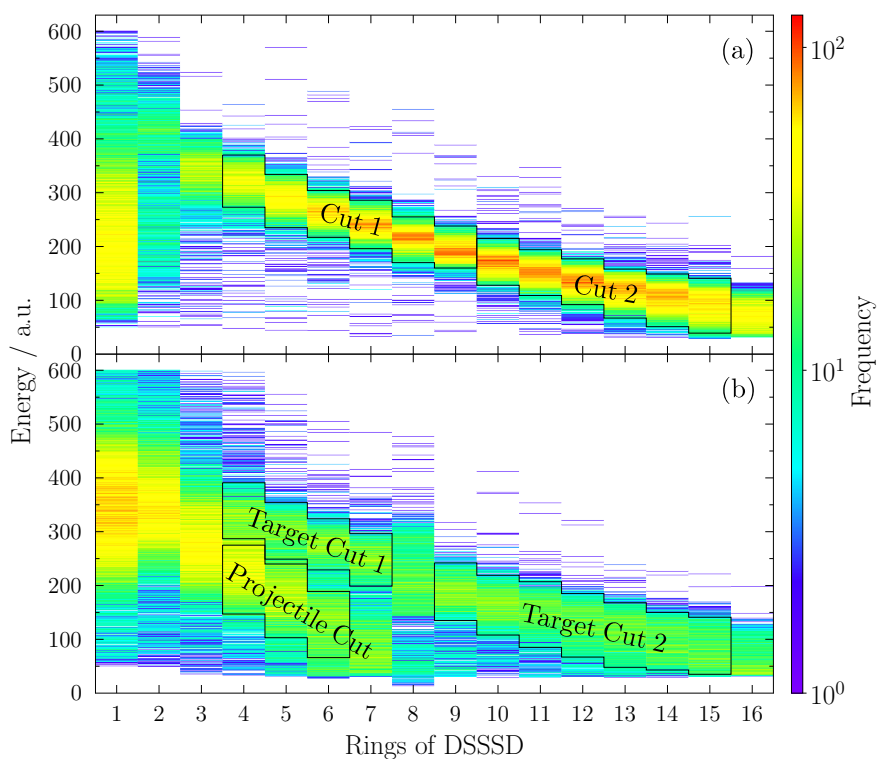


**Figure E.1.:** Particle- $\gamma$  coincidence particle spectra. (a) shows the data recorded with the  $^{48}\text{Ti}$  target. (b) shows the data recorded with the  $^{94}\text{Mo}$  target.

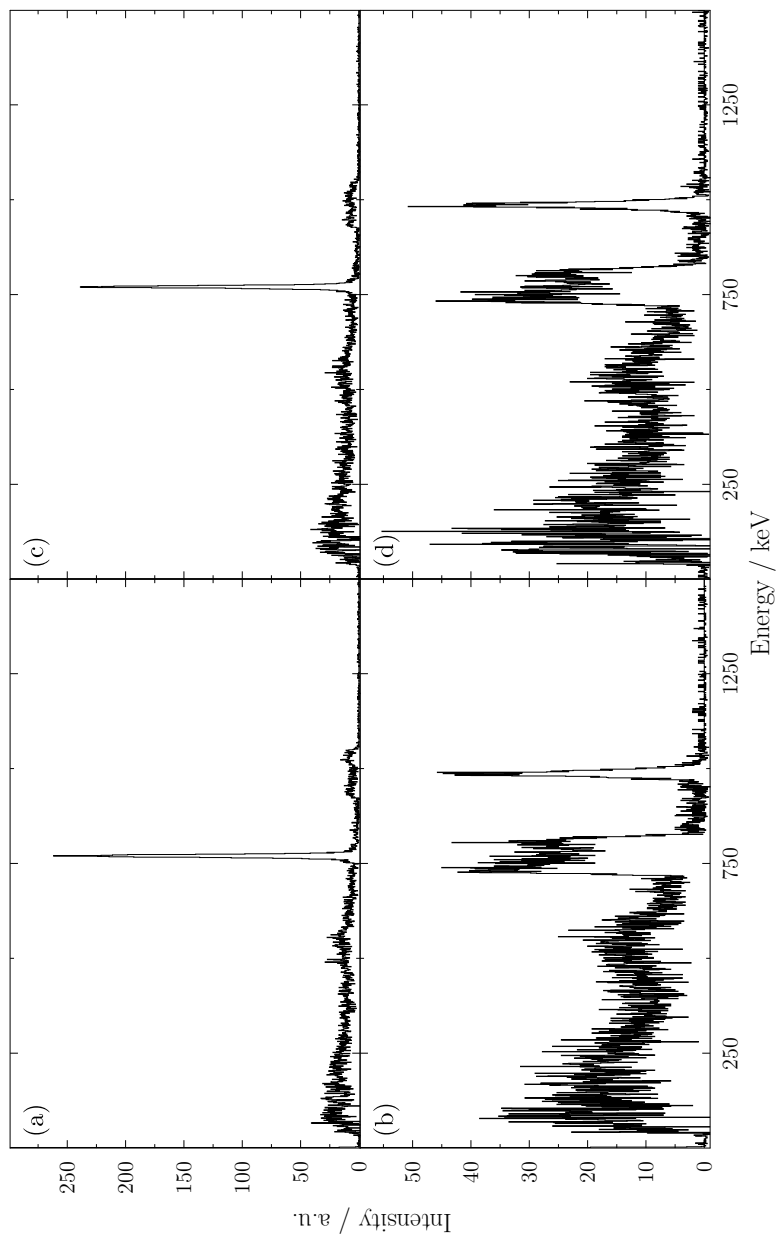


**Figure E.2.:** Background-subtracted  $\gamma$  ray spectra of the  $^{142}\text{Sm} + ^{48}\text{Ti}$  experiment. (a, c) are Doppler corrected to projectile nuclei (b, d) are corrected to target-like recoils. (a, b) are in coincidence with particles in "Cut 1", and (b, c) are in coincidence with particles in "Cut 2". The spectra are not corrected for efficiency.

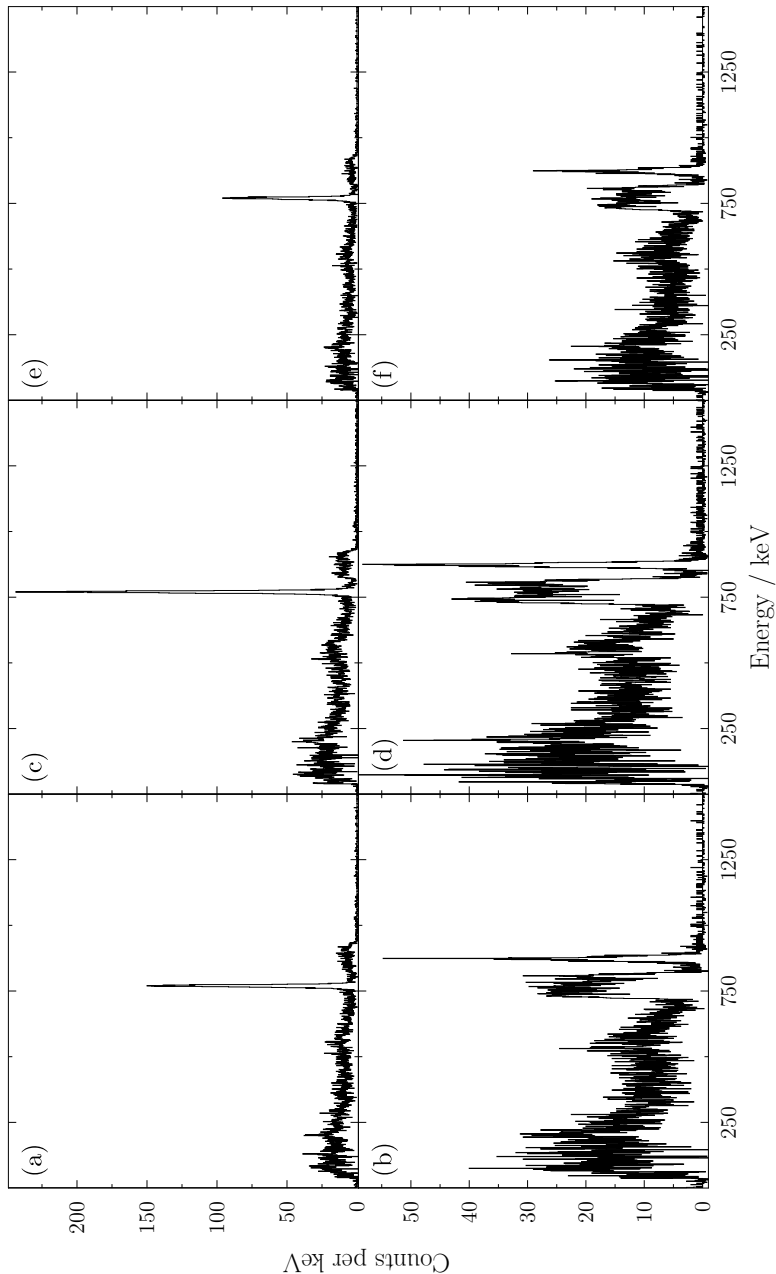


**Figure E.3.:** Background-subtracted  $\gamma$  ray spectra of the  $^{142}\text{Sm} + ^{94}\text{Mo}$  experiment. (a, c, e) are Doppler corrected to projectile nuclei (b, d, f) are corrected to target-like recoils. (a, b) are in coincidence with particles in "Target Cut 1", (b, c) are in coincidence with particles in "Target Cut 2", and (e, f) are in coincidence with particles in "Projectile Cut". The spectra are not corrected for efficiency.

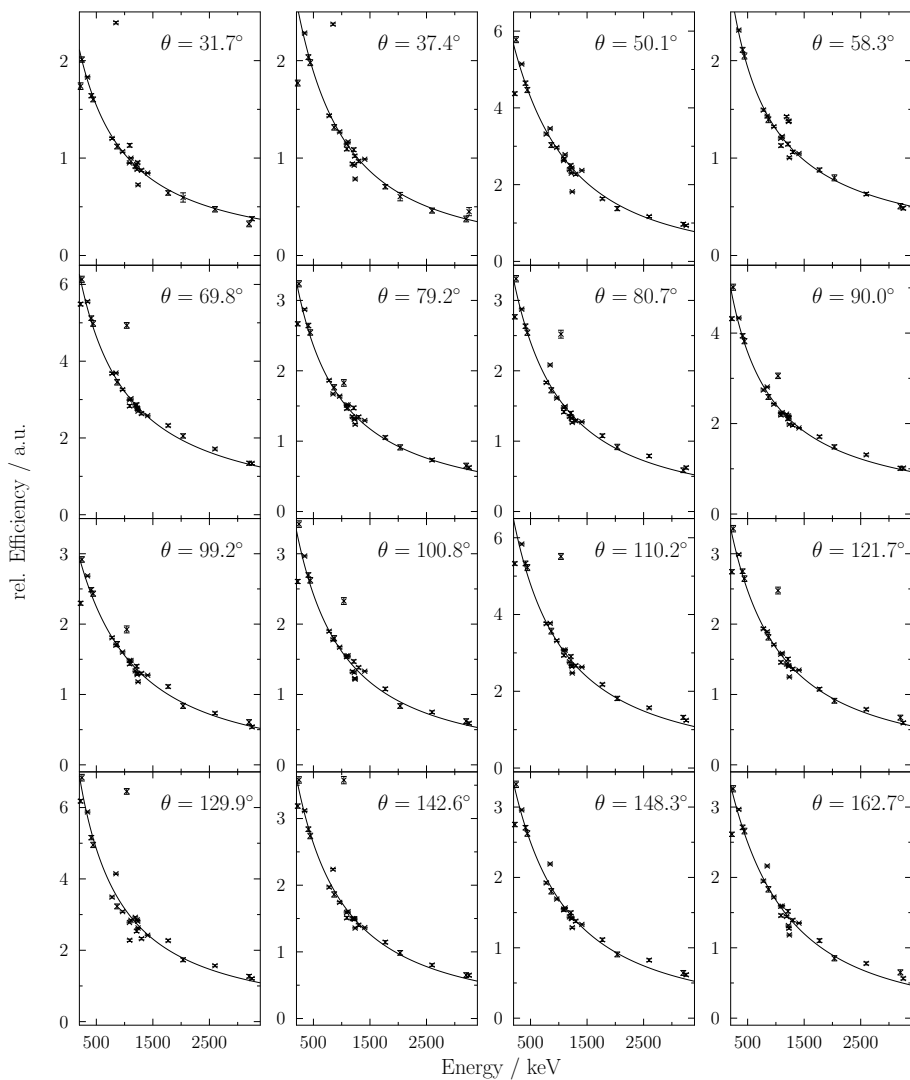


**Figure E.4:** Ringwise efficiency curves for the angular distribution analysis of the  $^{202}\text{Hg}$  experiment.



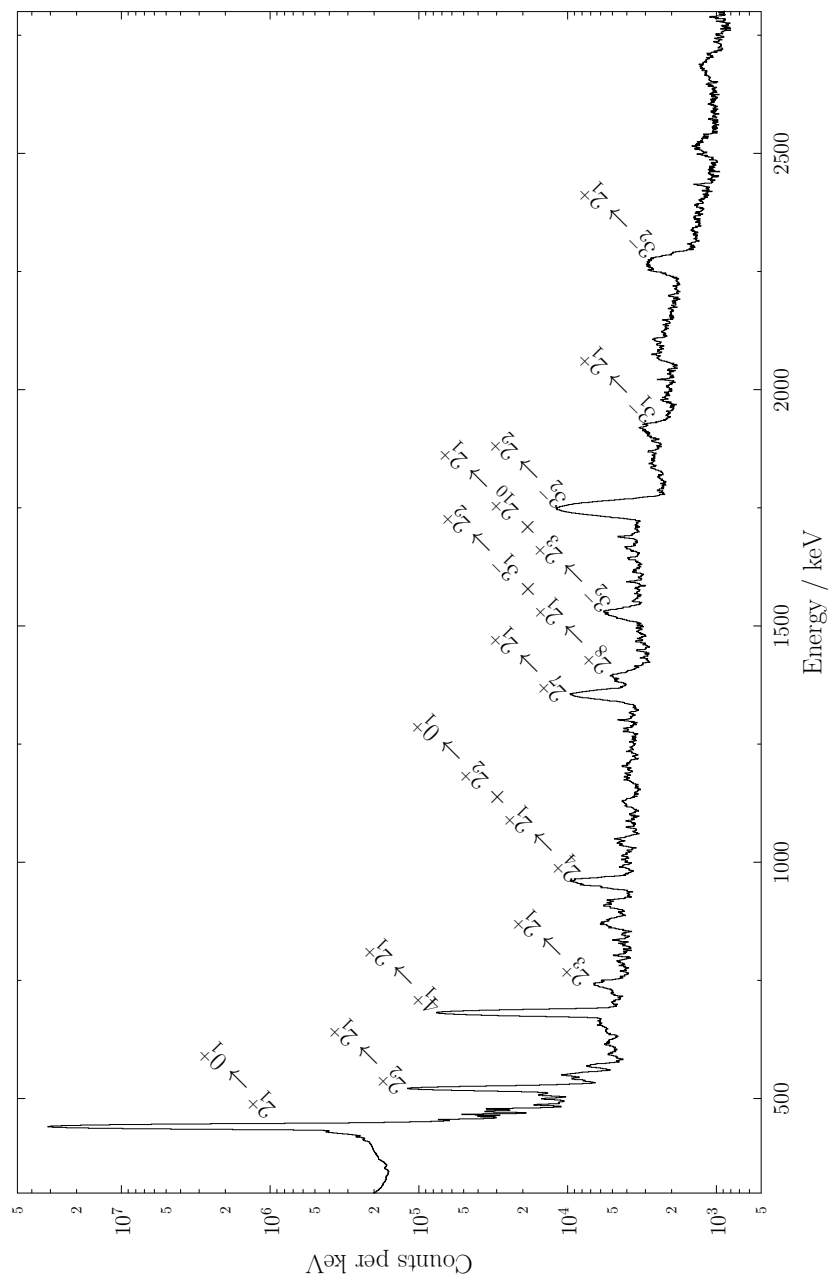


**Figure E.5.:** Background-subtracted  $\gamma$  ray singles spectrum of the  $^{202}\text{Hg}$  experiment, Doppler corrected to projectile nuclei, not corrected for efficiency.

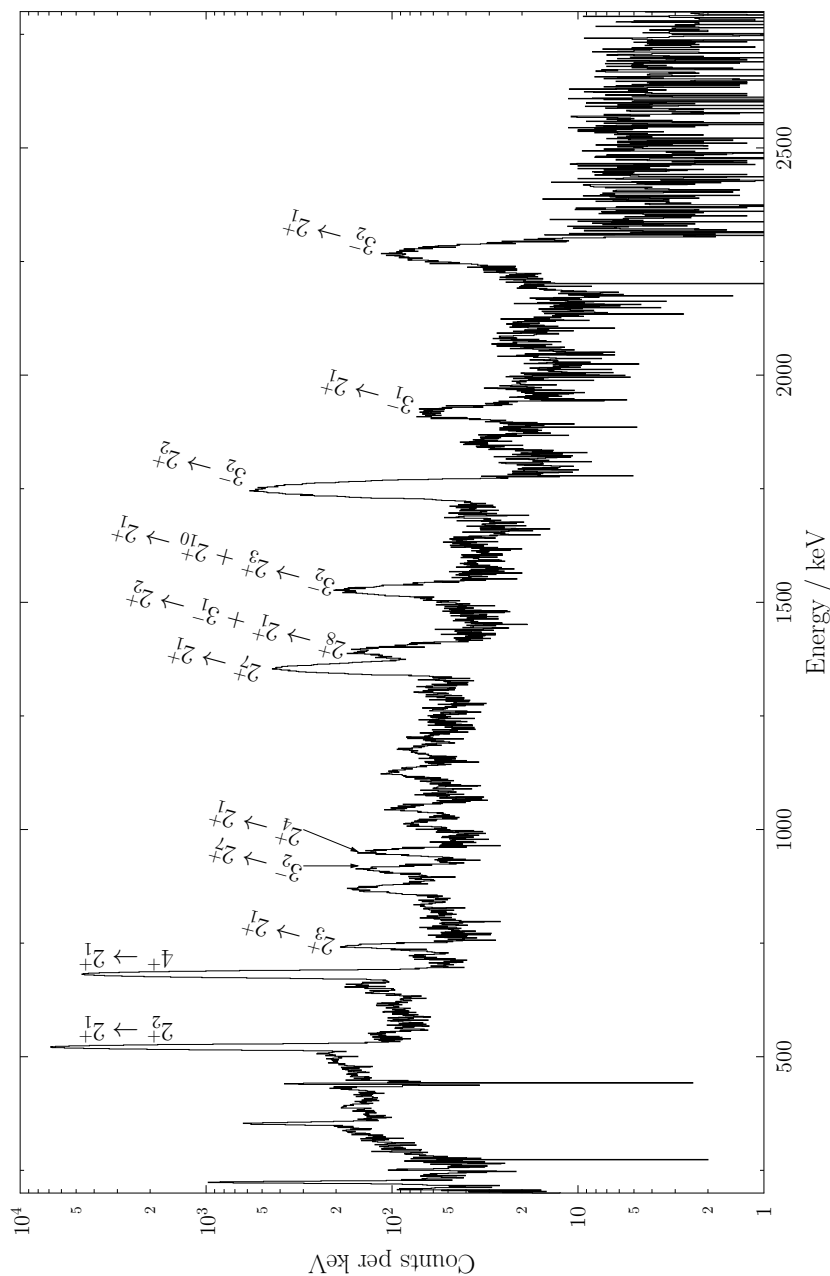


**Figure E.6.:** Background-subtracted spectrum of  $\gamma$  rays in coincidence with the  $2^+_1 \rightarrow 0^+_{1,gs}$  transition of  $^{202}\text{Hg}$ , Doppler corrected to projectile nuclei, not corrected for efficiency.

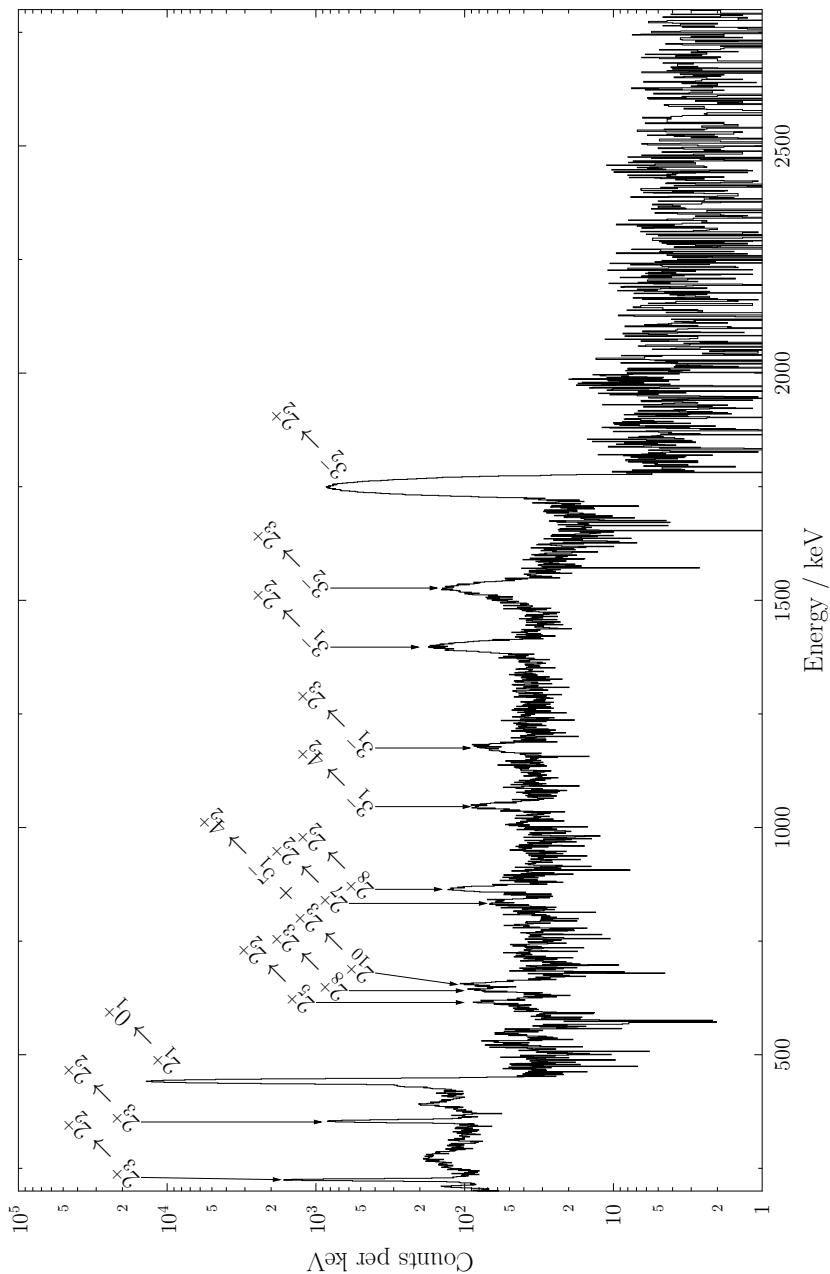


**Figure E.7.:** Background-subtracted spectrum of  $\gamma$  rays in coincidence with the  $2_2^+ \rightarrow 2_1^+$  transition of  $^{202}\text{Hg}$ , Doppler corrected to projectile nuclei; not corrected for efficiency.

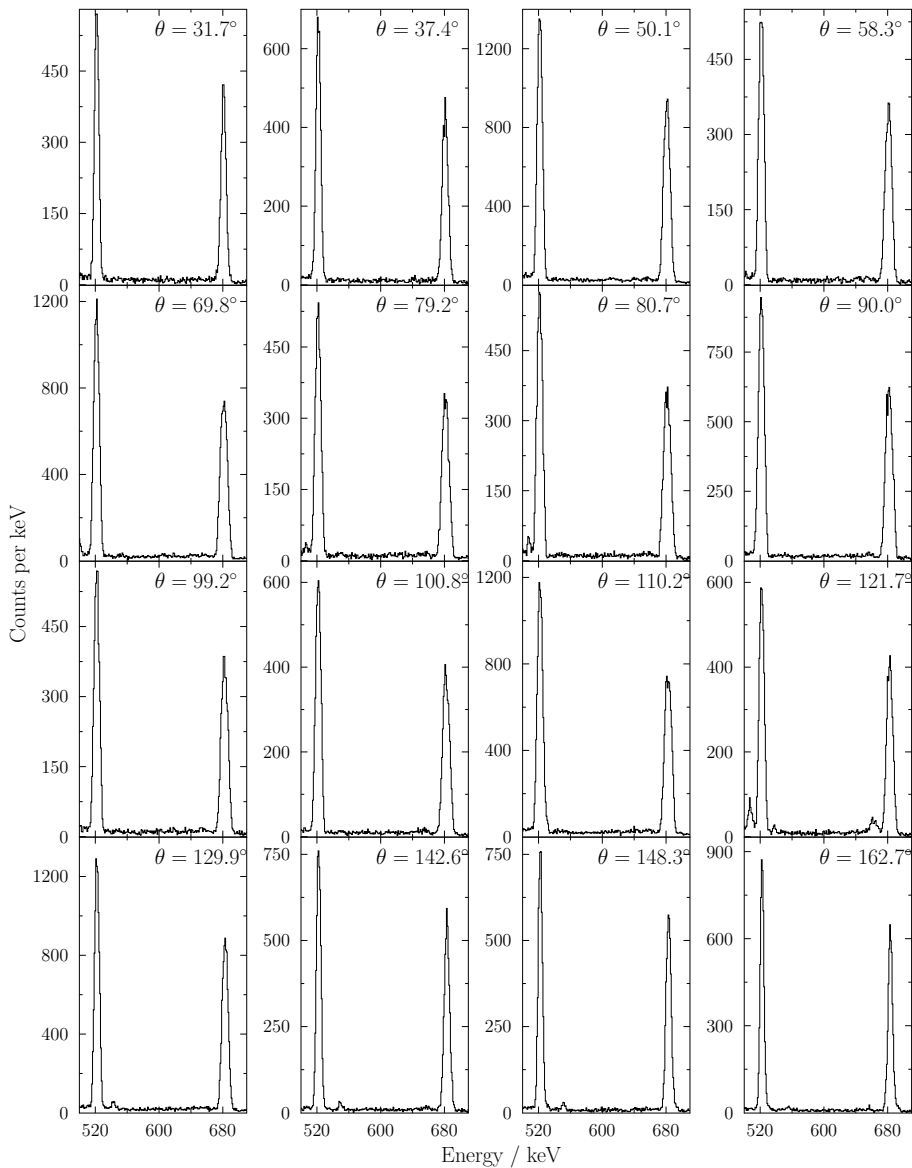


**Figure E.8.:** Ringwise  $\gamma$ -ray spectra of the 520-keV,  $2_2^+ \rightarrow 2_1^+$ , and the 680-keV,  $4_1^+ \rightarrow 2_1^+$  transitions, in coincidence with the 440-keV,  $2_1^+ \rightarrow 0_{1,gs}^+$  transition, of  $^{202}\text{Hg}$ .

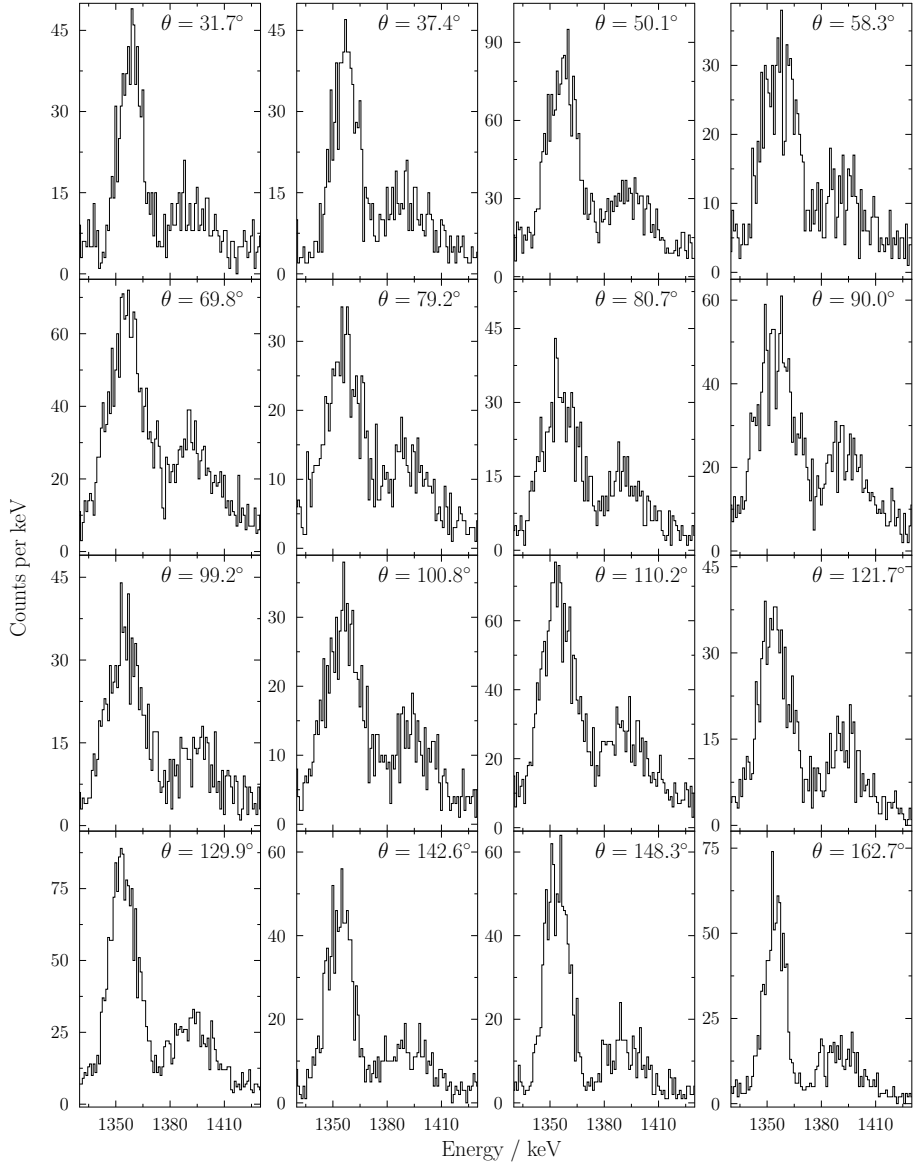


**Figure E.9.:** Ringwise  $\gamma$ -ray spectra of the 1354-keV,  $2_7^+ \rightarrow 2_1^+$ , the 1384-keV,  $2_8^+ \rightarrow 2_1^+$  and the 1397-keV,  $3_1^- \rightarrow 2_2^+$  transitions, in coincidence with the 440-keV,  $2_1^+ \rightarrow 0_{1,gs}^+$  transition, of  $^{202}\text{Hg}$ .

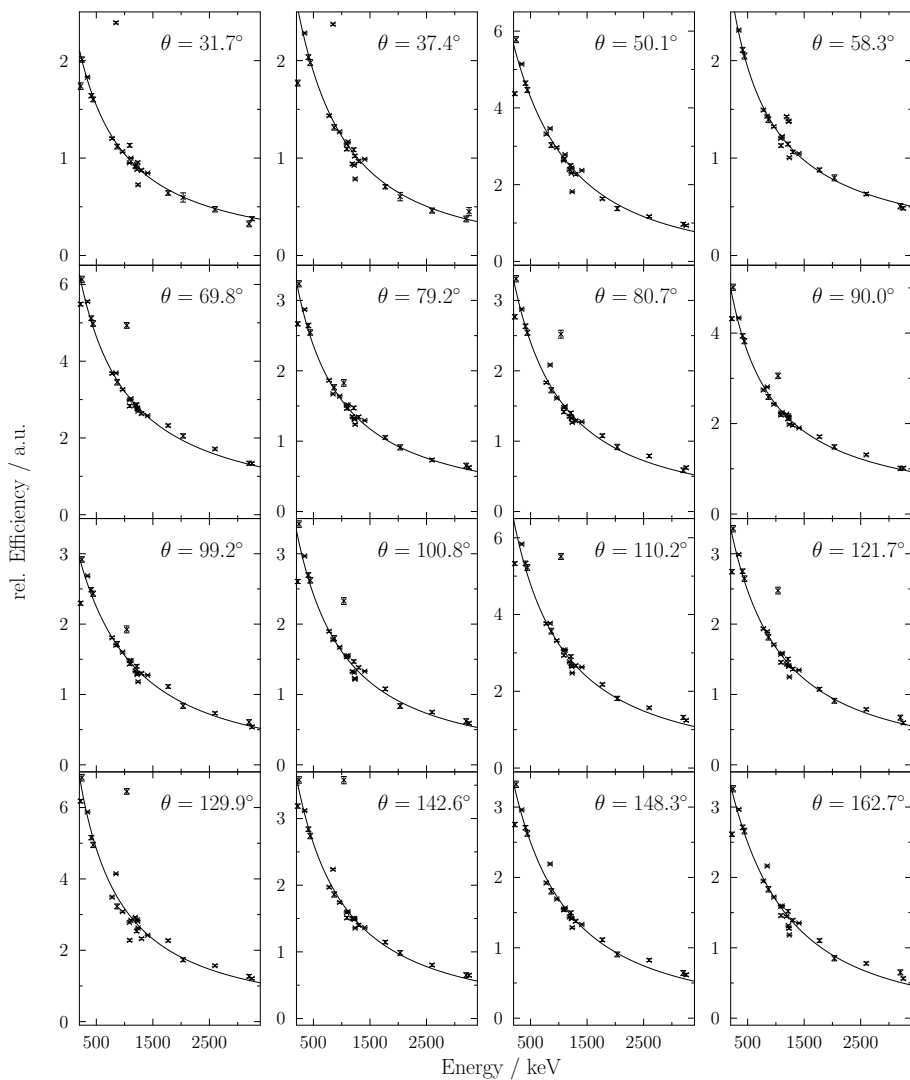


**Figure E.10.:** Ringwise efficiency curves for the angular distribution analysis of the  $^{204}\text{Hg}$  experiment.

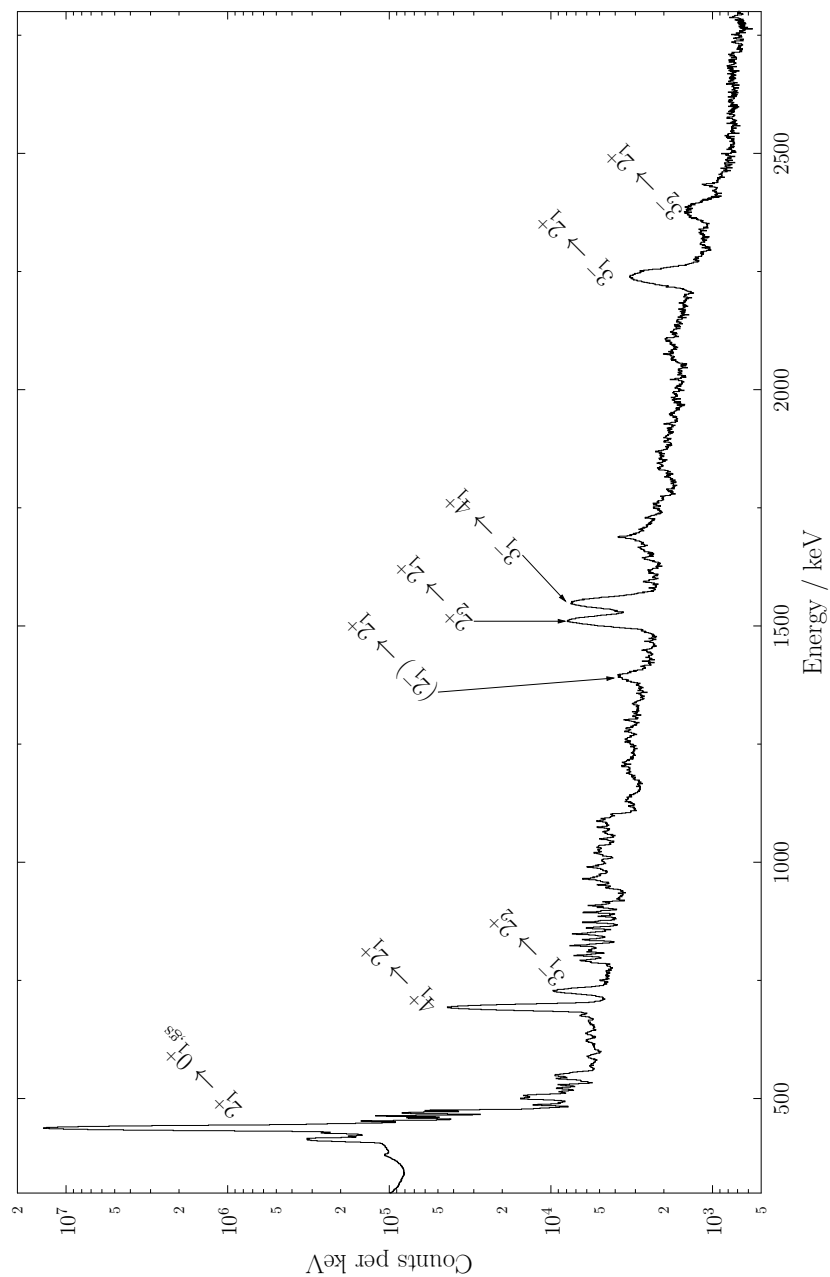


**Figure E.11.:** Background-subtracted  $\gamma$  ray singles spectrum of the  $^{204}\text{Hg}$  experiment, Doppler corrected to projectile nuclei, not corrected for efficiency.

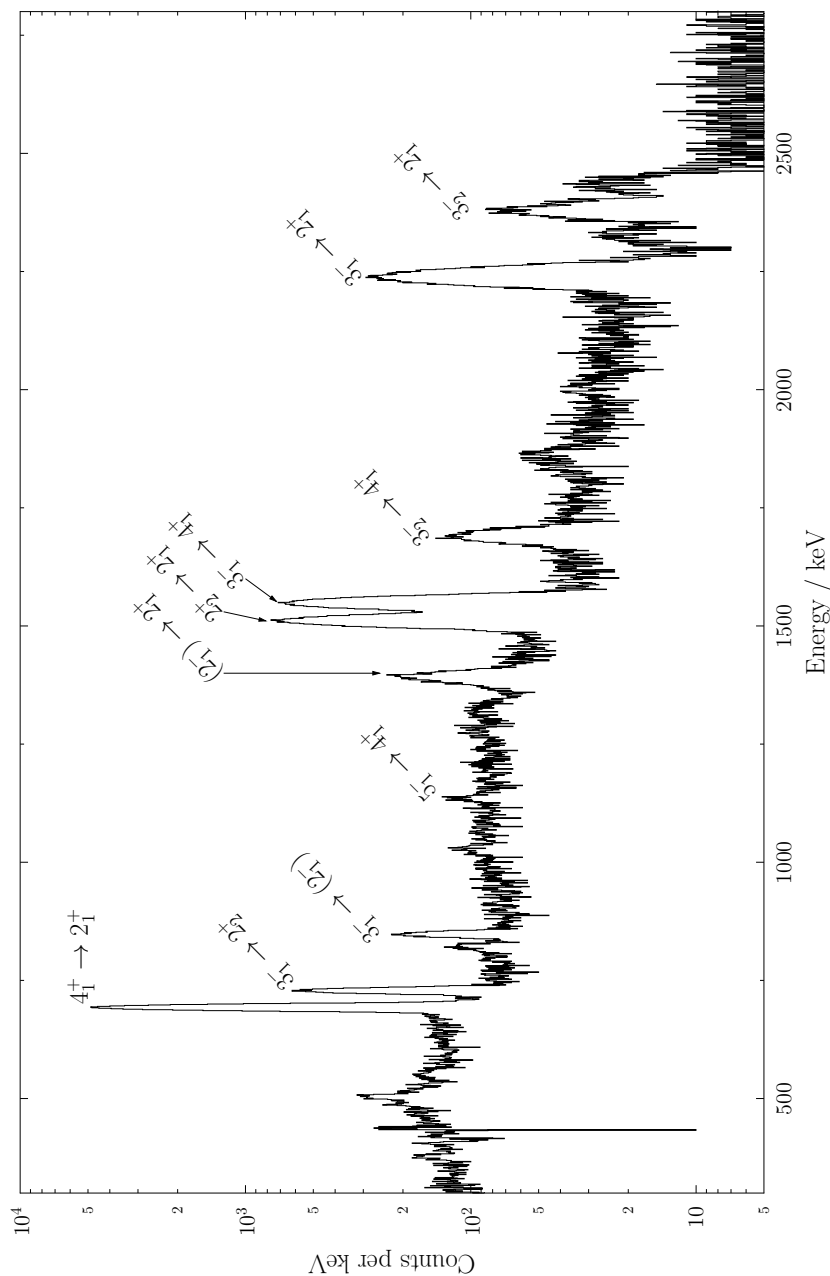


**Figure E.12.:** Background-subtracted spectrum of  $\gamma$  rays in coincidence with the  $2_1^+ \rightarrow 0_{1,gs}^+$  transition of  $^{204}\text{Hg}$ , Doppler corrected to projectile nuclei, not corrected for efficiency.



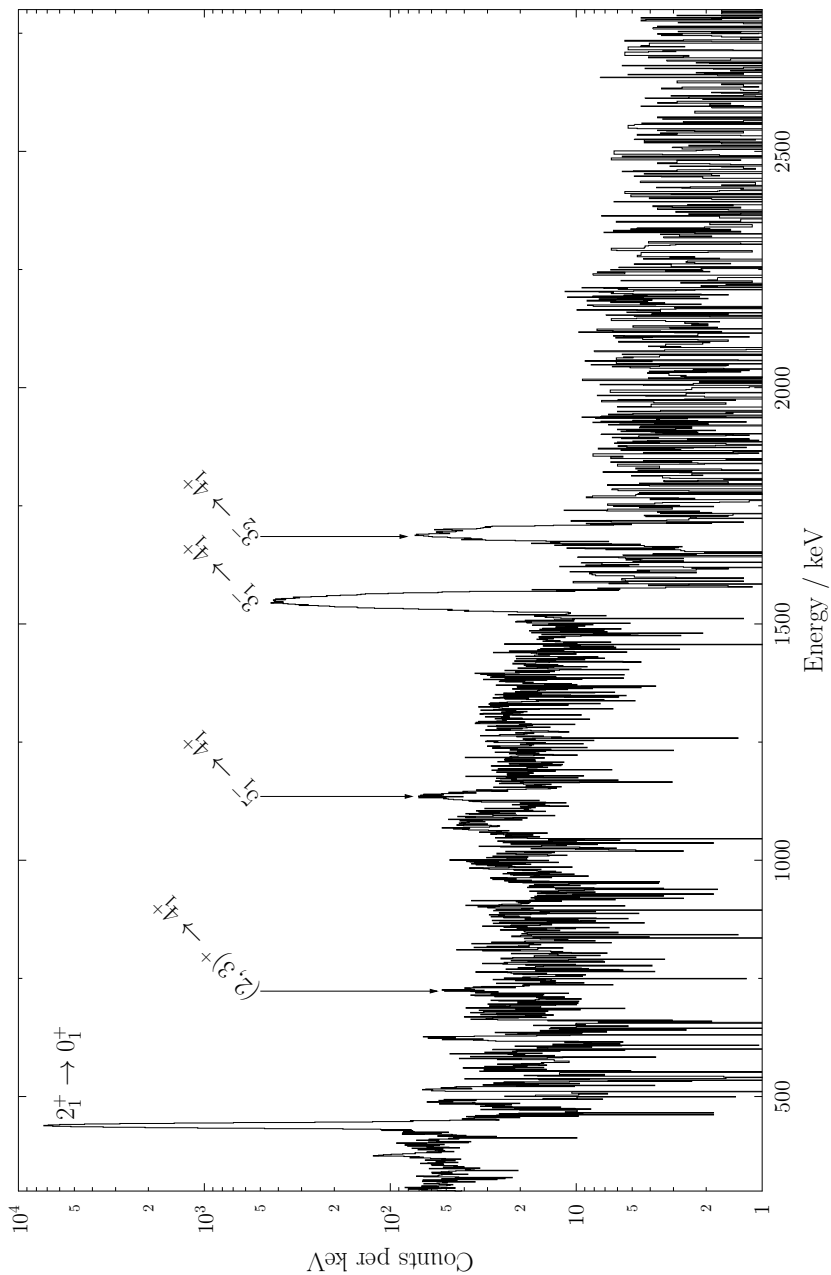


**Figure E.13:** Background-subtracted spectrum of  $\gamma$  rays in coincidence with the  $4_1^+ \rightarrow 2_1^+$  transition of  $^{204}\text{Hg}$ , Doppler corrected to projectile nuclei, not corrected for efficiency.

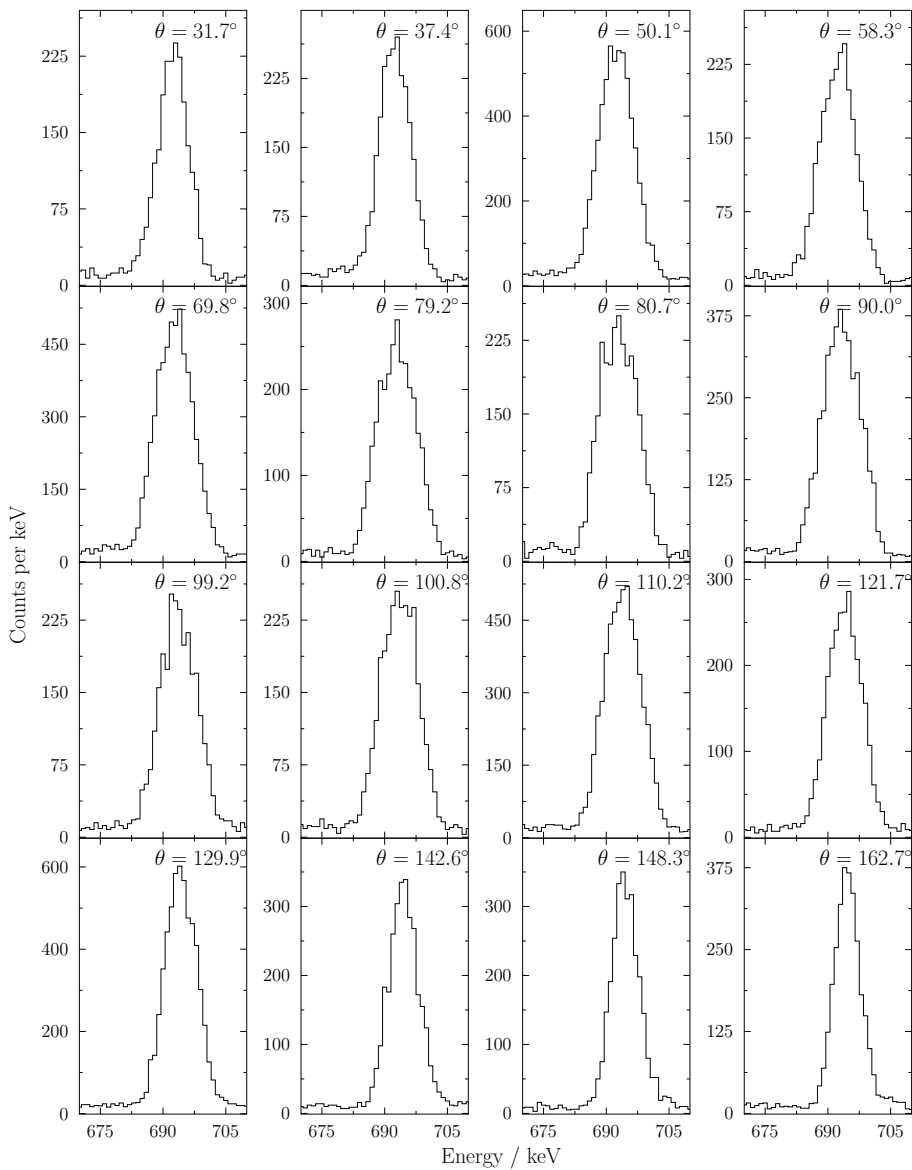


**Figure E.14.:** Ringwise  $\gamma$ -ray spectra of the 692-keV,  $4_1^+ \rightarrow 2_1^+$  transition, in coincidence with the 437-keV,  $2_1^+ \rightarrow 0_{1,gs}^+$  transition, of  $^{204}\text{Hg}$ .

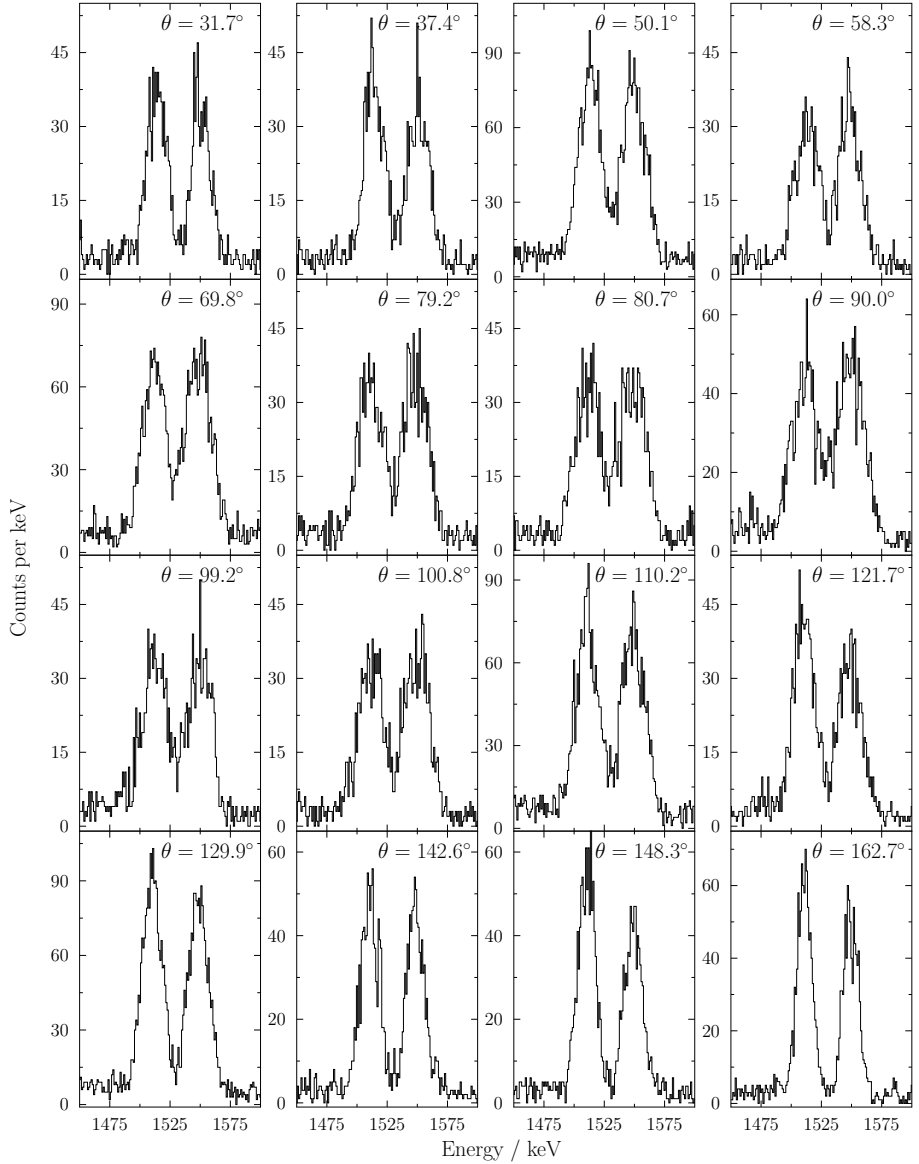


**Figure E.15.:** Ringwise  $\gamma$ -ray spectra of the 1511-keV,  $2_2^+ \rightarrow 2_1^+$ , and the 1547-keV,  $3_1^- \rightarrow 4_1^+$  transitions, in coincidence with the 437-keV,  $2_1^+ \rightarrow 0_{1,gs}^+$  transition, of  $^{204}\text{Hg}$ .



---

# Bibliography

- [1] BOHR, A.; MOTTELSON, B. R.: *Nuclear structure, Volume II: Nuclear Deformations*. W. A. Benjamin, Inc., Advanced Book Program Reading, Massachusetts, 1975
- [2] GOEPPERT-MAYER, M.; JENSEN, J. H. D.: *Elementary Theory of Nuclear Shell Structure*. John Wiley & Sons, 1955
- [3] ARIMA, A.; OHTSUKA, T.; IACHELLO, F. ; TALMI, I.: Collective nuclear states as symmetric couplings of proton and neutron excitations. In: *Physics Letters B* 66 (1977), 205
- [4] IACHELLO, F.; ARIMA, A.: *The Interacting Boson Model*. Cambridge University Press, Cambridge, 1987
- [5] DIRAC, P. A. M.: The Quantum Theory of the Emission and Absorption of Radiation. In: *Proceedings of the Royal Society of London A: Mathematical, Physical and Engineering Sciences* 114 (1927), 243
- [6] FOCK, V.: Konfigurationsraum und zweite Quantelung. In: *Zeitschrift für Physik* 75 (1932), 622
- [7] KREMER, C.; ASLANIDOU, S.; BASSAUER, S.; HILCKER, M.; KRUGMANN, A.; VON NEUMANN-COSEL, P.; OTSUKA, T.; PIETRALLA, N.; PONOMAREV, V. Y.; SHIMIZU, N.; SINGER, M.; STEINHILBER, G.; TOGASHI, T.; TSUNODA, Y.; WERNER, V. ; ZWEIDINGER, M.: First Measurement of Collectivity of Coexisting Shapes Based on Type II Shell Evolution: The Case of  $^{96}\text{Zr}$ . In: *Physical Review Letters* 117 (2016), 172503
- [8] TOGASHI, T.; TSUNODA, Y.; OTSUKA, T. ; SHIMIZU, N.: Quantum Phase Transition in the Shape of Zr isotopes. In: *Physical Review Letters* 117 (2016), 172502
- [9] PIETRALLA, N.; FRANSEN, C.; BELIC, D.; VON BRENTANO, P.; FRIESSNER, C.; KNEISSL, U.; LINNEMANN, A.; NORD, A.; PITZ, H. H.; OTSUKA, T.; SCHNEIDER, I.; WERNER, V. ; WIEDENHÖVER, I.: Transition Rates between Mixed Symmetry States: First Measurement in  $^{94}\text{Mo}$ . In: *Physical Review Letters* 83 (1999), 1303

- 
- [10] PIETRALLA, N.; BARTON, C. J.; KRÜCKEN, R.; BEAUSANG, C. W.; CAPRIO, M. A.; CASTEN, R. F.; COOPER, J. R.; HECHT, A. A.; NEWMAN, H.; NOVAK, J. R. ; ZAMFIR, N. V.: Coulomb excitation of the  $2^+_{ms}$  state of  $^{96}\text{Ru}$  in inverse kinematics. In: *Physical Review C* 64 (2001), 031301
- [11] WERNER, V.; BELIC, D.; VON BRENTANO, P.; FRANSEN, C.; GADE, A.; VON GARREL, H.; JOLIE, J.; KNEISSL, U.; KOHSTALL, C.; LINNEMANN, A.; LISETSKIY, A.; PIETRALLA, N.; PITZ, H.; SCHECK, M.; SPEIDEL, K.-H.; STEDILE, F. ; YATES, S.: Proton–neutron structure of the  $N = 52$  nucleus  $^{92}\text{Zr}$ . In: *Physics Letters B* 550 (2002), 140
- [12] RAINOVSKI, G.; PIETRALLA, N.; AHN, T.; LISTER, C. J.; JANSSENS, R. V. F.; CARPENTER, M. P.; ZHU, S. ; BARTON, C. J.: Stabilization of Nuclear Isovector Valence-Shell Excitations. In: *Physical Review Letters* 96 (2006), 122501
- [13] AHN, T.; COQUARD, L.; PIETRALLA, N.; RAINOVSKI, G.; COSTIN, A.; JANSSENS, R.; LISTER, C.; CARPENTER, M.; ZHU, S. ; HEYDE, K.: Evolution of the one-phonon  $2^+_{1,ms}$  mixed-symmetry state in  $N = 80$  isotones as a local measure for the proton–neutron quadrupole interaction. In: *Physics Letters B* 679 (2009), 19
- [14] COQUARD, L.; PIETRALLA, N.; RAINOVSKI, G.; AHN, T.; BETTERMANN, L.; CARPENTER, M. P.; JANSSENS, R. V. F.; LESKE, J.; LISTER, C. J.; MÖLLER, O.; ROTHER, W.; WERNER, V. ; ZHU, S.: Evolution of the mixed-symmetry  $2^+_{1,ms}$  quadrupole-phonon excitation from spherical to  $\gamma$ -soft Xe nuclei. In: *Physical Review C* 82 (2010), 024317
- [15] GLADNISHKI, K. A.; RAINOVSKI, G.; PETKOV, P.; JOLIE, J.; PIETRALLA, N.; BLAZHEV, A.; DAMYANOVA, A.; DANCHEV, M.; DEWALD, A.; FRANSEN, C.; HACKSTEIN, M.; KARAGYOZOV, D.; MÖLLER, O.; PISSULLA, T.; REESE, M.; ROTHER, W. ; TOPCHYNSKA, R.: Search for one-phonon mixed-symmetry states in the radioactive nucleus  $^{140}\text{Nd}$ . In: *Physical Review C* 82 (2010), 037302
- [16] DANCHEV, M.; RAINOVSKI, G.; PIETRALLA, N.; GARGANO, A.; COVELLO, A.; BAKTASH, C.; BEENE, J. R.; BINGHAM, C. R.; GALINDO-URIBARRI, A.; GLADNISHKI, K. A.; GROSS, C. J.; PONOMAREV, V. Y.; RADFORD, D. C.; RIEDINGER, L. L.; SCHECK, M.; STUCHBERY, A. E.; WAMBACH, J.; YU, C.-H. ; ZAMFIR, N. V.: One-Phonon Isovector  $2^+_{1,MS}$  State in the Neutron-Rich Nucleus  $^{132}\text{Te}$ . In: *Physical Review C* 84 (2011), 061306
- [17] AHN, T.; RAINOVSKI, G.; PIETRALLA, N.; COQUARD, L.; MÖLLER, T.; COSTIN, A.; JANSSENS, R. V. F.; LISTER, C. J.; CARPENTER, M. P. ; ZHU, S.: Identification of

- 
- the  $2^+_{1,ms}$  mixed-symmetry state in  $^{136}\text{Ce}$ . In: *Physical Review C* 86 (2012), 014303
- [18] KOICHEVA, D.; STEGMANN, R.; RAINOVSKI, G.; JOLIE, J.; PIETRALLA, N.; STAHL, C.; PETKOV, P.; BLAZHEV, A.; HENNIG, A.; BAUER, C.; BRAUNROTH, T.; CARPENTER, M.; CORTES, L.; DEWALD, A.; DJONGOLOV, M.; FRANSEN, C.; GLADNISHKI, K.; JANSSENS, R.; KARAYONCHEV, V.; LETTMANN, M.; LISTER, C.; LITZINGER, J.; MÖLLER, T.; MÖLLER-GATERMANN, C.; SCHECK, M.; SCHOLZ, P.; SCHRAMM, C.; THÖLE, P.; WERNER, V.; WÖLK, D.; ZHU, S. ; VAN ISACKER, P.: Search for mixed-symmetry states of nuclei in the vicinity of the double-magic nucleus  $^{208}\text{Pb}$ . In: *EPJ Web of Conferences* 107 (2016), 03004
  - [19] ALDER, K.; BOHR, A.; HUUS, T.; MOTTELSON, B. ; WINTHER, A.: Study of Nuclear Structure by Electromagnetic Excitation with Accelerated Ions. In: *Reviews of Modern Physics* 28 (1956), 432
  - [20] ALDER, K.; WINTHER, A.: *Coulomb Excitation*. Academic Press, 1966
  - [21] ALDER, K.; WINTHER, A.: *Electromagnetic excitation: Theory of Coulomb excitation with heavy ions*. North-Holland Publishing Company, Amsterdam-Oxford, 1975
  - [22] CLINE, D.; CZOSNYKA, T.; HAYES, A. B.; NAPIORKOWSKI, P.; WARR, N. ; WU, C. Y.: *GOSIA User Manual for Simulation and Analysis of Coulomb Excitation Experiments*, 2012
  - [23] JACKSON, J. D.: *Classical electrodynamics*. 3rd ed. Wiley, New York, 1999
  - [24] SUHONEN, J.: *From Nucleons to Nucleus*. Springer-Verlag Berlin Heidelberg, 2007
  - [25] YAMAZAKI, T.: Tables of coefficients for angular distribution of gamma rays from aligned nuclei. In: *Nuclear Data Sheets. Section A* 3 (1967), 1
  - [26] FERENTZ, M.; ROSENZWEIG, N.: In: *Argonne National Laboratory Report* , Nr. 5324
  - [27] RYBICKI, F.; TAMURA, T. ; SATCHLER, G.: Particle-gamma angular correlations following nuclear reactions. In: *Nuclear Physics A* 146 (1970), 659
  - [28] GOLDRING, G.: Hyperfine interactions in isolated ions. In: *Heavy Ion Collisions, Vol. 3*. North-Holland Publishing Company, Amsterdam, 1982, Chapter 3, 484–571

- 
- [29] STUCHBERY, A. E.; MANTICA, P. F.; WILSON, A. N.: Electron-configuration-reset time-differential recoil-in-vacuum technique for excited-state  $g$ -factor measurements on fast exotic beams. In: *Physical Review C* 71 (2005), 047302
- [30] STUCHBERY, A. E.; STONE, N. J.: Recoil in vacuum for Te ions: Calibration, models, and applications to radioactive-beam  $g$ -factor measurements. In: *Physical Review C* 76 (2007), 034307
- [31] ZHU, S.; KONDEV, F.: Nuclear Data Sheets for  $A = 202$ . In: *Nuclear Data Sheets* 109 (2008), 699
- [32] BOCKISCH, A.; BHARUTH-RAM, K.; KLEINFELD, A. M.; LIEB, K. P.: Reorientation Effect Measurements of Even Mercury Isotopes. In: *Zeitschrift für Physik A - Hadrons and Nuclei* 291 (1979), 245
- [33] SPEAR, R.; ESAT, M.; FEWELL, M.; KEAN, D.; ZABEL, T.; BAXTER, A.; HINDS, S.: Static quadrupole moments of the first excited states of  $^{200}\text{Hg}$  and  $^{202}\text{Hg}$ . In: *Nuclear Physics A* 345 (1980), 252
- [34] BILLOWES, J.: Nuclear deorientation of W, Os and Pt recoiling in vacuum at 0.02c. In: *Hyperfine Interactions* 30 (1986), 265
- [35] BALDWIN, A. M.; GOLDANSKIJ, W. I.; ROSENTAL, I. L.: *Kinematik der Kernreaktionen*. Akademie-Verlag Berlin, 1963
- [36] GREINER, W.: *Klassische Mechanik I*. Verlag Harri Deutsch, 2007
- [37] BIANCO, D.; ANDREOZZI, F.; LO IUDICE, N.; PORRINO, A.; KNAPP, F.: Matrix diagonalization algorithm and its applicability to the nuclear shell model. In: *Physical Review C* 84 (2011), 024310
- [38] SOLOVIEV, V. G.: *Theory of Atomic Nuclei: Quasiparticles and Phonons*. IOP Publishing Ltd., 1992
- [39] CASTEN, R. F.; HODGSON, P. E. (Hrsg.): *Nuclear Structure from a Simple Perspective*. Oxford Science Publications, 2005 (Oxford Studies in Nuclear Physics)
- [40] GOEPPERT-MAYER, M.: On Closed Shells in Nuclei. In: *Physical Review* 74 (1948), 235
- [41] GOEPPERT-MAYER, M.: On Closed Shells in Nuclei. II. In: *Physical Review* 75 (1949), 1969



- 
- [42] HAXEL, O.; JENSEN, J. H. D. ; SUESS, H. E.: On the "Magic Numbers" in Nuclear Structure. In: *Physical Review* 75 (1949), 1766
- [43] LIPAS, P. O.; BRENTANO, P. von ; GELBERG, A.: Proton-neutron symmetry in boson models of nuclear structure. In: *Reports on Progress in Physics* 53 (1990), 1355
- [44] PIETRALLA, N.; VON BRENTANO, P. ; LISETSKIY, A.: Experiments on multiphonon states with proton–neutron mixed symmetry in vibrational nuclei. In: *Progress in Particle and Nuclear Physics* 60 (2008), 225
- [45] VAN ISACKER, P.; HEYDE, K.; JOLIE, J. ; SEVRIN, A.: The F-spin symmetric limits of the neutron-proton interacting boson model. In: *Annals of Physics* 171 (1986), 253
- [46] BOHLE, D.; RICHTER, A.; STEFFEN, W.; DIEPERINK, A.; IUDICE, N. L.; PALUMBO, F. ; SCHOLTEN, O.: New magnetic dipole excitation mode studied in the heavy deformed nucleus  $^{156}\text{Gd}$  by inelastic electron scattering. In: *Physics Letters B* 137 (1984), 27
- [47] SMIRNOVA, N. A.; PIETRALLA, N.; MIZUSAKI, T. ; ISACKER, P. V.: Interrelation between the isoscalar octupole phonon and the proton–neutron mixed-symmetry quadrupole phonon in near-spherical nuclei. In: *Nuclear Physics A* 678 (2000), 235
- [48] LO IUDICE, N.; PONOMAREV, V. Y.; STOYANOV, C.; SUSHKOV, A. V. ; VORONOV, V. V.: Low-energy nuclear spectroscopy in a microscopic multiphonon approach. In: *Journal of Physics G: Nuclear and Particle Physics* 39 (2012), 043101
- [49] ISOLDE WEBPAGE: <https://isolde.web.cern.ch>
- [50] JONSON, B.; RICHTER, A.: More than Three Decades of ISOLDE Physics. In: *Hyperfine Interactions* 129 (2000), 1
- [51] KUGLER, E.: The ISOLDE facility. In: *Hyperfine Interactions* 129 (2000), 23
- [52] NÖRTERSHÄUSER, W.: Recent developments in collinear laser spectroscopy at COLLAPS/ISOLDE. In: *Hyperfine Interactions* 198 (2010), 73
- [53] BOLLEN, G.; BECKER, S.; KLUGE, H.-J.; KÖNIG, M.; MOORE, R.; OTTO, T.; RAIMBAULT-HARTMANN, H.; SAVARD, G.; SCHWEIKHARD, L. ; STOLZENBERG, H.: ISOLTRAP: a tandem Penning trap system for accurate on-line mass determination of short-lived isotopes. In: *Nuclear Instruments and Methods in*

- [54] HABS, D.; KESTER, O.; SIEBER, T.; BONGERS, H.; EMHOFFER, S.; REITER, P.; THIROLF, P.; BOLLEN, G.; AYSTÖ, J.; FORSTNER, O.; RAVN, H.; NILSSON, T.; OINONEN, M.; SIMON, H.; CEDERKALL, J.; AMES, F.; SCHMIDT, P.; HUBER, G.; LILJEBY, L.; SKEPPSTEDT, O.; RENSFELT, K.; WENANDER, F.; JONSON, B.; NYMAN, G.; VON HAHN, R.; PODLECH, H.; REPNOW, R.; GUND, C.; SCHWALM, D.; SCHEMPF, A.; KÜHNEL, K.-U.; WELSCH, C.; RATZINGER, U.; WALTER, G.; HUCK, A.; KRUGLOV, K.; HUYSE, M.; BERGH, P. Van d.; VAN DUPPEN, P.; WEISSMAN, L.; SHOTTER, A.; OSTROWSKI, A.; DAVINSON, T.; WOODS, P.; CUB, J.; RICHTER, A.; SCHRIEDER, G.: The REX-ISOLDE project. In: *Hyperfine Interactions* 129 (2000), 43
- [55] REX-ISOLDE WEBPAGE: <https://rex-isolde.web.cern.ch>
- [56] WARR, N.; WALLE, J. Van d.; ALBERS, M.; AMES, F.; BASTIN, B.; BAUER, C.; BILDSTEIN, V.; BLAZHEV, A.; BÖNIG, S.; BREE, N.; BRUYNEEL, B.; BUTLER, P. A.; CEDERKÄLL, J.; CLÉMENT, E.; COCOLIOS, T. E.; DAVINSON, T.; DE WITTE, H.; DELAHAYE, P.; DIJULIO, D. D.; DIRIKEN, J.; EBERTH, J.; EKSTRÖM, A.; ELSEVIERS, J.; EMHOFFER, S.; FEDOROV, D. V.; FEDOSSEEV, V. N.; FRANCHOO, S.; FRANSEN, C.; GAFFNEY, L. P.; GERL, J.; GEORGIEV, G.; GERNHÄUSER, R.; GRAHN, T.; HABS, D.; HESS, H.; HURST, A. M.; HUYSE, M.; IVANOV, O.; IWANICKI, J.; JENKINS, D. G.; JOLIE, J.; KESTELOOT, N.; KESTER, O.; KÖSTER, U.; KRAUTH, M.; KRÖLL, T.; KRÜCKEN, R.; LAUER, M.; LESKE, J.; LIEB, K. P.; LUTTER, R.; MAIER, L.; MARSH, B. A.; MÜCHER, D.; MÜNCH, M.; NIEDERMAIER, O.; PAKARINEN, J.; PANTEA, M.; PASCOVICI, G.; PATRONIS, N.; PAUWELS, D.; PETTS, A.; PIETRALLA, N.; RAABE, R.; RAPISARDA, E.; REITER, P.; RICHTER, A.; SCHAILE, O.; SCHECK, M.; SCHEIT, H.; SCHRIEDER, G.; SCHWALM, D.; SEIDLITZ, M.; SELIVERSTOV, M.; SIEBER, T.; SIMON, H.; SPEIDEL, K. H.; STAHL, C.; STEFANESCU, I.; THIROLF, P. G.; THOMAS, H. G.; THÜRAUF, M.; VAN DUPPEN, P.; VOULOT, D.; WADSWORTH, R.; WALTER, G.; WEISSHAAR, D.; WENANDER, F.; WIENS, A.; WIMMER, K.; WOLF, B. H.; WOODS, P. J.; WRZOSEK-LIPSKA, K.; ZELL, K. O.: The Miniball Spectrometer. In: *European Physical Journal A: Hadrons and Nuclei* 49 (2013), 1
- [57] WEISSHAAR, D. W.: *MINIBALL Ein neuartiges Gamma-Spektrometer mit ortsaufauflösenden Germaniumdetektoren*, Universität zu Köln, Ph.D. Thesis, 2003
- [58] WARR, N.: *The Miniball Double-Sided Silicon Strip Detector (CD)*, August 2007. – unpublished

- 
- [59] BILDSTEIN, V.; GERNHÄUSER, R.; KRÖLL, T.; KRÜCKEN, R.; WIMMER, K.; VAN DUPPEN, P.; HUYSE, M.; PATRONIS, N. ; RAABE, R.: T-REX. In: *European Physical Journal A: Hadrons and Nuclei* 48 (2012), 85
- [60] ATLAS WEBPAGE: <https://www.phy.anl.gov>
- [61] PARDO, R. C.; SAVARD, G. ; JANSSENS, R. V. F.: ATLAS with CARIBU: A Laboratory Portrait. In: *Nuclear Physics News* 26 (2016), Nr. 1, 5
- [62] LEE, I.-Y.: The GAMMASPHERE. In: *Nuclear Physics A* 520 (1990), 641c
- [63] BEAUSANG, C. W.; SIMPSON, J.: Large arrays of escape suppressed spectrometers for nuclear structure experiments. In: *Journal of Physics G: Nuclear and Particle Physics* 22 (1996), 527
- [64] RILEY, M.; HESHER, C.: <http://nucalf.physics.fsu.edu/~riley/gamma/gamma3.html>
- [65] NIEDERMAIER, O.: *Low-Energy Coulomb Excitation of the Neutron-Rich Mg Isotopes  $^{30}\text{Mg}$  and  $^{32}\text{Mg}$* , Combined Faculties for the Natural Sciences and for Mathematics of the Ruperto-Carola University of Heidelberg, Germany, Ph.D. Thesis, 2005, unveröffentlicht
- [66] BAUER, C.: *Level Lifetimes and Quadrupole Moments from Projectile Coulomb Excitation of  $A \approx 130$  Nuclei*, Technische Universität Darmstadt, Ph.D. Thesis, 2013
- [67] KENNEDY, G. G.; GUJRATHI, S. C. ; MARK, S. K.: Structure of  $^{142}\text{Sm}$  from the decay of  $^{142}\text{Eu}$ . In: *Physical Review C* 12 (1975), 553
- [68] STRUBLE, G. L.; MANN, L. G.; LANIER, R. G.; BUCKLEY, W. M.; KERN, J.; CRAWLEY, G.; GALES, S.; MUELLER, D. ; GIRSHICK, F: Influence of complex states and deformation on neutron pairing vibrations in the even Sm isotopes. In: *Physical Review C* 23 (1981), 2447
- [69] LACH, M.; STYCZEN, J.; JULIN, R.; PIIPARINEN, M.; BEUSCHER, H.; KLEINHEINZ, P. ; BLOMQVIST, J.: The  $10^+$  states of  $\nu h_{11/2}^{-2}$  and  $\pi h_{11/2}^2$  character in the  $N = 80$  isotones  $^{144}\text{Gd}$  and  $^{142}\text{Sm}$ . In: *Zeitschrift für Physik A - Hadrons and Nuclei* 319 (1984), 235
- [70] FIRESTONE, R. B.; GILAT, J.; NITSCHKE, J. M.; WILMARTH, P. A. ; VIERINEN, K. S.: Decay studies of neutron deficient nuclei near the  $Z=64$  subshell:  $^{142}\text{Dy}$ ,  $^{140,142}\text{Tb}$ ,  $^{140,142}\text{Gd}$ ,  $^{140,142}\text{Eu}$ ,  $^{142}\text{Sm}$ , and  $^{142}\text{Pm}$ . In: *Physical Review C* 43 (1991), 1066

- 
- [71] JOHNSON, T.; SYMOCHKO, D.; FADIL, M. ; TULI, J.: Nuclear Data Sheets for  $A = 142$ . In: *Nuclear Data Sheets* 112 (2011), 1949
- [72] PELTE, D.; SCHWALM, D.: In-Beam Gamma-Ray Spectroscopy with Heavy Ions. In: *Heavy Ion Collisions, Vol. 3*. North-Holland Publishing Company, Amsterdam, 1982, Chapter 1, 1–297
- [73] OWER, H.: *Coulombanregung von Hochspinzuständen in  $^{232}\text{Th}$ ,  $^{234}\text{U}$  und  $^{236}\text{U}$* , Johann Wolfgang Goethe-Universität Frankfurt am Main, Ph.D. Thesis, 1980
- [74] CZOSNYKA, T.; CLINE, D. ; WU, C. Y.: GOSIA, A Semiclassical Coulomb-Excitation Least-Squares Search Code. In: *Bulletin of the American Physical Society* 28 (1983), 745
- [75] WINTHER, A.; BOER, J. de: A Computer Program for Multiple Coulomb Excitation. In: *California Institute of Technology, Technical Report* (1965)
- [76] MÖLLER, T.: *Aspects of nuclear collectivity studied in projectile Coulomb excitation experiments*, Technische Universität Darmstadt, Ph.D. Thesis, 2014
- [77] STEGMANN, R.: *Investigation of the  $2_1^+$  state in radioactive  $^{140,142}\text{Sm}$  by Coulomb excitation*, Master's Thesis, 2013. – unpublished
- [78] STEGMANN, R.; BAUER, C.; RAINOVSKI, G.; PIETRALLA, N.; STAHL, C.; BÖNIG, S.; ILIEVA, S.; BLAZHEV, A.; DAMYANOVA, A.; DANCHEV, M.; GLADNISHKI, K.; JOLIE, J.; LUTTER, R.; PAKARINEN, J.; RADECK, D.; RAPISARDA, E.; REITER, P.; SCHECK, M.; SIEBECK, B.; STORA, T.; THÖLE, P.; THOMAS, T.; THÜRAUF, M.; VERMEULEN, M. J.; VOULOT, D.; WARR, N.; WENANDER, F.; WERNER, V. ; DE WITTE, H.: Evolution of quadrupole collectivity in  $N = 80$  isotones toward the  $Z = 64$  subshell gap: The  $B(E2; 2_1^+ \rightarrow 0_1^+)$  value of  $^{142}\text{Sm}$ . In: *Physical Review C* 91 (2015), 054326
- [79] ARLT, R.; BAIER, G.; MUSIOL, G.; PEKER, L. K.; PFREPPER, G. ; STRUSNY, H.: Decay Schemes of Short-Lived Neutron-Deficient Isotopes of Samarium and Promethium. A New Isotope  $^{141}\text{Sm}$ . In: *Izv. Akad. Nauk SSSR* (1970), Ser. Fiz. 34, 754
- [80] MALAN, H. P.; MUNZEL, H. ; PFENNIG, G.: The Europium Isotopes  $^{142}\text{Eu}$ ,  $^{143}\text{Eu}$  and  $^{144}\text{Eu}$ . In: *Radiochimica Acta* 5 (1966), 24

- 
- [81] ALKHAZOV, G. D.; BATIST, L. H.; BYKOV, A. A.; MOROZ, F. V.; ORLOV, S. Y.; TARASOV, V. K. ; WITTMANN, V. D.: Beta-decay energy measurements using total gamma-absorption spectroscopy. In: *Zeitschrift für Physik A - Hadrons and Nuclei* 344 (1993), 425
- [82] SOKAL, R. R.; ROHLF, F. J.: *Biometry : the principles and practice of statistics in biological research*. 2.ed. New York : Freeman, 1981. – ISBN 0-7167-2411-1
- [83] RAMAN, S.; NESTOR, C. W. ; TIKKANEN, P: Transition Probability from the Ground to the First-Excited  $2^+$  State of Even-Even Nuclides. In: *Atomic Data and Nuclear Data Tables* 78 (2001), 1
- [84] STONE, N.: Table of Nuclear Magnetic Dipole and Electric Quadrupole Moments. In: *Atomic Data and Nuclear Data Tables* 90 (2005), 75
- [85] PRITYCHENKO, B.; CHOQUETTE, J.; HOROI, M.; KARAMY, B. ; SINGH, B.: An Update of the B(E2) Evaluation for  $0_1^+ \rightarrow 2_1^+$  Transitions in Even-Even Nuclei near  $N \sim Z \sim 28$ . In: *Atomic Data and Nuclear Data Tables* 98 (2012), 798
- [86] SALÉM-VASCONCELOS, S.; BECHARA, M. J.; HIRATA, J. H. ; DIETZSCH, O.: Quadrupole Moment of the First  $2^+$  Excited State in  $^{64}\text{Zn}$ . In: *Physical Review C* 38 (1988), 2439
- [87] RAGHAVAN, P: Table of Nuclear Moments. In: *Atomic Data and Nuclear Data Tables* 42 (1989), 189
- [88] BERINGER, J.; ARGUIN, J. F.; BARNETT, R. M.; COPIC, K.; DAHL, O.; GROOM, D. E.; LIN, C. J.; LYS, J.; MURAYAMA, H.; WOHL, C. G.; YAO, W. M.; ZYLA, P. A.; AMSLER, C.; ANTONELLI, M.; ASNER, D. M.; BAER, H.; BAND, H. R.; BASAGLIA, T.; BAUER, C. W.; BEATTY, J. J.; BELOUSOV, V. I.; BERGREN, E.; BERNARDI, G.; BERTL, W.; BETHKE, S.; BICHEL, H.; BIEBEL, O.; BLUCHER, E.; BLUSK, S.; BROOIJMANS, G.; BUCHMUELLER, O.; CAHN, R. N.; CARENA, M.; CECCUCCI, A.; CHAKRABORTY, D.; CHEN, M. C.; CHIVUKULA, R. S.; COWAN, G.; D'AMBROSIO, G.; DAMOUR, T.; FLORIAN, D. de; GOUVÊA, A. de; DeGRAND, T.; JONG, P. de; DISSERTORI, G.; DOBRESU, B.; DOSER, M.; DREES, M.; EDWARDS, D. A.; EIDELMAN, S.; ERLER, J.; EZHELA, V. V.; FETSCHER, W.; FIELDS, B. D.; FOSTER, B.; GAISSER, T. K.; GARREN, L.; GERBER, H. J.; GERBIER, G.; GHERGHETTA, T.; GOLWALA, S.; GOODMAN, M.; GRAB, C.; GRITSAN, A. V.; GRIVAZ, J. F.; GRÜNEWALD, M.; GURTU, A.; GUTSCHE, T.; HABER, H. E.; HAGIWARA, K.; HAGMANN, C.; HANHART, C.; HASHIMOTO, S.; HAYES, K. G.; HEFFNER, M.; HELTSLEY, B.; HERNÁNDEZ-REY, J. J.; HIKASA, K.; HÖCKER, A.; HOLDER, J.; HOLTKAMP, A.; HUSTON, J.;

JACKSON, J. D.; JOHNSON, K. F.; JUNK, T.; KARLEN, D.; KIRKBY, D.; KLEIN, S. R.; KLEMP, E.; KOWALEWSKI, R. V.; KRAUSS, F.; KREPS, M.; KRUSCHE, B.; KUYANOV, Y. V.; KWON, Y.; LAHAV, O.; LAIHO, J.; LANGACKER, P.; LIDDLE, A.; LIGETI, Z.; LISS, T. M.; LITTENBERG, L.; LUGOVSKY, K. S.; LUGOVSKY, S. B.; MANNEL, T.; MANOHAR, A. V.; MARCIANO, W. J.; MARTIN, A. D.; MASONI, A.; MATTHEWS, J.; MILSTEAD, D.; MIQUEL, R.; MÖNIG, K.; MOORTGAT, F.; NAKAMURA, K.; NARAIN, M.; NASON, P.; NAVAS, S.; NEUBERT, M.; NEVSKI, P.; NIR, Y.; OLIVE, K. A.; PAPE, L.; PARSONS, J.; PATRIGNANI, C.; PEACOCK, J. A.; PETCOV, S. T.; PIEPKE, A.; POMAROL, A.; PUNZI, G.; QUADT, A.; RABY, S.; RAFFELT, G.; RATCLIFF, B. N.; RICHARDSON, P.; ROESLER, S.; ROLLI, S.; ROMANIOUK, A.; ROSENBERG, L. J.; ROSNER, J. L.; SACHRAJDA, C. T.; SAKAI, Y.; SALAM, G. P.; SARKAR, S.; SAULI, F.; SCHNEIDER, O.; SCHOLBERG, K.; SCOTT, D.; SELIGMAN, W. G.; SHAEVITZ, M. H.; SHARPE, S. R.; SILARI, M.; SJÖSTRAND, T.; SKANDS, P.; SMITH, J. G.; SMOOT, G. F.; SPANIER, S.; SPIELER, H.; STAHL, A.; STANEV, T.; STONE, S. L.; SUMIYOSHI, T.; SYPHERS, M. J.; TAKAHASHI, F.; TANABASHI, M.; TERNING, J.; TITOV, M.; TKACHENKO, N. P.; TÖRNQVIST, N. A.; TOVEY, D.; VALENCIA, G.; BIBBER, K. van; VENANZONI, G.; VINCTER, M. G.; VOGEL, P.; VOGT, A.; WALKOWIAK, W.; WALTER, C. W.; WARD, D. R.; WATARI, T.; WEIGLEIN, G.; WEINBERG, E. J.; WIENCKE, L. R.; WOLFENSTEIN, L.; WOMERSLEY, J.; WOODY, C. L.; WORKMAN, R. L.; YAMAMOTO, A.; ZELLER, G. P.; ZENIN, O. V.; ZHANG, J.; ZHU, R. Y.; HARPER, G.; LUGOVSKY, V. S. ; SCHAFFNER, P.: Review of Particle Physics. In: *Physical Review D* 86 (2012), 010001

[89] STAHL, C.: *Private communication*

[90] STEGMANN, R.; STAHL, C.; RAINOVSKI, G.; PIETRALLA, N.; STOYANOV, C.; CARPENTER, M.; JANSSENS, R.; LETTMANN, M.; MÖLLER, T.; MÖLLER, O.; WERNER, V. ; ZHU, S.: Identification of the one-quadrupole phonon  $2_{1,ms}^+$  state of  $^{204}\text{Hg}$ . In: *Physics Letters B* 770 (2017), 77

[91] CRAIG, D. A.; TAYLOR, H. W.: Spectroscopy of gamma rays from the decay of  $^{202,204}\text{Au}$ . In: *Journal of Physics G: Nuclear Physics* 10 (1984), 1133

[92] PAKKANEN, A.; KOMPPA, T. ; HELPPI, H.: New  $^{204}\text{Au}$  activity and the decay of  $^{202}\text{Au}$ . In: *Nuclear Physics A* 184 (1972), 157

[93] LEWIN, W.; BEZEMER, J. ; EIJK, C. V.: Some measurements on the decay of  $^{202}\text{Tl}$ . In: *Nuclear Physics* 62 (1965), 337

[94] LEUTZ, H.; SCHULZ, G. ; WENNINGER, H.: Electron capture ratios in the decay of  $^{202}\text{Tl}$ . In: *Nuclear Physics* 75 (1966), 81

- 
- [95] TAYLOR, H.: Relative  $\gamma$ -ray-emission probabilities in the decay of  $^{12.6\text{-d}}_{202}\text{Tl}$ . In: *The International Journal of Applied Radiation and Isotopes* 35 (1984), 421
- [96] BREITIG, D.; CASTEN, R. F.; KANE, W. R.; COLE, G. W.; CIZEWSKI, J. A.: Level structure and  $\gamma$  transitions in  $^{202}\text{Hg}$  studied by the  $(n, \gamma)$  reaction. In: *Physical Review C* 11 (1975), 546
- [97] LONE, M.; EARLE, E.; BARTHOLOMEW, G.: Resonance neutron capture in  $^{198,199,201}\text{Hg}$ . In: *Nuclear Physics A* 243 (1975), 413
- [98] MECCA, S.; ROTHAMEL, J.: Photoexcitation of  $^{209}\text{Bi}$  and  $^{\text{nat}}\text{Hg}$  using neutron-capture  $\gamma$ -rays from cobalt. In: *Nuclear Physics A* 201 (1973), 570
- [99] TENENBAUM, J.; MOREH, R.; NOF, A.: Properties of nuclear levels excited by neutron capture  $\gamma$ -rays from cobalt. In: *Nuclear Physics A* 218 (1974), 95
- [100] BACKE, H.; ENGFER, R.; KANKELEIT, E.; LINK, R.; MICHAELSEN, R.; PETITJEAN, C.; SCHELLENBERG, L.; SCHNEUWLY, H.; SCHRÖDER, W.; VUILLEUMIER, J.; WALTER, H.; ZEHNDER, A.: Nuclear excitation and isomer shifts in muonic atoms. In: *Nuclear Physics A* 234 (1974), 469
- [101] SCHULER, P.; RECHT, J.; WILZEK, H.; HARDT, K.; GUNTHER, C.; BLUME, K. P.; EULER, K.; KOLSCHBACH, V.: Investigation of  $^{196,198}\text{Pt}$  and  $^{202,204}\text{Hg}$  with the  $(d, p\gamma)$  Reaction. In: *Zeitschrift für Physik A - Hadrons and Nuclei* 317 (1984), 313
- [102] HOGENBIRK, A.; BLOK, H.; HARAKEH, M.: Inelastic proton scattering from  $^{198}\text{Hg}$ ,  $^{200}\text{Hg}$ ,  $^{202}\text{Hg}$  and  $^{204}\text{Hg}$  at  $E_{\text{rmp}}=28\text{MeV}$ . In: *Nuclear Physics A* 524 (1991), 251
- [103] MOYER, R. A.: Deuteron-Induced Reactions on the Even-Even Isotopes of Mercury. In: *Physical Review C* 5 (1972), 1678
- [104] AGARWAL, Y. K.; GUNTHER, C.; HARDT, K.; SCHULER, P.; STACHEL, J.; WOLLERSHEIM, H. J.; EMLING, H.; GROSSE, E.; KULESSA, R.; SPRENG, W.: Multiple Coulomb Excitation of  $^{202}\text{Hg}$  and  $^{204}\text{Hg}$ . In: *Zeitschrift für Physik A - Hadrons and Nuclei* 320 (1985), 295
- [105] LIM, C. S.; CATFORD, W. N.; SPEAR, R. H.: Measurements of E3 transition strength in the stable even-mass Hg isotopes. In: *Nuclear Physics A* 522 (1991), 635

- 
- [106] GATENBY, R.; KLEPPINGER, E. ; YATES, S.: Low-spin excitations of  $^{202}\text{Hg}$  and  $^{204}\text{Hg}$  from inelastic neutron scattering spectroscopy. In: *Nuclear Physics A* 492 (1989), 45
- [107] BACKE, H.; ENGFER, R.; JAHNKE, U.; KANKELEIT, E.; PEARCE, R.; PETITJEAN, C.; SCHELLENBERG, L.; SCHNEUWLY, H.; SCHRÖDER, W.; WALTER, H. ; ZEHNDER, A.: Study of X-rays and nuclear  $\gamma$ -rays in muonic thallium. In: *Nuclear Physics A* 189 (1972), 472
- [108] ELLEGAARD, C.; GARRETT, J. ; LIEN, J.: Studies of the  $^{204}\text{Hg}(p, t)^{202}\text{Hg}$  and  $^{204,205,206}\text{Pb}(p, t)^{202,203,204}\text{Pb}$  reactions. In: *Nuclear Physics A* 307 (1978), 125
- [109] BERAUD, R.: *Etude Spectroscopie des Isotopes  $^{202}\text{Hg}$ ,  $^{200}\text{Hg}$ ,  $^{198}\text{Hg}$  et  $^{196}\text{Hg}$* , University of Lyon, Ph.D. Thesis, 1973
- [110] BURGHARDT, A. J. C.: *The Influence of the Shell Closure on the Microscopic Structure of Even-Even Hg Isotopes. A Study with Electron and Muon Beams*, University of Amsterdam, Ph.D. Thesis, 1989
- [111] BAXTER, A. M.; HINDS, S.; SPEAR, R. H.; ZABEL, T. H. ; SMITH, R.: Octupole vibrations in the even mercury and lead isotopes. In: *Nuclear Physics A* 369 (1981), 25
- [112] POLETTI, A. R.; DRACOU LIS, G. D.; BYRNE, A. P.; STUCHBERY, A. E.; FABRICIUS, B.; KIBÈDI, T. ; DAVIDSON, P. M.: Structure of low-lying high-spin states in  $^{204}\text{Hg}$  and  $^{205}\text{Hg}$ . In: *Nuclear Physics A* 580 (1994), 64
- [113] ESAT, M. T.; FEWELL, M. P.; SPEAR, R. H.; ZABEL, T. H.; BAXTER, A. M. ; HINDS, S.: The electric quadrupole moment of the first excited state of  $^{204}\text{Hg}$ . In: *Nuclear Physics A* 362 (1981), 227
- [114] QUINT, E. N. M.; BARNETT, B. M.; BERG, A. M. d.; BRAND, J. F. J. d.; CLEMENT, H.; ENT, R.; FROIS, B.; GOUTTE, D.; GRABMAYR, P.; HERDER, J. W. A.; JANS, E.; KRAMER, G. J.; LANEN, J. B. J. M.; LAPIKÁS, L.; NANN, H.; STEENHOVEN, G. van d.; WAGNER, G. J. ; WITT HUBERTS, P. K. A.: Evidence for partial occupancy of the  $3s_{1/2}$  proton orbit in  $^{208}\text{Pb}$ . In: *Physical Review Letters* 58 (1987), 1088
- [115] DUBLER, T.; KAESER, K.; ROBERT-TISSOT, B.; SCHALLER, L.; SCHELLENBERG, L. ; SCHNEUWLY, H.: Precision test of vacuum polarization in heavy muonic atoms. In: *Nuclear Physics A* 294 (1978), 397



- 
- [116] GRABMAYR, P.; WAGNER, G.; CLEMENT, H. ; RÖHM, H.: Study of the proton shell closure of  $^{208}\text{Pb}$  through the  $^{205}\text{Tl}(p, ^3\text{He})^{204}\text{Hg}$  reaction. In: *Nuclear Physics A* 494 (1989), 244
- [117] BECCHETTI, F. D.; JÄNECKE, J.; OVERWAY, D.; COSSAIRT, J. D. ; SPROSS, R. L.:  $\alpha$  clustering in  $^{208}\text{Pb}$  from  $(d, ^6\text{Li})$  at  $E_d = 55$  MeV. In: *Physical Review C* 19 (1979), 1775
- [118] CHIARA, C.; KONDEV, F.: Nuclear Data Sheets for  $A = 204$ . In: *Nuclear Data Sheets* 111 (2010), 141
- [119] IACHELLO, F.: New Class of Low-Lying Collective Modes in Nuclei. In: *Physical Review Letters* 53 (1984), 1427
- [120] PIETRALLA, N.; BELIC, D.; VON BRENTANO, P.; FRANSEN, C.; HERZBERG, R.-D.; KNEISSEL, U.; MASER, H.; MATSCHINSKY, P.; NORD, A.; OTSUKA, T.; PITZ, H. H.; WERNER, V. ; WIEDENHÖVER, I.: Isovector quadrupole excitations in the valence shell of the vibrator nucleus  $^{136}\text{Ba}$  : Evidence from photon scattering experiments. In: *Physical Review C* 58 (1998), 796
- [121] BAUER, C.; RAINOVSKI, G.; PIETRALLA, N.; BIANCO, D.; BLAZHEV, A.; BLOCH, T.; BÖNIG, S.; DAMYANOVA, A.; DANCHEV, M.; GLADNISHKI, K. A.; KRÖLL, T.; LESKE, J.; LO IUDICE, N.; MÖLLER, T.; MOSCHNER, K.; PAKARINEN, J.; REITER, P.; SCHECK, M.; SEIDLITZ, M.; SIEBECK, B.; STAHL, C.; STEGMANN, R.; STORA, T.; STOYANOV, C.; TARPANOV, D.; VERMEULEN, M. J.; VOULOT, D.; WARR, N.; WENANDER, F.; WERNER, V. ; DE WITTE, H.: Local suppression of collectivity in the  $N = 80$  isotones at the  $Z = 58$  subshell closure. In: *Physical Review C* 88 (2013), 021302
- [122] KRÖLL, T.; KRÜCKEN, R.; BEHRENS, T.; BILDSTEIN, V.; FAESTERMANN, T.; GERNHÄUSER, R.; MAHGOUB, M.; MAIERBECK, P.; THIROLF, P.; MORGAN, T.; HABS, D.; LUTTER, R.; SCHEIT, H.; NIEDERMAIER, O.; SCHWALM, D.; WARR, N.; WEISSHAAR, D.; IWANICKI, J.; DELAHAYE, P.; WENANDER, F.; FRAILE, L.; KÖSTER, U.; VOULOT, D.; CEDERKÄLL, J.; GEORGIEV, G.; FRANCHOO, S.; SCHERILLO, A.; BUTLER, P.; HURST, A.; DUPPEN, P. V.; WALLE, J. V.; STEFANESCU, I.; HUYSE, M.; IVANOV, O.; EKSTRÖM, A.; KENT, P. ; DAVINSON, T.: Coulomb Excitation of Neutron-Rich  $A \approx 140$  Nuclei / CERN. Geneva, Jan 2006 (CERN-INTC-2006-013. INTC-P-156). – Forschungsbericht
- [123] LO BIANCO, G.; SCHMITTGEN, K. P.; ZELL, K. O. ; BRENTANO, P. v.: Electromagnetic transition probability from the ground to the first excited  $2^+$  state in  $^{138}\text{Ce}$ . In: *Zeitschrift für Physik A - Hadrons and Nuclei* 332 (1989), 103

- 
- [124] LO IUDICE, N.; STOYANOV, C.: Microscopic structure of low-lying positive parity states in nuclei near shell closure. In: *Physical Review C* 65 (2002), 064304
- [125] LO IUDICE, N.; STOYANOV, C. ; TARPANOV, D.: Fine Structure of Proton-Neutron Mixed Symmetry States in some  $N = 80$  Isotones. In: *Physical Review C* 77 (2008), 044310
- [126] STOYANOV, C.: *Private communication*
- [127] PRITYCHENKO, B.; BIRCH, M.; SINGH, B. ; HOROI, M.: Tables of E2 transition probabilities from the first states in even-even nuclei. In: *Atomic Data and Nuclear Data Tables* 107 (2016), 1
- [128] RADFORD, D.; BAKTASH, C.; BEENE, J.; FUENTES, B.; GALINDO-URIBARRI, A.; CAMPO, J. G.; GROSS, C.; HALBERT, M.; LAROCHELLE, Y.; LEWIS, T.; LIANG, J.; MAS, J.; MUELLER, P.; PADILLA, E.; SHAPIRA, D.; STRACENER, D.; VARNER, R.; YU, C.-H.; BARTON, C.; CAPRIO, M.; HARTLEY, D. ; ZAMFIR, N.: Nuclear Structure Studies with Heavy Neutron-Rich RIBS at the HRIBF. In: *Nuclear Physics A* 746 (2004), 83
- [129] MUELLER, W. F.; CARPENTER, M. P.; CHURCH, J. A.; DINCA, D. C.; GADE, A.; GLASMACHER, T.; HENDERSON, D. T.; HU, Z.; JANSSENS, R. V. F.; LISETSKIY, A. F.; LISTER, C. J.; MOORE, E. F.; PENNINGTON, T. O.; PERRY, B. C.; WIEDENHÖVER, I.; YURKEWICZ, K. L.; ZELEVINSKY, V. G. ; ZWAHLEN, H.: Variation with mass of  $B(E3; 0_1^+ \rightarrow 3_1^-)$  transition rates in  $A = 124 - 134$  even-mass xenon nuclei. In: *Physical Review C* 73 (2006), 014316
- [130] MACHLEIDT, R.: High-precision, charge-dependent Bonn nucleon-nucleon potential. In: *Physical Review C* 63 (2001), 024001
- [131] BIANCO, D.; ANDREOZZI, F.; LO IUDICE, N.; PORRINO, A. ; KNAPP, F.: Importance-Sampling Diagonalization Algorithm for Large-Scale Shell Model Calculations on  $N = 80$  Isotones. In: *Physical Review C* 85 (2012), 034332
- [132] LO IUDICE, N.: *Private communication*
- [133] CASTEN, R. F.; ZAMFIR, N. V.: The Evolution of Nuclear Structure: The  $N_p N_n$  Scheme and Related Correlations. In: *Journal of Physics G: Nuclear and Particle Physics* 22 (1996), 1521

- 
- [134] PIETRALLA, N.; FRANSEN, C.; VON BRENTANO, P.; DEWALD, A.; FITZLER, A.; FRIESSNER, C. ; GABLESKE, J.: Proton-Neutron Mixed-Symmetry  $3^+_{\text{ms}}$  State in  $^{94}\text{Mo}$ . In: *Physical Review Letters* 84 (2000), 3775
- [135] PIETRALLA, N.; FRANSEN, C.; GADE, A.; SMIRNOVA, N. A.; VON BRENTANO, P.; WERNER, V. ; YATES, S. W.: Proton-neutron structure of the effective quadrupole-octupole coupled  $E1$  transition operator. In: *Physical Review C* 68 (2003), 031305
- [136] FRANSEN, C.; PIETRALLA, N.; AMMAR, Z.; BANDYOPADHYAY, D.; BOUKHAROUBA, N.; BRENTANO, P von; DEWALD, A.; GABLESKE, J.; GADE, A.; JOLIE, J.; KNEISSL, U.; LESHER, S. R.; LISETSKIY, A. F.; MCELLESTREM, M. T.; MERRICK, M.; PITZ, H. H.; WARR, N.; WERNER, V. ; YATES, S. W.: Comprehensive studies of low-spin collective excitations in  $^{94}\text{Mo}$ . In: *Physical Review C* 67 (2003), 024307
- [137] KOICHEVA, D.; RAINOVSKI, G.; JOLIE, J.; PIETRALLA, N.; STAHL, C.; PETKOV, P.; BLAZHEV, A.; HENNIG, A.; ASTIER, A.; BRAUNROTH, T.; CORTÉS, M. L.; DEWALD, A.; DJONGOLOV, M.; FRANSEN, C.; GLADNISHKI, K.; KARAYONCHEV, V.; LITZINGER, J.; MÜLLER-GATERMANN, C.; SCHECK, M.; SCHOLZ, P.; STEGMANN, R.; THÖLE, P.; WERNER, V.; WITT, W.; WÖLK, D. ; VAN ISACKER, P.: Low-lying isovector  $2^+$  valence-shell excitations of  $^{212}\text{Po}$ . In: *Physical Review C* 93 (2016), 011303
- [138] GALÈS, S.; STOYANOV, C. ; VDOVIN, A.: Damping of high-lying single-particle modes in heavy nuclei. In: *Physics Reports* 166 (1988), 125
- [139] NIKOLAEVA, R.; STOYANOV, C. ; VDOVIN, A. I.: Microscopic Description of Low-Lying Isovector Quadrupole States in  $^{56}\text{Fe}$ . In: *Europhysics Letters* 8 (1989), 117



---

# List of Publications

- **STEGMANN R.**; STAHL, C.; RAINOVSKI, G.; PIETRALLA, N.; STOYANOV, C.; CARPENTER, M.; JANSSENS, R.; LETTMANN, M.; MÖLLER, T.; MÖLLER, O.; WERNER, V.; ZHU, S.: Identification of the one-quadrupole phonon  $2^+_{1,ms}$  state of  $^{204}\text{Hg}$ . In: *Physics Letters B* (2017), 77
- **STEGMANN R.**; STAHL, C.; RAINOVSKI, G.; PIETRALLA, N.; MÖLLER, T.; LETTMANN, M.; JANSSENS, R. V F; CARPENTER, M.; ZHU, S.: Investigation of the mixed-symmetric one-quadrupole phonon  $2^+_{1,ms}$  state of the heavy nucleus  $^{204}\text{Hg}$ . In: *Journal of Physics: Conference Series* 724 (2016), 012047
- KOICHEVA, D.; RAINOVSKI, G.; JOLIE, J.; PIETRALLA, N.; STAHL, C.; PETKOV, P.; BLAZHEV, A.; HENNIG, A.; ASTIER, A.; BRAUNROTH, T.; CORTÉS, M. L.; DEWALD, A.; DJONGOLOV, M.; FRANSEN, C.; GLADNISHKI, K.; KARAYONCHEV, V.; LITZINGER, J.; MÜLLER-GATERMANN, C.; SCHECK, M.; SCHOLZ, P; **STEGMANN R.**; THÖLE, P; WERNER, V; WITT, W; WÖLK, D. ; VAN ISACKER, P: Low-lying isovector  $2^+$  valence-shell excitations of  $^{212}\text{Po}$ . In: *Physical Review C* 93 (2016), 011303
- KOICHEVA, D.; **STEGMANN R.**; RAINOVSKI, G.; JOLIE, J.; PIETRALLA, N.; STAHL, C.; PETKOV, P; BLAZHEV, A.; HENNIG, A.; BAUER, C.; BRAUNROTH, T.; CARPENTER, M.; CORTES, L.; DEWALD, A.; DJONGOLOV, M.; FRANSEN, C.; GLADNISHKI, K.; JANSSENS, R.; KARAYONCHEV, V; LETTMANN, M.; LISTER, C.; LITZINGER, J.; MÖLLER, T.; MÖLLER-GATERMANN, C.; SCHECK, M.; SCHOLZ, P; SCHRAMM, C.; THÖLE, P; WERNER, V; WÖLK, D.; ZHU, S. ; VAN ISACKER, P: Search for mixed-symmetry states of nuclei in the vicinity of the double-magic nucleus  $^{208}\text{Pb}$ . In: *EPJ Web of Conferences* 107 (2016), 03004
- ALEXANDER, T.; PODOLYÁK, Z.; CORTES, M.; GERL, J.; RUDOLPH, D.; SARMIENTO, L.; AMEIL, F; ARICI, T; BAZZACCO, D.; BAUER, C.; BENTLEY, M.; BLAZHEV, A.; BOWRY, M.; BOUTACHKOV, P; CARROLL, R.; FAHLANDER, C.; GADEA, A.; GELLANKI, J.; GELLETLY, W; GIVECHEV, A.; GOEL, N.; GOLUBEV, P; GÓRSKA, M.; GOTTARDO, A.; GREGOR, E.; GUASTALLA, G.; HABERMANN, T.; HACKSTEIN, M.; JUNGCLAUS, A.; KOJOUHAROV, I.; KORTEN, W; KUMAR, S.; KURZ, N.; LALOVIĆ, N.; LETTMANN, M.; LIZARAZO, C.; LOUCHART, C.; MANDAL, S.; MERCHÁN, E.; MICHELAGNOLI, C.; MÖLLER, T.; MOSCHNER, K.; PATEL, Z.; PIETRALLA, N.; PIETRI, S.; RALET, D.; REESE, M.; REGAN, P; REITER, P; SCHAFFNER, H.; SINGH, P; STAHL, C.; **STEGMANN R.**; STEZOWSKI,

O.; TAPROGGE, J.; THÖLE, P.; WALKER, P.; WIELAND, O.; WENDT, A.; WILSON, E.; WOOD, R. ; WOLLERSHEIM, H.-J.: Isomeric Ratios in  $^{206}\text{Hg}$ . In: *Acta Physica Polonica, B* 46 (2015), 601

- **STEGMANN R.**; BAUER, C.; RAINOVSKI, G.; PIETRALLA, N.; STAHL, C.; BÖNIG, S.; ILIEVA, S.; BLAZHEV, A.; DAMYANOVA, A.; DANCHEV, M.; GLADNISHKI, K.; JOLIE, J.; LUTTER, R.; PAKARINEN, J.; RADECK, D.; RAPISARDA, E.; REITER, P.; SCHECK, M.; SIEBECK, B.; STORA, T.; THÖLE, P.; THOMAS, T.; THÜRAUF, M.; VERMEULEN, M. J.; VOULOT, D.; WARR, N.; WENANDER, F.; WERNER, V. ; DE WITTE, H.: Evolution of quadrupole collectivity in  $N = 80$  isotones toward the  $Z = 64$  subshell gap: The  $B(E2; 2_1^+ \rightarrow 0_1^+)$  value of  $^{142}\text{Sm}$ . In: *Physical Review C* 91 (2015), 054326
- BAUER, C.; **STEGMANN R.**; RAINOVSKI, G.; PIETRALLA, N.; BLAZHEV, A.; BÖNIG, S.; DAMYANOVA, A.; DANCHEV, M.; GLADNISHKI, K. A.; LUTTER, R.; MARSH, B. A.; MÖLLER, T.; PAKARINEN, J.; RADECK, D.; RAPISARDA, E.; REITER, P.; SCHECK, M.; SEIDLITZ, M.; SIEBECK, B.; STAHL, C.; THÖLE, P.; THOMAS, T.; THÜRAUF, M.; WARR, N.; WERNER, V. ; WITTE, H. de: Evolution of Collectivity in the  $N = 80$  Isotones. In: *Proceedings of the First International African Symposium on Exotic Nuclei* (2015)
- BÖNIG, S.; ILIEVA, S.; KRÖLL, T.; SCHECK, M.; BALABANSKI, D.; BAUER, C.; BLAZHEV, A.; BLOCH, T.; DELEANU, D.; DIRIKEN, J.; FERNIER, P.; GERNHÄUSER, R.; HADYŃSKA-KĘK, K.; JUNGCLAUS, A.; LUTTER, R.; NEGRET, A.; NOWAK, K.; ORLANDI, R.; PAKARINEN, J.; RAINOVSKI, G.; RODRÍGUEZ, T.; SCHMID, M. v.; SEIDLITZ, M.; SIEBECK, B.; SIMPSON, G.; SISÓN, A. I.; **STEGMANN R.**; STORA, T.; THIROLF, P.; THÜRAUF, M.; VERMEULEN, M.; VOULOT, D.; WARR, N.; WENANDER, F.; DE WITTE, H. ; MINIBALL COLLABORATION: Quadrupole collectivity in neutron-rich Cd isotopes. In: *EPJ Web of Conferences* 66 (2014), 02012
- JÜRGENSEN, L.; BONNES, U.; BURANDT, C.; FISCHER, M.; HUG, F.; KÜRZEDER, T.; PIETRALLA, N.; **STEGMANN R.** ; STEINHORST, M.: Installation of a Beam Loss Monitoring System at the S-DALINAC. In: *Proceedings of IBIC 2014, Monterey, CA, USA* (2014), 470
- BAUER, C.; RAINOVSKI, G.; PIETRALLA, N.; BIANCO, D.; BLAZHEV, A.; BLOCH, T.; BÖNIG, S.; DAMYANOVA, A.; DANCHEV, M.; GLADNISHKI, K. A.; KRÖLL, T.; LESKE, J.; LO IUDICE, N.; MÖLLER, T.; MOSCHNER, K.; PAKARINEN, J.; REITER, P.; SCHECK, M.; SEIDLITZ, M.; SIEBECK, B.; STAHL, C.; **STEGMANN R.**; STORA, T.; STOYANOV, C.; TARPANOV, D.; VERMEULEN, M. J.; VOULOT, D.; WARR, N.; WENANDER, F.; WERNER, V. ; DE WITTE, H.: Local suppression of collectivity in the  $N = 80$  isotones at the  $Z = 58$  subshell closure. In: *Physical Review C* 88 (2013), 021302

- 
- BAUER, C.; GUASTALLA, G.; LESKE, J.; MÖLLER, O.; MÖLLER, T.; PAKARINEN, J.; PIETRALLA, N.; RAINOVSKI, G.; RAPISARDA, E.; SEWERYNIAK, D.; STAHL, C.; **STEGMANN R.**; WIEDERHOLD, J. ; ZHU, S.: Level lifetimes and quadrupole moments from Coulomb excitation in the Ba chain and the  $N = 80$  isotones. In: *EPJ Web of Conferences* 38 (2012), 10003
  - **STEGMANN R.**; BONNES, U.; BURANDT, C.; EICHHORN, R.; HUG, E.; JÜRGENSEN, L.; PIETRALLA, N. ; PROFT, D.: Installation and Test of a Beam Loss Monitor System for the S-DALINAC. In: *Proceedings of IPAC 2012, New Orleans, LA, USA* (2012), 804





---

# List of Figures

1.1. Nuclear chart showing $R_{4/2}$ ratios . . . . .	10
2.1. Sketch of the Coulomb-excitation scattering process . . . . .	15
2.2. Schematic of first and second order Coulomb excitation processes . .	23
2.3. Cross sections for various static quadrupole moments . . . . .	24
2.4. Attenuation coefficients for the $2_1^+ \rightarrow 0_1^+$ transition in $^{202}\text{Hg}$ . . . . .	36
2.5. Angular distribution evolution of the $2_1^+$ decay in $^{202}\text{Hg}$ . . . . .	37
3.1. Vibrational and rotational low-lying level scheme . . . . .	45
3.2. Illustration of the shell model orbitals . . . . .	48
3.3. IBM-2 low-lying level scheme . . . . .	53
4.1. Schematic picture of the ISOLDE facility ground floor . . . . .	58
4.2. Schematic picture of the REX installation . . . . .	61
4.3. Schematic picture of the REX beam preparation . . . . .	62
4.4. Schematic picture of the REX acceleration structures . . . . .	63
4.5. Time structure of REX beams . . . . .	64
4.6. Schematic picture of the DSSS detector . . . . .	65
4.7. Schematic picture of the ATLAS facility . . . . .	67
4.8. Photography of the Gammasphere HPGe detector array . . . . .	69
4.9. Schematic transverse section of a Gammasphere HPGe detector . . .	72
5.1. Overview of the Gammasphere raw data format . . . . .	75
5.2. Miniball particle- $\gamma$ time difference spectrum . . . . .	81
5.3. Gammasphere time difference spectrum . . . . .	82
5.4. Background subtraction procedure . . . . .	83
5.5. Efficiency calibration of the Miniball experiments . . . . .	85
5.6. Efficiency calibration of the Gammasphere experiments . . . . .	86
5.7. Multiplicity distribution of the $^{202}\text{Hg}$ experiment . . . . .	88
5.8. Bare $\gamma$ - $\gamma$ matrix of the $^{202}\text{Hg}$ experiment . . . . .	88
5.9. Comparison of self-coincidence subtracted spectra . . . . .	89
5.10. Particle- $\gamma$ coincidence particle spectra of $^{142}\text{Sm}$ . . . . .	98
5.11. Particle- $\gamma$ coincidence $\gamma$ ray spectra of $^{142}\text{Sm}$ . . . . .	99

5.12.	Decay scheme for $A = 142$ beam components . . . . .	100
5.13.	Decay spectra of projectile nuclei . . . . .	101
5.14.	REX-ISOLDE bunch structure used in decay spectroscopy . . . . .	102
5.15.	Total $\gamma$ ray spectrum for $A = 142$ beam composition analysis . . . . .	103
5.16.	Activity of 768-keV $\gamma$ rays from $^{142g,m}\text{Eu}$ decay . . . . .	104
5.17.	Result of the $^{142}\text{Sm}$ Maximum-Likelihood Analysis . . . . .	108
5.18.	$\gamma$ ray spectra of $^{202}\text{Hg}$ . . . . .	110
5.19.	Partial experimental level scheme of $^{202}\text{Hg}$ . . . . .	111
5.20.	Angular distributions of $^{202}\text{Hg}$ . . . . .	114
5.21.	$\gamma$ ray spectra of $^{204}\text{Hg}$ . . . . .	119
5.22.	Partial experimental level scheme of $^{204}\text{Hg}$ . . . . .	120
5.23.	Angular distributions of $^{204}\text{Hg}$ . . . . .	122
6.1.	Evolution of $B(M1; 2_1^+ \rightarrow 2_1^+)$ in the $N = 80$ isotones . . . . .	126
6.2.	Evolution of $B(E2; 2_1^+ \rightarrow 0_{1,gs}^+)$ , $E_{2_1^+}$ and $R_{4/2}$ in the $N = 80$ isotones . . . . .	127
6.3.	Evolution of $B(E2; 2_1^+ \rightarrow 0_{1,gs}^+)$ in comparison to LSSM and QPM . . . . .	128
6.4.	Evolution of $B(E2; 2_1^+ \rightarrow 0_{1,gs}^+)$ with $N_\pi N_\nu$ scaling . . . . .	130
6.5.	Valence nucleon configuration of $^{202,204}\text{Hg}$ . . . . .	132
6.6.	Experimental and QPM level schemes . . . . .	136
6.7.	Comparison of the results for $^{204}\text{Hg}$ with literature and QPM . . . . .	138
6.8.	Overview over M1 strengths around $^{208}\text{Pb}$ . . . . .	142
E.1.	Particle- $\gamma$ coincidence particle spectra of $^{142}\text{Sm}$ . . . . .	167
E.2.	$\gamma$ ray spectra of the $^{142}\text{Sm} + ^{48}\text{Ti}$ experiment . . . . .	168
E.3.	$\gamma$ ray spectra of the $^{142}\text{Sm} + ^{94}\text{Mo}$ experiment . . . . .	169
E.4.	Ringwise efficiency curves for $^{202}\text{Hg}$ . . . . .	170
E.5.	$\gamma$ ray singles spectrum of $^{202}\text{Hg}$ . . . . .	171
E.6.	$\gamma$ ray spectrum in coincidence to the $2_1^+ \rightarrow 0_{1,gs}^+$ transition of $^{202}\text{Hg}$ . . . . .	172
E.7.	$\gamma$ ray spectrum in coincidence to the $2_2^+ \rightarrow 2_1^+$ transition of $^{202}\text{Hg}$ . . . . .	173
E.8.	Ringwise spectra of the $2_2^+ \rightarrow 2_1^+$ & $4_1^+ \rightarrow 2_1^+$ transitions of $^{202}\text{Hg}$ . . . . .	174
E.9.	Ringwise spectra of the $2_7^+ \rightarrow 2_1^+$ transition of $^{202}\text{Hg}$ . . . . .	175
E.10.	Ringwise efficiency curves for $^{204}\text{Hg}$ . . . . .	176
E.11.	$\gamma$ ray singles spectrum of $^{204}\text{Hg}$ . . . . .	177
E.12.	$\gamma$ ray spectrum in coincidence to the $2_1^+ \rightarrow 0_{1,gs}^+$ transition of $^{204}\text{Hg}$ . . . . .	178
E.13.	$\gamma$ ray spectrum in coincidence to the $4_1^+ \rightarrow 2_1^+$ transition of $^{204}\text{Hg}$ . . . . .	179
E.14.	Ringwise spectra of the $4_1^+ \rightarrow 2_1^+$ transition of $^{204}\text{Hg}$ . . . . .	180
E.15.	Ringwise spectra of the $2_2^+ \rightarrow 2_1^+$ transition of $^{204}\text{Hg}$ . . . . .	181

---

# List of Tables

4.1. Polar angles of the Gammasphere rings . . . . . 70

4.2. List of conducted experiments . . . . . 71

5.1. Total  $\gamma$  intensity for  $A = 142$  beam composition analysis . . . . . 105

5.2.  $\gamma$  ray intensities from  $^{142}\text{Sm} + ^{48}\text{Ti}$  . . . . . 106

5.3.  $\gamma$  ray intensities from  $^{142}\text{Sm} + ^{94}\text{Mo}$  . . . . . 106

5.4. Matrix elements of  $^{48}\text{Ti}$  and  $^{94}\text{Mo}$  for normalization . . . . . 107

5.5. Results of the analysis of the  $^{202}\text{Hg}$  data . . . . . 116

5.6. Results of the analysis of the  $^{204}\text{Hg}$  data . . . . . 124

6.1. Results of QPM calculations for  $^{204}\text{Hg}$  . . . . . 135



---

# Acknowledgments

I want to thank all the people supporting me during the years of this thesis, some of them directly with professional advice, some of them by caring about my well-being. I want to thank:

Professor **Norbert Pietralla** for giving me the opportunity to work on this thesis. He was always open for questions and discussions, providing valuable suggestions regarding issues which appeared during the analysis.


Professor **Georgi Rainovski**, with whom I had many discussions about numerous topics of nuclear structure physics, no matter whether it was on the interpretation of results or on experimental details.

Dr **Volker Werner** for various discussions about and explanations of physical details not directly related to my work.

The former crew of office 7, **Christopher Bauer** and **Thomas Möller**, for introducing me to the interesting topic of Coulomb excitation, and inducting me to the details of the analysis and the physics behind. **Christian Stahl**, who was not directly into the conventional Coulomb excitation business, but his expertise on various topics was nevertheless of big help. My student **Ralph Kern** for doing a nice Master's Thesis.

My colleagues and friends at the Institut für Kernphysik, in particular **Tobias Beck**, **Udo Gayer**, **Ruben Grewe**, **Tania Ilieva**, **Lars Jürgensen**, **Tobias Klaus**, **Marc Lettmann**, **Philipp Napiralla**, **Philipp Ries**, **Christopher Romig**, **Marcel Schilling**, **Urs Schulz**, **Michael Thürauf**, **Johannes Wiederhold**, **Markus Zweidinger**, and all the other people currently or former working at the IKP I forgot, for providing fruitful discussions, but also a lot of distraction and fun.

The group of people I met in the first semesters of my physics studies, which established a decent working atmosphere besides the lots of fun we had together, namely **Tobias Eggert**, **Dominik Geist**, **Dirk Heinen**, **Jonas Löbig**, **Antje Neumann**, **Nico Neumann**, and **Stefan Schürl**.



---

Last but not least, I want to thank my parents **Dieter** and **Sabine**, my girlfriend **Michaela** and my brother **Jürgen** for unconditionally and continuously supporting me throughout all the years.

This work was supported by the DFG under grant No. PI 393/2-3 and the BMBF by grant Nos. 05P12RDCIB and 05P15RDCIA.

---

# Lebenslauf

## Persönliche Daten

Name	Robert Stegmann
Geburtsdatum	26.11.1987
Geburtsort	Offenbach a.M.
Staatsangehörigkeit	Deutsch
Familienstand	Ledig

## Schul Ausbildung

1993 - 1998	Anna-Freud-Schule Mainflingen (Grundschule)
1998 - 2007	Einhardschule Seligenstadt (Gymnasium)
2007	Abitur

## Zivildienst

2007 - 2008	Agaplesion Simeonstift, Hainburg
-------------	----------------------------------

## Hochschulausbildung

2008 - 2011	TU Darmstadt B.Sc. Physik <i>Untersuchung der Deformation des ersten angeregten <math>2^+</math> Zustands im radioaktiven Isotop <math>^{142}\text{Ba}</math> mit Hilfe von Coulomb-Anregung</i>
2011 - 2013	TU Darmstadt M.Sc. Physik <i>Untersuchung des <math>2_1^+</math>-Zustands in den radioaktiven Isotopen <math>^{140,142}\text{Sm}</math> mit Hilfe von Coulomb-Anregung</i>
seit 2013	TU Darmstadt Doktorand, wissenschaftlicher Mitarbeiter





---

# Erklärung zur Dissertation

Hiermit versichere ich, die vorliegende Dissertation ohne Hilfe Dritter nur mit den angegebenen Quellen und Hilfsmitteln angefertigt zu haben. Alle Stellen, die aus Quellen entnommen wurden, sind als solche kenntlich gemacht. Diese Arbeit hat in gleicher oder ähnlicher Form noch keiner Prüfungsbehörde vorgelegen.

Darmstadt, den 13. Juni 2017

---

(R. Stegmann)

